UNIVERSITY OF SOUTHAMPTON

Faculty of Natural and Environmental Sciences
School of Ocean & Earth Science

A geochemical investigation of seafloor methane seepage at the landward limit of the hydrate stability zone offshore Western Svalbard

by

Carolyn Alice Graves

Thesis for the degree of Doctor of Philosophy

February 2015

UNIVERSITY OF SOUTHAMPTON

ABSTRACT

FACULTY OF NATURAL AND ENVIRONMENTAL SCIENCES

Ocean and Earth Science

Doctor of Philosophy

A GEOCHEMICAL INVESTIGATION OF SEAFLOOR METHANE SEEPAGE AT THE LANDWARD LIMIT OF THE HYDRATE STABILITY ZONE OFFSHORE WESTERN SVALBARD

by Carolyn Alice Graves

A significant proportion of the world's organic carbon is trapped in submarine methane hydrates. When ocean bottom waters warm, these hydrates may be destabilised, releasing gaseous methane into the surrounding sediments and potentially into the overlying water column and atmosphere. Increased atmospheric methane contributes to further warming as methane is a potent greenhouse gas. Release of methane from hydrate may have accompanied some paleoclimate warming events, but observations of hydrate destabilization due to current global warming remain unconfirmed. The discovery of more than 250 seafloor methane bubble plumes close to the limit of the gas hydrate stability zone offshore Western Svalbard has recently been linked to increases in bottom water temperature in this region over the past 30 years. To assess the source and fate of this methane, this thesis presents a geochemical study of hydrate, sediments, seawater, and gas in the vicinity of the seafloor methane seepage.

Analyses of the gas molecular and isotopic compositions reveals that hydrate-bound gas, free gas in shallow sediments, and gas bubbles entering the water column at seafloor seep sites all have the same source. The gas is thermogenic gas produced offshore that has migrated laterally to the continental slope and shelf region. Transport-reaction modelling of pore water chemistry shows that active anaerobic oxidation of methane in sediments is an effective barrier to release of methane into ocean bottom waters. However, small fractures and faults allow ~90% of the methane that enters near-surface sediments to bubble into the water column at localized seafloor seeps. Analyses of the methane distribution in the water column indicate that the methane in the bubbles rapidly dissolves in seawater, and is transported northwards at depth in the West Svalbard Current. As a result, there is limited vertical exchange of methane between deep and surface waters. Surface waters are nevertheless supersaturated due to isopycnal mixing with methane-rich waters from the shallow shelf onto the upper slope. Measurements of methane mixing ratios in air indicate that the sea to air methane flux offshore Western Svalbard does not make a significant contribution to the local atmospheric methane budget.

Sedimentary records of the $\delta^{13}C$-CH_4 signature of benthic foraminifera provide evidence for intermittent methane seepage at the current limit of hydrate stability (~400 m water depth) over the last ~20,000 years. Although this is likely due to changes in hydrate stability as a result of changes in bottom water temperature, we find no evidence for this in the current data set.

Contents

3. Methane in shallow subsurface sediments at the landward limit of the gas hydrate stability zone offshore Western Svalbard……………………………………..33

4. Fluxes and fate of dissolved methane released at the seafloor at the landward limit of the gas hydrate stability zone offshore Western Svalbard………………...….61

5. History of methane seepage on the upper continental margin offshore Western Svalbard……………………….……………………………………………………85

List of tables

List of figures

DECLARATION OF AUTHORSHIP

I, ***Carolyn Alice Graves*** declare that this thesis and the work presented in it are my own and has been generated by me as the result of my own original research.

A geochemical investigation of seafloor methane seepage at the landward limit of the hydrate stability zone offshore Western Svalbard

I confirm that:

1. This work was done wholly or mainly while in candidature for a research degree at this University;
2. Where any part of this thesis has previously been submitted for a degree or any other qualification at this University or any other institution, this has been clearly stated;
3. Where I have consulted the published work of others, this is always clearly attributed;
4. Where I have quoted from the work of others, the source is always given. With the exception of such quotations, this thesis is entirely my own work;
5. I have acknowledged all main sources of help;
6. Where the thesis is based on work done by myself jointly with others, I have made clear exactly what was done by others and what I have contributed myself;
7. None of this work had been published before initial submission. *Appendices A* and *B* have now been published as: Steinle, L., Graves, C.A., Treude, T., Ferre, B., Biastoch, A., Bussmann, I., Berndt, C., Krastel, S., James, R.H., Behrens, E., Boning, C.W., Greinert, J., Sapart, C.-J., Scheinert, M., Sommer, S., Lehmann, M.F. and Niemann, H. (2015) Water column methanotrophy controlled by a rapid oceanographic switch. *Nature Geoscience* **8**, 378-382, doi: 10.1038/ngeo2420.

Signed:………………………………………………………………………………………..

Date:…………………………………………………………………………………………..

Acknowledgements

This work could not have come together without the help and support of many people who I have been privileged to work with over the past three and a half years.

First, thank you to my supervisors, Rachael James and Doug Connelly, for your guidance, for providing direction when needed, and for allowing me to enrich my PhD experience by occasionally meandering from the most direct path. Thank you to my panel chair, Rachel Mills, for your encouragement and support.

I am fortunate to have a number of collaborators to thank: Giuliana Panieri, for patiently teaching me about foraminifera and providing endless enthusiasm, guidance, and support for that portion of my project; Lea Steinle, for your friendship and many productive conversations about our data; Helge Niemann and Tina Treude, for your guidance at sea and afterwards; Gregor Rehder for sharing your equilibrator system data with me and the resulting productive and motivational discussion of data interpretation in the water column; Andy Stott for patiently teaching me about isotopic analysis; Euan Nisbet's group at Royal Holloway (Rebecca, Dave, and James) for all things atmospheric and for guiding me around AGU; and Célia Sapart for deuterium isotope analysis. Additionally, thank you to everyone who I've had the pleasure of going to sea with, who I'm delighted are far too many to name. Thank you to the principal scientists of the cruises where the bulk of this data was collected: Ian Wright and Christian Berndt. Thank you Cathy Cole, I will always be indebted to you for your work on the nights shifts of JR253 collecting and analysing samples for this project, as well as being generally supportive, inspirational and understanding.

Vicky Bertics, I hope you knew what an enormous impact your kindness, honesty, and guidance, both scientific and general had on me as a researcher and as a person. I'm enormously lucky to have laughed, cried, sung, danced, and worked with you, my life is enriched for having known you.

Thank you to those who have supported this work at the National Oceanography Centre. In the NERC labs: Belinda Alker, Darryl Green, Kate Peel, and Suzie Maclachlan (BOSCORF). Anna Lichtschlag, for caring, and for your invaluable advice. Eleanor Frajka-Williams, for letting me explain my box model to you, and sharing your expertise. Everyone who listened to me talk at NOCS Svalbard meetings, especially Bedanta Goswami for many productive conversations.

Completing a PhD would have been impossible without the many friends who had nothing to do with the project, but provided endless advice, help, and support throughout the journey. Thank you all! To my wonderful officemates: Morelia, Cathy, Jessy, Sarah, Heather and Dave, and to the housemate family: Leah, Sara, Tom and Tish. To my fellow North Americans Wendy and Jen, and opposite-at-sea Hannah. To Lydia, for all the chats and friendship through this degree and the last (!); and to Jen Clarke for always being there and understanding how my brain works. A separate thank you to my wonderful supportive, inspirational, and caring parents and sister.

This work was funded by an International Studentship from the Graduate School of the National Oceanography Centre, and by Postgraduate Scholarships from the Natural Sciences and Engineering Research Council of Canada. Thank you for giving me this amazing opportunity.

Definitions and abbreviations

^{12}C	carbon-12
^{13}C	carbon-13
^{14}C	carbon-14; radiocarbon
^{18}O	oxygen-18
AOM	anaerobic oxidation of methane
$BaSO_4$	barite; barium sulphate
BOSCORF	British Ocean Sediment Core Research Facility
BP	before present
Br^-	bromide
BSR	bottom simulating reflector
C_1	methane
C_2	ethane
C_{2+}	ethane and heavier hydrocarbons
C_3	propane
C_4	butane
C_5	pentane
C_6	hexane
Ca	calcium
CF-IRMS	continuous flow isotope ratio mass spectrometer
CH_4	methane
CIE	carbon isotope excursion
Cl^-	chloride
CO_2	carbon dioxide
CTD	conductivity-temperature-depth
$\delta^{13}C$	carbon isotopic signature: $^{13}C/^{12}C$ relative to VPDB standard
δD	hydrogen isotopic signature: $D/^{1}H$ relative to VSMOW standard
$\delta^{18}O$	oxygen isotopic signature: $^{18}O/^{16}O$ relative to VSMOW standard
D	deuterium
DIC	dissolved inorganic carbon
ΔR	regional reservoir correction for radiocarbon dates
ESC	East Spitsbergen Current

Fe	iron
GHG	greenhouse gas
GHSZ	gas hydrate stability zone
H	hydrogen
HCO_3^-	bicarbonate
HO•	hydroxyl radical
ICP-OES	inductively coupled plasma optical emission spectrometry
IRMS	isotope ratio mass spectrometry
ka	thousand years
MCA	methane carbon dioxide analyser
MOx	aerobic oxidation of methane
N_2O	nitrous oxide
Na^+	sodium
NOC	National Oceanography Centre (Southampton, UK)
oa-ICOS	off axis integrated cavity output spectroscopy
ODP	Ocean Drilling Project
PETM	Palaeocene-Eocene thermal maximum
S	sulphur
S^{2-}	sulphide
SEM	scanning electron microscopy
SMTZ	sulphate-methane transition zone
SO_4	sulphate
TC	total carbon
Ti	titanium
TIC	total inorganic carbon
TOC	total organic carbon
VPDB	Vienna Pee Dee Belemnite
VSMOW	Vienna Standard Mean Ocean Water
WSC	West Spitsbergen Current

CHAPTER 1

Introduction

Contents

In the context of ongoing global warming and atmospheric greenhouse gas forcing, it is critical to understand how the many interconnected parts of the climate system are responding, and how this response might change in the future. Insight into these processes lies in the geological record of past periods of climate forcing and climate shifts, as well as in the detailed investigation of specific environments which provide examples of active climate response. This chapter outlines the global context for the role of marine methane hydrate in the earth's climate system in the past, present, and future.

1.1. Methane in the atmosphere

1.1.1. Greenhouse gases

The presence of greenhouse gasses in the earth's atmosphere is an important control on global climate. Greenhouse gases (GHGs) absorb the long wave solar energy reflected back into the atmosphere by the earth, acting to trap energy as heat near the earth's surface (*Figure 1.1*; Cubasch et al. [2013]). The natural greenhouse effect results in an average surface temperature 32 °C warmer than would be experienced without GHGs [IPCC, 1990].

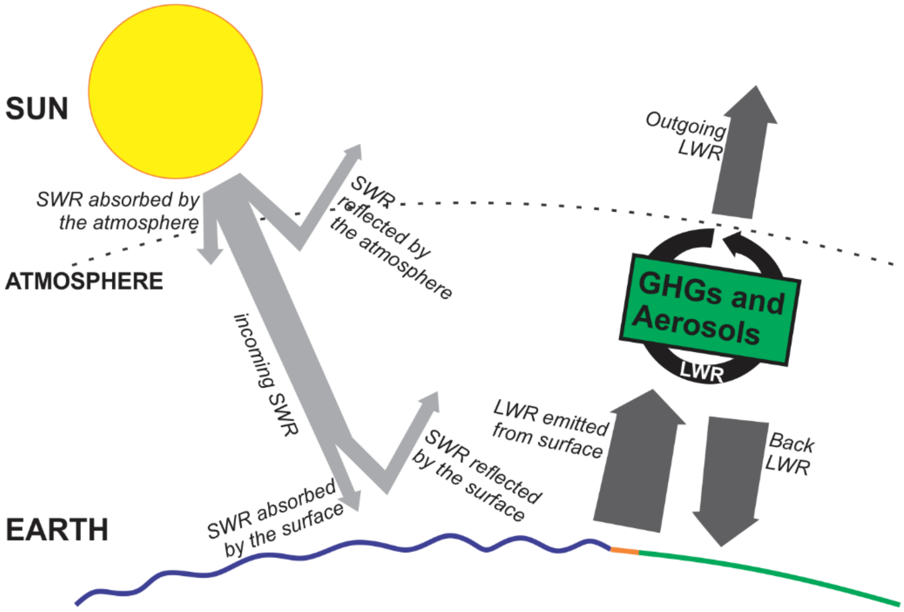

Figure 1-1 Schematic representation of the greenhouse effect. SWR: short wave radiation; LWR: long wave radiation; GHG: greenhouse gas. Adapted from Cubasch et al. [2013].

GHSs include water vapour, carbon dioxide (CO_2), methane (CH_4), nitrous oxide (N_2O) and many others. The relative importance of the GHGs is determined by the efficiency with which they trap energy (their radiative forcing), and their concentration and persistence in the atmosphere. Water vapour makes the strongest contribution to the natural greenhouse effect, but is not typically considered in the discussion of climate warming because concentrations are controlled largely by temperature, and it therefore responds to rather than forces climate [Myhre et al., 2013]. The concentrations, lifetimes, radiative forcing, and rate of concentration increase of the well-mixed greenhouse gases are shown in *Table 1-1* [Archer et al., 2009b; Hartmann et al., 2013].

A molecule of methane traps solar energy ~ 25 times more efficiently than CO_2, but is two orders of magnitude less abundant in the atmosphere and persists for only ~ 10 years. These parameters are considered together to estimate the global warming potential of CH_4 relative to CO_2: 85 over 20 years, and 29 over 100 years [Myhre et al., 2013].

Table 1-1 Atmospheric lifetimes, radiative efficiencies, concentrations, and recent concentration increases of the well-mixed greenhouse gases. Data from Hartmann et al. [2013]. Concentrations are in parts per thousand except where otherwise noted. No lifetime is given for CO_2 because its decay in the atmosphere is extremely non-linear, with substantial climate effects of strong emissions expected to persist for tens to hundreds of thousands of years [Archer et al., 2009].

	Lifetime (yr)	**Radiative Efficiency (W m^{-2} ppb^{-1})**	**Concentration (ppt, in 2011)**	**Concentration Increase from 2005 to 2011 (ppt)**
CO_2 (ppm)	**	1.37 x 10^{-5}	390.48 ± 0.28	11.67 ± 0.37
CH_4 (ppb)	9.1	3.63 x 10^{-4}	1803.1 ± 1.2	28.9 ± 6.8
N_2O (ppb)	131	3.03 x 10^{-3}	324 ± 0.1	4.7 ± 0.2
SF_6	3200	0.6	7.26 ± 0.02	1.64 ± 0.1
CF_4	50,000	0.1	79 ± 0.1	4 ± 0.2
C_2F_6	10,000	0.26	4.16 ± 0.02	0.5 ± 0.03
HFC-125	28.2	0.219	9.58 ± 0.04	5.89 ± 0.07
HFC-134a	13.4	0.159	62.4 ± 0.3	28.2 ± 0.4
HFC-143a	47.1	0.159	12.04 ± 0.7	6.39 ± 0.1
HFC-152a	1.5	0.094	6.4 ± 0.1	3 ± 0.2
HFC-23	222	0.176	24 ± 0.3	5.2 ± 0.6
CFC-11	45	0.263	236.9 ± 0.1	- 12.7 ± 0.2
CFC-12	100	0.32	529.5 ± 0.2	- 13.4 ± 0.3
CFC-113	85	0.3	74.29 ± 0.06	- 4.25 ± 0.08
HCFC-22	11.9	0.2	213.4 ± 0.8	44.6 ± 1.1
HCFC-141b	9.2	0.152	21.38 ± 0.09	3.7 ± 0.1
HCFC-142b	17.2	0.186	21.35 ± 0.06	5.72 ± 0.09
CCl_4	26	0.175	85 ± 0.1	- 6.9 ± 0.2
CH_3CCl_3	5	0.069	6.3 ± 0.1	- 11.9 ± 0.2

1.1.2. Sources and sinks of atmospheric methane

The atmospheric concentrations of GHGs are a balance of their sources and sinks; increasing concentrations result from a net excess of sources over sinks. Total global methane emissions are relatively well-constrained, but the contributions of individual sources remain much more uncertain [Dlugokencky et al., 2011]. Important sources of atmospheric methane and their contributions to the total atmospheric methane inventory over the last decade (2000-2009) are shown in *Table 1-2* and *Figure 1-2* [Kirschke et al., 2013].

Table 1-2 Sources of atmospheric methane for the period between 2000 and 2009. Numbers in square brackets indicate maximum and minimum values. Top-down estimates employ inversion models to fit atmospheric observations, while bottom-up estimates model specific processes using global datasets [Ciais et al., 2013; Kirschke et al., 2013].

	Tg CH_4 yr^{-1}	
	Top-down	**Bottom-up**
Natural sources	**218 [179 - 273]**	**347 [238 - 484]**
Natural wetlands	175 [142 - 208]	217 [177 - 284]
Other sources	43 [37 - 65]	130 [61 - 200]
Lakes and rivers		40 [8 - 73]
Wild animals		15 [15 - 15]
Wildfires		3 [1 - 3]
Termites		11 [2 - 11]
Geological (including oceans)		54 [33 - 75]
Hydrates		6 [2 - 9]
Permafrost (excluding lakes and wetland)		1 [0 - 1]
Anthropogenic sources	**335 [273 - 409]**	**331 [304 - 368]**
Agriculture and water	209 [180 - 241]	200 [187 - 224]
Biomass burning	30 [24 - 45]	35 [32 - 39]
Fossil fuels	96 [77 - 123]	96 [85 - 105]
Total	**548 [526 - 569]**	**678 [542 - 852]**
Growth rate	**6**	

The dominant sink of atmospheric methane is oxidation by the hydroxyl radical (HO• ; Myhre et al. [2013]). The rate of methane removal from the atmosphere is therefore sensitive to the availability of this oxidant. Many atmospheric species including methane and its oxidation products are involved in the production and removal of atmospheric HO•, which leads to a variable and uncertain methane atmospheric lifetime in the past and in future projections [Holmes et al., 2013]. The net result of the chemical coupling between atmospheric methane and HO• concentrations is an amplification of the effect of methane emissions on the climate system [Myhre et al., 2013]. The final carbon-containing product of methane oxidation in the atmosphere is carbon dioxide. Methane emissions therefore continue to contribute to the greenhouse effect over longer periods as carbon dioxide (e.g. Archer et al. [2009a]). Other atmospheric methane sinks are oxidation in soil and loss to the stratosphere, which account for ~ 7 and 5 % of total methane removal from the atmosphere, respectively [Wuebbles and Hayhoe, 2002].

Methane isotopic signatures provide important constraints on the atmospheric budget. The relative abundance of the two stable carbon isotopes (^{12}C and ^{13}C), as well as the presence of radiocarbon (^{14}C), and hydrogen isotopic ratios (^{1}H and deuterium: D), distinguish sources that variably favour incorporation of different isotopes [Dlugokencky et al., 2011; Kvenvolden and Rogers, 2005; Neef et al., 2010]. Isotopic signatures are reported relative to standards Vienna Pee Dee Belemnite (VPDB) for $^{13}C/^{12}C$ and Vienna Standard Mean Ocean Water (VSMOW) for D/H, in per mil (‰) notation [Whiticar, 1999]:

$$\delta^{13}C = \frac{\left(^{13}C/^{12}C\right)_{sample}-1}{\left(^{13}C/^{12}C\right)_{standard}} \cdot 1000\ ‰\ ;\ \delta D = \frac{(D/H)_{sample}-1}{(D/H)_{standard}} \cdot 1000\ ‰ \qquad (1\text{-}1)$$

$\delta^{13}C$ of atmospheric methane sources range from -17 ‰ for biomass burning to – 70 ‰ for enteric fermentation, while δD range from -175 ‰ for energy production to -323 ‰ for rice agriculture [Dlugokencky et al., 2011]. Fossil, or geological, methane which contains no ^{14}C is made up of carbon from organic matter more than 35,000 years old, and accounts for 18 to 30 % of the atmospheric methane budget [Kvenvolden and Rogers, 2005; Neef et al., 2010].

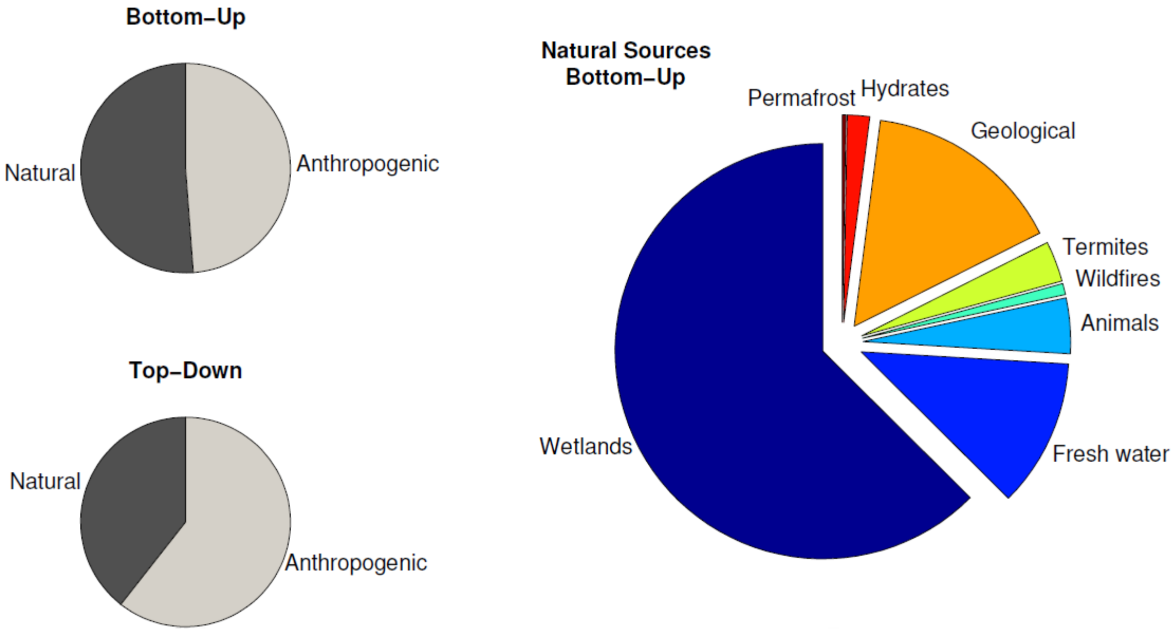

Figure 1-2 Sources of atmospheric methane between for the period 2000 and 2009. Uncertainties are given in *Table 1-2*. Data from Kirschke et al. [2013].

1.1.3. Atmospheric methane concentrations

The current global average atmospheric methane concentration is ~ 1800 ppb, with a $\delta^{13}C$ ~ -52.9 ‰ and a δD ~ -280 ‰ [Dlugokencky et al., 2011]. Since pre-industrial times (1750 AD), the amount of methane in the atmosphere has more than doubled (*Figure 1-3B*; Hartmann et al. [2013]). However, the rate of methane concentration increase slowed after 1990, and concentrations remained relatively constant from 1999 to 2006 before beginning

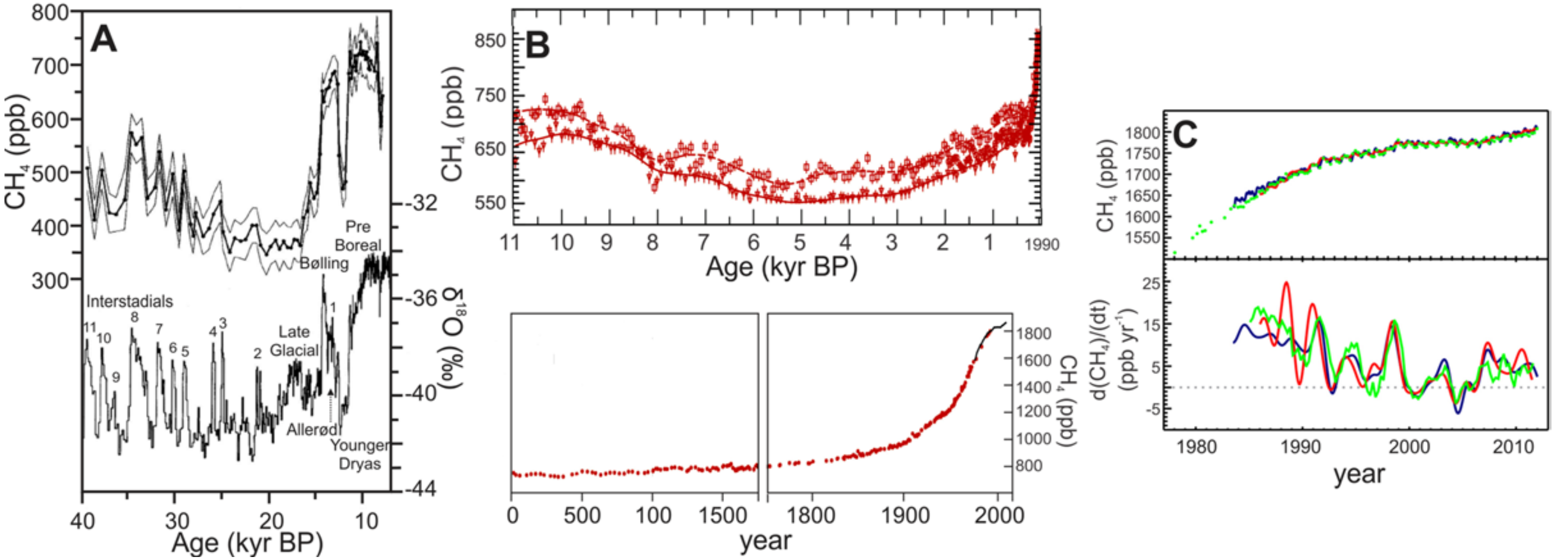

Figure 1-3 (**A**) Ice core record of methane concentration (upper panel, mean and 2σ experimental uncertainty) and the δ^{18}O temperature proxy (lower panel), with recent glacial and interglacial periods annotated. Reproduced from Chappellaz et al. [1993]. (**B**) Ice core methane concentration record for the Holocene (upper panel, Arctic and Antarctic cores), the pre-industrial era (lower left-hand panel), and the post-industrial era (lower right-hand panel). Historical direct atmospheric methane concentration measurements are indicated by the solid black line from ~ 1975 onwards. Modified from Ciais et al. [2013]. (**C**) Recent evolution of global average atmospheric methane concentration (upper panel) and instantaneous growth rates (lower panel). Colours indicate different global methane monitoring networks. Reproduced from Hartmann et al. [2013].

to increase again from 2007 onwards (*Figure 1-3C*; Hartmann et al. [2013]; Nisbet et al. [2014]). These recent changes in atmospheric methane concentrations remain poorly understood, highlighting the complexity of the overall atmospheric methane budget [Nisbet et al., 2014].

Considering longer timescales, methane concentrations during glacial cold periods were approximately half as high as during warm interstadials [Dlugokencky et al., 2011]. Ice cores from Greenland and Antarctica extend methane and temperature records beyond ~ 40,000 years before present (BP), covering four glacial cycles (*Figure 1-3A*; Chappellaz et al. [1993]; Ciais et al. [2013]; Moller et al. [2013]; Wuebbles and Hayhoe [2002]). The correlation between high methane concentrations and warm climate in the ice core record prompted debate of the role of different methane sources in forcing and/or responding to climate. For example, Kennett [2000]; [2003], Nisbet [2002] and O'Hara [2008] suggest that large-scale methane release following temperature-driven methane hydrate destabilization (see *Sections 1.2.3* and *1.4*) played an important role in glacial-interglacial global atmospheric methane concentration shifts. Other studies propose that variability of wetland and/or boreal methane sources dominates the atmospheric glacial-interglacial methane concentration changes in the ice core record based on isotopic data [Bock et al., 2010; Petrenko et al., 2009; Schaefer et al., 2006], comparison of Arctic and Antarctic ice core records [Baumgartner et al., 2012; Brook et al., 2000; Chappellaz et al., 1997], and the relative timing of changes in methane concentration and temperature [Brook et al., 2000; Chappellaz et al., 1993; Rosen et al., 2014].

Beyond the ice core record, large inputs of methane to the ocean and atmosphere carbon system during climate warming events such as the Palaeocene-Eocene thermal maximum (PETM) at ~ 55.5 Mya BP (before present) are inferred from negative carbon isotopic excursions (CIE) in the carbonate record [McInerney and Wing, 2011; Zachos et al., 2007]. The PETM is characterized by rapid global warming of 5-8 °C over less than 20,000 years accompanied by a 3-6 ‰ negative CIE [Bowen et al., 2014]. Carbon system mass balance supports a large methane-derived carbon source with a light carbon isotopic signature, rather than an incredibly large carbon dioxide source with a heavier δ^{13}C. The role of different possible carbon sources continues to be debated, with large-scale destabilization of marine hydrates remaining a potential mechanism for the PETM CIE [Bowen et al., 2014; Dickens, 2003; 2011; McInerney and Wing, 2011].

1.2. Methane in marine sediments

The principal sources and fate of methane in marine sediments, described in the following sections, are summarized in *Figure 1-4*, [Judd, 2004].

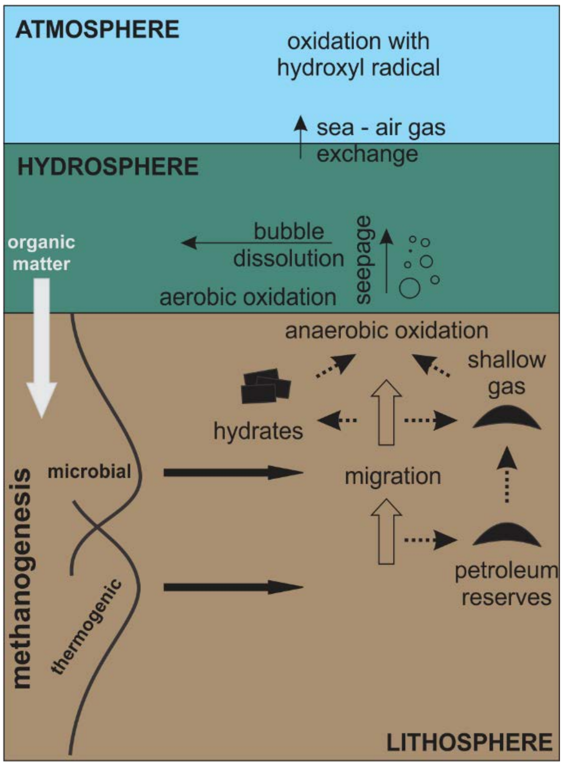

Figure 1-4 Principle sources and fates of methane in marine sediments. Modified from [Judd, 2004].

1.2.1. Methane formation

In marine sediments, methane is produced by the reduction of carbon dioxide derived from organic matter degradation [Regnier et al., 2011]. Methanogenesis occurs in sediments where the organic carbon supply is large and sedimentation rates are high [Reeburgh, 2007]. Remineralisation of organic carbon which accumulates in marine sediments occurs through a series of microbially-mediated reactions separated into depth zones on the basis of the chemical energy they release (*Figure 1-5*; Emerson and Hedges [2003]; Froelich et al. [1979]). With the exception of minor non-competitive processes [Valentine, 2011], microbial methanogenesis does not occur until the chemical species involved in more energetically favourable reactions are exhausted, and sulphate reducing bacteria become inactive [Whiticar, 1999]. When organic matter is buried to depths where sediments reach temperatures above ~ 100 °C [Pape et al., 2010], thermogenic methanogenesis occurs [Judd and Hovland, 2007]. Microbial and thermogenic methanogenesis yield characteristic molecular and isotopic signatures (*Figure 1-6*: Whiticar [1999]). In hydrothermal vent systems another process, abiogenic methanogenesis occurs [Judd and Hovland, 2007; Judd, 2003].

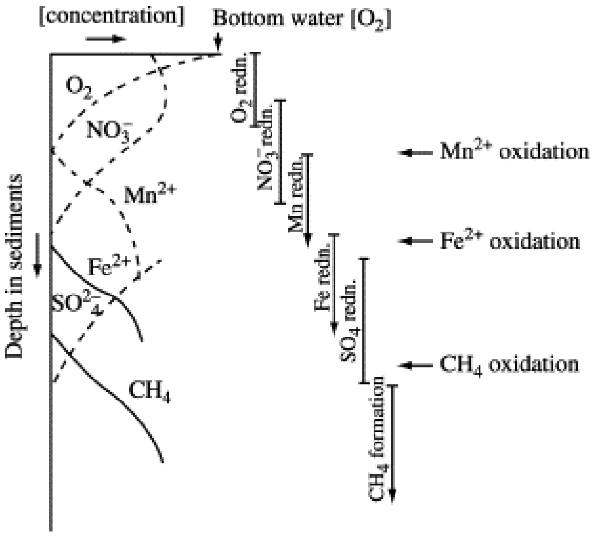

Figure 1-5 Depth zones of organic carbon remineralisation in marine sediments due to the availability of electron donors and energy yield of reactions. Redn: reduction. Reproduced from [Emerson and Hedges, 2003].

1.2.2. Migration of methane in marine sediments

After formation, methane migrates towards the seafloor driven by buoyancy [Boudreau, 2012; Judd and Hovland, 2007]. As free gas and dissolved in pore water, methane is advected and diffuses through permeable sediment strata and high-permeability paths such as faults and fractures. Methane accumulates where migration is restricted by low permeability features, and is trapped in the solid phase where sufficiently high concentrations are reached within the gas hydrate stability zone (GHSZ; see *Section 1.2.3*). Hydrate formation reduces the permeability of sediments. This leads to accumulation of high concentrations of free gas beneath the hydrate stability zone, and can also direct migration along the base of hydrate deposits (e.g.: Milkov et al. [2005]; Naudts et al. [2006]). In high gas flow regions, methane is often observed to migrate through the hydrate stability zone in the gas phase (e.g. Bünz et al. [2012]; Liu and Flemings [2006]; Smith et al. [2014]). Furthermore, hydrate destabilization may contribute to increased local permeability due to pressure from the release of a large volume of gas (e.g. Milkov et al. [2005]; Thatcher et al. [2013]). Methane seepage and methane hydrate are often associated with mud volcanoes and diapers: mobilized gas-containing pore fluids which rise from several sediment kilometres depth due to overpressure, liquefaction, and pressure inversions, predominantly near subduction zones and orogenic belts [Kopf, 2003]. Both thermogenic and biogenic gas are associated with high and low methane flux regimes in sediments [Milkov, 2005].

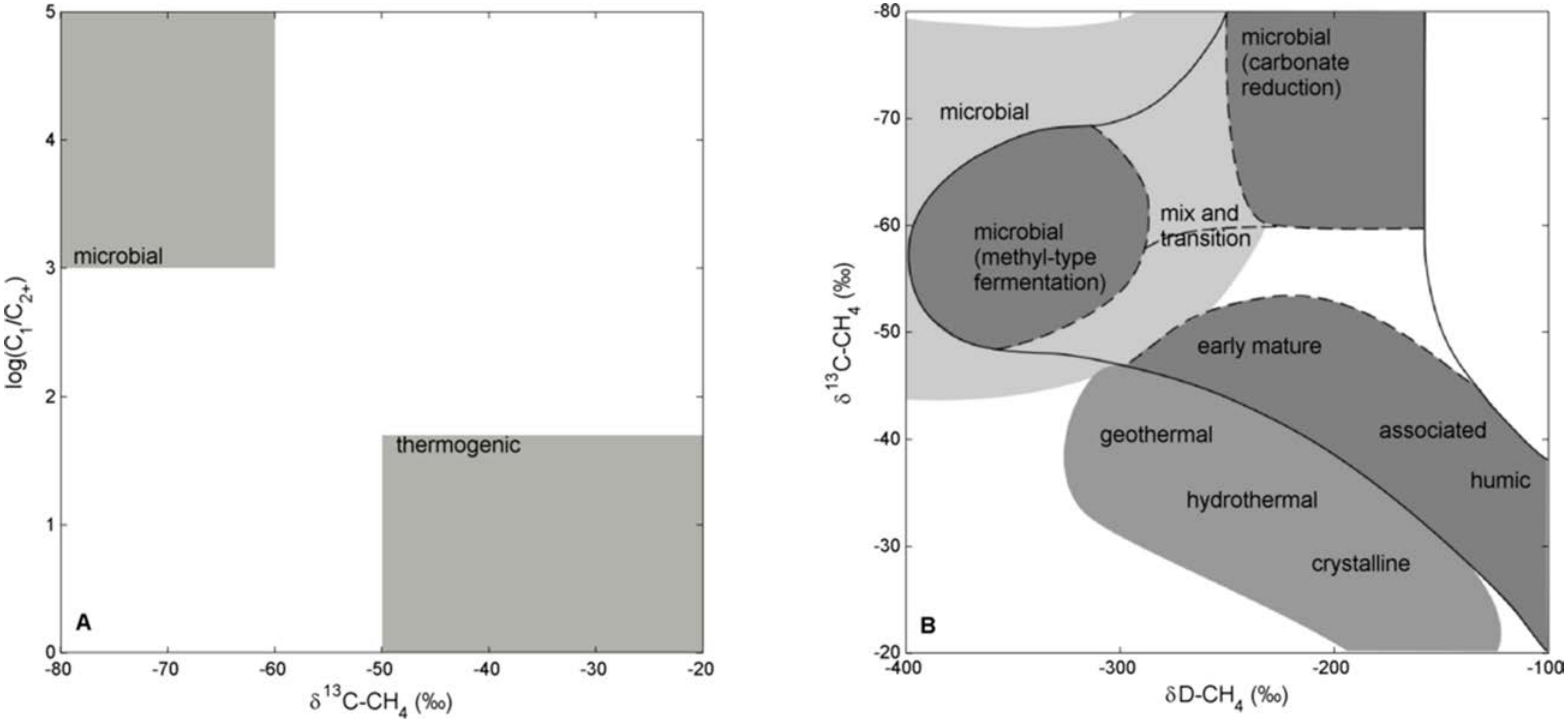

Figure 1-6 Geochemical distinction between microbial and thermogenic methane (**A**) based on molecular and carbon isotopic signatures, and (**B**) based on carbon and hydrogen isotopic signatures, modified from Whiticar [1999].

1.2.3. Methane hydrate

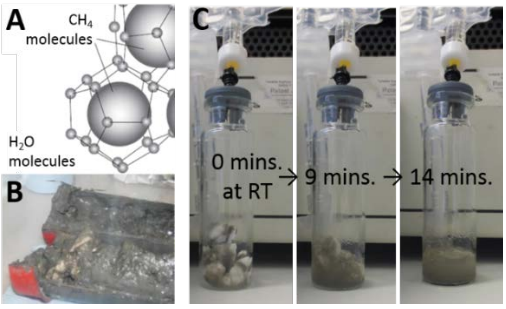

Figure 1-7 (**A**) Schematic molecular structure of the hydrate lattice, reproduced from Maslin et al. [2010]. (**B**) Hydrate recovered in a sediment core offshore Western Svalbard (890 m water depth, > 1.2 m sediment depth), photo curtesy of R. H. James. (**C**) Subsample of hydrate dissociating at room temperature (RT) in a 20 mL glass vial with methane gas collection into a bag connected through a septum.

Methane hydrate (clathrate) is an ice-like solid, in which cages of water molecules are stabilized by enclosed guest methane molecules (*Figure 1-7*, Hester and Brewer [2009]; Sloan and Koh [2008]). The hydrate structure allows accumulation of large amounts of gas: 1 L of hydrate dissociates to yield more than 160 L of gas at standard temperature and pressure [Kvenvolden, 1993]. Hydrate is stable at low temperature and high pressure, and forms naturally from methane-saturated water within this stability field (*Figure 1-8A*,*B*; Clennell et al. [1999]; Henry et al. [1999]; Hester and Brewer [2009]; Xu and Ruppel [1999]).

The geochemistry of hydrate-bound methane spans the range of molecular and isotopic signatures observed in natural gases [Kvenvolden, 1995; Milkov, 2005]. No isotopic fractionation occurs during methane hydrate formation [Lapham et al., 2012], while the incorporation of small amounts of heavier hydrocarbons can lead to molecular fractionation and formation of different crystal structures (e.g. Sassen et al. [2004]). The crystal structures are differentiated by the sizes and arrangement of the water molecule cages: structure I hydrates contain only small host molecules (methane and minor amounts of ethane), while structure II and structure H hydrates contain larger cages and are stabilized by incorporation of heavier hydrocarbons [Sloan, 2003]. The removal of water and exclusion of dissolved ions leads to enrichment of ionic species in pore fluids during hydrate formation, while hydrate dissociation dilutes surrounding pore fluids (e.g. Torres et al. [2004]).

Methane hydrate is found in sediments around the world (*Figure 1-9A*). It has been identified in both terrestrial and marine sediments (Milkov [2005]), forming stratigraphic-type (*Figure 1-8C*), structural-type (*Figure 1-8D*), and mixed deposits [Milkov and Sassen, 2002]. The

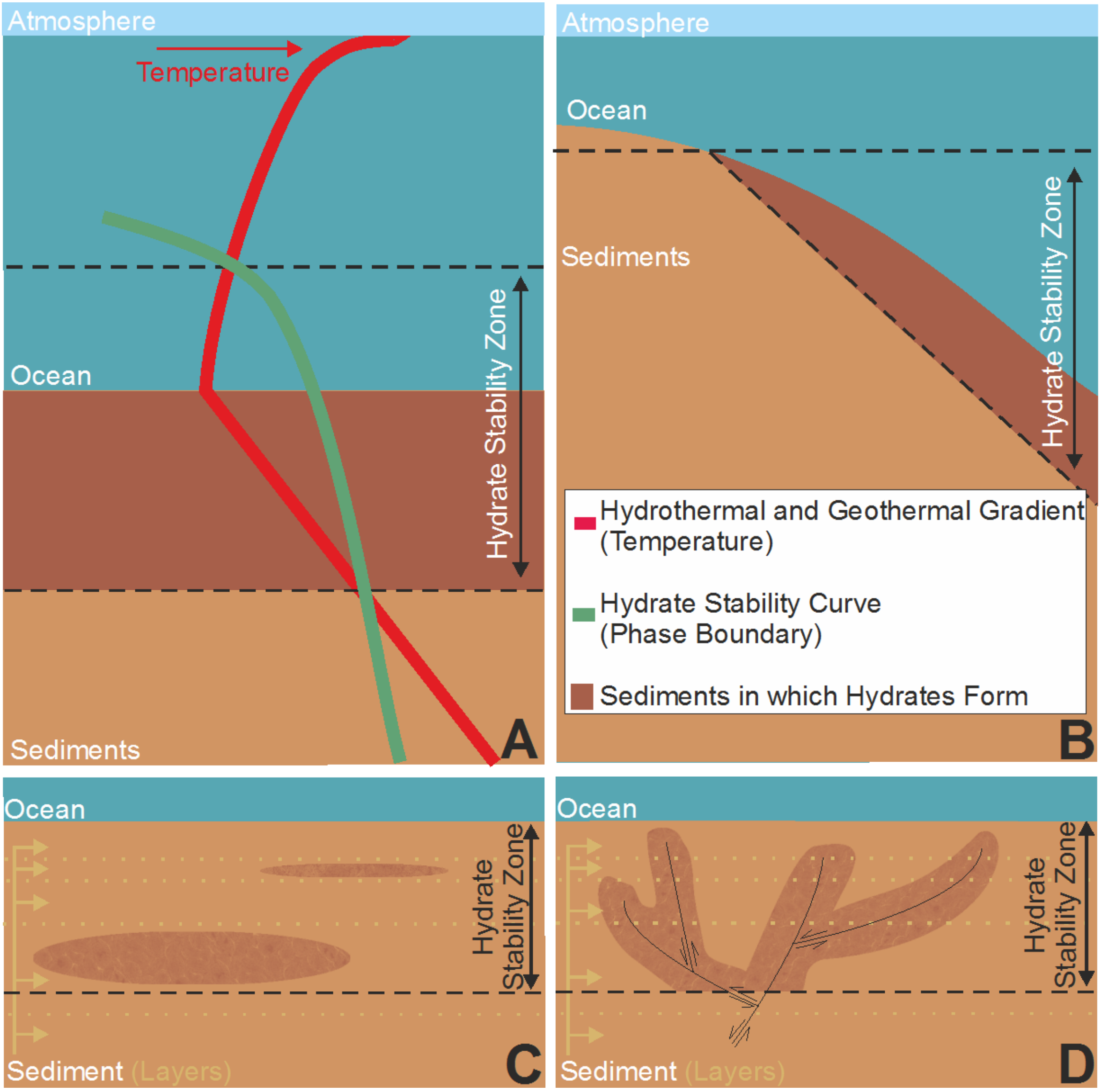

Figure 1-8 Schematic overview of the occurrence and distribution of marine hydrate deposits. (**A**) shows how the intersection of the hydrothermal and geothermal gradients with the hydrate stability curve determines the depth interval in which hydrates will form if pore water is saturated with methane. (**B**) illustrates the geometry of the landward limit of the hydrate stability zone on continental slopes. (**C**) and (**D**) show how the sub-seafloor morphology affects the type of hydrate deposit. (**C**) stratigraphic accumulation: the distribution of methane hydrates in relatively permeable sediments is controlled by sediment accumulation, pore fluid flow and microbial methanogenesis at depth. (**D**) structural accumulation: the distribution of methane hydrates is controlled by the supply of gaseous methane through faults or porous channels. Adapted from Hester and Brewer [2009]; Milkov and Sassen [2002] and Westbrook et al. [2009].

presence of hydrates is inferred from geophysical and geochemical evidence, including the presence of bottom simulating seismic reflectors (BSR; Haacke et al. [2007]; [2008]) and freshening of sediment pore fluids due to hydrate destabilization following core recovery [Hesse, 2003; Hesse and Harrison, 1981].

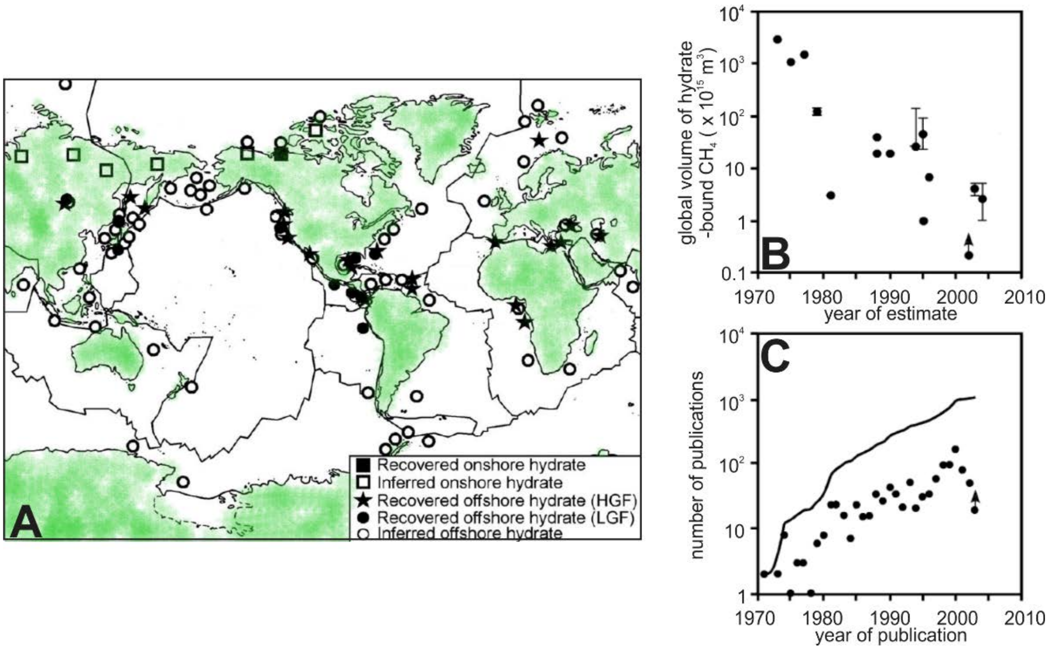

Figure 1-9 Known methane hydrate global distribution in 2005 (**A**) and inventory estimates (**B**), with increasing knowledge of natural hydrates indicated by the rise in relevant publications. Modified from Milkov [2004]; [2005].

While scientific research and understanding of natural methane hydrates have increased exponentially since their discovery in the 1960s, considerable uncertainty and debate remains about the current size of the global hydrate inventory in marine sediments (*Figure 1-9B,C*; Dickens [2011]; Hester and Brewer [2009]; Milkov [2004]). Dickens [2011] presented a detailed discussion of the challenges involved in estimating the amount of methane associated with hydrate in marine sediments. First, the volume of the gas hydrate stability zone must be calculated, which depends on ocean water depths and temperatures. Assumptions must then be made to determine the proportion of the stability zone which actually contains methane hydrate, and the volume percent of hydrate within those sediments. The distribution of methane-saturated pore fluid conditions necessary for hydrate formation within the GHSZ can be estimated by extrapolating limited observations, or modelled from organic carbon deposition and resulting methanogenesis in sediments. The problem is complicated by the dynamics of the ocean system through time. The long timescales associated with methane hydrate accumulation (> 10,000 years), require consideration of the variability of ocean bottom water temperature, sea level, and organic carbon deposition over glacial-interglacial cycles. While these factors have thus far precluded agreement on the volume of hydrate-associated methane, there is a consensus that hydrates are a significant piece of the global carbon system.

From the early ‘consensus’ global marine hydrate inventory estimate of approximately 10,000 Gt methane carbon (20 x 10^{15} m^3 STP, Kvenvolden [1993]), there has been a generally decreasing trend in published estimates which reflects better constrained but still widely varying underlying assumptions. Milkov [2004] reviewed available estimates and proposed 500 – 2,500 Gt (1 – 5 x 10^{15} m^3 STP) as the most appropriate estimate. Dickens [2011] reviewed estimates presented in the intervening years which ranged from 4 – 995 Gt [Burwicz et al., 2011] to 74,400 Gt [Klauda and Sandler, 2005], while subsequent publications propose ≥ 455 Gt [Wallmann et al., 2012] and ~ 550 Gt [Piñero et al., 2013]. Large quantities of free gas accumulate in sediments underlying hydrates in addition to the methane contained in the hydrate phase. For example, the modelling approach of Archer [2007] indicates the presence of 500 – 3,000 Gt of carbon in methane gas associated with an equal amount of hydrate-bound methane. To put the inventory in context, global fossil fuels (including coal) are estimated at 5,000 Gt carbon [Krey et al., 2009].

1.2.4. Oxidation of methane

The microbially-mediated oxidation of methane to form carbon dioxide occurs in the presence of an appropriate electron acceptor. In oxic environments including the seafloor, near surface sediments, and oxygenated ocean waters, aerobic methane oxidation is ubiquitous (*Equation 1-2*; Boetius and Wenzhofer [2013]; Hanson and Hanson [1996]; Valentine [2011]). In anoxic marine sediments, methane oxidation is coupled to sulphate reduction. When methane reaches sulphate-containing sediments, anaerobic oxidation of methane (AOM: *Equation 1-3*) occurs in a reaction zone termed the sulphate-methane transition zone (SMTZ; Knittel and Boetius [2009]; Reeburgh [2007]; Valentine and Reeburgh [2000]). Below the SMTZ sediments contain methane both produced *in situ* and migrated from depth. Above the SMTZ sediments contain sulphate which diffuses downwards from the overlying seawater. Within the SMTZ the concentrations of both reagents are reduced to approximately zero. Small amounts of methane are observed associated with non-competitive methanogenesis above the SMTZ [Valentine, 2011], and below the SMTZ low concentrations of sulphate (< 0.5 mM) are involved in geochemical cycling [Treude et al., 2014]. The SMTZ is also marked by depth profiles of other dissolved species involved in associated biogeochemical reactions, including sulphide (S^{2-}), dissolved inorganic carbon (DIC) and the carbon isotopic signatures of methane and DIC.

$$CH_4 + 2\,O_2 \rightarrow CO_2 + 2\,H_2O \qquad (1\text{-}2)$$

$$CH_4 + SO_4^{2-} \rightarrow HS^- + HCO_3^- + H_2O \qquad (1\text{-}3)$$

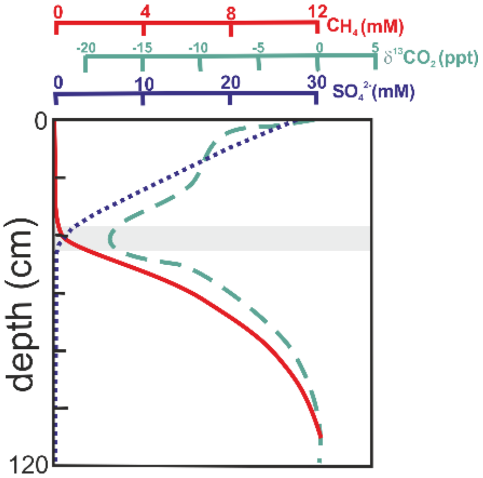

Figure 1-10 Profiles of methane (red, solid line), sulphate (dark blue, dotted line), and $\delta^{13}C$-CO_2 (green, dashed line) in sediments across the sulphate-methane transition zone (grey bar) in a diffusion dominated methane flow regime. Adapted from Reeburgh [2007].

The widespread observation of SMTZ in pore fluid geochemical profiles (*Figure 1-10*; Reeburgh [2007]) provides strong evidence for sulphate-driven methane oxidation. Boetius et al. [2000] identified a consortium of methane-oxidizing archaea and sulphate-reducing bacteria which facilitate the reaction. Methanotrophic archaea are hypothesized to operate reverse methanogenesis to provide electrons to sulphate-reducing partners in syntrophic cooperation [Hoehler et al., 1994; Knittel and Boetius, 2009]. Subsequent studies have shown that AOM can be coupled with metal oxide reduction [Beal et al., 2009], performed by a bacterium which mediates methane oxidation by producing an oxygen intermediate from nitrite ions [Ettwig et al., 2010], and that some anaerobic methanotrophic archaea can operate without a bacterial partner by mediating sulphate reduction to a zero-valent sulphur product [Milucka et al., 2012]. Active microbial populations have been shown to be closely associated with near-seafloor methane hydrates and may slowly oxidize hydrate-bound methane [Orcutt et al., 2004].

The sediment depth at which the SMTZ occurs is related to the upward flux of methane. Where the methane flux is diffusive and high enough to dominate net sulphate removal from sediments, linear downwards diffusive sulphate profiles can be used to estimate the methane flux from depth [Borowski et al., 1996]. In these settings oxidation of methane is essentially complete [Knittel and Boetius, 2009]. More sophisticated models are required to determine methane fluxes in advective settings, and in non-steady-state situations (e.g. Hong et al. [2014]; Vanneste et al. [2011]). Increases and decreases in methane supply and sediment transport events lead to kink-type sulphate profiles which can persist over thousands of years [Henkel et al., 2011; Hensen et al., 2003; Zabel and Schulz, 2001].

When the SMTZ is fixed in a given sediment interval for long periods of time, it leaves a geochemical imprint on the sediment solid phase which can be used to trace the evolution of methane fluxes in time. Proxies include: (i) precipitation of ^{13}C-depleted authigenic carbonates due to methane oxidation in the SMTZ (e.g. Luff et al. [2004]; Nöthen and Kasten [2011]), (ii) remobilization of biogenic barium sulphate from the sulphate-undersaturated sediments below the SMTZ and re-precipitation into barite fronts just above the SMTZ (e.g. Dickens [2001]; Kasten et al. [2012]; Nöthen and Kasten [2011]; Riedinger et al. [2006]; Snyder et al. [2007a]; Torres et al. [1996a]; Torres et al. [1996b]) and (iii) alteration of the magnetic properties of sediments through reductive dissolution of iron (oxyhydr)oxides by sulphide at the SMTZ, and precipitation of paramagnetic pyrite and ferrimagnetic greigite (e.g. Dewangan et al. [2013]; Garming et al. [2005]; Riedinger et al. [2005]).

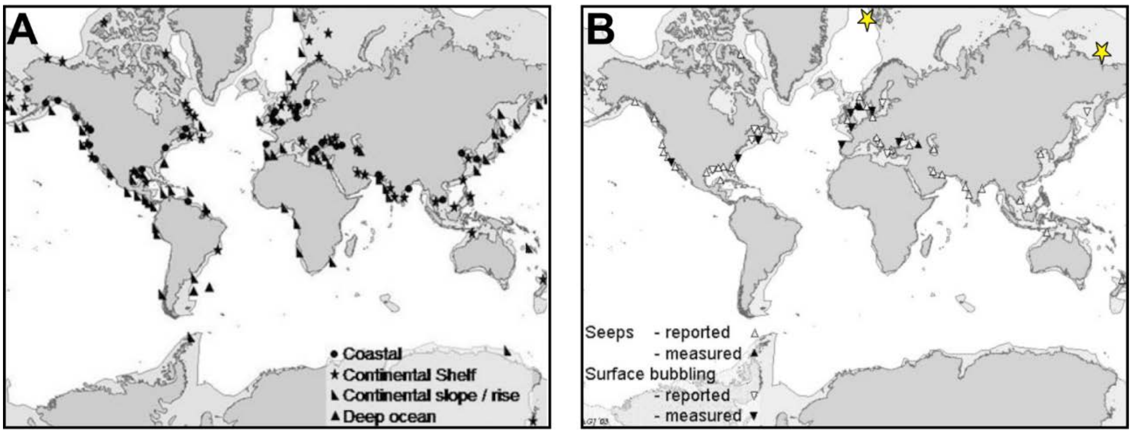

Figure 1-11 (**A**) global distribution of seafloor methane seeps [Judd, 2003]. (**B**) distribution of seeps in shallow continental shelf settings showing the scarcity of measurements up to 2004 [Judd, 2004]. Notable more recently discovered and studied shallow seeps in the Arctic are added as yellow stars: East Siberian Arctic Shelf [Shakhova and Semiletov, 2007; Shakhova et al., 2010a; 2010b; 2014], and off Western Svalbard [Sahling et al., 2014].

Where high methane fluxes allow high concentrations of methane to reach the seabed, distinct cold-seep chemosynthetic communities are established. Seafloor methane seeps are observed globally in a broad range of oceanographic and geological settings (*Figure 1-11*, Judd [2003]). AOM fails to efficiently remove methane beneath the seafloor where fluxes are high and focused [Knittel and Boetius, 2009]; gas phase methane is not available to microbes. Cold seep environments are characterized by dramatic spatial heterogeneity and sharp biogeochemical gradients [Niemann et al., 2006]. Thick authigenic carbonate crusts can form on the seafloor (e.g.: Joseph et al. [2013]; Luff et al. [2004]). The type of chemosynthetic community is related to the underlying methane flux regime (*Figure 1-12*; Suess [2010]).

While no species are endemic to seep environments, benthic foraminifera have been found to live in active cold-seep settings. Methane-derived ^{13}C-depleted carbon is incorporated into their tests as they calcify, apparently both from locally ^{13}C-depleted dissolved inorganic carbonate in pore water, and from ingestion of ^{13}C-depleted biomass (e.g. Hill et al. [2004]; Mackensen et al. [2006]; Martin et al. [2010]; Panieri et al. [2014a]). Foraminiferal calcite can thus provide an additional proxy for past seafloor seepage activity.

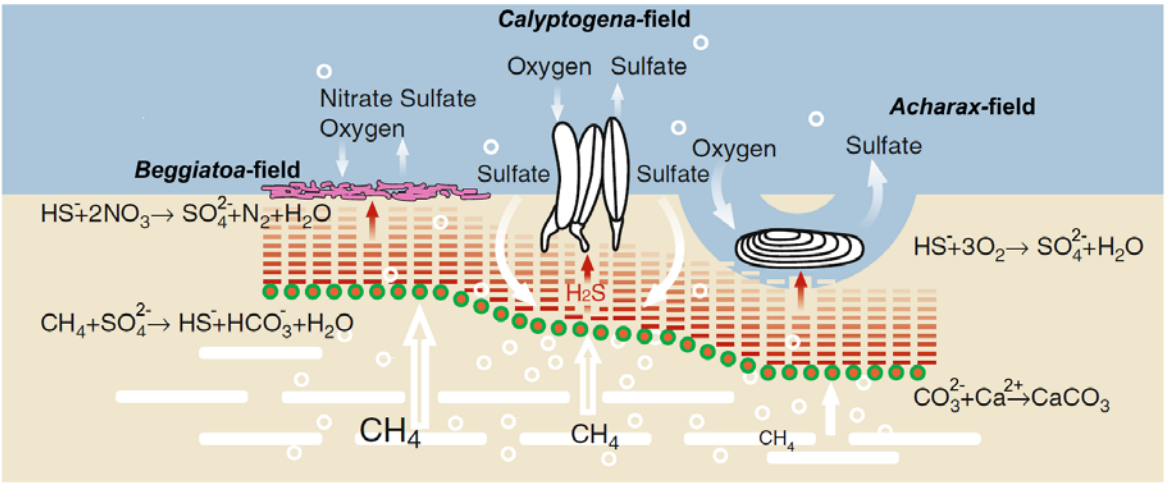

Figure 1-12 Schematic representation of methane-seep associated chemosynthetic communities associated with different methane flux regimes. Green circles and red bars represent microbial consortia mediating anaerobic oxidation of methane. Methane fluxes decrease from left to right. Modified from Suess [2010] and Sahling et al. [2002].

1.3. Methane in the water column

1.3.1. Bubbles

Where methane escapes oxidation in sediments it enters the ocean in the dissolved phase, and in high volumes as streams of gas bubbles. Bubble dynamics are parameterized by models which account for a long list of interrelated properties including bubble shape, size and rigidity, rise speed, the presence of contaminants or surfactants and aqueous phase salinity, gas partial pressure, solubility, diffusion and internal circulation [Leifer and Patro, 2002; McGinnis et al., 2006]. As a bubble rises, the ambient pressure decreases, allowing the gas to expand. Concentration gradients between dissolved and gaseous phases dictate the flow of material across the gas-water interface (*Figure 1-13*). Methane in a rising bubble dissolves and is subsequently oxidized, while dissolved gasses in the water column (predominantly oxygen and nitrogen) flow into the bubble. The balance between decreasing bubble size as methane is dissolved and increasing bubble size as the pressure is reduced is complicated by the inflow and subsequent re-dissolution of other gasses [McGinnis et al., 2006]. Smaller bubbles dissolve faster because of their high surface to volume ratio, and therefore only large bubbles are likely to reach the surface from depth [McGinnis et al., 2006]. However, due to gas inflow, bubbles which reach the ocean surface will often contain mostly oxygen and nitrogen, and only minor amounts of methane. Modelling and observation in the Black Sea and the North Sea indicate that methane does not reach the atmosphere from depths greater than 200 m [McGinnis et al., 2006; Schmale et al., 2005; Schneider von Deimling et al., 2011].

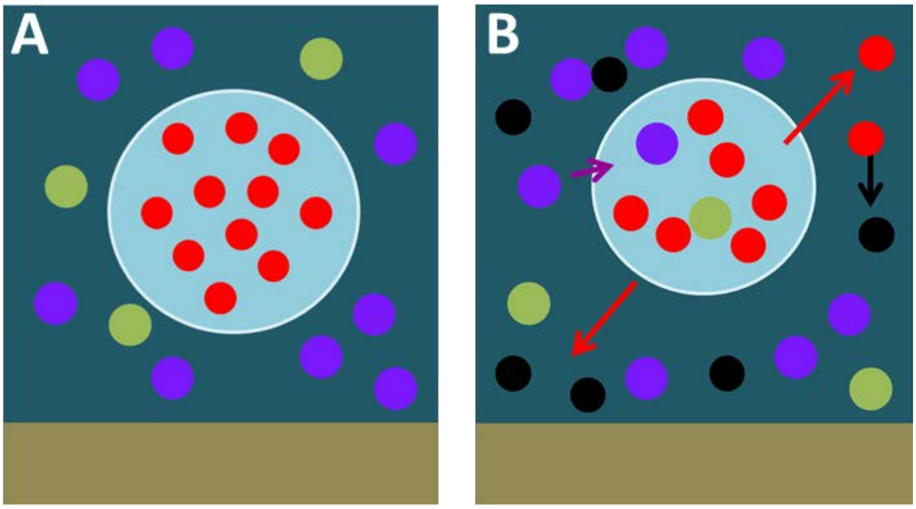

Figure 1-13 Schematic representation of the flow of gasses between dissolved and gas phases as an isolated methane bubble rises through the water column. Red circles represent methane molecules, black carbon dioxide, green nitrogen and purple oxygen. Initially (**A**) the bubble contains only methane gas, as the bubble rises (**B**) methane is dissolved and subsequently oxidized to carbon dioxide while nitrogen and oxygen enter the bubble from the water column, overall the bubble shrinks with rise height as a balance of evasion and invasion of gaseous species and the decreasing pressure.

The rise height of bubbles can be enhanced by the formation of outer films or coatings which restrict mass transfer between the bubble and the surrounding water. Coatings form from higher hydrocarbons and biological material [Leifer and Patro, 2002]. Methane hydrate shells are observed within the hydrate stability field [Rehder et al., 2002; Rehder et al., 2009; Warzinski et al., 2014]. Localized enhanced methane concentrations in the dissolved phase and strong upwelling flows resulting from rising dense bubble streams can further provide mechanisms for bubbles to survive closer to the seafloor than is expected from single bubble models [Leifer et al., 2006]. Solomon et al. [2009] found that significant methane reached the surface mixed layer from depths of > 500 m in the Gulf of Mexico as a result these processes, and suggested that conventional shipboard methods of observing methane seeps were poorly-suited for measurement of these localized processes.

Recent advances have been made in quantifying the amount of methane input to the water column at seafloor seepage sites using shipboard echosounder sonar supported by ground-truthing observations by submersible and remotely operated vehicles (e.g.: Kannberg et al. [2013]; Sahling et al. [2014]; Weber et al. [2014]). Significant uncertainty remains due to the spatial heterogeneity and temporal variability of these environments.

1.3.2. Dissolved methane in seawater

Dissolved methane in seawater is subject to mixing away from the point of input by diffusion, dilution, and advection with ocean currents. These processes occur simultaneously with aerobic oxidation, reducing methane to background ocean concentrations of approximately 3 nM [Rehder et al., 1999; Yoshikawa et al., 2014]. The rates of aerobic oxidation span several orders of magnitude, generally decreasing with methane concentrations such that they are highest near methane seeps, and low in the open ocean [Elliott et al., 2011]. The fate of methane input from seafloor seeps into the water column has been investigated by combining methane concentration and isotopic measurements with local current speeds and oxidation rates, and applying simplified box models (e.g. Heeschen et al. [2005]; Mau et al. [2007]). Significant uncertainties as to the final downstream fate of dissolved methane remain due to both the limited temporal and spatial resolution of direct observations, and the temporal and spatial small scale heterogeneity of all processes involved.

1.3.3. Sea-air gas exchange

Methane in the surface mixed layer of the ocean equilibrates with the overlying atmosphere. Significant surface water methane supersaturation can result from local seafloor seepage (e.g.: Shakhova et al. [2010a,b]; Solomon et al. [2009]). Slight supersaturation in open ocean environments and in the absence of seafloor sources is attributed to aerobic methanogenesis at the pycnocline (e.g. Florez-Leiva et al. [2013]; Karl et al. [2008]; Rhee et al. [2009]). Equilibration between sea surface and atmospheric methane depends on a number of physical parameters in addition to the concentration gradient, most notably wind speed [Wanninkhof et al., 2009]. The development of equilibrator systems which allow near-continuous measurement of methane concentrations in surface waters at sea (e.g. Gülzow et al. [2011]) has dramatically improved the temporal and spatial resolution of sea-air methane fluxes.

The global ocean sea to air methane flux has recently been estimated at 0.6 – 1.2 Tg CH_4 yr-^{1} based on an Atlantic ocean measurement transect [Rhee et al., 2009]. However, the atmospheric methane flux associated with seafloor seepage observed on the shallow East Siberian Arctic Shelf is an order of magnitude higher (> 10 Tg CH_4 yr^{-1}; Shakhova et al. [2014]; [2010a,b]). Similar large localized fluxes are reported by Solomon et al. [2009] from discrete water column measurements in the Gulf of Mexico near seafloor seepage into deeper water, in disagreement with a subsequent study of the same area using near-continuous surface seawater measurements from which Hu et al [2012] concluded that the region is not a significant source of atmospheric methane. Additional measurements are needed to further constrain the ocean methane source now and in the future.

1.4. Temperature-driven methane hydrate destabilization

Dissociation of hydrates in warming continental margin sediments is likely occurring both in the Arctic [Ferré et al., 2012; Sahling et al., 2014; Thatcher et al., 2013; Westbrook et al., 2009] where current global warming is amplified (e.g. Parmentier et al. [2013]), and also at lower latitudes [Hautala et al., 2014; Phrampus and Hornbach, 2012; Skarke et al., 2014]. A number of modelling studies have investigated local [Ferré et al., 2012; Frederick and Buffett, 2014; Hautala et al., 2014; Marín-Moreno et al., 2013; Phrampus and Hornbach, 2012; Reagan and Moridis, 2007, 2008, 2009; Thatcher et al., 2013], regional [Biastoch et al., 2011; Elliott et al., 2011], and global [Archer et al., 2009a; Buffett and Archer, 2004; Hunter et al., 2013; Lamarque, 2008] methane hydrate stability in the recent past and the future.

Models of the response of marine hydrates to changes in temperature are subject to the same uncertainties which limit estimates of the global methane hydrate inventory, with the additional uncertainty of the evolution of climate in the future. Predicted changes in sea level are expected to have a relatively minor effect on the hydrate stability field (e.g. Buffett and Archer [2004]; Hunter et al. [2013]; Reagan and Moridis [2008]). Methane release in response to on-going and modelled future warming is likely to be concentrated where hydrate has accumulated near the limits of the current stability zone. This includes near-surface high concentration deposits such as those in the Gulf of Mexico, and hydrate in continental margin sediments, particularly in the Arctic (e.g. Reagan and Moridis [2007]; [2008]). The recent modelling of Hunter et al. [2013] indicates that business-as-usual climate warming scenarios predict that methane release from hydrates could exceed estimated natural methane fluxes (> 30 – 50 Tg CH_4 yr^{-1}) fluxes within the next century.

To establish a climate feedback, methane released from hydrate must reach the atmosphere. The physical barriers of the overlying sediments and water column and the biogeochemical filters they contain are expected to significantly limit direct gas escape. For example, in their model Hunter et al. [2013] consider that only 0.5 % of methane released from temperature-driven shallow hydrate destabilization reaches the atmosphere. Sediment instability caused by hydrate destabilization is proposed as a potentially important mechanism for more substantial gas escape (e.g.: Archer [2007]; Kvenvolden [1999]).

Large amounts of methane released from hydrates can also impact the ocean and atmospheric systems after oxidation to carbon dioxide. Archer et al. [2009a] consider scenarios in which methane released from hydrates is oxidized to carbon dioxide before and after reaching the atmosphere and demonstrate the long-term (> 10,000 year) impacts of large-scale methane release on the climate system in both scenarios. Recent work coupling potential hydrate-destabilization-driven escape of methane from Arctic continental margin with ocean circulation and biogeochemical models indicates limited direct methane release to the overlying atmosphere, but potential ocean acidification and deoxygenation resulting from aerobic methane oxidation [Biastoch et al., 2011; Elliott et al., 2011].

The emerging consensus on the potentially serious, but unlikely catastrophic, result of temperature-driven methane hydrate destabilization in the Arctic is exemplified by the response to the recently published ‘Comment’ article in *Nature* entitled “Vast costs of Arctic change” by Whiteman et al. [2013]. The authors use an integrated assessment model which calculates the costs of mitigation of and adaption to climate change to investigate the societal impacts of the release of 50 Gt of CH_4 from hydrate on the East Siberian Arctic Shelf over decadal timescales, providing an estimate of > $ 73 trillion. Responses from the international community recognized the importance of this type of impact modelling in the discussion of Arctic methane climate feedbacks, but categorically condemned the absence of any consideration of the significant outstanding uncertainty related to both the magnitude, duration, and sources of current and future Arctic methane fluxes [Nisbet et al., 2013; Notz et al., 2013; Parmentier and Christensen, 2013].

1.5. Rationale and project objectives

Current increases in atmospheric greenhouse gas concentrations and the associated global warming could release significant amounts of methane from gas hydrates into marine sediments. If this methane is able to escape the sediments, rise through the overlying ocean, and equilibrate with the atmosphere, a climate feedback would be established. In the Arctic region offshore Western Svalbard, seafloor methane seepage from sediments where observed rises in temperature predict recent hydrate destabilization provides the first opportunity to study the processes involved in hydrate climate feedback in an active setting. Specific objectives of this work were:

- To further constrain the source of methane to seafloor seeps at on the upper continental slope offshore Western Svalbard;
- To determine the role of anaerobic methane oxidation in limiting methane escape from shallow sediments in which hydrate has recently destabilized;
- To quantify dissolved-phase methane fluxes from sediments into the overlying water column in the vicinity of seafloor methane seeps at the limit of hydrate stability offshore Western Svalbard;
- To determine the relative importance of different chemical and physical processes in the water column on the fate of seafloor methane inputs at the limit of hydrate stability;
- To assess the linkages between methane seepage and climate offshore Svalbard in the past.

1.6. Thesis structure

This dissertation presents a geochemical study of seafloor methane seepage offshore Western Svalbard. This site is the first known example of present-day methane seepage from temperature-sensitive shallow methane hydrates in marine sediments. Knowledge of the distribution and origin of methane in sediments, the water column, and the atmosphere offshore Western Svalbard is summarized in *Chapter 2*, along with the relevant oceanographic and geological background.

In *Chapter 3*, the geochemistry of methane and other associated geochemical species in shallow sediments is presented. Characterization of the molecular composition of gases and the isotopic signatures of methane in hydrate, sediments, and bubble plume gas provides new insight into the shallow gas flow system. Depth profiles of dissolved species altered by anaerobic oxidation of methane allow modelling of local methane fluxes, and investigation of their temporal stability. Comparison of sediments from the active seepage region with sediments at (i) shallower water depths where hydrate has not been stable in recent times, and (ii) deeper water depths where hydrate is presently stable, shows the spatial heterogeneity within and between these environments.

In *Chapter 4*, observations of methane in the water column and the atmosphere above the seepage area are presented in order to evaluate the fate of methane released in the seafloor bubble plumes. Dissolved methane concentrations were measured along depth transects in the study area during two summer seasons. An extensive survey of surface waters was achieved using an equilibrator-system. Concentration data are complemented by methane oxidation rate measurements and observations of physical parameters. The data set is used to inform a model of the methane budget in the water column and to calculate the present-day methane contribution to the atmosphere.

To order to assess the future importance of seafloor seepage from methane hydrate destabilization offshore Svalbard, geochemical proxies for methane seepage are investigated in *Chapter 5*. Bulk sediment magnetic susceptibility, sedimentary barium, and carbonate data are presented along with preliminary results of a micropalaeontological study of planktonic and benthic foraminiferal $\delta^{13}C$. Sediment cores provide a record of shallow sediment methane fluxes over the past ~ 25,000 years.

On-going, past, and future methane hydrate destabilization in upper continental margin sediments offshore Western Svalbard are discussed in *Chapter 6*. Key conclusions are presented, and recommendations for future work to further improve understanding of the role of temperature-driven methane destabilization in global climate events are provided.

CHAPTER 2

Study area: The West Svalbard margin

Contents

2.1. Geological setting

The West Svalbard margin (*Figure 2-1*) was shaped by the Pleistocene-Pliocene advance and retreat of the Svalbard-Barents Sea ice sheet [Sarkar et al., 2012]. It is punctuated by cross-shelf troughs and trough mouth fans of eroded glacial sediments deposited by ice streams connected by inter-fan segments [Sarkar et al., 2011]. The continental slope is relatively steep (up to 5°), and the shelf is relatively narrow (60-85 km wide; Elverhøi et al. [1995]). The most recent full glaciation of the shelf occurred approximately 21 ka BP (before present) during the last glacial maximum (23 – 19 ka BP) with deglaciation interrupted by a glacial re-advance at 14.5 ka BP at the beginning of the Bølling-Allerød interstadial, which preceded the Younger Dryas stadial from ~12.8 to ~11.6 ka BP [Elverhøi et al., 1995; Jessen et al., 2010; Zamelczyk et al., 2014]. *Figure 2-2* shows a timeline of global and local climate events focusing on the past 30,000 years.

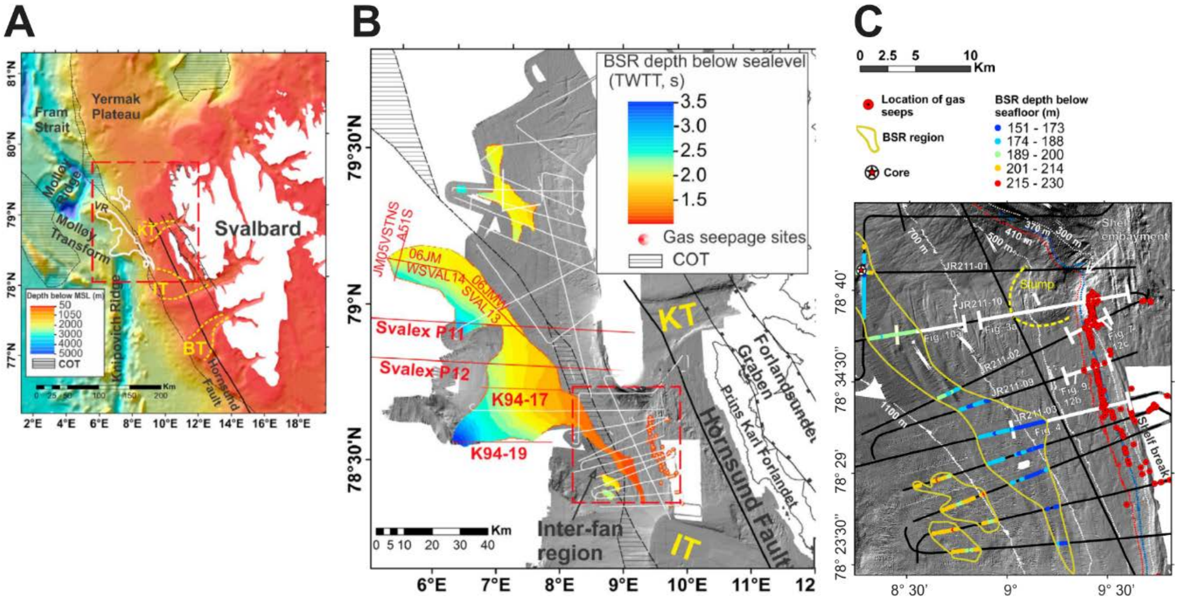

Figure 2-1 Evidence for gas in sediments of the West Svalbard continental margin. (**A**) shows the regional bathymetry, faults (black lines), and the location of the area expanded in (**B**), which shows the extent of bottom simulating reflectors (BSR) and seismic lines (white) and the location of the area expanded in (**C**), which shows seismic lines (black and white), the depth of the BSR beneath the seafloor, the location of a sediment core in which hydrate was recovered, and locations of seafloor seeps. COT: Continent-ocean transition, TWTT: two way travel time. Modified from Sarkar et al. [2012].

On the shelf and upper slope, patchy glacial sediments overlie a sequence of seaward-dipping marine hemipelagic sediments [Rajan et al., 2012; Sarkar et al., 2012]. Rapid bottom water currents over the upper slope lead to a low accumulation environment [Winkelmann and Knies, 2005]. Sediment cores reveal highly variable sedimentation rates and broad hiatuses (e.g. Elverhøi et al. [1995]; Jessen et al. [2010]; Zamelczyk et al. [2014]).

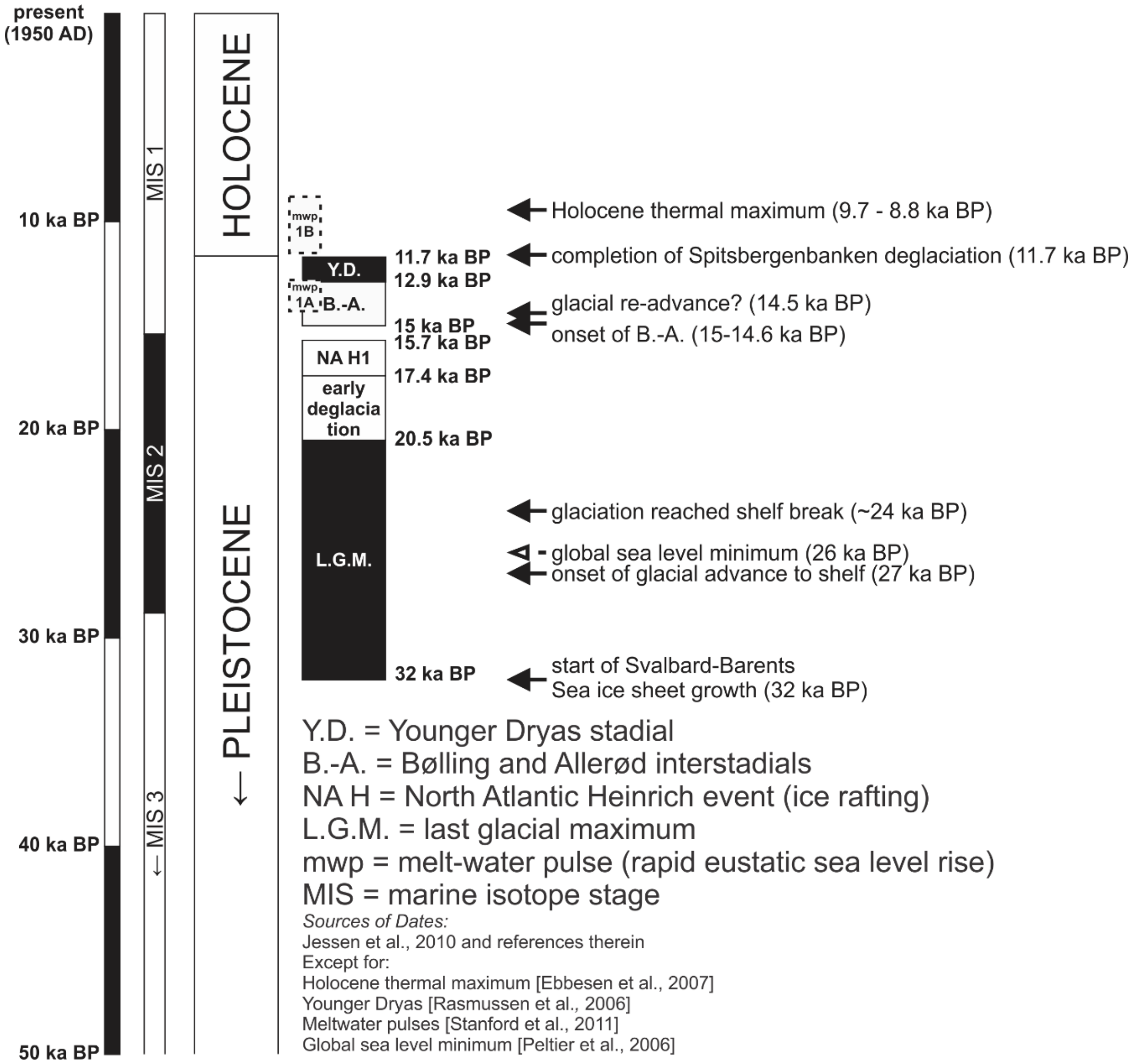

Figure 2-2 Timeline of global and local climate events focusing on the last 30,000 years..

2.2. Oceanographic setting

The westward branch of the West Spitsbergen Current (WSC) carries warm saline Atlantic Water over the upper continental margin [Aagaard et al., 1987; Saloranta and Haugan, 2004]. The WSC provides the dominant transport of water and heat towards the Arctic Ocean. North of Svalbard, the current splits into two main branches with shallower waters continuing along the shelf edge while deeper waters follow the western edge of the Yermak Plateau [Schauer, 2004]. On the continental shelf, the slower East Spitsbergen Current (ESC) carries fresher colder polar water northward. Surface water consists of an onshore-thickening wedge of fresh Arctic Water [Saloranta and Svendsen, 2001]. Oceanographic currents and the front between the WSC and ESC are shown schematically in *Figure 2-3* [Saloranta and Haugan, 2004].

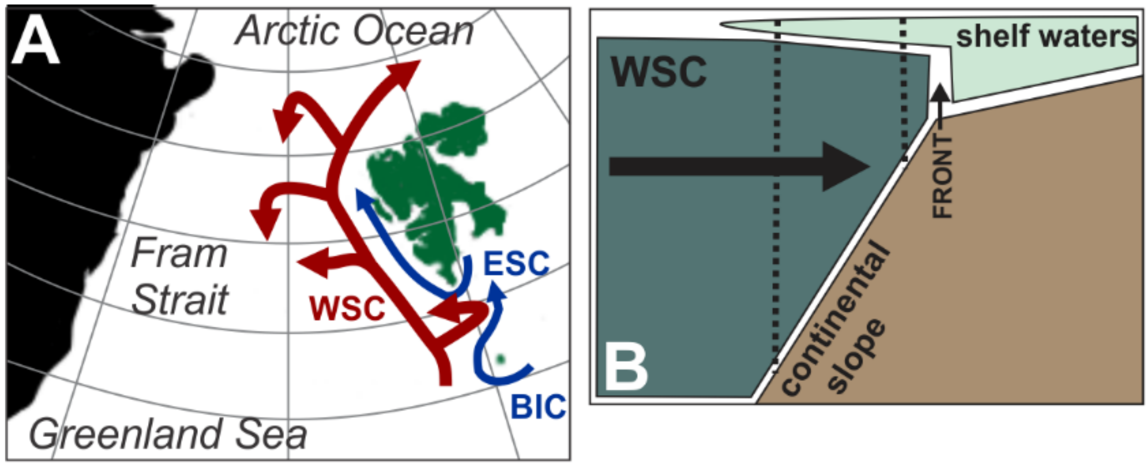

Figure 2-3 (**A**) Schematic illustration of principal ocean currents off Western Svalbard. The warm West Spitsbergen Current (WSC) is shown in red, and the cold East Spitsbergen Current (ESC) and Bear Island Current (BIC) are shown in blue. (**B**) Schematic representation of the front between WSC and ESC waters near the shelf break. Thick black arrow indicates increasing temperature, speed, and topographic steering of the WSC. Dashed vertical lines indicate the upper slope domain (~1200 - 300 m water depth). Modified from [Saloranta and Haugan, 2004]

Recent warming of the WSC is documented in the observational record over the last 30 [Westbrook et al., 2009] and 60 [Ferré et al., 2012] years. The sediment record indicates that the current warming is unprecedented in the last 2,000 years [Spielhagen et al., 2011].

Modern sea level was established at ~ 5.2 ka BP [Werner et al., 2013]. Isostatic rebound following deglaciation led to an approximately 50 m lowering of local sea level [Winkelmann and Knies, 2005].

2.3. Seafloor methane seepage

The continental margin offshore Western Svalbard is underlain by extensive gas hydrate deposits at water depths of >700 m [Carcione et al., 2005; Eiken and Hinz, 1993; Fisher et al., 2011; Smith et al., 2014; Vanneste et al., 2005; Vogt et al., 1999]. The presence of hydrate is both inferred from extensive bottom simulating reflectors (BSR), and directly evidenced by recovery of hydrate samples in sediment cores (*Figure 2-1*). The absence of a BSR at shallower water depths is attributed to the change in lithology, as the upper slope is dominated by low permeability glaciomarine sediments [Sarkar et al., 2012]. Hydrate may be present at low concentrations (4- 5 %) in the sediment pore space [Chabert et al., 2011]. Patchy shallow gas is observed in sediments of the upper slope (e.g. Ker et al. [2014]).

Drilling during Ocean Drilling Program (ODP) leg 151 west of the Knipovich ridge at > 1200 m water depth and north of Svalbard on Yermak Plateau at < 1000 m water depth provides evidence for biogenic methanogenesis beginning between 25 and 90 m below the seafloor [Stein et al., 1995]. At the deepest site near the Knipovich Ridge hydrocarbon measurements indicate significant thermogenic gases below ~ 1 km sediment depth, potentially due to migration from deeper sediments. Active methanogenesis is attributed to high sedimentation rates and organic content, conditions typically favouring methane production by promoting rapid depletion of oxygen and other terminal electron acceptors in near-surface sediments and survival of reactive organic matter to burial depths where methanogenesis can be established.

At the present-day, the gas hydrate stability zone (GHSZ) is expected to taper out at its landward limit at water depths of ~ 400 m [Berndt et al., 2014; Ferré et al., 2012; Westbrook et al., 2009]. A downslope retreat of the GHSZ limit from 360 m water depth resulted from a 1 °C average bottom water warming over the last 30 years, which corresponds to potential hydrate destabilization beneath a 950 m segment of upper slope sediments due to the shallow slope gradient [Westbrook et al., 2009]. Seasonal bottom water temperature variability of 1.5° C leads to a maximum wintertime GHSZ limit at 410 m water depth, and a minimum summertime GHSZ limit at 360 m [Berndt et al., 2014]. For comparison, the maximum expected GHSZ extent in the historical temperature record was to 338 m water depth in 1978 [Ferré et al., 2012]. Hydrate dissociation modelling based on past temperature data supports methane hydrate destabilization as a contributing source present-day seafloor seepage [Reagan and Moridis, 2009; Thatcher et al., 2013], and models of future climate warming indicate significant ongoing methane release at the landward limit of the GHSZ [Marín-Moreno et al., 2013].

Seafloor seepage was discovered offshore Western Svalbard in 2008, with the observation of more than 250 bubble plumes rising from the seafloor into the water column aligned upslope of the present-day GHSZ limit offshore Prins Karls Forland, in the inter-fan region between the Isfjorden and Kongsfjorden cross-shelf troughs [Westbrook et al., 2009]. Seepage from shelf sediments was reported in the detailed mapping and bubble quantification work of Sahling et al. [2014] (Figure *2-4*). Gas appears to migrate into the area from further offshore through permeable prograding hemipelagic sediment sequences which are variably capped by less permeable glaciogenic sediments on the upper slope and shelf [Rajan et al., 2012; Sarkar et al., 2012; Thatcher et al., 2013]. In the northern segment of the seepage region, the presence of a low-permeability glaciogenic sequence shifts gas escape into the water column upslope to ~ 240 m water depth [Rajan et al., 2012]. No geological control is observed to explain the focusing of the majority of seeps between 360 and 410 m water depth [Sarkar et al., 2012].

Prior to the discovery of the seafloor seeps, emissions of methane from upper slope and shelf sediments was inferred from the presence of pockmarks [Forwick et al., 2009] and from high concentrations of methane in shallow sediments [Knies et al., 2004] and parts of the water column [Damm et al., 2005; Knies et al., 2004]. However, dating of ^{13}C-depleted authigenic carbonates at the present-day seepage site indicates that they precipitated, in association with shallow anaerobic oxidation of methane, between 3 and 23 ka BP [Berndt et al., 2014]. Further offshore, where shallow methane hydrate and seafloor methane seepage are associated with faults providing a gas conduit through the GHSZ [Fisher et al., 2011; Smith et al., 2014; Vogt et al., 1994], the foraminiferal calcite carbon isotopic record suggests intervals of seepage and quiescence during the last 23.5 ka BP [Panieri et al., 2014b].

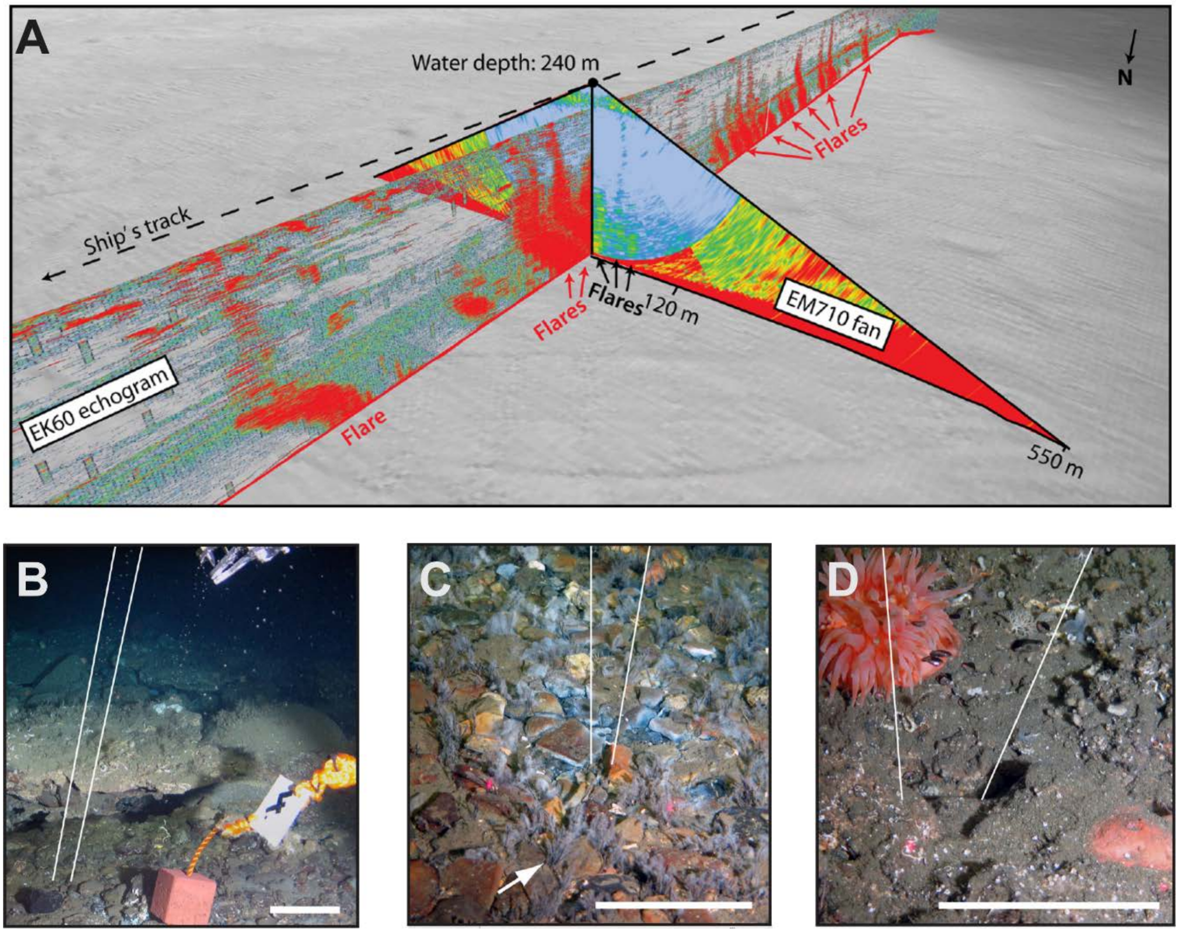

Figure 2-4 (**A**) Echosounder detection of seafloor seeps offshore Svalbard, (**B**-**D**) photos of methane seeps at the seafloor. White lines indicate the path of rising bubble streams, scale bar is 10 cm, arrow in (**C**) indicates filamentous (probably sulphur-oxidizing) bacteria and pogonophora. (**B** and **D**) are ~ 240 m water depth (northern segment of seepage), (**C**) shows seepage at ~ 400 m water depth. Modified from [Sahling et al., 2014].

At present, the total methane flux into the water column from both the main and northern seepage areas, quantified by combined acoustic and direct (remotely operated vehicle) measurements, is ~53 x 10^6 mol CH_4 yr^{-1} [Sahling et al., 2014]. Seep gas is > 99.7 %

methane, with $\delta^{13}C\text{-}CH_4$ -55.7 ‰ [Sahling et al., 2014]. Bubbles appear to dissolve completely in the lower ~200 m of the water column, losing the majority of their methane in the lower ~100 m [Gentz et al., 2014]. This results in bottom waters containing > 500 nM CH_4 and 4 -11 nM in overlying surface waters [Berndt et al., 2014; Chabert et al., 2011; Gentz et al., 2014; Westbrook et al., 2009]. Supersaturation of surface waters relative to atmospheric equilibrium (~ 3 nM) implies transfer of methane to the atmosphere, though shipboard air sampling in 2008 and 2009 did not indicate a local seep contribution to atmospheric methane [Fisher et al., 2011].

32

CHAPTER 3

Methane in shallow subsurface sediments at the landward limit of the gas hydrate stability zone offshore Western Svalbard

This chapter is intended for submission to *Geochimica et Cosmochimica Acta*

Contents

Abstract

Plumes of gas bubbles rising from the seafloor at the landward limit of the gas hydrate stability zone (GHSZ; ~400 m water depth) were discovered offshore Western Svalbard in 2008 and thermal modelling indicates that hydrate in the sediments beneath the plumes may be releasing methane gas as it dissociates in response to recent warming of bottom waters. To better constrain the role of hydrate in the supply of methane to the seafloor sediments, and the role of anaerobic oxidation of methane (AOM) in regulating methane fluxes across the sediment-seawater interface, we have characterised the chemical and isotopic compositions of the gases, and sediment pore waters. Molecular and isotopic signatures of gas bubble plumes (C_1/C_{2+}: 1×10^4, $\delta^{13}C\text{-}CH_4$: -55 to -51 ‰, and $\delta D\text{-}CH_4$: -187 to -184 ‰) indicate lateral migration of thermogenic gases produced at depth further offshore. Sediment methane and sulphate concentration profiles indicate upward diffusive methane fluxes of 30-550 mmol m^{-2} yr^{-1} into shallow subsurface sediments within the bubble plume region, and less than 20 mmol m^{-2} yr^{-1} at water depths of > 400 m where gas hydrate is expected to be stable or absent. AOM prevents transport of dissolved methane into ocean bottom waters, but most (>90%) of the methane that enters the shallow subsurface sediments is transported through small fractures and fissures in the gas phase, which bypasses the AOM filter and provides a mechanism for substantial methane release into the water column. Pore water sulphate profiles indicate that subsurface methane fluxes are predominantly at steady state in the bubble plume region at the GHSZ limit, but may be increasing in sediments immediately downslope, where hydrate is currently stable. This is evidence for movement of hydrate towards the seafloor in response to changes in bottom waters temperatures offshore western Svalbard.

3.1. Introduction

Methane (CH_4) is a potent greenhouse gas, and its atmospheric concentration has increased by more than 10% over the past three decades [Nisbet et al., 2014]. Atmospheric methane concentrations are closely correlated with temperature over glacial-interglacial cycles (e.g. Moller et al. [2013]), and methane emissions may have played a key role in major climate excursions in the past, including the Paleocene-Eocene thermal maximum (e.g. Bowen et al. [2014]; Dickens [2011]). Many natural sources of methane are sensitive to climate including wetlands, permafrost, and methane hydrate in terrestrial and marine environments [Ciais et al., 2013]. Characterization of emissions from these sources is paramount to the assessment of how levels of atmospheric methane will evolve in the context of a changing global climate.

In marine sediments, methane is produced by microbial and thermal remineralisation of organic carbon. If sediment pore waters become methane saturated, and temperature is low and pressure relatively high, then methane hydrate, an ice-like solid in which gas molecules are trapped in cages of water molecules, may form [Sloan and Koh, 2008]. Methane hydrate is stable on the continental margins at water depths > 200 m at high latitudes (or shallower in some permafrost settings [Sloan and Koh, 2008; Krey et al., 2009]), and on a global scale may contain > 500 Gt carbon, more than 10 % of that stored in fossil fuels [Archer 2007; Milkov, 2004; Pineiro et al, 2013; Wallmann et al, 2012].

A key uncertainty for climate models is the proportion of methane produced in deep marine sediments that escapes to reach the sediment-seawater interface and potentially the atmosphere. Methane rises from depth through permeable sediment strata, faults, fractures and cracks in solution, and as gas if sediment pore waters are supersaturated [Judd and Hovland, 2007]. In near-surface sediments, dissolved methane is oxidised where it comes into contact with pore waters that contain sulphate (SO_4), which diffuses downwards from overlying seawater, in a microbially-mediated process known as anaerobic oxidation of methane (AOM, *Equation 3-1*) [Boetius et al., 2000]:

$$CH_4 + SO_4^{2-} \rightarrow HCO_3^- + HS^- + H_2O \qquad (3\text{-}1)$$

The sub-seafloor depth interval in which concentrations of methane and sulphate fall to zero as a result of consumption by AOM is known as the sulphate-methane transition zone, or SMTZ. Bicarbonate (HCO_3^-) ions produced by AOM subsequently react with calcium ions present in sediment pore waters to form calcium carbonate [Sun and Turchyn, 2014] such that AOM acts to trap carbon in the solid phase (*Equation 3-2*):

$$Ca^{2+} + 2HCO_3^- \rightarrow CaCO_3 + CO_2 + H_2O \qquad (3\text{-}2)$$

However, if the methane flux is sufficient to overwhelm the oxidising capacity of the microbial consortia [Archer et al., 2009a], or the re-supply of sulphate from seawater by diffusion [Knittel and Boetius, 2009], then methane is released into the water column and potentially into the atmosphere. Methane in the gas phase is not available to microbes.

As the Earth and its oceans warm, there is concern that hydrate in marine sediments will be destabilized, releasing sufficient quantities of methane gas to reinforce the warming (e.g. Krey et al. [2009]). The recent discovery of more than 200 methane bubble plumes rising from the seabed at water depths close to the limit of the gas hydrate stability zone (GHSZ) offshore Western Svalbard [Westbrook et al., 2009] is suggested to be related to warming-induced dissociation of hydrate-bound methane in shallow sediments. In this study, we characterise the chemical composition of gases in sediments from offshore Svalbard and assess the spatial distribution and temporal variability of methane fluxes into the shallow sediments and across the sediment-seawater interface. We investigate the potential role of gas hydrate dissociation in regulating the supply of methane to the shallow sediments, and the role of AOM in regulating methane release from the seafloor.

3.2. Study area and sampling

The continental margin offshore Western Svalbard (*Figure 3-1*) was shaped by the Pleistocene-Pliocene advance and retreat of the Svalbard-Barents Sea ice sheet [Sarkar et al., 2012]. Glacial ice withdrew from the continental shelf about 13 thousand years ago [Elverhøi et al., 1995; Jessen et al., 2010]. On the shelf and upper slope, patchy glacial sediments overlie a sequence of seaward-dipping marine sediments [Rajan et al., 2012; Sarkar et al., 2012]. Sediments are underlain by extensive gas hydrate deposits at water depths of > 700 m [Carcione et al., 2005; Eiken and Hinz, 1993; Fisher et al., 2011; Smith et al., 2014; Vanneste et al., 2005; Vogt et al., 1999]. At the present-day, the GHSZ is expected to taper out at its landward limit at water depths of ~400 m [Berndt et al., 2014; Ferré et al., 2012; Westbrook et al., 2009].

The present-day landward limit of the GHSZ at the seabed is defined by water depth (pressure) and the temperature of overlying bottom water of the West Spitsbergen Current

(WSC) which flows along the upper slope. Observations indicate that the WSC has warmed over the last 30 – 60 years [Ferré et al., 2012; Westbrook et al., 2009], and the present rate of warming appears to be unprecedented in the last 2,000 years [Spielhagen et al., 2011].

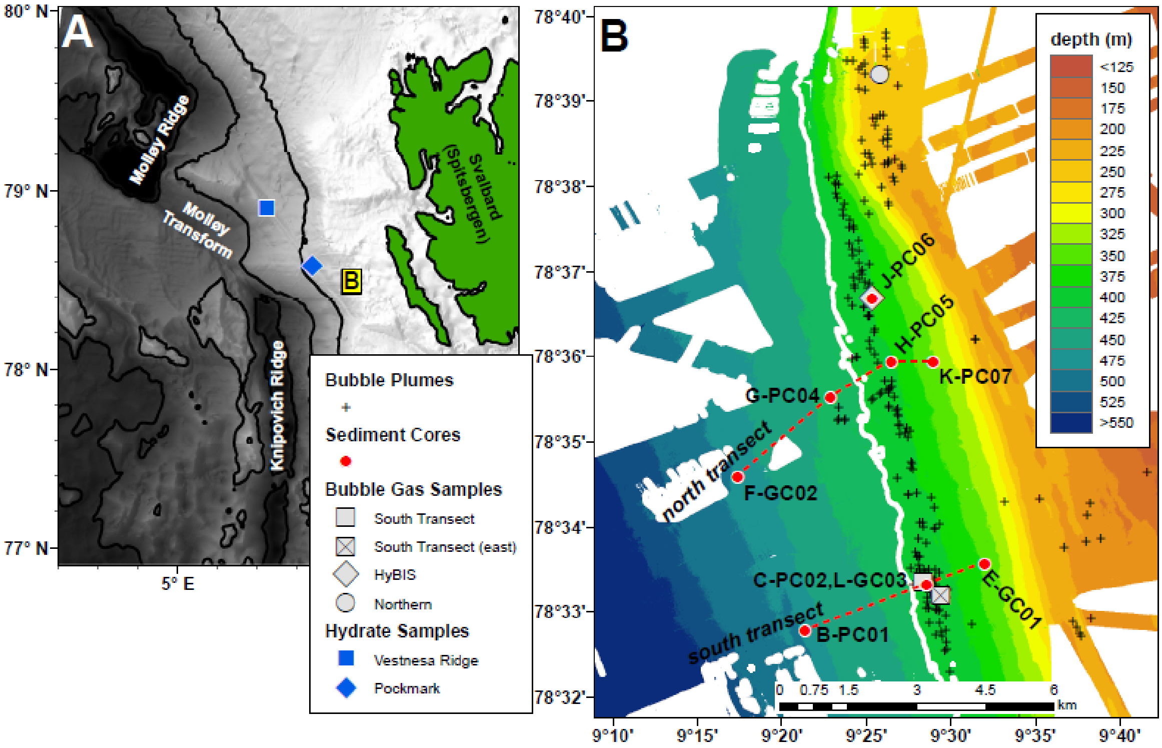

Figure 3-1 Location of the West Svalbard continental margin and the study area. (**A**) Regional map indicating the locations of hydrate samples (blue symbols) and the main study site (yellow rectangle labelled *B*), bathymetry data from GEBCO (The GEBCO_08 Grid, version 20100927, http://www.gebco.net) with 1000 m depth contours. (**B**) Main study site, showing shipboard bathymetry (cruise JR253), 400 m depth contour (white line), seafloor gas bubble plumes (black crosses), sediment core locations (red circles), and bubble plume sampling sites (grey symbols).

The distribution of seafloor bubble plumes offshore Western Svalbard is shown in *Figure 3-1b*. Critically, the seaward limit of the occurrence of bubble plumes, approximately along the ~400m bathymetric contour, coincides with the landward limit of the GHSZ [Berndt et al., 2014; Sahling et al., 2014; Westbrook et al., 2009]. Prior to the discovery of the seafloor bubble plumes, emissions of methane from the upper slope and shelf area were inferred from the presence of pockmarks [Forwick et al., 2009] and from high concentrations of methane in shallow sediments [Knies et al., 2004] and parts of the water column (Damm et al., 2005; Knies et al., 2004). Dating of authigenic carbonates that form as a result of methane oxidation (*Equation 3-2*) indicates that the seeps have been active for more than 500 years [Berndt et al., 2014].

Sediment samples for this study were collected from the continental slope offshore Svalbard at water depths of between 320 and 460 m during RRS *James Clark Ross* cruise 253 in July

Table 3-1 Locations of sampling sites. GC: gravity core, PC: piston core. MSM21/4: RV *Maria S. Merian* cruise 21/4, JR211: RRS *James Clark Ross* cruise 211, JR253: RRS *James Clark Ross* cruise 253. Distance from bubble plume estimated from shipboard mapping of bubbles by echosounder during JR253.

Cruise	Station ID	Lat. N (°)	Long. E (°)	Sample Location	Water Depth (m)	Date Sampled	core length (cm)	distance from bubble plume (km)
bubble plumes								
MSM21/4	577	78:33.34	9:28.404	south transect	394	23/08/2012	-	0
MSM21/4	585	78:33.34	9:28.411	south transect	394	24/08/2012	-	0
MSM21/4	597	78:36.68	9:25.497	HyBIS	384	25/08/2012	-	0
MSM21/4	599	78:36.68	9:25.507	HyBIS	385	25/08/2025	-	0
MSM21/4	611	78:33.17	9:29.438	south transect - eastern edge of flares	395	28/08/2012	-	0
MSM21/4	620	78:39.30	9:26.056	northern seep region	246	29/08/2012	-	0
MSM21/4	647	78:33.34	9:28.406	south transect	394	02/09/2012	-	0
hydrate								
JR211	33GC	78:41.07	8:16.36	pockmark, > 126 cm sediment depth	890	18/09/2008	-	-
JR211	26GC	79:00.39	6:54.26	Vestnesa Ridge, >193 cm sediment depth	1210	16/09/2008	-	-
sediment cores								
JR253	B-PC01	78:32.76	9:21.40	south transect - shallow	458	03/08/2011	379	2.6
JR253	C-PC02	78:33.29	9:28.57	south transect - on seep	384	04/08/2011	92	0.03
JR253	E-GC01	78:33.54	9:32.09	south transect - shallow	340	06/08/2011	209	1.0
JR253	F-GC02	78:34.58	9:17.45	north transect - deep	454	07/08/2011	360	2.5
JR253	G-PC04	78:35.50	9:23.00	north transect - deep seep	407	09/08/2011	343	0.02
JR253	H-PC05	78:35.92	9:26.63	north transect - near seep	374	10/08/2011	351	0.3
JR253	J-PC06	78:36.66	9:25.53	north transect - on seep	374	11/08/2011	224	0.02
JR253	K-PC07	78:35.91	9:29.10	north transect - shallow	323	13/08/2011	137	1.0
JR253	L-GC03	78:33.30	9:28.64	south transect - on seep	386	15/08/2011	162	0.01

and August 2011 (*Table 3-1*). Locations of methane seeps were determined using the ship's hull-mounted sonar systems (Simrad EK60 and Simrad EM122, *Figure 3-1b*). A series of gravity and piston cores were collected aligned roughly along two transects from water depths shallower than the GHSZ through the region of the seafloor bubble plumes to greater water depths within the GHSZ. Samples of gas bubbles emanating from the seafloor were collected in a pressurized gas sampler using the manned submersible JAGO during RV *Maria S. Merian* cruise 21/4 in August and September 2012. Locations of the sediment cores and bubble plume samples are shown in *Figure 3-1b*. Hydrate was recovered in sediment cores during RRS *James Clark Ross* cruise 211 in August and September 2008 from two sites: a pockmark at 890 m water depth located ~30 km northwest of our study site, and from Vestnesa Ridge at 1,210 m water depth [Fisher et al., 2011]. Locations of these samples are shown in *Figure 3-1a* and listed in *Table 3-1*.

3.3. Analytical procedures and modelling

3.3.1. Geochemical analyses

Back onboard the ship, sediment cores were immediately sectioned, split, and subsampled under a nitrogen atmosphere. For gas analysis, ~ 3 mL of sediment was withdrawn using a cut-off plastic syringe and placed in a 20 mL glass vial containing 5 mL of 1 M sodium hydroxide to prevent microbial activity [Hoehler et al., 2000]. The vials were crimp sealed and shaken vigorously to release adsorbed gases from sediment. A subsample of sediment (~ 3 g) was placed in a pre-weighed plastic pot and stored at 4 ˚C for porosity analysis back onshore. Pore waters were extracted by centrifugation under a nitrogen atmosphere and filtered through 0.2 μm cellulose acetate filters. Subsamples for analysis of cations were stored in acid-cleaned low density polyethylene bottles and acidified to pH 2 with thermally distilled nitric acid. Subsamples for analysis of anions were diluted by a factor of 200 with Milli-Q water. Where present, gas hydrate was quickly removed from the spilt sediment core, wrapped in cotton, and stored in liquid nitrogen.

Concentrations of methane, ethane, propane, isobutane, butane, isobutane, pentane, isopentane, and hexane (C_1-C_6) in sediment headspace gases were determined onboard the ship by gas chromatography (Agilent 7890). Analytical reproducibility, based on replicate analysis of standards (20 and 100 ppm, Air Products, UK), is better than ± 2 %, and the detection limits are 2 ppm for C_6 and C_5, 1.5 ppm for C_4, 1 ppm for C_3, 0.6 ppm for C_2 and 0.5 ppm for C_1, which correspond to pore water concentrations of between ~0.2 μM for methane and ~0.7 µM for hexane. Reported concentrations are considered to represent minimum values because the samples may have degassed during recovery. Gas bubble and hydrate hydrocarbons were determined by the same method at the National Oceanography Centre (NOC).

The stable carbon isotope composition of methane was determined by trace gas isotope ratio mass spectrometry (IRMS, Isoprime Ltd.) at the Natural Environment Research Council Life Science Mass Spectrometry Facility at the Centre for Hydrology and Ecology in Lancaster, UK. The reproducibility of these analyses is better than ± 0.2 ‰. The hydrogen isotopic composition of methane was measured by a Continuous Flow-Isotope Ratio Mass Spectrometer (CF-IRMS) system at the Institute for Marine and Atmospheric Research Utrecht, Utrecht University following the method described in Brass and Röckmann [2010] and Sapart et al. [2011]. For δD, the analytical error is between 0.1 to 3.9‰ depending on the amount of methane present. Isotope data are given in δ^{13}C and δD notation relative to the Vienna Pee Dee Belemnite (VPDB) and Vienna Standard Mean Seawater (VSMOW) standards for the carbon and hydrogen isotopic signature, respectively.

The porosity of the sediments (ϕ) was calculated from the difference between the mass of wet sediment, and the mass of the sample after drying in an oven at ~60 °C overnight. The densities of the sediment and fluid were assumed to be 2.65 and 1.00 g cm^{-3}, respectively. For determination of total inorganic and total carbon (TIC, TC), sediment subsamples were oven dried at > 70 ˚C for > 24 hours, ground to a homogenous fine powder, and measured using a carbon dioxide coulometer (model CM5012, UIC Inc.) equipped with an acidification module (model CM5130), and a furnace module (model CM5120). The concentration of total organic carbon (TOC) was determined by subtracting TIC from TC. The reproducibility of these analyses is better than ± 10 %.

The total alkalinity of the pore waters was determined onboard ship by titration with 0.02 M hydrochloric acid, using a mixture of methyl red and methylene blue as an indicator while bubbling nitrogen through the solution. Analyses were calibrated against a seawater standard (IAPSO), and the reproducibility of the analyses is better than ± 1.5 %. Back onshore, cation concentrations in the pore waters were determined by inductively coupled plasma optical emission spectrometry (ICP-OES, Perkin Elmer Optima 4300DV) at the NOC. The accuracy and reproducibility of this technique was assessed by multiple (n = 3) analyses of a seawater certified reference material (High Purity Standards™). Measured concentrations agree with certified values to within ± 3 %, and the reproducibility of the analyses was better than ±

1 % for all analytes. Anion concentrations were determined at the NOC by ion chromatography (Dionex ICS250). Reproducibility of replicate analyses is better than ± 0.2 % for chloride, ± 2.5 % for bromide, and ± 1 % for sulphate. Hydrogen sulphide was determined spectrophotometrically by absorbance at 670 nm following addition of N,N-dimethyl-1,4-phenylenediamine dihydrochloride and an iron(III) chloride catalyst. The working hydrogen sulphide standard was calibrated daily by titration with sodium thiosulphate against a potassium iodate standard (1.667 mM, OSIL environmental instruments and systems, UK). The reproducibility of the sulphide analyses was better than ± 10 %, and the limit of detection is 10 μM.

3.3.2. Modelling

If sulphate is principally removed by AOM, then concentrations of pore water SO_4^{2-} will decrease from seawater values at the sediment-seawater interface to zero at the depth of the SMTZ (e.g. Borowski et al. [1996]). At steady state, the upward diffusive flux of methane (J_{CH4}) is balanced by the downward diffusive flux of sulphate (J_{SO4}), which can be calculated using Fick’s First Law (*Equation 3-3*):

$$J = D_0 \left(1 - ln(\phi^2)\right)^{-1} \phi \left({}^{\delta C}/_{\delta x}\right) \qquad (3\text{-}3)$$

where D_0 is the diffusion coefficient of sulphate in water (1.7×10^{-10} m^2 s^{-1} at 3°C and a salinity of 35), the term $1\text{-}ln(\phi^2)$ is the tortuosity correction, ϕ is the porosity, and $\delta C/\delta x$ is the sulphate concentration gradient [Boudreau, 1997; Mazumdar et al., 2012]. Upward methane fluxes were estimated from linear least squares fitting of sulphate profiles from beneath the depth of the irrigated surface layer to the SMTZ. Profiles were linearly extrapolated to the depth of the SMTZ where this was deeper than the length of the sediment core.

Even in regions of high methane flux, oxidation of organic matter using SO_4^{2-} as the terminal electron acceptor also contributes to sulphate removal above the SMTZ. As a result, the simple model described above can only provide an upper limit on diffusive methane fluxes (Hoehler et al., 2000). In many cold seep environments, methane is transported by advection in upwelling fluids in addition to diffusion (e.g. Haese et al. [2003]; Vanneste et al. [2011]). If concentrations of methane in pore waters exceed saturation, methane will be transported in the gas phase until it reaches undersaturated pore waters. The steady-state distributions of methane and sulphate are therefore better described by partial differential equations that account for transport by diffusion, advection, and irrigation, and for reactions including sulphate reduction, methanogenesis, and AOM (*Equation 3-4*):

$$\left(\frac{\delta \emptyset C_i}{\delta t}\right) = D_i \frac{\delta}{\delta x}\left(\frac{\emptyset}{1-ln(\phi^2)} \frac{\delta C_i}{\delta x}\right) - \left(\frac{\delta \emptyset u C_i}{\delta x}\right) - \emptyset\, \alpha_{(x)} \left(C_{i_{(x)}} - C_{i_{(0)}}\right) + \emptyset \left(R_{\mathrm{SO_4}} + R_{\mathrm{CH_4}}\right) \quad (3\text{-}4)$$

where

$$\alpha_{(x)} = \alpha' e^{-(x_b - x_{mix})}$$

$$R_{\mathrm{SO_4}} = -k_G \frac{C_{org}}{2} \frac{C_{\mathrm{SO_4^{2-}}}}{K_{SO4} + C_{\mathrm{SO_4^{2-}}}} - R_{AOM}$$

$$R_{\mathrm{CH_4}} = k_G \frac{C_{org}}{2} \frac{Ki_{SO4}}{Ki_{SO4} + C_{\mathrm{SO_4^{2-}}}} - R_{AOM}$$

and

$$R_{AOM} = K_{AOM} C_{\mathrm{CH_4}} \frac{C_{\mathrm{SO_4^{2-}}}}{K_{S,AOM} + C_{\mathrm{SO_4^{2-}}}}$$

C_i is the concentration of dissolved species i (i=CH_4, SO_4^{2-}), u is the advective fluid flow velocity, $\alpha_{(x)}$ is the depth (x) dependent irrigation exchange coefficient, α' is the pore water mixing coefficient, x_b is a depth exceeding the irrigation zone, x_{mix} is the depth of the mixed layer, ($C_{i(x)} - C_{i(0)}$) is the difference between concentrations of species i at depth x and in overlying seawater (x = 0) and R_i are the reaction terms relevant for species i [Treude et al., 2003; Vanneste et al., 2011]. The reactions considered are: (i) remineralisation of particulate organic matter coupled to sulphate reduction, described by the kinetic constant (k_G), organic matter concentration (C_{org}), and the half saturation constant (K_{SO4}); (ii) methanogenesis, described by k_G and C_{org} and the inhibition constant for initiation (Ki_{SO4}); and (iii) anaerobic oxidation of methane, described by the rate constant K_{AOM} and the Monod inhibition constant $K_{S,AOM}$. The choice of rate law formulation for AOM follows Vannesete et al [2011], accounting for experimentally observed limitation of methane oxidation in the presence of low sulphate concentrations. Transport of methane in the gas phase is not included in this model. Bubble formation only occurs in saturated pore waters (~76 mM CH_4 in shallow sediments at ~400 m water depth (calculated following Dale et al. [2008a] and Meister et al. [2013] assuming a geothermal gradient of 0.87 °C/m; Reagan and Moridis [2009]). Information on all of these parameters is given in *Table 3-2*.

The one dimensional transport model was solved numerically using the ordinary differential equation solver ODE15s in MATLAB®, using code described in [Vanneste et al., 2011; Vanneste, 2010]. The irrigation parameters α' and x_{mix} were determined by fitting the model to the upper part of the pore water sulphate profiles. The methane concentration at the lower limit of the model domain (the length of the core) was determined by fitting the depth of the modelled SMTZ to the pore water sulphate and methane profiles. The rate of AOM was determined by fitting the shape and slope of the modelled sulphate and methane profiles near the SMTZ to the measured data. Coarse fitting was performed by visual comparison of modelled pore water profiles with measured concentrations at discrete depths, and verified by calculating the residuals of the modelled data to sulphate measurements. This model was only applied to cores where the SMTZ was sampled to allow fitting of modelled profiles to measured data in this critical interval. Steady state was reached within 10^3 years from arbitrary initial conditions using a depth step of 0.5 cm. The uncertainty of model results was assessed by sensitivity analysis of all input parameters.

Table 3-2 Transport-reaction model parameters.

parameter	symbol	units	value	source
diffusion coefficient for sulphate in water	D_{SO4}	$cm^2\ yr^{-1}$	167	calculated for temperature, pressure, and salinity (T,P,S) conditions after Boudreau [1997], following Vanneste et al. [2011]
diffusion coefficient for methane in water	D_{CH4}	$cm^2\ yr^{-1}$	273	calculated for T,P,S conditions after Hayduk and Laudie [1974], following Vanneste et al. [2011]
concentration of species i (i = CH_4, SO_4^{2-})	$C_{i(x)}$	mM	-	depth profiles, fit to measured data
bottom seawater methane concentration	$C_{\mathrm{CH4}(0)}$	mM	0.00	measured concentration in near-surface sediments
bottom seawater sulphate concentration	$C_{\mathrm{SO4}(0)}$	mM	28	measured concentration in near-surface sediments
porosity	ϕ	-	0.5	average measured value
pore water advection	u	$cm\ yr^{-1}$	0.03	sedimentation rate from Jessen et al. [2010]
pore water mixing coefficient	α'	yr^{-1}	10	fit to measured sulphate concentration depth profile
depth of irrigation mixing	x_{mix}	cm	5-30	fit to measured sulphate concentration depth profile
depths exceeding mixing zone	x_b	cm	-	model domain beneath irrigation mixing zone
rate constant for organic matter remineralisation	k_G	yr^{-1}	1×10^{-6}	as in Vanneste et al. [2011] see discussion in *Section 3.4.3*
organic carbon content	C_{org}	mM	1300	average measured value (0.6 ± 0.3 weight %) expressed as mmol per L of dry sediment for sediment density of 2.65 g mL^{-1}
half saturation constant for sulphate reduction coupled to organic matter remineralisation	K_{SO4}	mM	1	as in Vanneste et al. [2011], value is assumed due to absence of constraints available for natural systems
inhibition constant for initiation of methanogenesis	Ki_{SO4}	mM	1	as in Vanneste et al. [2011], value is assumed due to absence of constraints available for natural systems
rate constant for anaerobic oxidation of methane	K_{AOM}	yr^{-1}	0.2 - 5	fit to measured sulphate and methane concentration depth profiles within the SMTZ
Monod inhibition constant for AOM	$K_{S,AOM}$	mM	1	as in Vanneste et al. [2011], based on data from Nauhaus et al. [2002]

3.4. Results

3.4.1. Chemical and isotopic composition of gas bubble plumes and hydrate

Chemical and stable carbon and hydrogen isotope compositions of the gas bubble plume and gas hydrate samples are given in *Table 3-3*. Bubble plume gases collected at the seafloor consist of > 99.99 % methane, and contain very small amounts of ethane (< 90 ppm). Concentrations of all higher hydrocarbons (C_3 to C_6) were below detection limits. All bubble plume samples have methane (C_1) to higher hydrocarbon (C_{2+}) molar ratios of ~10 000. Hydrate recovered from the Vestnesa Ridge at ~ 2 m below the seafloor contained small amounts of ethane, propane, butane, and pentane, and consequently has a lower methane to higher hydrocarbon ratio ($C_1/C_{2+} = 65$). Hydrate recovered in sediments from the pockmark site, which lies closer to the area of seafloor bubble plumes, has higher ethane concentrations than seep gas ($C_1/C_{2+} = 500$), but concentrations of C_3 to C_6 are below detection limit.

Table 3-3 Molecular and isotopic composition of bubble plume and hydrate gas. MSM21/4: RV *Maria S. Merian* cruise 21/4, JR211: RRS *James Clark Ross* cruise 211. Hydrate $\delta^{13}C$-CH_4 data from Fisher *et al.*, [2011]. Uncertainty of $\delta^{13}C$-CH_4 measurements of bubble plume samples is reported as the standard deviation of three subsamples; uncertainty of $\delta^{13}C$-CH_4 measurements of hydrate is reported as the standard deviation of analyses of three separate pieces of hydrate from an individual core.

Cruise	Station ID	C_1/C_2+ (mol/mol, x 10^3)	$\delta^{13}C$-CH_4 (‰)[a]	δD-CH_4 (‰)
bubble plumes				
MSM21/4	577	9.8	-54.6 ± 0.3	-187 ± 1
MSM21/4	585	9.6	-54 ± 1	-179 ± 3
MSM21/4	597	11	-51.1 ± 0.8	-
MSM21/4	599	12	-51.3 ± 0.1	-178 ± 2
MSM21/4	611	12	-51.6 ± 0.1	-
MSM21/4	620	11	-55.5 ± 0.4	187.0 ± 0.1
MSM21/4	647	9.7	-55.0 ± 0.5	-
hydrate				
JR211	33GC	0.50	-54.6 ± 2	-174 ± 4
JR211	26GC	0.06	-45.6 ± 3	-180 ± 2

The stable carbon ($\delta^{13}C$-CH_4) and hydrogen (δD-CH_4) isotopic signatures of methane in gas bubble plumes range from -55.5 to -51.1 ‰ and -187 to -178 ‰, respectively (Table 3). These values are similar to those reported for gas bubbles collected from close to the seafloor at ~ 240 and 400 m water depth within our study area in late summer 2012 (C_1/C_{2+} = 9,700 – 15,200, $\delta^{13}C$-CH_4 = -53.8 to -57.4 ‰; Sahling et al. [2014]). Methane from hydrate recovered at the pockmark site has $\delta^{13}C$-CH_4 = -54.6 ± 1.7 ‰ [Fisher et al., 2011] and δD-

CH_4 = -174 ± 4 ‰, close to the range of the bubble plume gas samples. Hydrate recovered from Vestnesa Ridge has a slightly higher $\delta^{13}C\text{-}CH_4$ value (-45.7 ±2.7 ‰; Fisher et al. [2011]), and a $\delta D\text{-}CH_4$ value of -180 ± 2 ‰. Our data for Vestnesa Ridge hydrate are similar to those reported for hydrate recovered nearby in 2012 (C_1/C_{2+} = 26, $\delta^{13}C\text{-}CH_4$ = -47.7 ‰; Smith et al. [2014]). The $\delta^{13}C\text{-}CH_4$ and C_1/C_{2+} data for hydrates fall within the range reported for hydrates worldwide [Milkov, 2005].

3.4.2. Chemical composition of sediment pore waters

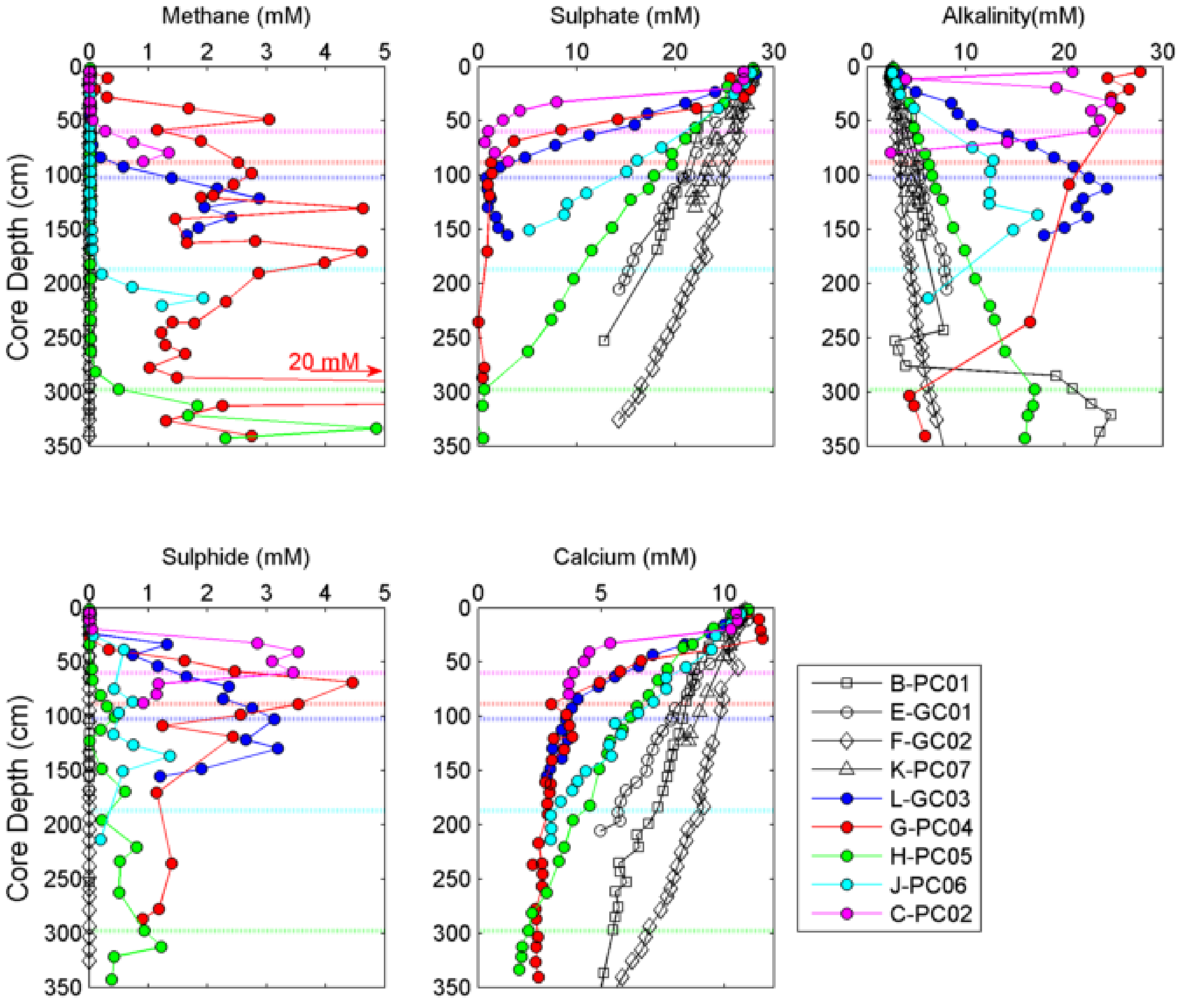

Figure 3-2 Profiles of pore water methane, sulphate, alkalinity, sulphide, and calcium. Cores collected from less than ~ 0.01 to 0.3 km away from bubble plumes are shown by the coloured symbols. Dashed horizontal lines indicate the depth of the SMTZ, where sampled. Sulphide was not determined in cores E-GC01 and K-PC07

The SMTZ was sampled in 5 of the 9 sediment cores (*Figure 3-2*). The depth of the SMTZ is relatively shallow (< 300 cm below the seafloor) in the immediate vicinity (within 30 m) of the methane seeps. Cores recovered from 1 to 3 km outside of the bubble plume region did not sample the SMTZ. Sulphate profiles are almost linear above the SMTZ. Methane concentrations are generally less than 20 nM in the presence of more than 1 mM sulphate, with the exception of core G-PC04 where pore waters are methane-saturated (i.e. methane concentrations greater than atmospheric saturation, which is ~1.8 mM) up to 40 cm below the seabed, even in the presence of > 20 mM sulphate. The concentration of dissolved SO_4 is close to bottom seawater in the uppermost 20 – 30 cm of the sediment column in cores G-PC04 and C-PC02, which is indicative of drawdown of seawater into the sediments (irrigation).

Depth profiles of pore water alkalinity, sulphide, and calcium confirm that AOM occurs in sediments at the depth of the SMTZ (*Figure 3-2*, *Equation 3-1*). Total alkalinity increases from a seawater value of ~2.3 mM to 12 - 25 mM at the SMTZ due to production of HCO_3^- (*Equation 3-1*). Hydrogen sulphide was only detected in pore waters from cores which sampled the SMTZ, reaching ~4 mM in cores with the shallowest SMTZ (G-PC04 and C-PC02). Calcium concentrations decrease abruptly at the SMTZ, due to the formation of authigenic calcium carbonate (*Figure 3-2*); carbonate nodules were recovered in cores where the SMTZ was sampled.

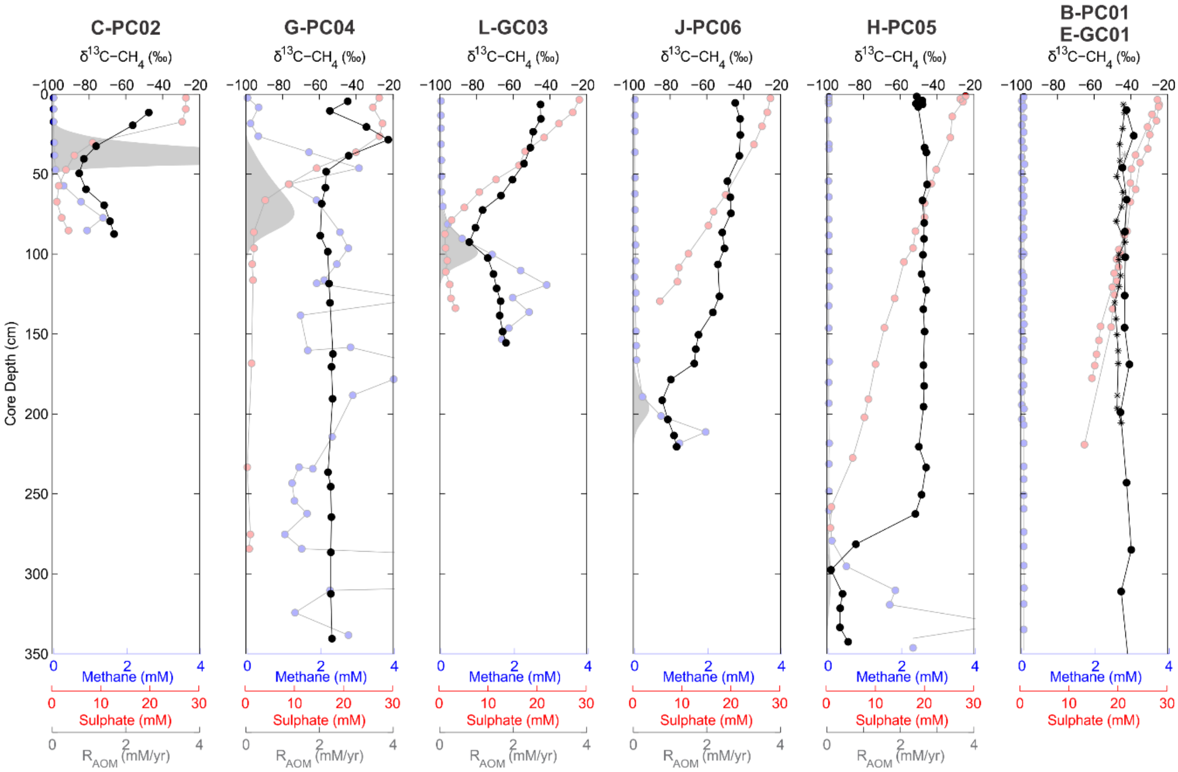

Figure 3-3 Profiles of pore water methane carbon isotopic ratio ($\delta^{13}C\text{-}CH_4$; black).Profiles of methane (blue) and sulphate (red) concentrations, and modelled rates of anaerobic oxidation (see *Section 3.4.3* and *Figure 3-5*) of methane (grey shaded areas) are also shown.

Pore waters from below the SMTZ, which are methane-saturated, have $\delta^{13}C\text{-}CH_4$ values of ~ -53 ‰ (*Figure 3-3*). This is within the range of values measured in the seafloor bubble plume gases and hydrate from the pockmark site. At all but one site (G-PC04) where the

SMTZ was sampled, very low $\delta^{13}C$ values (-84 to -97 ‰) are observed within the depth interval where the rate of AOM is highest (*Figure 3-3*). Above the SMTZ, $\delta^{13}C$-CH_4 values increase to ~ -44 ‰. At sites away from the seafloor bubble plumes, $\delta^{13}C$-CH_4 values show little variation with depth, and are close to -44 ‰. In core G-PC04, there is a marked increase in $\delta^{13}C$-CH_4 (to ~ -20 ‰) immediately above the depth of the SMTZ.

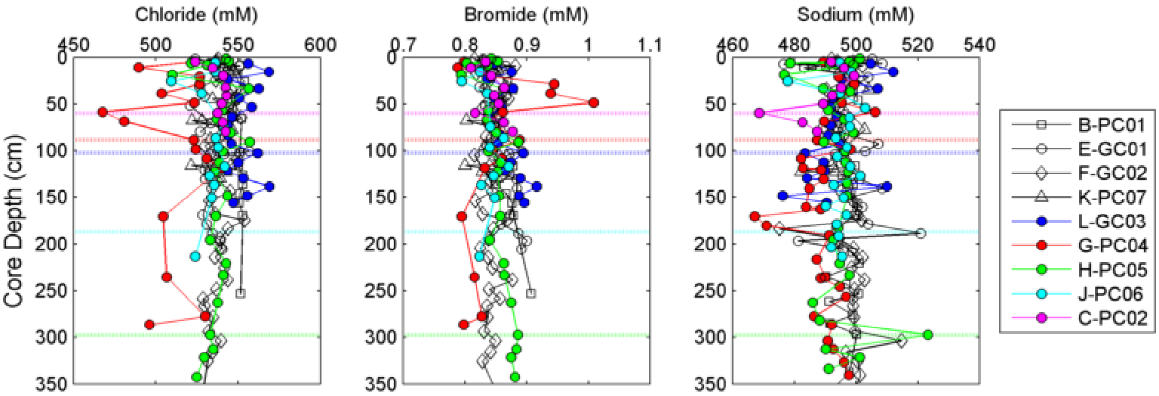

Figure 3-4 Pore water profiles of chloride, bromide, and sodium. Cores collected from less than ~0.01 to 0.3 km away from active bubble seeps are shown by the coloured symbols. Dashed horizontal lines indicate the depth of the SMTZ, where sampled.

Concentrations of species that are not produced or consumed during shallow diagenetic reactions (chloride: Cl^-, bromide: Br^-, and sodium: Na^+) show little variation with depth at all sampling sites, whether close to, or distant from, seafloor bubble plumes (*Figure 3-4*). The average and standard deviation of all of Cl^- measurements is 537 ± 14 mM. Where high methane concentrations are observed close to the sediment-seawater interface (G-PC04), pore waters appear to have slightly lower Cl^- concentrations, with 7 of the 16 samples for G-PC04 having Cl^- values that are more than two standard deviations lower than the average. Three pore water samples from the same interval are also slightly enriched in Br^- (940 – 1,010 μM, compared to the average of 850 ± 24 μM for all other pore water samples).

3.4.3. Methane fluxes

The porosity and total organic carbon (TOC) content of the sediments show no systematic variation with depth or between coring locations. Average porosity is 0.47 ± 0.05, and the average TOC content is 0.6 ± 0.3 wt %; these values are used in all model calculations and are within the range of those reported elsewhere for surface sediments of the upper continental margin west of Prins Karls Foreland [Winkelmann and Knies, 2005].

The relatively low TOC content supports the low rate of organic matter remineralisation (k_G = 10^{-6} yr^{-1}) used in the transport-reaction model, and the assumption that organic matter remineralisation is not a significant sulphate sink in the diffusion-only model. However, this rate constant could be orders of magnitude higher: values up to 10^{-1} have been used in models of AOM which employ the same organic matter degradation formulation (1-G) used here [Regnier et al., 2011]. Furthermore, this 1-G formulation may not be appropriate for shallow sediments, as reactivity of organic matter is expected to change dramatically with depth in this interval of initial deposition, especially in a continental shelf environment (e.g. Arndt et al. [2013]). Modelled sulphate and methane profiles and flux estimates are insensitive to halving or doubling k_G and TOC. A small upward shift in the depth of the SMTZ (by < 10 cm), and increased curvature in the (concave up) sulphate profile shape are obtained only if k_G is increased by more than an order of magnitude. If the choice and k_G and formulation of the organic matter remineralisation reaction kinetics in the model lead to an underestimation of the contribution of organic matter degradation to sulphate removal, results are likely to underestimate rates of AOM. The impact of this potential underestimation of organic matter sulphate reduction contribution can be expected to be most significant where upwards methane fluxes (and thus AOM rates) are lowest, and may be insignificant for all the sites modelled here, where the depth of the SMTZ is within 10 m of the seafloor [Regnier et al. 2011].

Uniformity of the porosity values simplifies the transport-reaction model and, as profiles of conservative species (Cl^-, Na^+ etc.) show no evidence for pore water advection, upwards advection (u) is attributed to sediment compaction only, and assumed to be equal to the sedimentation rate (~ 0.03 cm/year; Jessen et al. [2010]) [Malinverno and Pohlman, 2011]. Doubling or halving the advection rate by changing the sedimentation rate changes the modelled methane flux by < 1 %. If porosity is increased by 0.05 (the standard deviation of measured values), then both the flux of methane into the sediment column and the rate of AOM increase by ~ 20 %, so there is no change in the methane flux across the seafloor and the modelled pore water profiles are not significantly affected.

Results of modelling pore water profiles using both the diffusion-only model and the transport-reaction model are shown in *Figure 3-5*. Values of the input and output parameters are given in *Table 3-4*. Highest methane fluxes are modelled for sites that have the shallowest SMTZ, i.e. those sites located closest to the seafloor bubble plumes. There is large spatial heterogeneity in pore water profiles within the bubble plume region: for example, the depth of the SMTZ is 0.5 m deeper in core L-GC03 compared to C-PC02, and its modelled methane flux is three times lower, even though the cores were taken within 30 m of each other. Modelled rates of anaerobic oxidation at the STMZ are 0.3 - 30 nmol cm^{-3} day^{-1}, within the range of those measured elsewhere in coastal and margin sediments (0.1 – 50 nmol cm^{-3} day^{-1}; Knittel and Boetius [2009]). It is difficult to meaningfully compare the modelled rate constants of AOM (K_{AOM}) to other AOM modelling studies as the formulation of the models varies widely, and rate constants incorporate a range of site-specific physical parameters (e.g. K_{AOM} for bimolecular rate laws ranges from 1 - 10^{7} mM yr^{-1}; see review in Regnier et al. [2011]). The K_{AOM} values obtained (0.2 – 5 yr^{-1}) are in agreement with and lower than values obtained with the same model for the Carlos Ribeiro mud volcano (7-25 yr^{-1}; Vanneste et al. [2011]), which likely reflects the different seafloor seepage environments.

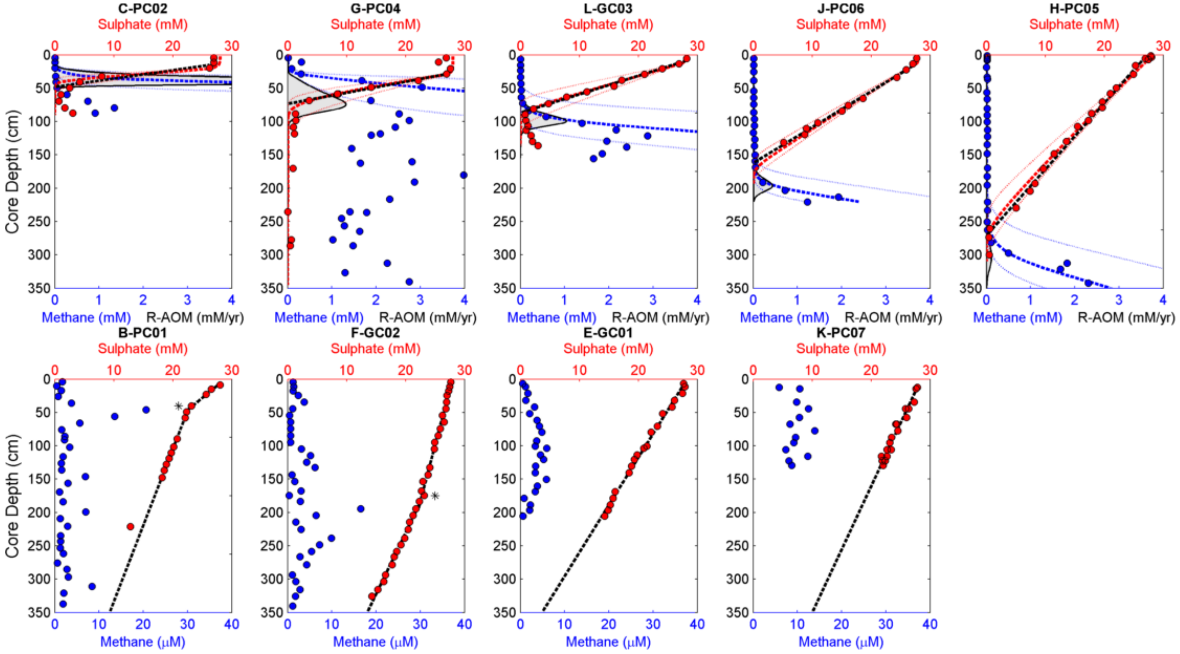

Figure 3-5 Modelled pore water profiles: methane (blue), sulphate (red) and anaerobic methane oxidation rate (R$_{AOM}$, grey shading). Measured data are shown by the coloured circles. Results of the diffusion-only model are shown by the black dashed lines (sulphate only, R^{2} values given in *Table 3-4*). Results for the transport-reaction model for sulphate and methane are shown, respectively, by the red and blue dashed lines. Dotted red and blue lines indicate the effect of doubling and halving the methane flux to the base of the sediment column. The maximum rate of AOM rate found in core C-PC02 is 9.9 mM yr^{-1}.

There is good agreement between results from the two different models for cores with moderate rates of methane seepage (L-GC03, H-PC06, J-PC07). Setting advection and organic matter remineralisation terms to zero in the transport-reaction model has a negligible effect on the modelled pore water profiles, indicating that diffusive transport and AOM are the dominant controls on the chemical composition of the pore waters. The agreement between the models is less for cores with high methane fluxes (C-PC01 and G-PC04). While the measured pore water profiles from core G-PC04 can be reproduced by both models, there is a large discrepancy in the predicted methane flux into shallow subsurface sediments (190 mmol m^{-2} yr^{-1} for the diffusion-only model versus 310 mmol m^{-2}yr^{-1} for the transport-reaction model). In C-PC02, the transport-reaction model cannot simultaneously reproduce the depth of zero sulphate and the depth at which methane reaches saturation. Moreover,

Table 3-4 Values of input and output parameters for the diffusion and transport-reaction models. Depth of SMTZ and sulphate/methane fluxes estimated using the diffusion model for cores F-GC02 and B-PC01 are provided by considering the fit of the model both above, and below, the kink in the sulphate profile. See text for more details. OM=organic matter.

parameter	units	C-PC02	G-PC04	L-GC03	J-PC06	H-PC05	E-GC01	K-PC07	F-GC02	B-PC01
diffusion model										
SMTZ	m	0.5	0.7	1.0	1.9	3.1	4.0	5.5	9.5 ; 5.8	2.4 ; 6.4
fit (R^2)	-	0.86	0.99	0.99	1.00	0.99	0.99	0.95	0.98	0.99
downward diffusive sulphate flux (J_{SO4}) = upward methane flux to SMTZ	mmol m^{-2} yr^{-1}	**250**	**190**	**100**	**50**	**30**	**20**	**15**	**10 ; 20**	**40 ; 10**
transport-reaction model inputs										
[CH_4] at bottom of core	mM	50	150	12	2.4	3	-	-	-	-
irrigation depth (x_{mix})	cm	22	30	15	15	5	-	-	-	-
AOM rate constant (K_{AOM})	yr^{-1}	5	0.2	2	3	0.5	-	-	-	-
transport-reaction model outputs										
methane flux to shallow subsurface sediments	mmol m^{-2} yr^{-1}	**550**	**310**	**120**	**50**	**30**	-	-	-	-
methanogenesis	mmol m^{-2} yr^{-1}	0.2	0.9	0.2	0.1	0.3	-	-	-	-
AOM rate	mmol m^{-2} yr^{-1}	540	240	120	50	30	-	-	-	-
SO_4 reduction rate for OM remineralisation	mmol m^{-2} yr^{-1}	0.1	0.2	0.3	0.6	0.9	-	-	-	-
methane flux to seawater by irrigation	mmol m^{-2} yr^{-1}	10	70	0	0	0	-	-	-	-
methane flux to seawater by diffusion	mmol m^{-2} yr^{-1}	0.01	0.02	0.0004	0.0003	0.0009	-	-	-	-
ratio of modelled methane flux to linear diffusion model result	-	**2.2**	**1.7**	**1.2**	**1.0**	**1.1**	-	-	-	-

fitting the transport-reaction model to the measured sulphate data requires methane concentrations of > 1.8 mM (i.e. higher than the surface saturation concentration) at a depth which is 40 cm shallower than observed, while fitting this model to the measured methane data requires a linear sulphate profile and results in zero sulphate concentrations at depths ~40 cm deeper than was observed. Sediments recovered in cores G-PC04 and C-PC01 are irrigated to a depth of ~20 cm below the seafloor, resulting in a modelled flux of methane (respectively, 70 and 10 mmol m^{-2} yr^{-1}) to the overlying water column.

The cores recovered at deeper water depths (~ 450 m) within the GHSZ (B-GC01 and F-GC02) have kinked sulphate profiles that cannot be reproduced by the diffusion-only model. The sulphate profiles can, however, be reproduced by applying separate linear fits to the upper and lower segments. The shift in the sulphate gradient is different for the two cores, with a steeper sulphate profile (shallower inferred SMTZ) in the shallower sediments of B-GC01 and a steeper profile in the deeper sediments in F-GC02. In B-GC01, the sulphate gradient observed in surface sediments implies that the SMTZ should be located within the sampled core, which is not consistent with the pore water profiles.

3.5. Discussion

3.5.1. Source of methane in bubble plumes and hydrate from offshore Western Svalbard

The absence of propane and heavier hydrocarbons and the very small amounts of ethane in the seep gas samples (C_1/C_{2+} ~10,000) suggests that the seep gases are derived from a microbial source [Bernard et al., 1976; Whiticar, 1999]. By contrast, the carbon isotopic signature of the methane ($\delta^{13}C\text{-}CH_4$ = -55 to -51 ‰) falls between the characteristic $\delta^{13}C\text{-}CH_4$ values of microbial (< -60 ‰) and thermogenic (> -50 ‰) gas sources (*Figure 3-6a*; Bernard et al. [1976]). The carbon isotopic signature of methane in gas hydrate recovered from the pockmark site ($\delta^{13}C\text{-}CH_4$ = -54.6 ‰; Fisher et al. [2011]) is similar to that of the bubble plume gases, although the C_1/C_{2+} ratio is lower (~500). The C_1/C_{2+} ratio of hydrate gas from Vestnesa Ridge is lower still (~ 60), and $\delta^{13}C\text{-}CH_4$ is slightly higher (-45.6 ‰; Fisher et al. [2011]), consistent with a greater proportion of methane from thermogenic sources (*Figure 3-6a*).

Figure 3-6a demonstrates that simple mixing between microbial and thermogenic sources cannot explain both the chemical composition of the gas and $\delta^{13}C$ value of the methane in either bubble plumes or hydrate. The hydrogen isotope composition of the methane cannot distinguish between microbial and thermogenic methanogenesis as there is considerable overlap in δD-CH_4 values of these sources (*Figure 3-6b*; Whitical [1999]).

Chemical and isotopic compositions of natural gas can be modified during migration away from its source. Anaerobic oxidation of methane lowers the C_1/C_{2+} ratio and increases δ^{13}C-

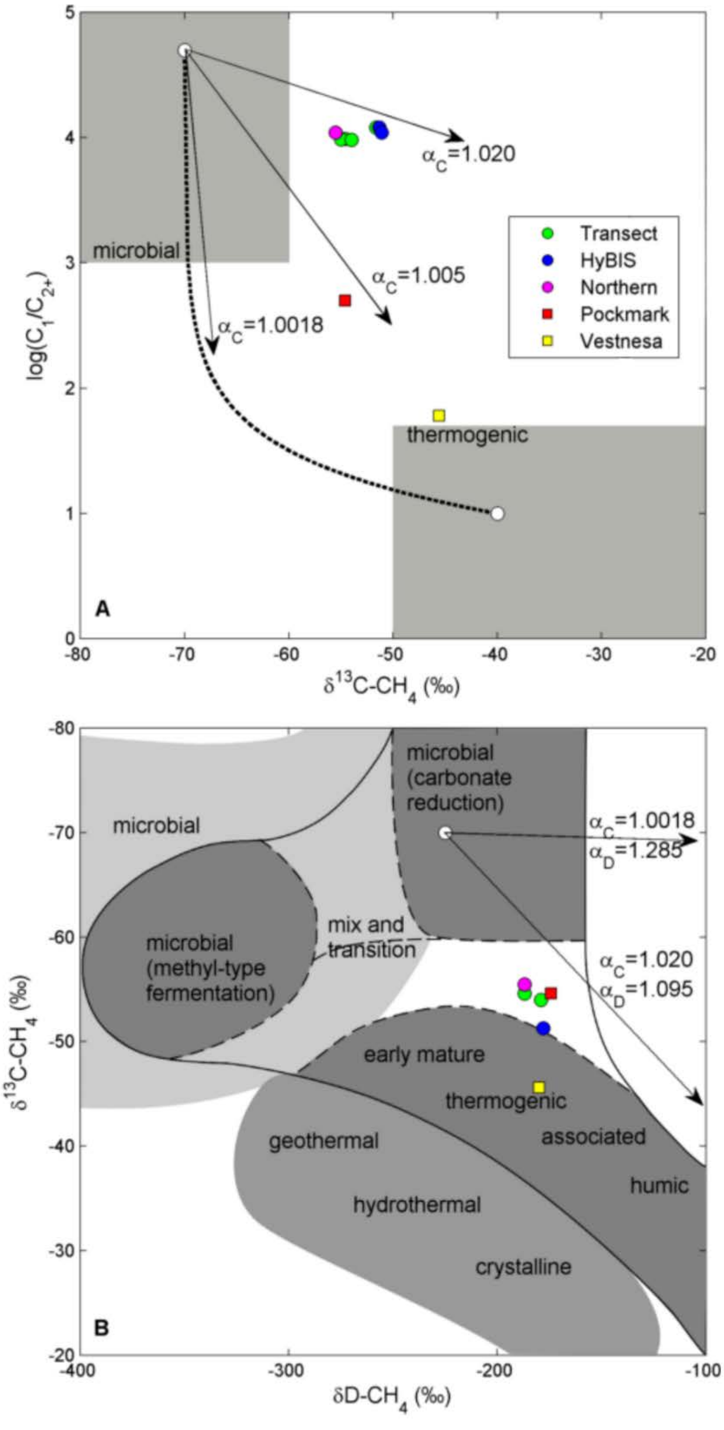

Figure 3-6 Molecular and isotopic composition of hydrate and bubble plume gases. (**A**) 'Bernard diagram' modified after Whiticar [1999], (**B**) Cross plot of methane carbon and hydrogen isotopic data with classification according to Whiticar [1999]. White open circles indicate typical end member microbial (δ^{13}C-CH_4: -70 ‰, C_1/C_{2+}: 50,000, δD-CH_4: -225 ‰, in **A** and **B**) and thermogenic (**A** only: δ^{13}C-CH_4: -40 ‰, C_1/C_{2+}: 10); source signatures, connected by a black dashed mixing line (**A** only). Arrows show the effects of anaerobic oxidation of a microbial source in carbon and hydrogen isotopes, for the range of isotope fractionation factors reported in the literature [Whiticar, 1999]. Hydrate δ^{13}C-CH_4 data are from Fisher et al. [2001].

CH_4 and δD-CH_4 of residual gas by preferentially oxidising isotopically light CH_4 (arrows in *Figure 3-6*; Whiticar [1999]). Reported isotope fractionation factors for carbon (α_C) range from 1.0018 to 1.029, and isotope fraction factors for hydrogen (α_D) range from 1.095 to 1.285 [Whiticar, 1999]. Low α_C are likely to be more appropriate for cold high latitude sediments [Whiticar, 1999], and recent observations in Bothnian Sea sediments also suggest α_C and α_D values at the lower end of these ranges ($\alpha_C = 1.009$ and $\alpha_D = 1.098$; Egger et al [2015]). *Figure 3-6* shows that only oxidation of a microbial source with high α_C and low α_D is consistent with the molecular and isotopic signatures of bubble plume samples. Furthermore, significant methane oxidation is unlikely during gas migration through sediments at depth, as sulphate is not available [Milkov et al., 2005]. In support of this, the δ^{13}C-CH_4 of gas beneath the STMZ matches that of bubble plume samples (*Figure 3*-3).

As thermogenic gases migrate through sediments, they may become progressively depleted in heavier hydrocarbons because lighter molecules move faster [Schoell, 1983]. In the same way, faster diffusion of lighter isotopes may lead to enrichment of ^{12}C in gases that have been transported a significant distance from their source, although this does not seem to be significant in most natural settings [Nuzzo et al., 2009; Prinzhofer and Pernaton, 1997; Schoell, 1983; Zhang and Krooss, 2001]. Transport-induced molecular fractionation provides the best explanation for the observed C_1/C_{2+}, δ^{13}C-CH_4, and δD-CH_4 values of seep and hydrate gases. We infer that thermogenic gas produced at depth offshore has been stripped of higher hydrocarbons as a result of significant lateral migration along upward dipping hemipelagic sediment beds. This is consistent with the model presented by Thatcher et al. [2013], and with seismic studies of gas migration through sediments offshore Svalbard [Rajan et al., 2012; Sarkar et al., 2012].

While chemical and isotopic compositions of bubble plume gas and hydrate suggest that they have the same source, these data cannot distinguish between gas derived from hydrate dissociation and gas which has migrated without ever being in the hydrate phase, because no isotopic fractionation of methane occurs during hydrate formation or dissociation [Lapham et al., 2012]. As hydrate from offshore Western Svalbard is likely to be Structure I (based on C_1/C_{2+} measurements), it will preferentially incorporate ethane and exclude the heavier hydrocarbons [Claypool et al., 2006; Milkov et al., 2004a; Pape et al., 2010]. Gas recently released from hydrates could therefore be expected to have low C_1/C_2 and low concentrations of C_{3+} but unaltered δ^{13}C-CH_4 relative to the gas source [Pape et al., 2010]. Bubble plume gas from offshore Svalbard is low in both C_2 and C_{3+} but, as no hydrate sample was recovered at the landward limit of the GHSZ, we cannot distinguish between potential hydrate-related molecular fractionation and that expected to occur during transport of gas to the slope region from offshore. However, some pore waters from core G-PC04, which is located close to a seafloor bubble plume within the GHSZ, have notably lower chloride concentrations (*Figure 3-4*), which allows for the possibility that small volumes of hydrate were present and dissociated during recovery. Some pore waters from the same depth interval are slightly enriched in Br^-; pore waters with low Cl^- and high Br^- in association with gas hydrates have also been observed at Hydrate Ridge (offshore Oregon) and Blake Ridge (offshore Southeastern USA) [Egeberg and Dickens, 1999; Fehn et al., 2006].

3.5.2. Spatial distribution of methane

Modelled fluxes of methane into shallow subsurface sediments vary by an order of magnitude in cores taken close to (within ~0.01 to 0.3 km) the seafloor bubble plumes (30 – 550 mmol CH_4 m^{-2} yr^{-1}; *Table 3-4*). Methane fluxes into shallow subsurface sediments located at greater distance (~1 to 2.6 km) from the bubble plumes are slightly lower (10 – 20 mmol m^{-2} yr^{-1}; *Table 3-4*), but it is clear that methane pervades sediments across the entire west Svalbard continental margin. At most sites sampled in this study, only a tiny fraction of the methane delivered to the subsurface sediments is transferred across the seafloor by molecular diffusion, $< 0.02 \times 10^{-3}$ mol m^{-2} yr^{-1}. However, bubble induced irrigation [Haeckel et al., 2007] of surface sediments is observed in two cores (C-PC02 and G-PC04) taken very close to seafloor bubble plumes. Transport-reaction modelling indicates that, in these circumstances, the flux of dissolved methane from the sediments into the overlying water column is higher, $10\text{-}70 \times 10^{-3}$ mol m^{-2} yr^{-1}. Nevertheless, pore waters in sediment cores taken directly on top of gas bubble plumes in our study area have much higher methane concentrations (up to 11 mM; Berndt et al. [2014]), and the gas bubble (ebullition) flux of methane across the sediment-seawater interface is far higher (~0.9 - 16 mol CH_4 m^{-2} yr^{-1}; Sahling et al. [2014]; *Table 3-5*) than fluxes of methane delivered to the water column by diffusion or irrigation.

The spatial distribution of sediment cores indicates that diffusive fluxes of methane across the sediment-seawater interface persist up to at least 300 m from bubble plumes, while irrigation fluxes are restricted to within ~30 m of plumes. Although the area of the seafloor affected by seepage of methane via diffusion is far greater than the area of seafloor affected by seepage via irrigation or bubble ebullition, the total amount of methane emitted to the water column by ebullition (4×10^6 to 5×10^7 mol yr^{-1}; *Table 3-5*) is far greater than that emitted via irrigation (2×10^4 to 1×10^5 mol yr^{-1}; *Table 3-5*) or diffusion (2 to 5 mol yr^{-1};

Table 3-5). Fluxes of methane delivered to the water column by diffusion or irrigation are slightly lower than those estimated for the Håkon Mosby mud volcano located in the Barents Sea to the south (~6 × 10^6 mol yr^{-1}: Milkov et al. [2004b]). The total methane flux density (ebullition + irrigation + diffusion; 1.1 – 13.1 mol m^{-2} yr^{-1}; *Table 3-5*) is similar to that reported for methane ebullition on the East Siberian Arctic Shelf (0.2 to 14 mol m^{-2} yr^{-1}; Shakhova et al. [2014]).

Table 3-5 Methane fluxes across the sediment-seawater interface, and methane consumption by anaerobic oxidation of methane beneath the seafloor for the region of seepage at the limit of the GHSZ offshore Western Svalbard (360-415 m water depth). Seep bubble methane flux, seep density, and area of seepage are from Sahling et al. [2014]. Rate of AOM at bubble seeps is from Berndt et al. [2014] and has been converted to a depth integrated rate assuming a depth distribution similar to those modelled in this study. Total fluxes are calculated for the maximum areal extent. We assume no overlap of the irrigation flux regions based on a homogeneous distribution of flares within the seep area surveyed by Sahling et al. [2014], and that the diffusive fluxes apply to the entire seep area, extended by 300 m.

	flux per unit area [mol m^{-2} yr^{-1}]		**spatial extent**	**total flux [mol yr^{-1}]**		**reference**
	min	max		min	max	
methane flux across the sediment-seawater interface						
seep bubbles	1.1	13	3.72 km^2, containing 384 (min) to 534 (max) bubble flares	4 × 10^6	5 × 10^7	Sahling et al. [2014]
pore water irrigation	0.01	0.07	1.5 km^2: 30 m radius around each flare	2 × 10^4	1 × 10^5	this study
dissolved phase diffusive	4 × 10^{-7}	9 × 10^{-7}	~ 7 km^2:300 m radius area around the 3.72 km^2 bubble plume region	2	5	this study
methane consumption by AOM						
seep bubble sediments	-	200	~ 10 m^2: within 0.01 to 0.1 m of flares	30	4000	Berndt et al. [2014]
irrigation zone	0.3	0.6	1.5 km^2: 30 m radius around each flare	5 × 10^5	8 x 10^5	this study
diffusive zone	0.03	0.1	~5.5 km^2: diffusive zone, excluding inner irrigation zone	5 × 10^4	2 × 10^5	this study
regional background	-	0.02	80 km^2: extent of sampling in this study	-	2 × 10^6	this study

Model results reported in *Table 3-5* indicate that > 80 % of the methane that enters the shallow subsurface sediments in the irrigation zone (within 30 m of seafloor bubble plumes), and > 99.99 % of the methane that enters the shallow subsurface sediments between 30 m and 300 m away from the bubble plumes is consumed by AOM. The rate of AOM is much higher at bubble plume sites (up to 11 μmol cm^{-3} day^{-1}; Berndt et al. [2014]) than modelled in this study (<0.6 μmol cm^{-3} day^{-1}; *Table 3-4*, *Figure 3-5*), but the proportion of methane oxidised is far lower (<0.1 %; *Table 3-5*). Reduced AOM efficiency with increasing methane flux has been observed in other cold seep environments (e.g. Felden et al. [2013]; Vanneste et al. [2011]), Overall, the proportion of methane entering the shallow subsurface sediments offshore western Svalbard which is consumed by AOM amounts to ~10 % of the total flux to the shallow subsurface sediments. Focusing of fluid flow through cracks within the relatively low permeability glaciogenic sediments offshore Svalbard [Thatcher et al., 2013] therefore plays a critical role in allowing discharge of methane into the water column.

3.5.3. Temporal variability of methane supply to the shallow subsurface sediments

With the exception of site C-PC02, both models provide an excellent fit to the pore water chemistry profiles measured outside of the GHSZ. This suggests that the supply of methane to these sediments has been stable over time, as changes in methane fluxes generate non-linear sulphate profiles that persist for up to several thousand years [Henkel et al., 2011; Hensen et al., 2003]. It also implies that the supply of methane to the shelf and slope region is unaffected by seasonal and decadal variations in bottom water temperature, which may affect hydrate dynamics [Berndt et al., 2014; Ferré et al., 2012; Marín-Moreno et al., 2013].

By contrast, pore water sulphate profiles from all sites within the GHSZ (B-PC01, G-PC04 and F-GC02) are poorly described by steady-state diffusion models. This either implies that the methane flux at these sites has changed, or that there are changes in sediment properties that affect upward transport of dissolved constituents [Henkel et al., 2011; Hensen et al., 2003]. In support of the former, sulphate profiles in F-GC02 and the lower portion of B-PC01 are slightly concave up, which points to a relatively recent increase in methane supply [Hensen et al., 2003; Nöthen and Kasten, 2011]. In G-PC04, methane concentrations are very high (> 1 mM) in the near-surface, sulphate-containing (> 20 mM) pore waters, which suggests that AOM is unable to keep up with a recent increase in methane supply from depth. By contrast, there are no obvious changes in sediment porosity, TIC, or TOC, at the depth of the kink in the sulphate profiles in these cores, nor any visual evidence of a change in the sediment properties. In core B-PC01 there is a sharp increase in alkalinity at ~280 cm sediment depth which coincides with a decrease in pore water calcium, suggesting that the SMTZ occurs just beneath the depth of the recovered sediments. This depth is much shallower than predicted by applying a linear fit to the lower portion of the sulphate profile, and is consistent with an increase in the supply of methane to subsurface sediments.

Water depths at these three sites provide sufficient pressure for hydrate stability at current bottom-water temperatures [Berndt et al., 2014]. However, the thickness of the hydrate stability zone near its landward limit is expected to decrease in response to bottom water warming (e.g. Marín-Moreno et al. [2013]). When temperature-driven destabilization is initiated at the base of the hydrate bearing sediments, and released gas re-forms hydrate when it migrates upwards into overlying sediments that remain within the stability zone. Furthermore, cycles of warming and cooling will redistribute hydrate closer to the seafloor [Thatcher et al., 2013]. In the presence of hydrate, pore fluids are methane saturated, so methane migrates upward to the SMTZ where AOM reduces the methane concentration to approximately zero. If hydrate in sediments within the GHSZ moves closer to the seafloor, the depth of the SMTZ will therefore also move closer to the seafloor [Bhatnagar et al., 2011].

The pore water sulphate profile at the highest methane flux site outside the limit of the GHSZ (C-PC02) is also poorly described by the steady-state transport-reaction model. Methane concentrations are negligible ~ 40 cm below the depth predicted by fitting the model to the sulphate profile, implying that the methane supply has recently decreased at this site [Hensen et al., 2003]. This may be due to the disappearance of a hydrate methane source, or simply a change in the local gas migration pathways.

Rates of AOM are determined by the supplies of methane and sulphate, and methanotroph biomass [Knittel and Boetius, 2009]. If the SMTZ is located several meters beneath the sediment-seawater interface, the rate of AOM is regulated by the supply of methane [Sivan et al., 2007]. If the methane flux from below increases, the SMTZ moves closer to the sediment-seawater interface, and the rate of AOM becomes limited by the rate at which sulphate is supplied by diffusion from the overlying water column. When the rate of AOM is not high enough to reduce methane concentrations to below saturation, methane is transported to the seafloor in the gas phase. Escape of methane gas leads to irrigation of the surface sediments, allowing infiltration of sulphate from seawater to depths of several tens of centimetres into the sediments [Haeckel et al., 2007]. The presence of sulphide-oxidizing bacterial mats, tubeworms, and other burrowing organisms also enhances the supply of sulphate to the sub-surface sediments. High fluxes of methane and sulphate at cold seep environments support dense communities of methanotrophic archaea of $> 10^{10}$ cells cm^{-3} [Knittel and Boetius, 2009], and measured rates of AOM can be tens of $\mu mol\ cm^{-3}\ day^{-1}$ (e.g. Berndt et al. [2014]). In contrast, methanotrophic communities sampled from the depth of the SMTZ typically constitute $< 10^6$ cells cm^{-3} [Knittel and Boetius, 2009]. The archaea in these lower flux environments likely provide seed populations for higher flux environments, but their growth rate is limited by the low energy yield associated with AOM [Knittel and Boetius, 2009]. Accordingly, it takes > 50 years for the microbial community to respond to significant increases in methane flux [Dale et al., 2008b]. Thus, the increase in methane supply to the shallow sediments at site G-PC04, implied by the shape of the pore water methane profile, must be relatively recent enabling methane to escape the microbial filter and be released into the overlying water column.

Methane carbon isotopic profiles across the STMZ (*Figure 3-3*) also provide evidence for changes in the supply of methane at some sites. During AOM, kinetics favour the oxidation of ^{12}C-CH_4, producing ^{13}C-depleted carbonate and a residual methane pool that is ^{13}C-enriched [Whiticar, 1999]. However, δ^{13}C-CH_4 values measured at the depth of the SMTZ are often very low (i.e. ^{12}C rather than ^{13}C enriched), which is typically attributed to carbon cycling, where AOM immediately above the SMTZ progressively enriches the local carbonate pool in ^{12}C which is recycled to methane with additional ^{12}C enrichment by methanogenesis immediately below the SMTZ [Borowski et al., 1997]. Alternatively, if the supply of sulphate from the overlying seawater is limited, chemical equilibrium can be established, which produces a ^{13}C-enriched methane pool without coupled methanogenesis [Yoshinaga et al., 2014]. Thus, if the supply of methane increases, the SMTZ moves towards the seafloor and oxidation of methane occurs in the presence of high sulphate which results in ^{12}C-enriched methane, while stable or decreasing methane supply leads to diffusion controlled methane oxidation results in a ^{13}C-enriched methane residual methane pool.

The shape of the pore water δ^{13}C-CH_4 profiles at the two highest methane flux sites, C-PC02 and G-PC04, are distinctly different. At site G-PC04, methane fluxes appear to have increased (see above), and there is a small, negative (- 5 ‰) shift in δ^{13}C-CH_4 at the SMTZ, and a large positive shift of +30 ‰ ~ 40 cm above the SMTZ. These changes in δ^{13}C-CH_4 values indicate that oxidation of methane occurs in the presence of high sulphate, and that carbon cycling at the SMTZ is not well established, supporting our interpretation that the methane flux has recently increased. By contrast, fluxes of methane are thought to have decreased at site C-PC02, and there is a shift towards lower δ^{13}C-CH_4 values across the SMTZ (by – 30 ‰). This suggests either that chemical equilibrium is established at this site, or that significant carbon cycling occurs at the SMTZ. Both mechanisms are consistent with stable or decreasing supply of methane from depth.

At other sites in the vicinity of the seafloor bubble plumes, where pore water sulphate profiles appear to be at steady state, $\delta^{13}C\text{-}CH_4$ profiles are characterised by a negative shift at the SMTZ. The magnitude of the shift (30 – 45 ‰) is similar to that observed at site C-PC02. These data point to equilibrium isotope fractionation processes, with the accumulation of ^{12}C due to carbon cycling at a fixed depth. The interval of time required to establish a stable SMTZ, and to allow accumulation of ^{13}C-depleted methane remains to be determined.

3.6. Summary and conclusions

The molecular and isotopic composition of gas bubbles released from the seafloor at the landward limit of the gas hydrate stability zone offshore Western Svalbard indicate that the gas is thermogenic, produced in deep sediments further offshore. Methane migrates up the continental slope through permeable units in the sequence of seaward-dipping marine sediments identified in geophysical studies. Analyses of the composition of gas hydrate collected further offshore suggests that gas bubble plumes and hydrate have the same gas source, but our molecular and isotope data cannot distinguish between gas that may have been released by dissociating hydrate and gas that has never been in the hydrate phase.

The chemical composition of the sediment pore waters indicates that methane pervades the subsurface sediments, but the flux of methane into the shallow subsurface is highly heterogeneous. In areas of relatively low subsurface methane flux (30-120 mmol m^{-2} yr^{-1}), methane is largely consumed by anaerobic oxidation below the seabed, and the flux of methane across the seafloor is negligible. At higher subsurface flow rates (up to ~550 mmol m^{-2} yr^{-1}), bubble-induced irrigation of sediment pore waters enhances the transfer of methane into the water column (up to ~70 mmol m^{-2} yr^{-1}), but this flux is nevertheless insignificant compared with the quantity of methane that enters the water column in gas bubble plumes (up to ~16,000 mmol m^{-2} yr^{-1}). Focusing the outflow of gas through cracks and small fractures in the sediments allows methane to circumvent the AOM filter such that, overall, AOM only prevents < 10% of the methane delivered to shallow sub-surface sediments from reaching the overlying water column.

Modelling and carbon isotope analyses of sediment pore waters from within the present-day gas hydrate stability zone (i.e. > ~400 m water depth) indicate that the flux of methane to the sub-surface sediments has increased within the last few thousand years. This may be evidence for movement of hydrate towards the seafloor due to temperature cycling, as predicted by models [Thatcher et al., 2013]. By contrast, evidence for a change in methane supply to the shallow sub-surface at the present-day landward limit of the GHSZ was only found in one core, which supports a recent reduction in methane supply. This may be due to the disappearance of hydrate and consequently loss of methane supply. Our pore water geochemical data are thus consistent with downslope retreat of the GHSZ in response to temperature changes in bottom waters offshore western Svalbard.

CHAPTER 4

Fluxes and fate of dissolved methane released at the seafloor at the landward limit of the gas hydrate stability zone offshore Western Svalbard

This chapter is intended for submission to *Continental Shelf Research*

Supplementary material is provided in **Appendix C**

Contents

Abstract

Seepage of methane from seafloor sediments offshore Svalbard may partly be driven by destabilization of gas hydrates as a result of bottom water warming. As the world’s oceans are expected to continue to warm, particularly in the Arctic, destabilization of hydrate may become an important source of methane to ocean bottom waters and potentially to the overlying atmosphere where it contributes to further warming. We present methane concentration data from discrete depth-profiles and a continuous equilibrator-online surface seawater system, as well as oxidation rate measurements and atmospheric methane observations from the upper slope and shelf offshore Western Svalbard in late summer of 2011 and 2012. A simple box model considering horizontal and vertical mixing as well as oxidation in bottom waters indicates that the majority of seep methane is oxidized at depth. A plume of elevated dissolved methane concentrations is expected to persist for more than 100 km downstream of the seepage area in the rapid barotropic West Spitsbergen Current (WSC), which flows northward into the Arctic Ocean. Enhanced vertical mixing within the WSC may allow dissolved methane sourced from seafloor seeps at the limit of hydrate stability to reach the surface mixed layer downstream of the studied region. However, methane in the upper water column at the gas hydrate stability zone limit is likely sourced by isopycnal turbulent mixing from shallower shelf waters where seafloor seepage also occurs. As vertical dissolved methane transport is slower than northward advection, elevated methane concentrations in intermediate and surface waters cannot reflect underlying seafloor seepage. We calculate that the diffusive sea-air flux of methane is largest on the shallow shelf, reaching 36 μmol m^{-2} day^{-1}. Over the entire Western Svalbard region there is a persistent, but small, source of methane from surface seawater to the overlying atmosphere. Simultaneous shipboard measurements of the atmospheric methane carbon isotope signature indicate that the seafloor seeps do not make a significant contribution to atmospheric methane in this region.

4.1. Introduction

Seepage of methane from seafloor sediments on continental margins is widespread, but poorly quantified [Judd and Hovland, 2007]. Active microbially-mediated oxidation maintains ocean water methane undersaturation with respect to the atmosphere [Reeburgh, 2007]. The world's oceans are thus likely to make only a minor contribution to the global atmospheric methane budget [Kirschke et al., 2013]. However, new sites of seafloor methane seepage continue to be discovered (e.g. Römer et al. [2014]; Skarke et al. [2014]), and recent studies suggest that sea to air methane fluxes at some seepage locations are as high as previously estimated for the whole ocean [Shakhova et al. 2010a]. Seepage of methane from seafloor sediments in the Arctic Ocean has been linked to destabilisation of methane from temperature-sensitive shallow marine sediment reservoirs, including permafrost and methane hydrates [Berndt et al., 2014; Ferré et al., 2012; Sahling et al., 2014; Shakhova et al., 2014; Westbrook et al., 2009]. As Earth's climate continues to warm [Stocker et al., 2013], there is a need to constrain the potential for feedback between the seafloor and atmospheric methane systems.

Methane hydrate is an ice-like solid in which methane molecules are trapped in cages of water molecules. It forms under specific high pressure and low temperature conditions where water is supersaturated with methane [Sloan and Koh, 2008]. Naturally occurring submarine methane hydrate is estimated to contain ~ 500 to 2500 Gt of carbon globally [Milkov, 2004], mostly in continental margin sediments, as the landward limit of hydrate stability lies at water depths of > 200 m [Krey et al., 2009]. The presence of hydrate reduces sediment permeability, such that subsurface gas flow can be directed along the base of hydrate formation, with seafloor seepage occurring in waters shallower than the landward limit of the hydrate stability zone [Naudts et al., 2006; Schmale et al., 2011]. Destabilization of methane hydrate in seafloor sediments is proposed to have contributed to previous episodes of major climate change, including the Paleocene-Eocene thermal maximum (e.g. Dickens [2011]), and recent discoveries of methane emissions from the seafloor offshore Western Svalbard may, at least in part, be related to hydrate dissociation linked to warming of bottom waters [Berndt et al, 2014; Biastoch et al., 2011; Reagan and Moridis, 2009; Thatcher et al., 2013; Westbrook et al., 2009].

Methane that enters ocean bottom waters in bubble form rapidly dissolves and is subsequently diluted by mixing with overlying water masses and dispersed by ocean currents. In the presence of oxygen dissolved methane is oxidised to carbon dioxide (CO_2; *Equation 4-1*; Heeschen et al. [2005]).

$$CH_4 + 2\ O_2 \rightarrow CO_2 + 2\ H_2O \qquad (4\text{-}1)$$

The combined effects of these processes rapidly reduce concentrations of dissolved methane in the water column near active seafloor methane seeps to background levels [Valentine, 2011]. The rate of bubble dissolution mainly varies as a function of bubble size, temperature, salinity and pressure, the presence of coatings (organic material, or hydrate skin), and bubble rise velocity [Leifer and Patro, 2002; Rehder et al., 2009]. In water depths greater than 200 m, bubbles less than 10 mm in diameter are expected to dissolve before they reach the surface mixed layer, preventing direct venting of methane from seafloor seeps into the atmosphere [Gentz et al., 2014; McGinnis et al., 2006]. Aerobic oxidation of methane acts to lower oxygen concentrations and results in seawater acidification by production of carbon dioxide (*Equation 4-1*), both of which may have adverse consequences for marine ecosystems [Biastoch et al., 2011; Kessler et al., 2011].

The discovery of more than 250 plumes of methane gas seeping from the seafloor at the landward limit of the gas hydrate stability zone (GHSZ) on the upper continental margin offshore Western Svalbard [Westbrook et al., 2009] provides an ideal setting to investigate the fate of methane in the water column, and the potential for sediment-derived methane to reach the atmosphere. To this end, we have determined the distribution of methane in the water column in the vicinity of the GHSZ limit for three separate sampling campaigns. Our observations demonstrate that there is a persistent sea-air flux of methane across much of the continental slope and shelf. We use a simplified box model to quantify the fate of methane seeping from the seabed, and provide the first estimates of the sea-air methane flux for this area. Our results reinforce the crucial role of even the relatively shallow ocean water at the limit of Arctic hydrate stability zone as an efficient barrier to significant methane release from seafloor seeps into the overlying atmosphere.

4.2. Oceanographic setting

The location of the methane seeps offshore Western Svalbard is shown in *Figure 4-1*. The seafloor at the landward limit of the GHSZ is overlain by the warm saline Atlantic Water of the westward branch of the West Spitsbergen Current (WSC) which provides the primarily influx of water and heat into the Arctic Ocean [Aagaard et al., 1987; Saloranta and Haugan, 2004]. Both the mean temperature and speed of the WSC increase towards the shelf break

[Saloranta and Haugan, 2004]. Deeper WSC waters to the west of this region lose heat and recirculate in the Fram Strait, while the shallower eastern waters are subject to mixing across a density-compensated halocline near the shelf edge [Cottier and Venables, 2007; Saloranta and Svendsen, 2001] as well as relatively less important vertical mixing and heat loss to the atmosphere [Fahrbach et al., 2001]. North of Svalbard, the WSC splits in two, with shallower waters (< ~1000 m) continuing along the shelf edge and deeper waters moving along the western edge of the Yermak Plateau [Schauer, 2004]. On the continental shelf east of the landward limit of the GHSZ, the slower East Spitsbergen Current (ESC) carries fresher and colder polar water northward. Surface waters in the vicinity of the methane seeps consist of relatively fresh Arctic Water, which penetrates to deeper water depths towards the coast [Saloranta and Svendsen, 2001].

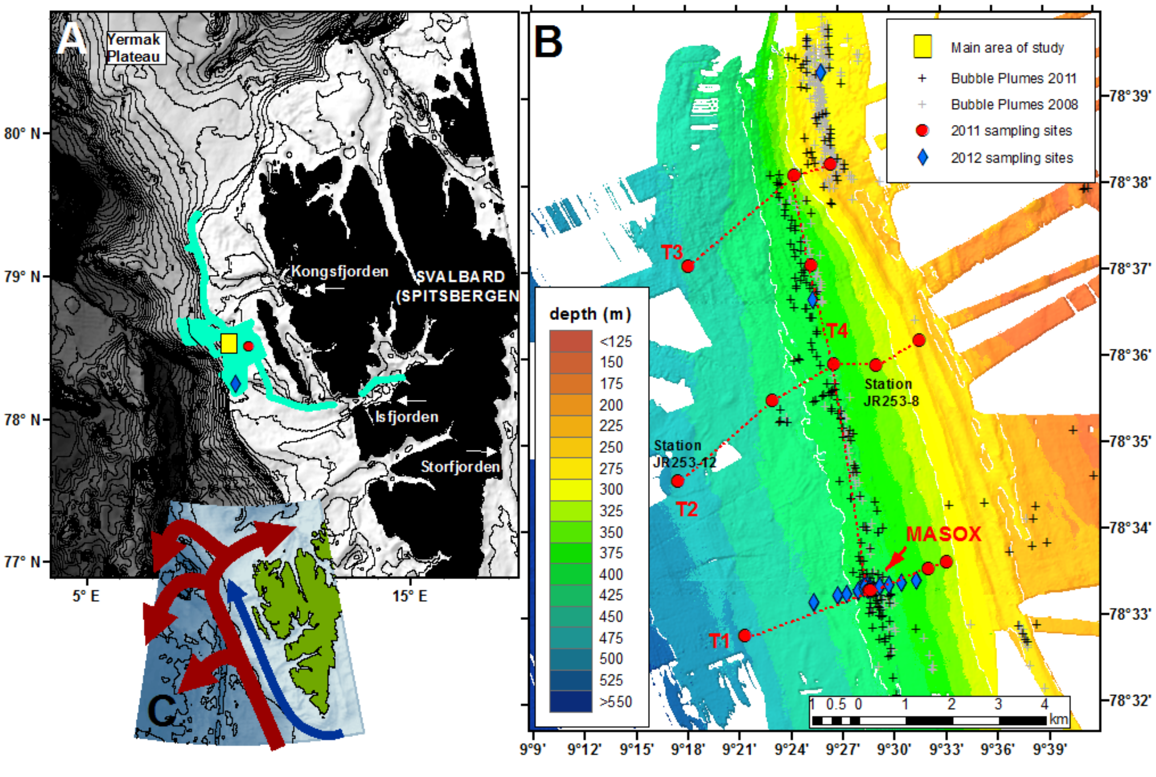

Figure 4-1 Map of the study area and water column sampling sites. Bathymetry in (**A**) is from the GEBCO_08 Grid version 20100927 (http://gebco.net), contour interval is 100 m, light blue indicates He-386 cruise track. (**B**) shows shipboard bathymetry from cruise JR253. Red lines indicate sampling transects T1 – T3. (**C**) shows the dominant direction of the main ocean currents in this region: the West Spitsbergen Current (WSC) is shown in red, and the East Spitsbergen Current (ESC) is shown in blue [Saloranta and Svendensen, 2001].

4.3. Sampling and analytical methods

4.3.1. Sample collection

A suite of seawater and air samples were collected from the vicinity of the methane seeps close to the landward limit of the GHSZ offshore Western Svalbard on RRS *James Clark Ross* cruise JR253 (7th – 23rd July, 2011), and on RV *Maria S. Merian* cruise MSM 21/4 (18th July – 4th August, 2012). Seawater sampling sites are shown in *Figure 4-1* and listed in *Supplemental Table C-1*, and locations of air sampling sites are shown in *Supplemental Figure C-1*. Bubble plumes were identified by shipboard sonar: a Simrad EK60 'fishfinder' sonar (38 kHz, 120 kHz and 200 kHz) and a 12kHz Simrad EM122 sonar were used on the RRS *James Clark Ross*, and a PARASOUND sonar (18 kHz parametric echosounder) was used on the RV *Maria S. Marian*. In 2012, an equilibrator system [Gülzow et al., 2011] was used to record a complimentary data set of surface water methane concentrations continuously along the cruise track of RV *Heincke* during cruise He-387 (20th August – 6th September, 2012; the area covered by the cruise track is shown in *Figure 4-1a*; [Sahling et al., 2014]).

In 2011, seawater samples were taken along three transects (*Figure 4-1b*) of ~ 6 km in length, extending from ~200 m water depth through the methane seeps at ~400 m water depth, to water depths of ~ 500 m. Each transect consisted of between 3 and 5 vertical profiles. In 2012, Transect 1 was sampled more intensively, with 27 vertical profiles representing 5 sampling time-points over 16 days. An additional station located ~ 30 km south of the main study at ~300 m water depth area was also sampled (*Figure 4-1a*).

Seawater was collected in 10 L Niskin bottles mounted on a 24-bottle rosette frame fitted with a Seabird SBE911 conductivity-temperature-depth (CTD) sensor (Sea-bird Scientific). Samples for methane analysis were collected immediately upon recovery of the rosette frame into 1 L and 0.5 L triple-layer Evarex Barrier Bags (Oxford Nutrition, U.K.) which had been flushed twice with nitrogen. Water was introduced to the equilibrator system using the ship's underway pumped water system; the pump inlet was located 2.8 m below the sea surface. Details of this system are given in Gülzow et al. [2011]. Air samples were collected from the ship's bridge by directing a hose into the direction of incoming wind and pumping into 5 L Tedlar bags.

4.3.2. Chemical analysis

Methane concentrations were measured by adding 20 mL of high-purity nitrogen gas to each sample bag, shaking vigorously, and allowing the seawater sample to equilibrate with the headspace gas for several hours before subsampling 2 mL for analysis by gas chromatography (Agilent 7890A, 6 ft., 2 mm i.d.; 80/100 mesh HayeSep Q packed stainless steel column, flame ionization detector, 60 °C, with nitrogen carrier gas at 33 mL min^{-1}). Calibration was performed with an external standard (20 ppm methane standard, Air Liquide, Germany). The seawater methane concentration was calculated from the headspace and seawater sample volumes, measurement temperature, and seawater salinity [Wiesenburg and Guinasso, 1979]. Reproducibility was evaluated by triplicate analysis of seawater subsamples for which standard deviation was < ± 5 %.

The equilibrator system measured methane concentrations in air equilibrated with surface seawater at 5 second intervals by off-axis integrated cavity output spectroscopy (oa-ICOS, Los Gatos Research methane carbon dioxide-Analyser: MCA). The precision of the MCA, assessed with gas calibration standards, is better than ± 0.1 % [Gülzow et al., 2011].

Methane concentrations and $\delta^{13}C$-CH_4 in air were determined at Royal Holloway University of London by cavity ring-down spectroscopy (PICARRO G1301) and a trace gas-continuous flow gas chromatography isotope ratio mass spectrometry (IsoPrime; Fisher et al. [2006]) , respectively. The isotopic precision on secondary standards and samples analysed at least in triplicate for both cruises averaged better than ±0.05 per mil.

4.3.3. Box model

A simplified box model is used to assess the relative importance of the chemical and physical processes which modify the dissolved methane concentration of bottom waters in the vicinity of the seep sites. The processes considered in the model are: (i) aerobic oxidation (MOx), (ii) isopycnal mixing, and (iii) diapycnal mixing. The box is defined to represent the volume of water into which methane from seafloor seep bubbles dissolves: the width is equivalent to the segment of the upper margin upslope of the gas hydrate stability zone limit from which focused seafloor seepage is observed (450 m, perpendicular to the bathymetry), and the height is given by the upper limit of significant direct methane input by bubble dissolution (75 m, as evidenced by both dissolved methane concentration profiles (*Section 4.1*), and the bubble modelling for the northern segment of the seep site [Gentz et al., 2014]). The dissolved methane concentration in the box therefore represents the input from seafloor seeps.

The change in dissolved methane concentration with time after bubble dissolution is given by:

$$\delta C/\delta t = -[\delta C_{MOx} + \delta C_{I(west)} + \delta C_{I(east)} + \delta C_{D}]/\delta t \qquad (4\text{-}2)$$

where C denotes methane concentration, and the summed terms represent the change in concentration due to the four processes considered (indicated by subscripts): aerobic oxidation of methane (MO_x), offshore isopycnal mixing ($I(west)$), onshore isopycnal mixing ($I(east)$), and upward diapycnal mixing (D). The rate of methane oxidation is assumed to be first order, with a concentration-independent rate constant k_{MOx}:

$$\delta C_{MOx}/\delta t = -k_{MOx} \bullet C(t) \qquad (4\text{-}3)$$

Isopycnal and diapycnal mixing (turbulent diffusion) are described by Fick’s first law of diffusion following [Mau et al., 2012]:

$$\delta C/\delta t(isopycnal) = -x \bullet D_I \bullet \Delta C(t)/\Delta x \text{ and } \delta C/\delta t(diapycnal) = -z \bullet D_D \bullet \Delta C(t)/\Delta z \qquad (4\text{-}4)$$

where x is the width of the box perpendicular to bathymetry (450 m), and z is the height of the box (75 m), $\Delta C(t)/\Delta x$ and $\Delta C(t)/\Delta z$ are the methane concentration gradients away from the seep site in mol m^{-2} in both the horizontal (x) and upward vertical (z) directions, and D_I and D_D are the isopycnal and diapycnal turbulent diffusion coefficients. Isopycnal mixing in the north-south direction is neglected because the methane seeps are aligned approximately north-south with the bathymetry, and because the dominant current is barotropic and northwards so the diffusion term will be small relative to advection of bottom waters. In support of this, the methane concentration gradient in the north-south direction is small. Downwards loss of methane is not considered because the bottom of the box is defined at the seafloor.

The initial (on-seep) concentration of methane in the box was estimated by depth-averaging measured concentrations in the lower 75 m (box height) of the water column. The measured oxidation rate constants (k_{MOx}, data from Steinle et al. [In Review]) were similarly averaged, as were concentrations outside the box (for off-seep stations and the upper water column). No correlation between methane concentration and k_{MOx} was observed in the study area [Steinle et al., In Review]. However, no downstream measurements were made, so the evolution of oxidation rate constants as bottom water is advected northwards is unconstrained.

A range of isopycnal and diapycnal mixing coefficients are reported in the literature. We choose an isopycnal coefficient of $0.07 \pm 0.04\ m^2\ s^{-1}$ as calculated for length scales of 0.1 to 1 km based on a tracer study with sulphur hexafluoride at ~310 m water depth in the Atlantic Ocean [Ledwell et al., 1993, 1998]. This is much lower than the value of $\sim 1000\ m^2\ s^{-1}$ calculated for longer length scales [Ledwell et al., 1998; Sundermeyer and Price, 1998], which is higher than the rate of methane input from seafloor seeps [Sahling et al., 2014] meaning that methane would not accumulate in seawater above the seeps, clearly inconsistent with our observations. The choice of a low isopycnal mixing coefficient is further supported by Largier, [2003], who shows that mixing decreases in near-shore environments from $1000\ m^2\ s^{-1}$ at 100-1000 km away from the coast to $100\text{-}0.1\ m^2\ s^{-1}$ at 10 to 0.1 km from the coast. Coefficients of diapycnal mixing are typically 10^{-7} to 10^{-8} times lower than coefficients for isopycnal mixing [Deng et al., 2014]. Based on the water depth and latitude of our site [Deng et al., 2014], we use an upper limit for the diapycnal mixing coefficient of $10^{-3}\ m^2\ s^{-1}$ as measured in tracer experiments in bottom waters in the abyssal ocean [Ledwell et al., 2000]. As a lower limit, we choose the value of $10^{-4}\ m^2\ s^{-1}$ cited as 'typical' in a similar methane mixing study [Mau et al., 2012]. Similar and even lower diapycnal mixing coefficients were calculated for a methane mixing study in the Black Sea, of $0.02 - 1 \times 10^{-4}\ m^2\ s^{-1}$ [Schmale et al., 2011]. The uncertainty in the values of these coefficients is taken into account in the model output, but we stress that as these uncertainties are large our model must be considered to be qualitative, or at best semi-quantitative, rather than fully quantitative.

4.3.4. Sea-air fluxes

The flux of methane from surface waters to the atmosphere is given by:

$$Flux = k\,([CH_4]_{surface} - [CH_4]_{equilibrium}) \qquad (4\text{-}5)$$

where k is the gas transfer velocity and $[CH_4]_{surface}$ and $[CH_4]_{equilibrium}$ are, respectively, the measured concentration of methane in surface seawater and the calculated concentration of methane in surface seawater at equilibrium with the atmosphere [Liss and Slater, 1974]. The equilibrium concentration is calculated from the total atmospheric pressure and the partial pressure of methane in dry air using the Bunsen solubility coefficient of methane at the temperature and salinity of surface seawater [Wiesenburg and Guinasso, 1979].

The gas transfer velocity (k) can be estimated from the molecular diffusivity (D) of the gas, the kinematic viscosity of seawater (μ), and the atmospheric wind speed at a height of 10 m (u_{10}) [Wanninkhof, 1992; Wanninkhof et al., 2009]. D and μ are combined in the Schmidt number ($Sc=\mu/D$), such that:

$$k=0.24\cdot u_{10}^{2}\cdot(Sc/660)^{-1/2} \tag{4-6}$$

where k has units of cm hr^{-1} and u_{10} is in m s^{-1} [Wanninkhof et al., 2009]. Further details of this calculation and choice of k parameterisation are given in the supplementary material (*Appendix C*). Briefly, different k parameterizations [Liss and Merlivat, 1986; McGillis et al., 2001; Nightingale et al., 2000; Wanninkhof, 1992] yield overall sea-air fluxes ranging from 20 % to 35 % lower and 30 % to 75 % higher than those calculated with *Equation 4-6*, depending on the wind speed.

Measured wind speeds were corrected for ship speed and relative direction of travel, as well as for the height of measurement (z_{meas}) above the sea surface (~29 m for RV *Maria S Marian*, ~25 m for RV *Heincke* and ~15.5 m for RSS *James Clark Ross*) using the relationship $u_{10} = u_{\mathrm{measured}}\cdot(z_{\mathrm{meas}}/10)^{-0.11}$ [Hsu et al., 1994]. To estimate fluxes from discrete surface seawater methane samples, shipboard wind speed data measured every minute (2011) and every 10 minutes (2012) were spatially filtered to include only measurements within 1 km of mapped seep sites. The temporal variability in wind speed was accounted for by calculating the sea-air flux over the distribution of observed winds, bin averaged in 1 m s^{-1} intervals.

Fluxes are calculated from measurements of the methane concentration in the discrete water samples and estimates of the equilibrium methane concentration and gas transfer velocity. The equilibrium methane concentrations are calculated from surface seawater temperature and salinity, and the average measured atmospheric methane partial pressure and total atmospheric pressure observed for the study site during water sampling. Gas transfer velocities are calculated for the wind speed distribution observed during the measurement period, and sampled surface seawater temperatures. Detailed information on the uncertainty of these calculated fluxes can be found in the supplementary material (*Appendix C*). Briefly, variations in atmospheric methane concentration, atmospheric pressure, and surface seawater temperature and salinity lead to uncertainties in methane fluxes of $< \pm 10$ %. The most significant contribution to the overall uncertainty in the average regional sea-air fluxes is the variation in the methane concentration of surface seawater, which is ~ ± 30 - 40 %.

Fluxes were also calculated for the equilibrator surface seawater methane concentration data. This data set provided simultaneous measurement of wind speed, surface seawater methane concentration temperature and salinity, and atmospheric pressure. Fluxes were therefore calculated for each individual concentration measurement (5 second intervals). Atmospheric methane concentrations were not simultaneously measured, so the average value of the air samples collected in 2012 was used. This estimation contributes less than ± 5 % to the overall uncertainty of the sea-air flux.

4.4. Results and discussion

4.4.1. Distribution of dissolved methane

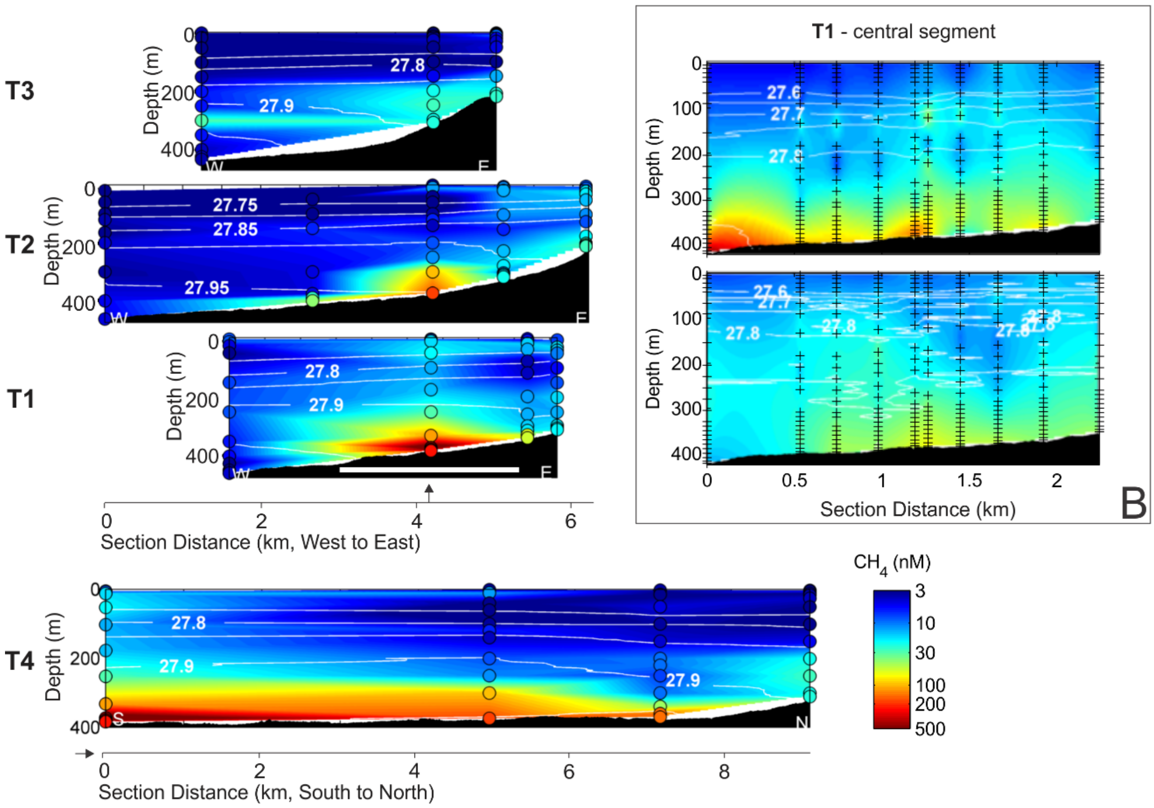

Figure 4-2 A Distribution of methane along transects T1 to T3. Sampling points are shown by the open circles. Contours show the density anomaly (σ_θ; kg/m^3). Inset **B** shows the central segment of T1 (indicated by the white bar) re-sampled, twice, at higher spatial resolution in 2012.

The distribution of methane in the water column is shown for Transects 1-3, and a transect from south-north through the main seep region (Transect 4), in *Figure 4-2*. The range of methane concentrations measured here is consistent with those previously reported for this area [Damm et al., 2005; Gentz et al., 2014; Knies et al., 2004; Westbrook et al., 2009]. The variation in the concentration of methane with depth in the vicinity of the methane seeps (i.e. close to the landward limit of the GHSZ) is consistent throughout the study area, and there are no obvious differences in either methane concentrations or the shape of the depth profiles measured in 2011 and 2012 (*Figure 4-3*). Highest methane concentrations are typically found a few meters above the seabed, rather than at the seabed itself, which is consistent with observations at Hydrate Ridge on the Cascadia Margin [Heeschen et al., 2005]. Methane concentrations in the upper ~ 250 m of the water column are lower and far less variable than they are at depth. Nevertheless, the entire water column is supersaturated with respect to the atmosphere (~3 nM CH_4, see *Section 4.2.3*).

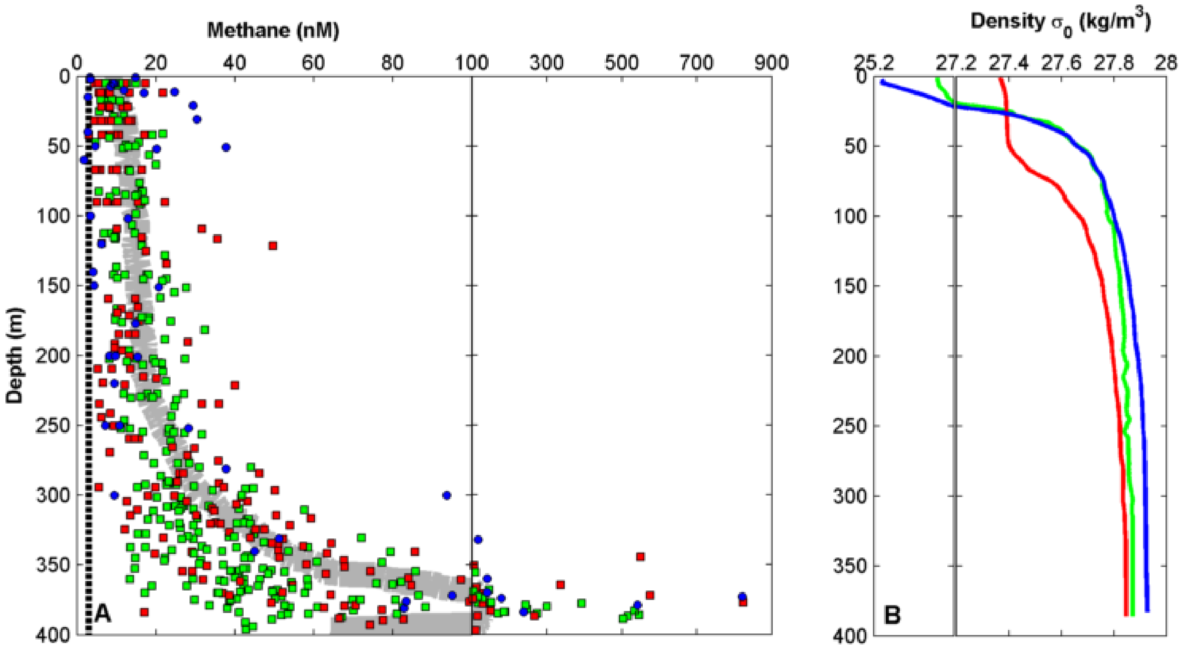

Figure 4-3 Profiles of (**A**) dissolved methane concentration and (**B**) density anomaly at the landward limit of the GHSZ. Circles (blue) are data from 2011, squares (red and green) are data from 2012. The thick grey line shows the smoothed mean of all measurements. The atmospheric equilibrium methane concentration (~3nM) is shown by the vertical dashed black line. Density profiles shown are representative for methane concentrations of the corresponding colours.

At distances of < 3 km from the seafloor methane seeps, there is no correlation between the methane concentration of surface waters (defined as $\sigma_\theta < 27.5$ kg m^{-3} based on density profiles) and distance from the seafloor seeps. The average methane concentration of surface seawater collected by Niskin bottles was ~9 nM (range 3-9 nM) in 2011 and ~11 nM (range 4-17 nM) in 2012. The average concentration measured by the equilibrator system was slightly lower at 4.7 nM (range 3.1 – 6.4 nM). This difference may reflect sampling depths: on average, 'surface' seawater collected by Niskin bottles was slightly deeper (~1 – 12 m below the sea surface), than 'surface' seawater sampled by the equilibrator system (~2.8 m below the sea surface). Similar differences between methane concentrations measured in Niskin bottle samples and in seawater measured using an equilibrator system have also been reported in the Gulf of Mexico [Hu et al., 2012; Solomon et al., 2009].

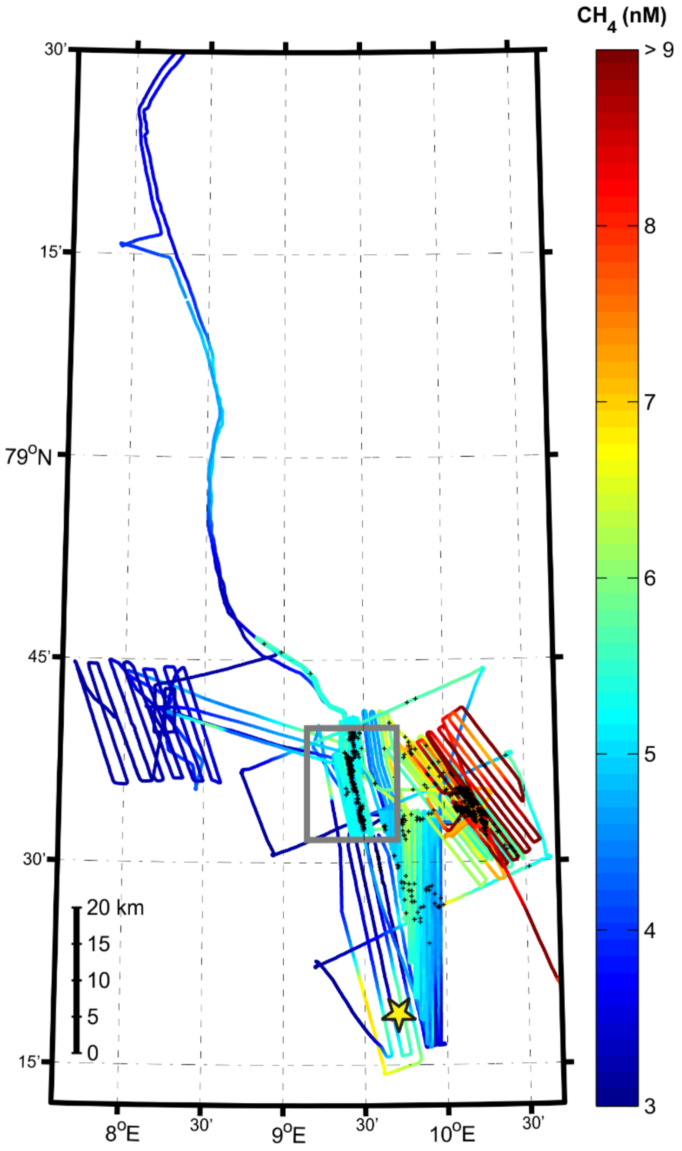

Figure 4-4 Methane concentration in surface seawater measured using the equilibrator system during RV *Heincke* cruise He-387. Black crosses show the location of seafloor methane seeps mapped during the cruise [Sahling et al., 2012; 2014]. Grey square indicates the area of the map shown in *Figure 4-1b* yellow star indicates the position of the 'background' station to the south of our study area.

Surface waters are supersaturated with respect to methane not only in the immediate vicinity of the seafloor methane seeps, but up to at least 35 km to the west of the landward limit of the GHSZ, > 80 km to the north along the 400 m depth contour, and > 15 km to the south (*Figure 4-4*). Highest supersaturation (52 nM) was observed at shallow water depths (< 100 m) on the continental shelf. Although no methane seeps have been found to date to the south of our study area, high levels of methane in surface waters (which cannot be derived from the known methane seeps to the north, as the currents flow from south to north) suggest that there is likely to be a methane source in this area. In support of this, the methane concentration in surface seawater measured at the 'background' station sampled in 2012, which lies ~30 km south of our study area, was > 9 nM, dissolved methane concentrations increase with depth to a bottom water maximum of 40 nM (*Supplemental Figure C-2*).

4.4.2. Fluxes, sources and fate of dissolved methane in the water column offshore Svalbard

4.4.2.1. Loss of methane from bottom waters

As described above, highest concentrations of dissolved methane are restricted to the lower 75 m of the water column. Bubble observations and modelling at this site, and elsewhere, indicate that essentially all methane released in bubbles can be expected to dissolve in this depth zone [Gentz et al., 2014; Leifer and Patro, 2002; Westbrook et al., 2009]. As soon as the methane is in the dissolved phase, it is subject to microbially mediated aerobic oxidation, advection by water currents, and turbulent diffusion across concentration gradients. The proportion of methane released at the seafloor which reaches the upper water column depends on the relative rates of these processes, and may be estimated using our simplified box model.

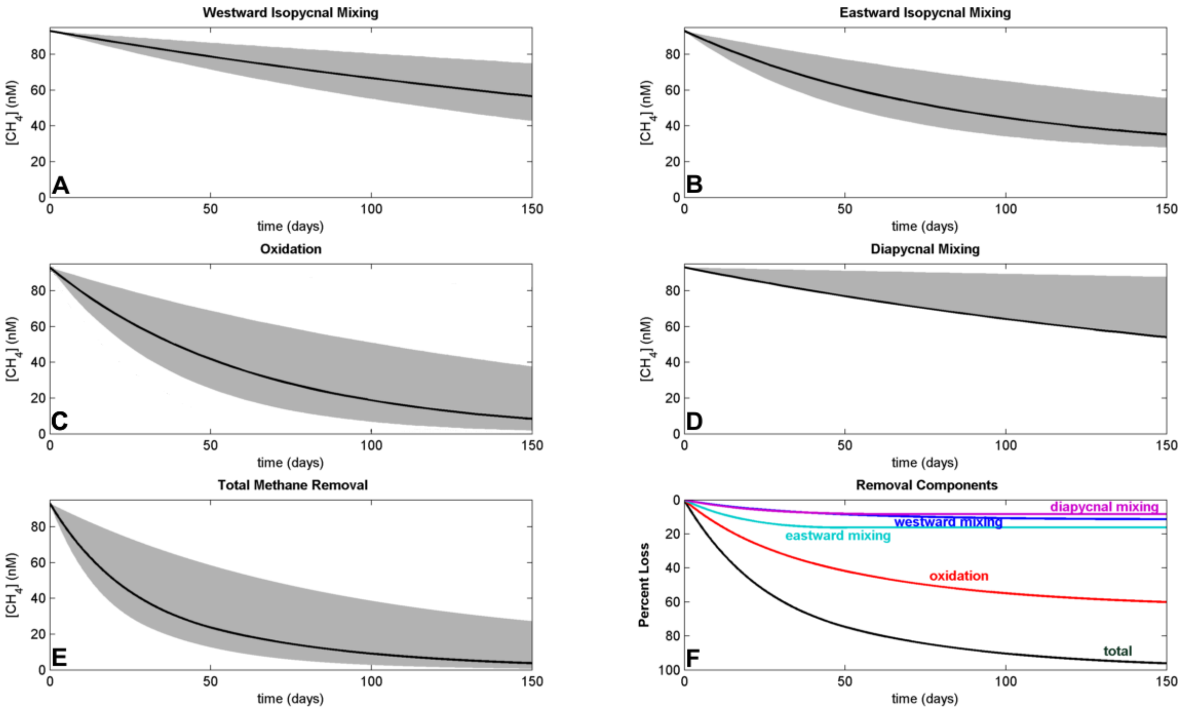

Figure 4-5 Loss of methane from bottom waters due to (**A**) offshore isopycnal mixing, (**B**) onshore isopycnal mixing, (**C**) oxidation, and (**D**) upward diapycnal mixing calculated by the box model. The grey shaded regions represent the uncertainty in fluxes due to the uncertainty in the rate constants. These are: isopycnal mixing coefficient ± 0.04 $m^2 s^{-1}$, diapycnal mixing coefficient 10^{-4} $m^2 s^{-1}$ - 10^{-3} $m^2 s^{-1}$, and k_{MOx} ± 0.01 day^{-1}. Panel (**E**) shows the total methane removal and panel (**F**) shows the percentage concentration loss due to each term.

The results of the model are shown in *Figure 4-5*, and input parameters are given in *Table 4-1*, with additional details are provided in *Supplemental Table C-1*. There is a large uncertainty associated with all methane flux terms, as the isopycnal and diapycnal mixing coefficients are poorly constrained, and the measured methane oxidation rate constants were highly variable in both space and time [Steinle et al., In Review]. For the modelled average observed conditions and best estimate mixing coefficients, the observed bottom water concentrations decay to background concentrations of ~ 3 nM within 150 days, under the assumption that the oxidation rate constants measured at the seep site remain appropriate as methane concentrations are depleted and water is advected northward in the WSC. Oxidation is responsible for the majority of methane concentration depletion, consuming ~ 60 % of methane released at the seafloor before it is mixed outside of the modelled bottom water volume. Isopycnal mixing towards the measured off-seep background concentrations accounts for ~ 27 % of the methane loss. Eastward mixing at depth is limited by the intersection of isopycnals with the continental slope ~ 2 km from the seep site. Upwards diapycnal mixing between deep and surface waters accounts for the remaining 9 % of methane removal from the modelled bottom water volume.

The model is restricted to describing the fate of methane released at the seafloor which dissolves in the lower part of the water column; it does not include the effects of continuing methane release. As bottom water currents in this area are very high, the modelled volume of methane-containing water is rapidly flushed away from the methane source towards the north in the WSC. Previous measurements of the WSC offshore Western Svalbard record very high current speeds averaging up to ~24 cm s^{-1} on the upper continental slope in this area [Fahrbach et al., 2001], with wintertime peaks in exceeding 50 cm s^{-1} [Teigen et al., 2010]. The net effects of tidal displacement are expected to be minor, as neither methane concentrations nor other bottom water properties were related to the tidal phase during sampling.

In currents moving at 24 cm s^{-1} a volume of water would pass over the seepage region in approximately 0.6 days, during which time the total input of methane at the seafloor from seep bubbles is estimated to be ~10 mol (assuming a bubble seep methane flux of 16 mol day^{-1} m^{-1}, from Sahling et al. [2014]). For this input flux, the accumulated dissolved methane concentration in the box is 50 – 700 nM, in good agreement with measured concentrations. These rates of methane input exceed the rate of methane loss estimated using our box model, such that methane will accumulate and establish concentrations of dissolved methane higher than background values, as observed. Thus, our model of methane loss is consistent with both our observations, and measurements of methane fluxes across the seabed. Within the time required for half of the methane anomaly to be consumed by oxidation and lost by mixing, advection in the WSC is expected to transport the modelled volume of high-methane bottom water northwards from the seepage site to a latitude of > 80 °N, where the WSC flows over the Yermak Plateau and is partially recirculated through

Table 4-1 Box model input parameters. Methane oxidation rate data are from Steinle et al [In Review] .

parameter	symbol	units	value	description
modelled box height	z	m	75	height of box above seafloor; methane concentration > 75 nM
modelled box width	x	m	450	width of box; approximate width of seafloor affected by methane seepage perpendicular to the 400 m bathymetric contour
initial methane concentration	$[CH_4]_i$	nM	93	initial methane concentration: average methane concentration within 75 m of the seafloor measured in 2012
oxidation rate	k_{MOx}	day^{-1}	0.016	oxidation rate: average value measured in 2012
standard deviation			0.01	
minimum			0.0009	*depth-integrated single profile value*
maximum			0.04	*depth-integrated single profile value*
initial westward concentration gradient	$(\Delta C/\Delta x)_{W\,i}$	$nM\ m^{-1}$	0.05	offshore concentration gradient; measured between seep sites aligned along the 400m bathymetric contour and station JR253-12
initial eastward concentration gradient	$(\Delta C/\Delta x)_{E\,i}$	$nM\ m^{-1}$	0.09	onshore concentration gradient: measured between seep sites aligned along the 400m bathymetric contour and station JR253-8
initial vertical concentration gradient	$(\Delta C\Delta x)_{Z\,i}$	$nM\ m^{-1}$	0.06	vertical concentration gradient; measured above and below 75 m above the seafloor at seep sites aligned along the 400 m bathymetric contour

the Fram Strait [Gascard et al., 1995]. Although this water will still contain methane sourced from the seepage region, the pattern of circulation in this region means that it is not expected to come into contact with the atmosphere [Elliott et al., 2011].

4.4.2.2. Sources of methane to the upper water column

The complete dissolution of methane bubbles below 200 m water depth precludes direct input of methane to the upper water column, and slow diapycnal mixing coupled with high bottom water current speeds mean that the seafloor seeps cannot contribute significant dissolved methane to these waters. Even with the choice of an ‘upper limit’ high diapycnal mixing coefficient (10^{-3} m^2 s^{-1}; Ledwell et al. [2000]), vertical methane transport transfers minimal methane towards the surface mixed layer before northward advection sweeps the water away from the seep site. However, elevated methane concentrations persist in intermediate waters (depth < 200 m, $\sigma_\theta > 27.5$ kg m^{-3}) and surface waters ($\sigma_\theta < 27.5$ kg m^{-3}). Potential alternative sources of methane to the upper water column include: (i) isopycnal mixing of methane from seafloor seeps located on the shelf; (ii) diapycnal mixing of methane from seafloor seeps upstream (to the south), and (iii) production of methane in surface waters.

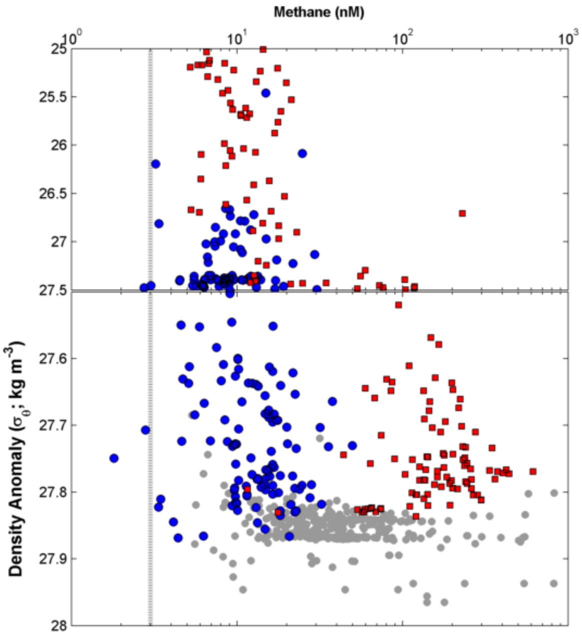

Figure 4-6 Variation in dissolved methane concentration with density over the shelf region (80-150 m water depth; red squares) and on the upper slope near the landward limit of the GHSZ (380-400 m water depth; circles). The latter samples are divided into bottom water (> 200 m depth, grey), intermediate (< 200 m water depth, $\sigma_\theta > 27.5$ kg m^{-3}, blue, lower panel), and surface water ($\sigma_\theta < 27.5$ kg m^{-3}, blue, upper panel). The dashed vertical line shows the atmospheric equilibrium methane concentration (~3 nM).

Seafloor methane seeps were discovered on the continental shelf offshore Svalbard approximately 15 km east of the landward limit of the GHSZ in 2011 [Sahling et al., 2014].

Here, the water depth on the shelf is relatively shallow (< 100 m), which allows some methane bubbles to rise all the way through the water column and ventilate directly to the atmosphere. Methane dissolution occurs as bubbles rise, and leads to high methane concentrations throughout the water column, establishing a large concentration gradient between shelf and upper slope waters. Cold Arctic ESC water of the shelf is separated from upper slope warm Atlantic WSC water by a strong, density-compensated halocline (the Arctic Front; e.g. Cottier and Venables [2007]; Saloranta and Svendsen [2001]), which allows offshore isopycnal mixing of methane from shelf seeps towards the upper water column at the GHSZ limit (*Figure 4-6*). Mechanisms for enhanced isopycnal turbulent diffusion across the Arctic Front include barotropic instability due to the difference in current speed between WSC and ESC waters [Saloranta and Svendenson, 200l; Teigen et al, 2010] and interleaving and cabbeling enhanced eddy diffusivities driven by the contrasting temperatures and salinities across the front [Cottier and Venables, 2007].

The unexpected observation of elevated concentrations of dissolved methane at the seafloor and in surface waters to the south of the region of seafloor seeps at the limit of the GHSZ suggests that seafloor methane seeps exist in this area, and therefore that WSC water flowing northwards into our study area is likely to carry dissolved methane from upstream sources. Upwards diapycnal transport of methane from bottom water into intermediate-depth waters is likely to occur between upstream seafloor methane sources and our study site. While the recent discovery of extensive seafloor methane seeps aligned along the landward limit of hydrate stability offshore North America [Skarke et al., 2014] supports the idea that the location of seafloor methane seeps is regulated by hydrate dissociation, extensive acoustic surveys offshore Western Svalbard found no evidence for seepage along the landward limit of the GHSZ < 80 km to the north of our study area and < 20 km to the south [Sahling et al., 2014]. However, there is some evidence for elevated methane concentrations in water on the upper slope ~150 km south of our study area [Damm et al., 2005], which supports our southern equilibrator system and background station high-methane concentration observations. The distribution of seafloor methane seeps in the vicinity of the GHSZ offshore Svalbard appears to be patchy, and/or temporally variable. More extensive echosounder surveys and water column measurements are needed to properly quantify the potential contribution of sources to the south of our study area.

Production of methane within the upper water column is well documented throughout the world's oceans [Damm et al., 2010; Florez-Leiva et al., 2013; Sasakawa et al., 2008] with supersaturation often observed at the pycnocline [Reeburgh, 2007]. Dissolved methane concentrations of up to 55 nM in surface waters on the shelf to the south of Spitsbergen (Storfjorden) have been attributed to *in situ* methanogenesis [Damm et al., 2008]. In this setting, methane is able to accumulate because oxidation is slow and waters are strongly stratified, preventing exchange with the atmosphere. Several, but not all, of our methane depth profiles collected at the GHSZ limit site (~ 400 m water depth) show local increases in dissolved methane (to ~ 25 nM) close to the pycnocline. However, our 2012 survey reveals that the shallow pycnocline is intermittently absent (*Figure 4-3b*) due to absence of low salinity surface waters, preventing the development of a permanent pycnocline. An alternative explanation for accumulation of dissolved methane at the pycnocline is that is that methane rising from the seafloor seeps pools beneath the density barrier [Solomon et al., 2009].

4.4.2.3. Methane flux to the atmosphere

All methane dissolved in the surface mixed layer, irrespective of source, is subject to exchange with the overlying atmosphere. Sea to air methane fluxes calculated from measured surface water methane concentrations in both Niskin bottle samples and by the equilibrator system are given together with ancillary data in *Table 4-2*. The spatial distributions of methane saturation in surface seawater and the sea to air methane flux measured using the equilibrator system are shown in *Figure 4-7*. Methane saturation in surface waters mainly reflects methane concentrations; solubility effects due to variations in surface water salinity and temperature and atmospheric pressure are minor. Methane fluxes are also regulated by wind speed.

Both methane saturation and sea to air methane fluxes are highest on the shelf, where the water depth is relatively shallow. Fewer seafloor seeps are present on the outer part of the shelf and water depths become progressively deeper, so methane fluxes are lower and close to those calculated at the landward limit of the GHSZ. Lowest methane fluxes are found furthest offshore, where water depths are highest (~ 900 m) and the distance from on-shelf methane seeps is greatest. High methane saturation in surface waters along the 400 m bathymetric contour to the north of the main study site suggest that methane transported at depth in the WSC from the seeps at the limit of the GHSZ may mix vertically during northward advection and reach surface waters downstream. Enhanced vertical mixing in excess of that modelled by diapycnal mixing coefficients is suggested by wintertime WSC heat loss studies, which show that mass exchange between the upper 10-20 m of the water column and the stratified interior occurs on timescales faster than a day [Boyd and D'Asaro, 1994].

Table 4-2 Sea to air methane fluxes, with associated sampled parameters. The regional divisions of the equilibrator data are shown in *Figure 4-7*.

		surface seawater CH_4 nM	**temperature** °C	**salinity** psu	**atmospheric pressure** mbar	**atmospheric methane** ppb	**percent saturation** %	**wind speed (u_{10})** $m\ s^{-1}$	**sea→air flux** $mmol\ m^{-2}\ day^{-1}$
equilibrator system									
main study area	*average*	**4.7**	**5.4**	**34**	**1007**	-	**145**	**7**	**4**
	minimum	3.1	4.4	33	1016	-	100	0	0
	maximum	6.4	8.5	35	990	-	191	17	17
offshore	*average*	**3.4**	**6.7**	**34**	**1004**	-	**111**	**8**	**1**
	minimum	3.1	5.3	33	1012	-	100	2	0
	maximum	5.9	9.6	34	994	-	187	13	10
north	*average*	**4.2**	**8.4**	**34**	**1013**	-	**139**	**4**	**1**
	minimum	3.2	4.8	33	1014	-	107	0	0
	maximum	5.7	9.7	34	1012	-	173	8	4
south	*average*	**4.4**	**5.9**	**34**	**9936**	-	**139**	**8**	**3**
	minimum	3.1	4.1	33	1002	-	101	3	0
	maximum	6.9	7.2	34	9913	-	210	17	18
outer shelf	*average*	**5.0**	**5.1**	**33**	**1006**	-	**154**	**9**	**6**
	minimum	3.2	4.2	32	1017	-	101	4	0
	maximum	6.9	7.0	34	9871	-	212	17	25
inner shelf	*average*	**8.5**	**4.6**	**33**	**1001**	-	**258**	**7**	**8**
	minimum	4.4	3.7	32	1012	-	138	0	0
	maximum	52	5.5	34	9866	-	1579	14	36
depth profiles									
2012	*average*	**11**	**5.0**	**34**	**999**	**1891**	**336**	**9**	**30**
	minimum	4.5	4.8	34	989	1883	136	3	15
	maximum	17	7.0	35	1005	1899	572	17	45
2011	*average*	**8.9**	**5.0**	**33**	**1014**	**1866**	**271**	**8**	**16**
	minimum	2.9	3.4	29	989	1852	81	0	8
	maximum	9.0	6.5	35	1023	1890	298	18	32

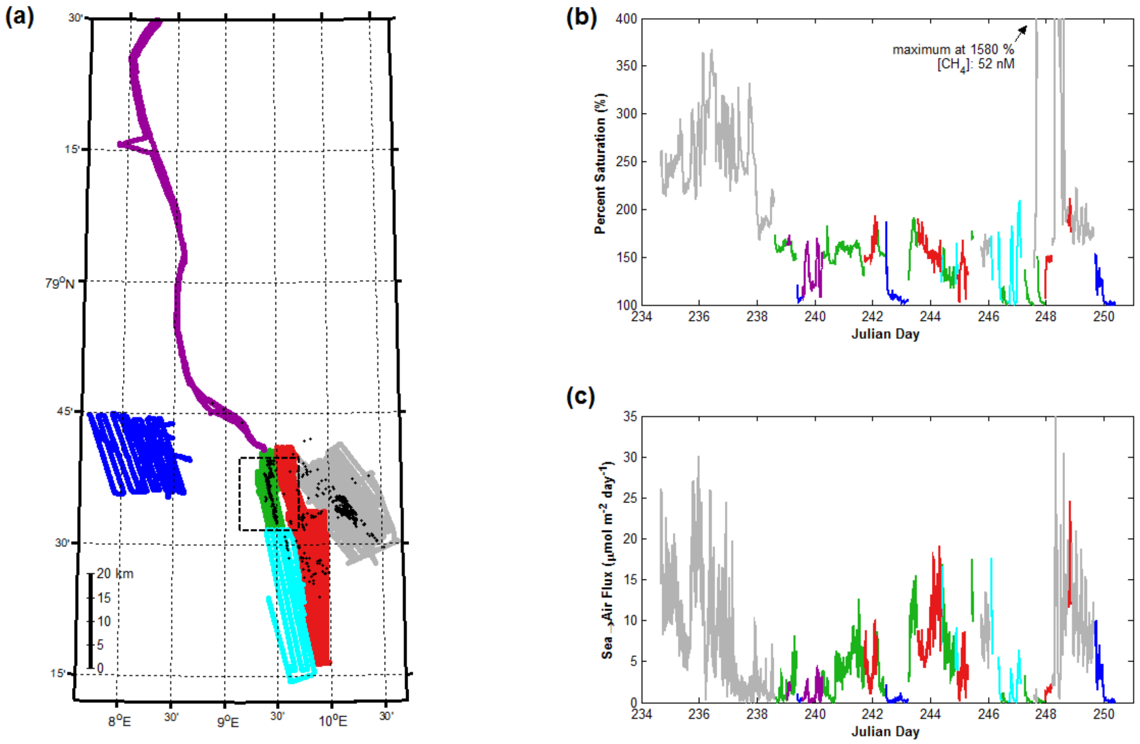

Figure 4-7 (**a**) Ship track where methane concentration in surface seawater was measured by the equilibrator system. Colours indicate regional divisions of Table 2: purple = north, green = main study area, light blue = south, dark blue = offshore, red = outer shelf, grey = inner shelf. Black crosses indicate positions of methane seeps, and black dashed rectangle indicates the extent of the map shown in *Figure 4-1b*. (**b**) Equilibrator data expressed as methane saturation with respect to atmospheric equilibrium, and (**c**) Sea-air methane flux for each region.

Table 4-3 Sea to air methane fluxes. Values in brackets are minimum and maximum fluxes.

Location	**Water depth** (m)	**Diffusive Flux** (μmol m^{-2} day^{-1})	**Reference**
upper slope offshore Western Svalbard	~400 m	20 (8 – 45)	This study, Niskin bottle samples.
		4 (0 – 17)	This study, equilibrator system.
shelf offshore Western Svalbard	~ 100 m	8 (0 – 36)	This study, equilibrator system.
East Siberian Arctic Sea	< 60 m	230 (190 – 300)*	[*Shakhova et al.*, 2010]
open Arctic Ocean north of Alaska	~ 3500 m	125 (30 – 500)	[*Kort et al.*, 2012]
Atlantic Ocean:			
open ocean		0.2	[*Rhee et al.*, 2009]
coastal regions		2	

* corrected for differences in the choice of gas transfer coefficient (*k*)

Fluxes of methane from the upper slope and shelf region offshore Svalbard to the atmosphere are compared to other sources of atmospheric methane in the Arctic and elsewhere in *Table 4- 3*. The Svalbard source is small compared to that reported for the East Siberian Arctic (ESA) Sea, where methane (likely derived from thawing permafrost) is ejected from the seafloor at very shallow water depths (< 60 m; Shakhova et al. [2014;2010b]). The fluxes that we measure are also lower than those observed during an aircraft survey over open leads and regions with fractional ice cover in the Arctic Ocean (30-500 µmol m^{-2} day^{-1}; Kort et al. [2012]). The source of this methane is unlikely to be the seafloor and is rather attributed to release of methane that may accumulate under ice in the winter months [Shakhova et al., 2010a], and also to biological production of methane in the vicinity of melting ice [He et al., 2013].

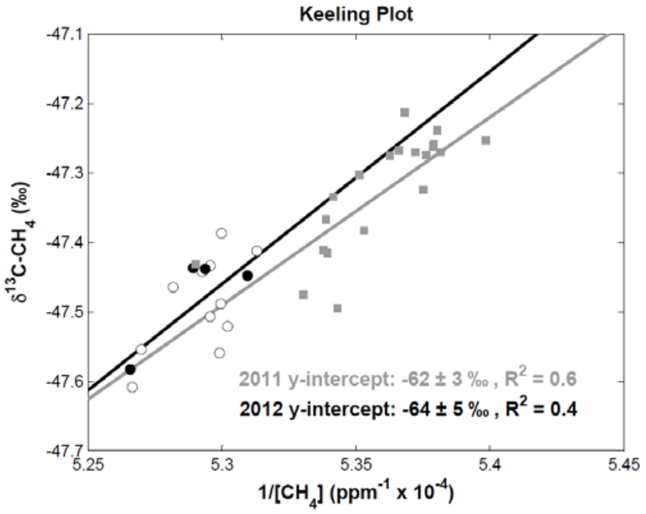

Figure 4-8 Keeling plot of atmospheric methane concentration versus δ^{13}C-CH_4: 2011 data (grey squares) were all collected within 3 km of seafloor methane seeps, 2012 data were within 5 km of seeps (filled circles), and within > 5 km and < 50 km from the seeps (open circles).

The relatively low sea to air methane flux offshore Western Svalbard is supported by measurements of atmospheric methane. The methane concentration of air in the study region collected during our sampling campaigns in 2011 and 2012 was not significantly elevated compared to sites sampled between 5 to > 50 km from the seafloor seeps. Keeling plots of the δ^{13}C signature of CH_4 (*Figure 4-8*) indicate that the overall δ^{13}C-CH_4 signature of the methane sources to this area is -62 ± 3 ‰ for 2011 and -64 ± 5 ‰ for 2012. This is slightly higher than the bulk source signature of shipboard data for the same area from summer and autumn 2008-2010 (-73.1 to -64.1 ‰), which has been interpreted to indicate that high-latitude wetlands (δ^{13}C-CH_4 < - 60 ‰) are the dominant source of methane to the atmosphere in this area and that local submarine hydrates (δ^{13}C-CH_4 > - 55 ‰) and other isotopically heavier methane sources make a small contribution [Fisher et al., 2011]. The slightly heavier bulk isotopic signature of the 2011 and 2012 shipboard data could be interpreted to indicate a larger contribution from the local sea-air fluxes of both the shelf and the slope offshore Svalbard fuelled by seafloor methane seepage. However, it is more likely that the difference between this atmospheric data set and previously reported observations is due to unrelated inter-annual variably in relative contributions and isotopic signatures of other Arctic atmospheric methane sources. In either case, the overall light atmospheric methane source signatures clearly indicates that methane input from seafloor seeps at the depth of the hydrate stability zone limit does not make more than a minor contribution to local atmospheric methane.

4.5. Summary and conclusions

Dissolution of methane from seafloor bubble seeps at the landward limit of gas hydrate stability offshore Western Svalbard leads to high concentrations of dissolved methane (up to 825 nM) in bottom waters of the northward flowing West Spitsbergen Current. Methane concentrations close to the seafloor are highly variable in time and space, while concentrations in upper and intermediate waters are lower and less variable (2 - 50 nM), but nevertheless supersaturated with respect to methane in equilibrium with the atmosphere (~ 3 nM). Simple box modelling indicates that the seafloor seeps are not the source of methane to the immediately overlying intermediate and surface waters, because upwards diapycnal mixing is much slower than northwards advective transport in the West Spitsbergen Current. Rather, we show that the most likely source of this methane is isopycnal mixing with waters on the shelf, which have elevated dissolved CH_4 due to dissolution of methane from seafloor bubble seeps. Downstream surface methane supersaturation in the absence of local seafloor seeps suggests that vertical mixing may provide a mechanism for methane escape from seafloor seeps at the GHSZ limit to the atmosphere on longer timescales. Future studies downstream of the seep site are suggested to further constrain the partitioning of the dissolved methane plume between eventual oxidation at depth, and equilibration into the atmosphere. Our data additionally provide evidence for seafloor methane seepage to the south of our study area.

Although surface waters are supersaturated with methane throughout our study area, the sea-air methane flux is relatively small. In support of this, measurements of local atmospheric methane concentrations and the carbon isotopic composition do not detect the local seafloor seepage methane source over the regional background. This emphasises that the ~ 400 m water depth overlying focused seepage at the GHSZ limit provides an effective barrier for direct release of significant quantities of methane to the atmosphere, and furthermore that seafloor seepage into the shallower (~ 100 m) shelf waters does not represent a significant atmospheric methane source despite direct seep bubble venting to the surface mixed layer.

CHAPTER 5

History of methane seepage on the upper continental margin offshore Western Svalbard

Supplementary Material is provided in **Appendix D**

Contents

Abstract

Large-scale methane release from hydrates in continental margin sediments may be an important feedback to global climate warming. In the Arctic, offshore Western Svalbard, seafloor methane seepage is linked to hydrate destabilization in response to bottom water warming in the past few decades. The potential for methane release offshore Svalbard, and from accumulated shallow methane hydrate globally, can be assessed by the investigation of the relationship between seafloor seepage activity and methane hydrate stability over glacial-interglacial timescales. Sedimentary records of magnetic susceptibility, barium, carbonate and foraminiferal carbon isotopic signatures provide proxies for the presence of methane seepage and high methane fluxes. We present results from near-surface sediments in the vicinity of seafloor methane seeps located close to the landward limit of the gas hydrate stability zone (GHSZ) on the upper continental margin offshore Western Svalbard, in order to both evaluate the applicability of these proxies to this setting, and determine the relationship between seafloor methane seepage and climate-driven migration of the GHSZ. In the past ~ 30,000 years, there is no evidence for higher methane fluxes at shallower water depths than where seepage presently occurs, indicating that upslope migration of the GHSZ in times of colder bottom water conditions was not accompanied by a shift in seafloor seepage locations. There is evidence for episodic activity of seeps at the present-day GHSZ over the past ~ 30 000 years, likely in response to the accumulation and release of methane from the local hydrate reservoir. However, better age control is required to fully understand the links between methane release and climate.

5.1. Introduction

Methane hydrate, an ice-like solid stable at high pressure and low temperature [Hester and Brewer, 2009], accumulates large volumes of CH_4 beneath the seafloor: ~ 500 – 2500 Gt carbon globally [Milkov, 2004]. Substantial release of methane into the oceans and potentially the overlying atmosphere following thermal destabilization of methane hydrates may have played a role in role in past global climate warming events (e.g. the Palaeocene-Eocene thermal maximum [Bowen et al., 2014; Dickens, 2011]). In response to climate warming in the Anthropocene, hydrates are likely destabilizing and releasing methane into ocean bottom waters in the Arctic, North Atlantic, and North Pacific [Berndt et al., 2014; Hautala et al., 2014; Phrampus and Hornbach, 2012; Skarke et al., 2014; Westbrook et al., 2009].

Biogenic and thermogenic methane are produced at depth and rise towards the seafloor [Reeburgh, 2007; Whiticar, 1999]. Where upwards diffusing methane encounters downwards diffusing pore fluid sulphate (SO_4^{2-}) it is anaerobically oxidized by a consortium of archaea and bacteria to produce dissolved inorganic carbon (DIC: CO_2, HCO_3^-, CO_3^{2-}) and sulphide (S^{2-}) [Boetius et al., 2000]. The presence of active anaerobic oxidation of methane (AOM, *Equation 5-1*) is evidenced by sediment methane and pore water profiles which define a narrow reaction depth interval termed the sulphate-methane transition zone (SMTZ). In addition to methane and sulphate concentrations approaching zero at the SMTZ, concentrations of dissolved inorganic carbon (DIC) and sulphide increase. Resulting carbonate supersaturation of pore waters leads to authigenic carbonate precipitation at the SMTZ (*Equation 5-2*; Sun and Turchyn [2014]). The inorganic carbon produced by AOM reflects the light carbon isotopic signature of methane in sediments ($\delta^{13}C\text{-}CH_4 < -40$ ‰; Whiticar [1999]). The depth at which the SMTZ occurs is determined by the upward flux of methane, with higher methane fluxes pushing it closer to the sediment-seawater interface [Borowski et al., 1996]. Linear sulphate profiles are interpreted to reflect steady-state diffusion to a temporally stable SMTZ depth, while kink-type sulphate profiles indicate relatively recent changes in the local methane flux from depth (e.g. Hensen et al. [2003]).

$$CH_4 + SO_4^{2-} \rightarrow HCO_3^- + HS^- + H_2O \qquad (5\text{-}1)$$

$$Ca^{2+} + 2HCO_3^- \rightarrow CaCO_3 + CO_2 + H_2O \qquad (5\text{-}2)$$

While pore fluid geochemistry reflects the present-day STMZ, the interaction of AOM with the sediment solid phase can leave a record of past methane fluxes. The timescales of response of pore fluids and the solid phase to changes in methane fluxes are relatively poorly constrained. Modelling studies have shown that pore fluid geochemistry responds to changes in methane fluxes in tens to hundreds to thousands of years [Henkel et al., 2011; Hensen et al., 2003], while significant diagenetic alteration of sediments occurs on timescales longer than approximately 10,000 years (e.g. Kasten et al. [2012]; Riedinger et al. [2006]; Snyder et al. [2007a]). If stable methane fluxes maintain the SMTZ at a fixed depth relative to the seafloor, the interval of time during which a volume of sediment is exposed to AOM conditions is controlled by the sedimentation rate. Three proxies for past seepage are explored: (i) alteration of magnetic iron phases, (ii) dissolution, mobilization, and re-precipitation of barite, and (iii) foraminiferal calcite carbon isotopes ($\delta^{13}C$, ^{14}C-dating).

The dominant magnetisable component of marine sediments is ferromagnetic magnetite (Fe_3O_4), and other iron (oxyhydr)oxides [Stoner and St-Onge, 2007]. Sediment magnetic susceptibility is used as a stratigraphic tool on local and basin scales, because deposition of magnetic sediments varies with changes in oceanographic and glacial conditions [Jessen et al., 2010]. Diagenetic alteration of the magnetic properties of sediments in shallow oxic environments (upper few cm) is well documented (e.g. Karlin and Levi [1983]; Liu et al. [2012]). Similarly, sulphide released during sulphate reduction has been shown to dramatically alter the iron speciation in sediments and thus the sediment magnetic properties (e.g. Garming et al. [2005]; Neretin et al. [2004]; Rowan et al. [2009]). The presence of sulphide in sediment pore fluids leads to reductive dissolution of iron (oxyhdr)oxides and formation of paramagnetic pyrite (FeS_2), through the thermodynamically metastable intermediate ferrimagnetic greigite (Fe_2S_4). This alteration is given by *Equations 5-3* to *5-6* [Dewangan et al., 2013; Neretin et al., 2004; Riedinger et al., 2005], where *Equations 5-5* and *5-6* show two proposed pathways for pyrite formation through a greigite intermediate [Dewangan et al., 2013]. Post depositional alteration of sediment magnetic components is reflected in a range of magnetic properties, including magnetic susceptibility which is often observed to be dramatically reduced close to the STMZ due to pyrite formation (e.g. Dewangan et al. [2013]; Garming et al. [2005]; März et al. [2008]; Riedinger et al. [2005]), but can also be enhanced in association with AOM where conditions including sulphide or iron limitation favour greigite preservation (e.g. Dewangan et al. [2013]; Larrasoaña et al. [2007]; Neretin et al. [2004]).

$$Fe_3O_{4(s)} + HS^- + 7H^+ \rightarrow 2Fe^{2+} + S^0 + 4H_2O \qquad (5\text{-}3)$$

$$Fe^{2+} + HS^- \rightarrow FeS_{(s)} + H^+ \qquad (5\text{-}4)$$

$FeS + S^0 \rightarrow Fe_2S_4 + 2S^0 \rightarrow 3FeS_2$ (5-5)

$FeS + HS^- \rightarrow Fe_2S_4 + 2HS^- \rightarrow 3FeS_2$ (5-6)

Barium of both biogenic and detrital origin accumulates in marine sediments. Biogenic barite ($BaSO_4$) is insoluble in anoxic and suboxic sediments, and is used as a proxy for paleo-productivity [Calvert and Pedersen, 2007; Gingele et al., 1999]. However, when buried to depths where pore water sulphate is depleted, undersaturation of sulphate causes dissolution and remobilization of barium. Dissolved barium in pore fluids diffuses along concentration gradients, re-precipitating when it encounters sulphate. Where high methane fluxes lead to sulphate depletion due to removal by AOM, barite dissolves below the SMTZ and re-precipitates above the SMTZ. When the SMTZ is fixed in a sediment interval for long periods of time, the accumulation of barite produces barium fronts immediately above the STMZ [Dickens, 2001; Kasten et al., 2012; Nöthen and Kasten, 2011; Riedinger et al., 2006; Snyder et al., 2007a; Torres et al., 1996a; Torres et al., 1996b]. If the SMTZ moves upwards in the sediment due to an increase in the methane flux, previously deposited barite fronts are re-dissolved as they move into sulphate-undersaturated pore fluids. Conversely, downward retreat of the SMTZ can leave a series of barite fronts as a record of higher methane fluxes in the past. The amount of barite accumulation depends on both the amount of available labile biogenic barite in the sediments, and the period of time for which the depth of the SMTZ has been stable. Calculations of the time required for the accumulation of barite fronts observed in sediments of the Congo Fan, Blake Ridge (offshore Eastern North America), and offshore Namibia range from 1,000 to 100,000 years [Dickens, 2001; Kasten et al., 2012; Riedinger et al., 2006; Snyder et al., 2007a].

The ability of benthic and planktonic foraminifera to record past seafloor methane seepage is the subject of some debate (e.g. Herguera et al. [2014]; Hill et al. [2004]; Panieri [2006]; Panieri et al. [2014a]; Stott et al. [2002]; Torres [2003]; Torres et al. [2010]). In non-seep environments, the carbon isotopic signatures of foraminiferal calcite reflects that of dissolved inorganic carbon in seawater, with variable small species-specific offsets ('vital effects'; e.g. Martin et al. [2007]; Ravelo and Hillaire-Marcel [2007]). Planktonic foraminifera record δ^{13}C-DIC of surface seawater while benthic foraminifera record bottom water or shallow subsurface (upper few centimetres) pore water δ^{13}C-DIC values. Pore water δ^{13}C-DIC values usually decrease with depth due to remineralisation of photosynthetic carbon which is enriched in ^{12}C (e.g. Stott et al. [2002]). Seawater and near-surface pore waters typically have δ^{13}C-DIC values of ~ 0 ‰ (-1 to 1 ‰; Ravelo and Hillaire-Marcel, [2007]), and foraminiferal calcite in normal marine environments typically have δ^{13}C-DIC values of ~ -1 to 0 ‰. Incorporation of methane-derived carbon from both ^{13}C-depleted DIC and ingested ^{13}C-depleted chemosynthetic biomass at present-day seafloor seepage sites is reported to produce δ^{13}C values of as low as -21.2 ‰ in living and recently dead benthic foraminifera [Hill et al., 2004; Mackensen et al., 2006; Martin et al., 2010; Panieri et al., 2014a]. However, a number of studies have found no difference between δ^{13}C values of living on-seep foraminifera and those from off-seep settings (e.g. Herguera et al. [2014]; Panieri [2006]; Torres [2003]). Offsets between surface sediment pore fluid δ^{13}C-DIC and foraminiferal δ^{13}C may be significantly higher in seep environments where δ^{13}C-DIC values are lower than -40‰ [Herguera et al., 2014; Stott et al., 2002; Torres, 2003].

There is significant debate about the significance of overprinting of the primary foraminiferal δ^{13}C signal by secondary (diagenetic) calcite overgrowths in methane seep environments. Authigenic carbonates, with δ^{13}C of ~ -30 to – 60 ‰ (e.g. Bayon et al., [2007]; Berndt et al. [2014]; Greinert et al. [2001]; Ritger et al. [1987]) form in surface sediments during active methane seepage and also at depth throughout the sediment column where AOM produces carbonate saturation. Deconvolution of foraminiferal primary and secondary calcite geochemical signals has been the subject of significant study and method development (e.g. Millo et al.[2005b]; Panieri et al. [2012]; Panieri et al. [2014b]; Pena et al. [2005]; Torres et al. [2010]). Diagenetic carbonate overgrowths have a distinct crystal structure from the primary calcite [Pena et al., 2008]. The inner chamber walls of tests provide an ideal surface for growth of diagenetic crystals [Millo et al., 2005a; Millo et al., 2005b; Pena et al., 2008]. The more reactive overgrowth structure is expected to be preferentially removed by oxidative and reductive cleaning procedures to leave behind the primary calcite [Millo et al., 2005b; Pena et al., 2005].

Here, we present magnetic susceptibility, solid phase elemental analysis, and foraminiferal isotope geochemistry of four sediment cores from the upper continental margin offshore Western Svalbard, near the landward limit of the present-day gas hydrate stability zone (GHSZ). More than 250 seafloor methane seeps were discovered aligned along the GHSZ limit in 2008 [Westbrook et al., 2009], and seafloor seepage is likely related to temperature-driven hydrate dynamics [Ferré et al., 2012; Reagan and Moridis, 2009; Sahling et al., 2014; Sarkar et al., 2012]. Dating of authigenic carbonates at the site of present-day seepage indicates that the seeps have been active for at least 3,000 years before present (BP) [Berndt et al., 2014]. If methane seepage is related to warming of bottom waters and downslope retreat of the GHSZ, then seepage should have occurred further upslope when bottom waters were colder. We compare the sedimentary records of methane seepage proxies in cores from current seep sites, and in cores recovered from shallow water depths, in order to investigate the history of seafloor methane seepage in both environments.

5.2. Study site

The present-day landward limit of hydrate stability offshore Western Svalbard is at ~ 400 m water depth [Berndt et al., 2014]. Seafloor seepage occurs west of Prins Karls Forland in the inter-fan region between the Isfjorden and Kongsfjorden cross-shelf troughs (*Figure 5-1*) [Sahling et al., 2014; Westbrook et al., 2009]. Seismic surveys indicate the presence of shallow gas in the upper continental margin sediments, and shallow methane hydrate deposits further offshore [Chabert et al., 2011; Rajan et al., 2012; Sarkar et al., 2012]. Gas migration appears to occur through permeable prograding hemipelagic sediment sequences, which are variably capped by less permeable glaciogenic sediments on the upper slope and shelf [Rajan et al., 2012; Sarkar et al., 2012; Thatcher et al., 2013]. To the north of the study site lithological control of gas migration causes focused seafloor seepage to be shifted upslope to ~ 240 m water depth [Rajan et al., 2012]. Focusing of seafloor seeps between 360 and 415 m water depth [Sahling et al., 2014], corresponding to sediments where increases of local ocean bottom water temperature in the past decades [Ferré et al., 2012; Westbrook et al., 2009] would have destabilized hydrate, is not associated any with geological controls [Sarkar et al., 2012].

Seafloor pockmark structures on the outer continental shelf which are not currently the sites of active seafloor seepage provide evidence for past methane seepage in this area [Rajan et al., 2012]. Authigenic carbonates on the surface and buried up to 240 cm depth at the present seepage site (385-395 m water depth) with extremely light carbon isotopic signatures indicating incorporation of methane-derived carbon precipitated ~ 3 to 23 ka BP [Berndt et al., 2014]. Further offshore, where shallow methane hydrate and seafloor methane seepage are associated with faults providing a gas conduit through the GHSZ [Smith et al., 2014; Vogt et al., 1994], the foraminiferal calcite carbon isotopic record suggests intervals of seepage and quiescence which may be linked to climate events [Panieri et al., 2014b].

Warm and saline Atlantic Water of the West Spitsbergen Current (WSC) [Aagaard et al., 1987] flows over the upper slope offshore Western Spitsbergen, while colder Arctic water of the East Spitsbergen Current flows northward over the shelf [Saloranta and Svendsen, 2001]. Historical temperature measurements in the WSC record multiple warming and cooling events since 1950, with overall warming since 1975 [Ferré et al., 2012; Westbrook et al., 2009]. Spielhagen et al. [2011] showed that the current Fram Strait ocean temperatures represent a maximum for the last 2,000 years. A Holocene thermal maximum occurred at ~9.7-8.8 ka BP [Ebbesen et al., 2007]. The final deglaciation of the shelf occurred following the Younger Dryas stadial (11.7 – 12.9 ka BP; Rasmussen et al. [2006]), and was preceded by a glacial re-advance at 14.5 ka BP at the transition into the Bølling-Allerød interstadial (15 – 14.6 ka BP; Jessen et al. [2010] and references therein). During the last glacial maximum (32 – 20.5 ka BP) full glaciation of the shelf occurred at ~ 24 ka BP (Jessen et al. [2010] and references therein).

Along with temperature variability, glacial cycles were accompanied by local and global sea level changes due to ice volume changes and ice loading [Forman et al., 2004]. Global sea level was at a minimum at 26 ka BP [Jessen et al., 2010]. Modern sea level was established at ~ 5.2 ka BP [Werner et al., 2013]. Isostatic rebound following deglaciation led to ~ 50 m lower sea level at ~ 2.6 ka BP [Winkelmann and Knies, 2005].

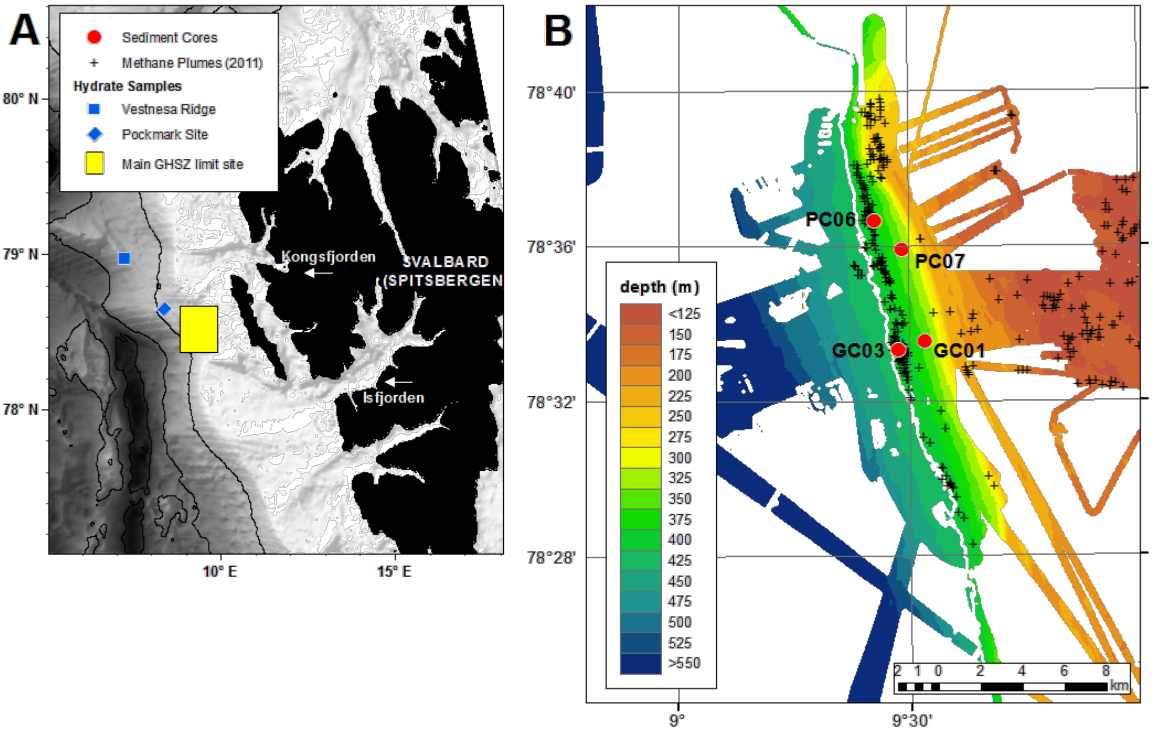

Figure 5-1 Map of the study site. (**A**) Regional map of the island of Svalbard, Spitsbergen, showing locations where hydrate samples have been recovered (Vestnesa Ridge and Pockmark Site, blue symbols), and the main GHSZ limit study site expanded in (**B**). Bathymetry in (**A**) is from GEBCO (The GEBCO_08 Grid, version 20100927, http://www.gebco.net) with 1000m depth contours, in (**B**) is shipboard data from cruise JR253, with the 400 m depth contour shown (solid white line). Seafloor methane flares (black crosses) observed during JR253 are shown in (**B**), along with sediment core locations (red circles).

5.3. Methods

5.3.1. Sampling

Sediment cores were collected during *RRS James Clark Ross* cruise 253 in August 2011. Locations are shown in *Figure 5-1*, and sampling sites are listed in *Table 5-1*. Two cores were collected within the area of seafloor methane seepage near the present-day landward limit of the GHSZ, at 386 m water depth (L-GC03) and at 374 m water depth (J-PC06), and two cores were collected further upslope landward of the current seafloor seepage area at 340 m water depth (E-GC01) and at 323 m water depth (K-PC07). Hereafter, the cores are referred to as “GHSZ-limit” cores and “landward” cores. The GHSZ-limit cores were recovered within a few meters of active methane seeps identified by shipboard sonar, while the landward cores were ~ 1 km from the nearest seeps.

Table 5-1 Locations of sediment cores, from *RRS* James Clark Ross cruise *JR253*. GC=gravity core, PC=piston core.

Station ID	Date Sampled	Lat (°N)	Long. (°E)	Water Depth (m)	Core Length (cm)	Distance from Seep (km)
E-GC01	06/08/2011	78:33.54	9:32.09	340	209	1.0
J-PC06	11/08/2011	78:36.66	9:25.53	374	224	0.02
K-PC07	13/08/2011	78:35.91	9:29.10	323	137	1.0
L-GC03	15/08/2011	78:33.30	9:28.64	386	162	0.01

Upon recovery, sediment cores were cut into ~ 50 cm sections and split lengthwise on deck. The working halves were immediately subsampled under a nitrogen atmosphere for methane and pore fluid analysis. For methane quantification, ~ 3mL of sediment was withdrawn using a cut-off plastic syringe and placed in a 20 mL glass vial containing 5 mL of 1 M sodium hydroxide. A subsample of sediment (~3 g) was placed in a pre-weighed plastic pot and stored at 4 ˚C for porosity analysis. Pore waters were extracted by centrifugation and filtered through 0.2 μm cellulose acetate filters. Subsamples for analysis of cations were stored in acid-cleaned low density polyethylene bottles and acidified to pH 2 with thermally distilled nitric acid. Subsamples for analysis of anions were diluted by a factor of 200 with Milli-Q water. Subsamples for sulphide were fixed with zinc acetate and stored at 4°C. Core sections were stored at 4 °C on board ship, and then at the British Ocean Sediment Core Research Facility (BOSCORF, National Oceanography Centre, Southampton, UK). Subsampling of the sediment solid phase for micropalaeontology was performed at 1 cm depth intervals at BOSCORF.

5.3.2. Methane

The methane content of sediment headspace gases was determined on-board ship by gas chromatography (Agilent 7890, 6 Ft HayeSep Q 80/100, stainless steel column). Analytical reproducibility, based on replicate analysis of standards (20 and 100 ppm, Air Products, UK), was better than ± 2 %. The detection limit was 0.5 ppm, which corresponds to a sediment pore water concentration of ~ 0.2 µM. Reported concentrations are minimum values because the samples may have degassed during recovery. Concentrations in pore fluids were calculated using porosities determined by the difference between the mass of the wet sample, and the mass of the sample after drying at ~ 60 °C overnight. Densities of the sediment and fluid were assumed to be 2.65 and 1.00 g cm^{-3}, respectively.

5.3.3. Pore water

Total alkalinity of pore waters was determined on board ship by titration with 0.02 M hydrochloric acid, using a mixture of methyl red and methylene blue as an indicator, and bubbling nitrogen gas through the solution. Analyses were calibrated against a seawater standard (IAPSO), and the reproducibility was better than ± 1.5 %. Cation concentrations were determined at the National Oceanography Centre (NOC), Southampton, UK, by inductively coupled plasma optical emission spectrometry (ICP-OES, Perkin Elmer Optima 4300DV). Accuracy and reproducibility were assessed by multiple (n = 3) analyses of certified reference material seawater (High Purity Standards™). Measured concentrations agree with certified values to within ± 3 %, and the reproducibility of the analyses was better than ± 1 % for all analytes. Anion concentrations were determined at the NOC by ion chromatography (Dionex ICS250). Reproducibility of replicate standards was better than ± 0.2 % for chloride, ± 2.5 % for bromide, and ± 1 % for sulphate. Hydrogen sulphide was determined spectrophotometrically by absorbance at 670 nm following addition of N,N-dimethyl-1,4-phenylenediamine dihydrochloride (colour reagent) and $FeCl_3$ (catalyst). The working hydrogen sulphide standard was calibrated daily by titration using a sodium thiosulphate titration standard (1.667 mM, OSIL environmental instruments and systems, UK). Reproducibility was better than ± 10 %, limit of detection was 10 µM.

5.3.4. Sediment carbon content

To quantify the total inorganic carbon (TIC) and total carbon (TC) content of the sediments, subsamples (~ 3 g) were dried in the oven at > 70 ˚C for > 24 hours, ground to a homogenous fine powder, and measured (~ 50 mg) using a carbon dioxide coulometer (model CM5012, UIC Inc.) equipped with an acidification module (model CM5130), and a furnace module (model CM5120). The concentration of total organic carbon (TOC) was determined by subtracting TIC from TC. Reproducibility of these analyses was better than ± 10 %.

5.3.5. Core scanning

The archive half of each sediment core was logged for magnetic susceptibility and x-ray fluorescence elemental composition at BOSCORF, UK. Scanning was performed following ~ 14 months storage under oxic conditions. The surface layer of the sediments was removed prior to scanning. Magnetic susceptibility (χ) was measured on an XYZ Multi-Sensor Core Logger (Geotek) at 0.5 cm intervals. Elemental abundance was determined using the ITRAX core-scanning X-ray fluorescence system (Cox Analytical; Croudace et al. [2006]) at 1 mm intervals (molybdenum x-ray tube, 30 second measurement time, 30 kV, 50 mA). Both data sets were processed to remove intervals where sharp changes in core surface height interfered with the detectors. Elemental abundance results are presented as total counts normalized to titanium (Ti) as a terrigenous input proxy [Calvert and Pedersen, 2007].

5.3.6. Foraminifera stable isotopes

Sediment samples for micropalaeontological analysis were dried, then weighed, soaked in distilled water and wet sieved at 44 μm. The residues were dried, and sieved at 500 μm. For oxygen and carbon stable isotope analyses monospecific benthic and planktonic foraminifera samples were hand-picked from the 44 – 300 μm size fraction. For each interval, 3-10 (benthic) or 10-30 (planktonic) tests were analysed after being gently crushed between clean glass plates to break open individual chambers and cleaned with methanol. The benthic species *Cassidulina neoteretis*, *Melonis barleanum*, and *Nonionella labradorica* and the planktonic species *Neoglobquadrina pachyderma sin.* were selected because they are abundant and common in this area. The preservation of tests was assessed by scanning electron microscopy (SEM, Hitachi TM3030 table top microscope). Selected benthic foraminifera samples from J-PC06 with very light carbon isotopic signatures were also analysed after carrying out an oxidative cleaning procedure. For oxidative cleaning, foraminifera tests were first gently crushed between clean glass plates, then subjected to repeated rinsing with Milli-Q water and sonication to remove clays. Tests were then cleaned in alkali buffered 1 % hydrogen peroxide at 100 °C for 5 minutes, twice. Finally, samples were rinsed and sonicated in 1 mM nitric acid, three times. This protocol was adapted from Panieri et al. [2012]; [2014b] and [2008] and Pena et al. [2005]. Micropaleontology work was performed at the National Research Council Institute of Marine Science (CNR, ISMAR, Bologna, Italy) and the Centre for Artic Gas Hydrate, Environment and Climate (CAGE, UiT the Arctic University of Norway, Tromsø, Norway).

Stable isotope values ($\delta^{13}C$ and $\delta^{18}O$) were determined using a Europa GEO 20-20 mass spectrometer equipped with an automated carbonate preparation device at the University of Southampton, and a ThermoFinnigan MAT252 mass spectrometer coupled to a CarboKiel-II carbonate preparation device at the Serveis Cientifico-Técnics of the University of Barcelona. Results are reported relative to the Vienna Pee Dee Belemnite (VPDB) and Vienna Standard Mean Ocean Water (VSMOW) standards in per mil (‰) notation for carbon and oxygen, respectively. External precision was better than ± 0.1 ‰ for both $\delta^{13}C$ and $\delta^{18}O$ based on analysis the NBS-19.

5.3.7. Radiocarbon dating

AMS radiocarbon dating was performed on 11 samples of mixed planktonic foraminifera (predominantly *N. pachyderma s*). A total weight of 1.3 to 2.8 mg of clean, well-persevered specimens were hand-picked from the 44 – 300 µm size fraction. The picked material was submitted for analysis at the National Ocean Sciences Accelerator Mass Spectrometry Facility (NOSAMS) radiocarbon laboratory at Woods Hole Oceanographic Institution (USA). Radiocarbon ages were calibrated using the marine calibration curve Marine13 (calibration curve maximum 46,806 yr BP; Reimer et al. [2013]) and the program Calib 7.0 [Stuvier and Reimer, 2014]. A regional reservoir correction (ΔR) of 7 ± 11 years was applied, as recommended by Bondevik and Gullikesen in Mangerud et al. [2006], following Panieri et al. [2014b].

5.4. Results

5.4.1. Core description

Photographs of sediment cores together with their lithological logs are shown in *Figure 5-2*. The major lithology of all cores is homogenous dark grey clay, with thin (<0.3 cm) horizontal laminae (Giuliana Panieri, personal communication 2013). All cores contain multiple sandy layers with sharp bottom and top contacts varying in width from ~2 to ~ 10 cm. Sand intervals with normal grading are interpreted as turbidites (Giuliana Panieri, personal communication 2013). Silt layers and isolated mud clasts are present in all cores except

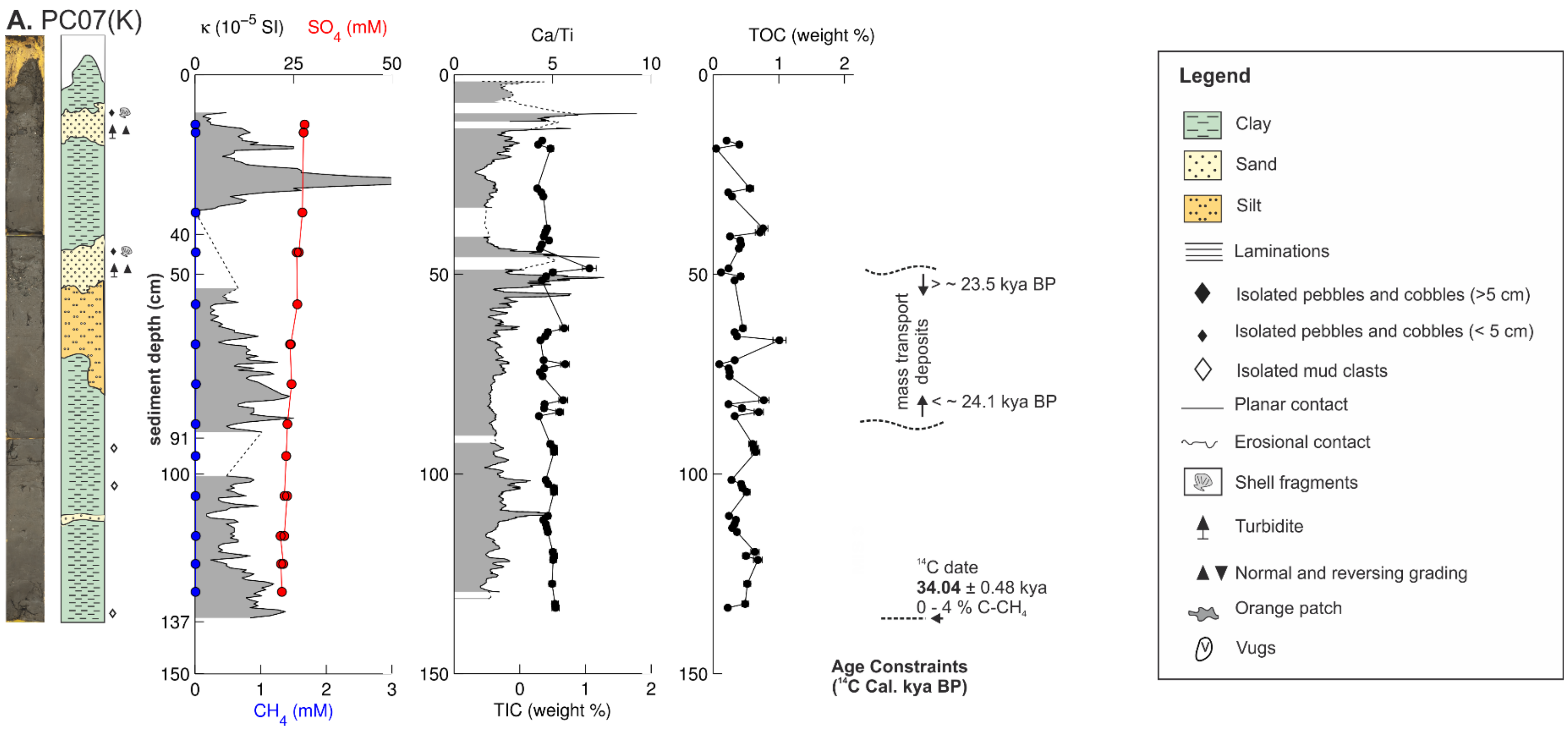

Figure 5-2 Sediment core photos, lithological logs, and other stratigraphic properties. From left to right: magnetic susceptibility (κ, grey fill), methane (CH_4, blue), pore fluid sulphate and sulphide (SO_4, red and H_2S, black – L-GC03 and J-PC06 only), planktonic foraminiferal carbon and oxygen isotopic signatures ($\delta^{13}C$, $\delta^{18}O$ circles: *N. pachyderma s.*, squares: mixed planktonic foraminiferal samples for radiocarbon dating), bulk sediment solid phase calcium (Ca) content (grey fill, ITRAX XRF counts as a ratio to titanium (Ti)), total organic and inorganic carbon (TIC, TOC). No planktonic foraminifera data are available for J-PC07. Core photos and lithological logs are courtesy of Giuliana Panieri. Gaps in shaded core-scanning data are due to the uneven surface of split core. Thick horizontal dashed black lines show the present-day SMTZ in L-GC03 and J-PC06. Stratigraphic age constraints shown on the right-hand side of each log are described in the text. The NGRIP ice core $\delta^{18}O$ stratigraphy [Andersen et al., 2004] is shown in **B**.

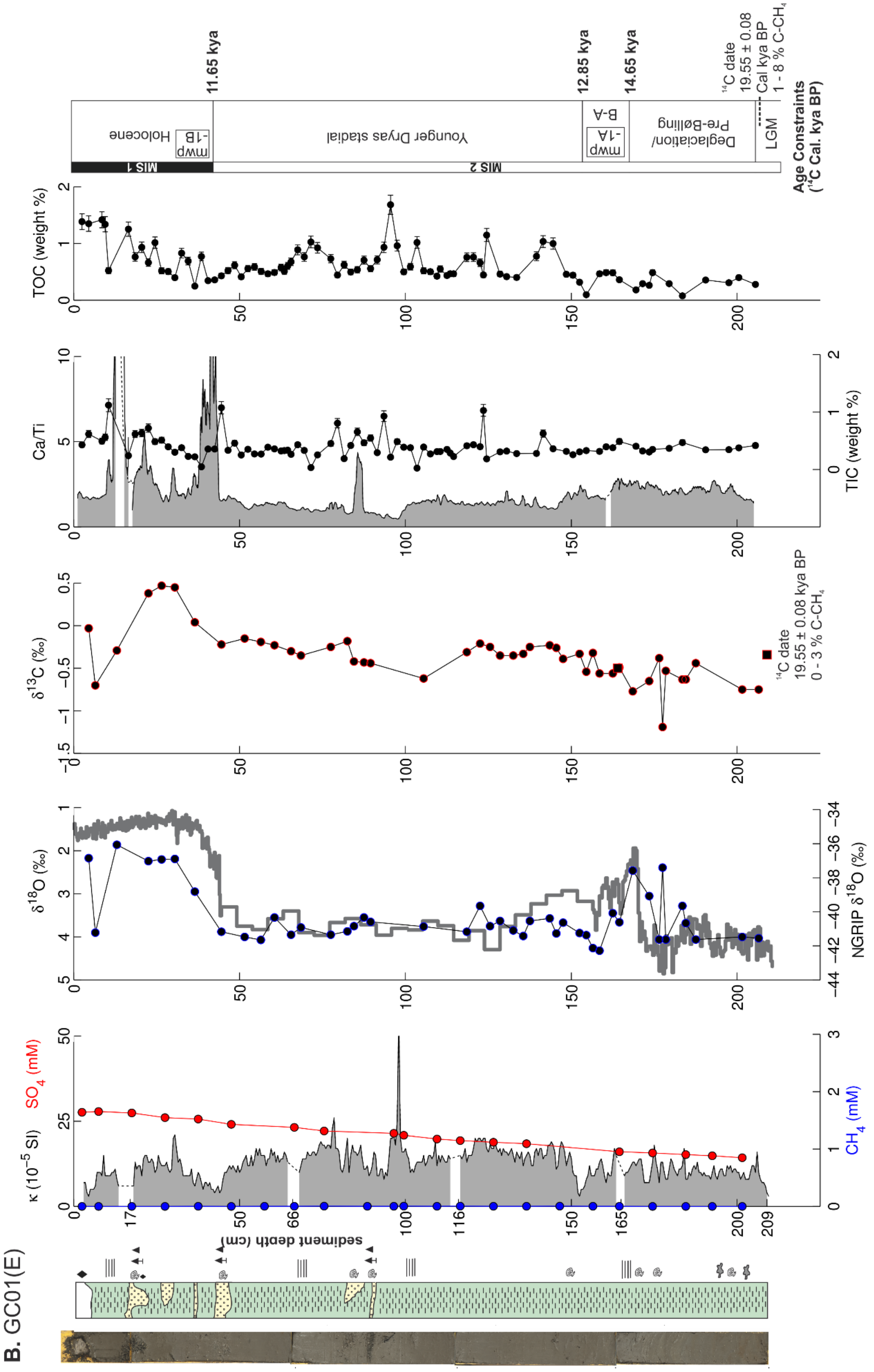

Figure 5-2 (continued)

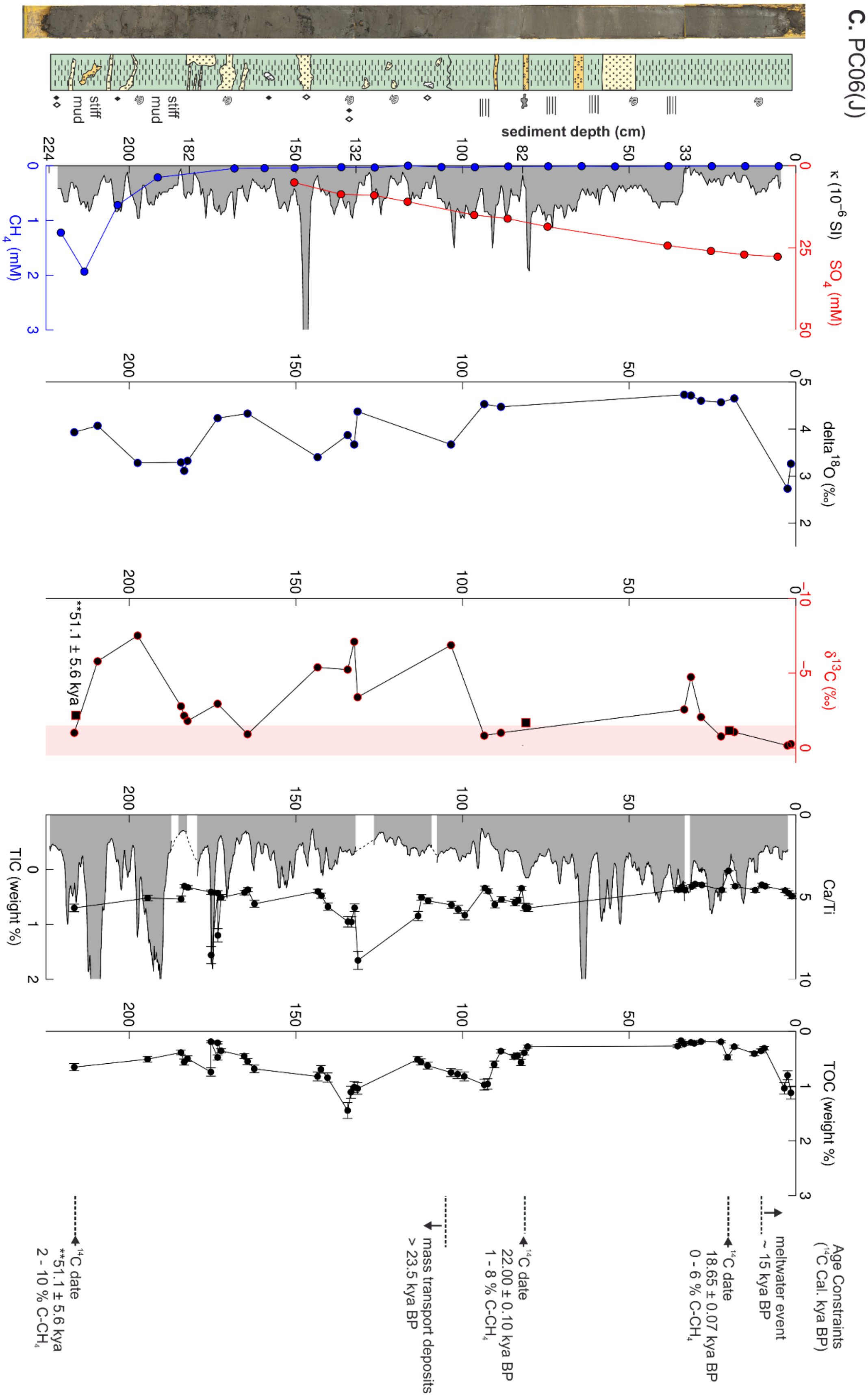

Figure 5-2 (continued)

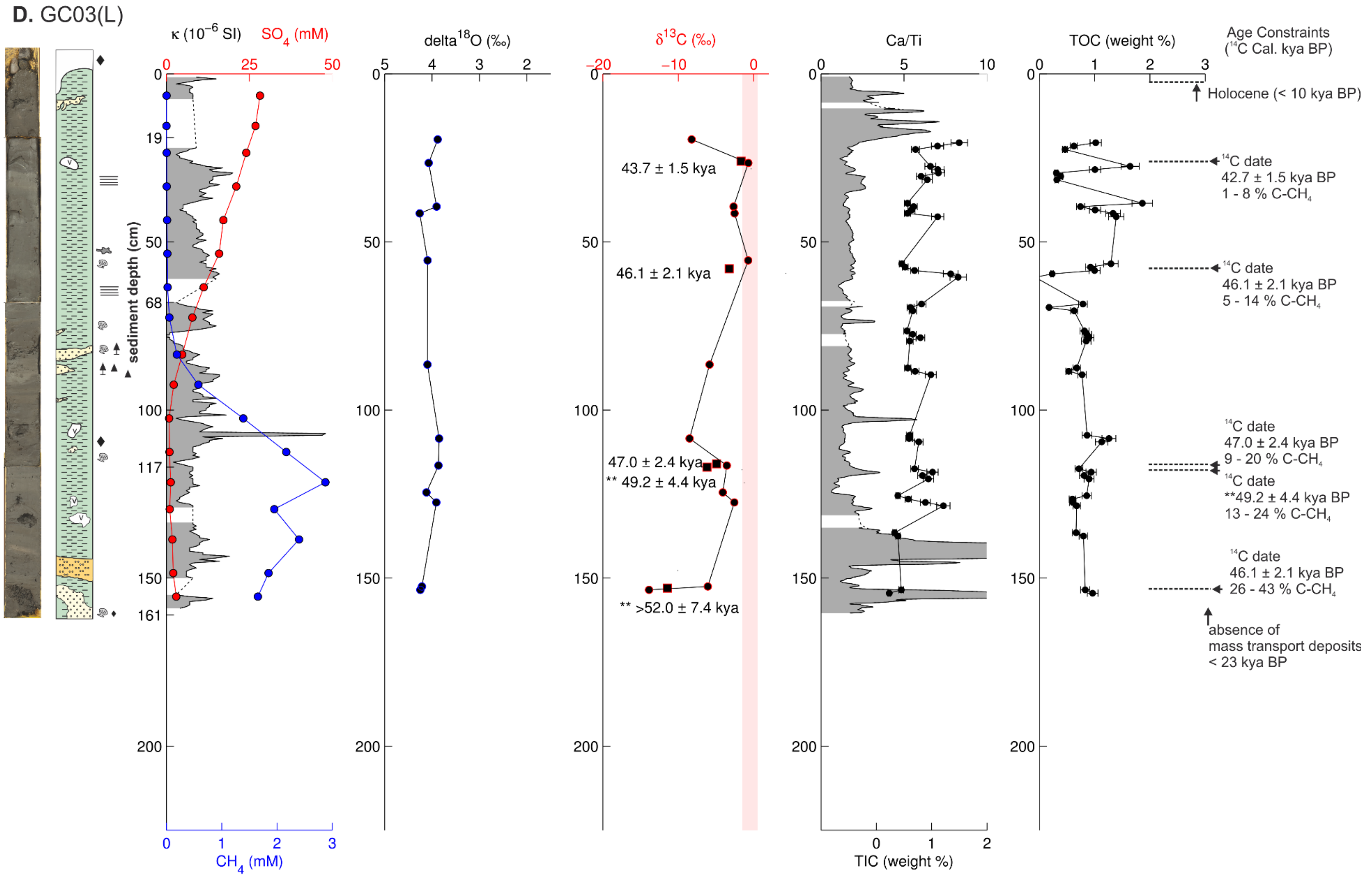

Figure 5-2 (continued)

E-GC01. Intervals containing shell fragments were observed in all cores, mostly in sandy sediments but also in clays in the two GHSZ-limit cores (L-GC03 and J-PC06). The GHSZ-limit cores contain voids throughout. The lowermost section of J-PC06 appears to have been moderately disturbed during sampling or recovery, possibly by expansion of gassy sediments. Isolated pebbles and cobbles occur at different intervals in E-GC01, J-PC06, and L-GC03, but are rare in K-PC07. Both E-GC01 and L-GC03 were recovered with large stones (>5 cm diameter) at the surface, while J-PC06 and K-PC07 contained large stones at the bottom. The top of K-PC07 appeared disturbed upon recovery. Carbonate clasts ~2-5 cm in size were recovered in J-PC06 at 147 cm and L-GC03 at 42, 58, 79, 83, 125, 129, and 153 cm.

5.4.2. Pore fluids

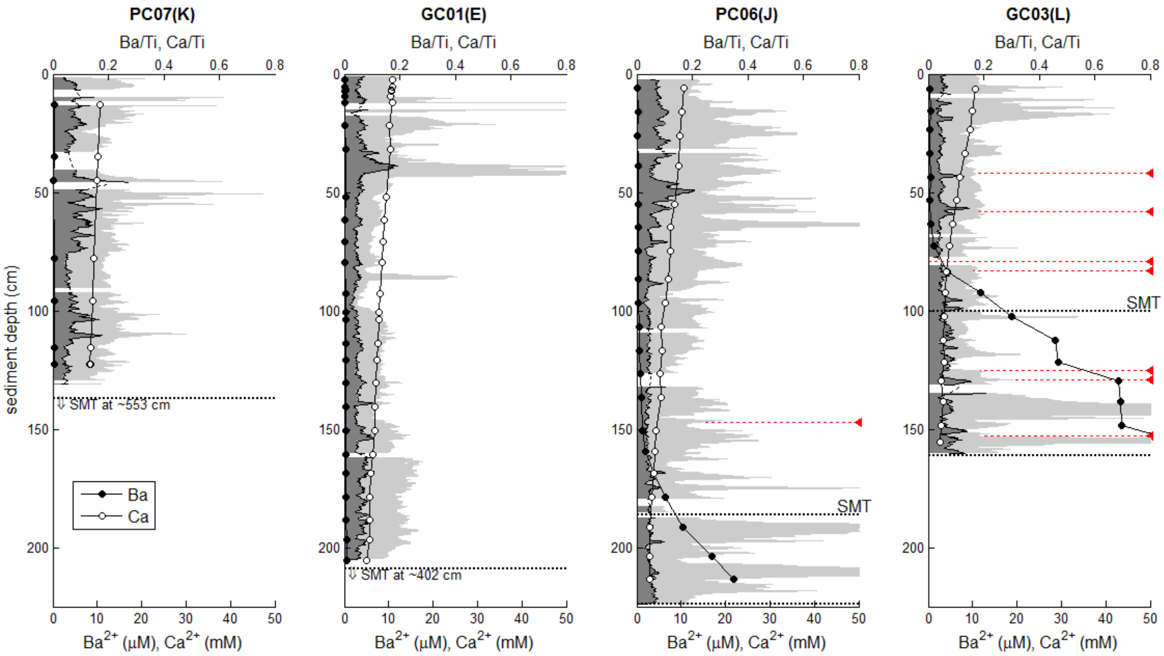

Figure 5-3 Profiles of pore fluid and bulk sediment barium (Ba) and calcium (Ca). Sediment data are given as relative abundance normalized to titanium (Ti) on the upper axis: Ca/Ti is in light grey, and Ba/Ti in foreground is dark grey with black outline. Gaps are due to gaps and roughness in the split core surface. Pore fluid data are shown in circles on the bottom axis: Ba in black and Ca in white. Horizontal lines indicate the depth of sediment recovered, and the depth of the SMTZ where it was encountered. Red triangles and dashed lines indicate depths from which carbonate nodules were recovered.

Pore fluid geochemistry is reported in detail in *Chapter 3*. Linearly decreasing sulphate profiles suggest that AOM at the SMTZ is mainly responsible for removal of sulphate, and that methane fluxes are at steady state [Borowski et al., 1996]. Depth profiles of methane, sulphate and sulphide (*Figure 5-2*) identify the depth of the present-day SMTZ: 186 cm in J-PC06 and 100 cm in L-GC03. In the landward cores the SMTZ is deeper than the length of sediment recovered. Extrapolated SMTZ depths are 4 m for E-GC01 and 5.5 m for K-

PC07. Sulphide was detected in pore fluids throughout GHSZ-limit cores, and highest concentrations (~3 mM) were recorded near the SMTZ. Sulphide was not measured in the landward cores.

Pore fluid calcium (Ca) and barium (Ba) profiles are shown in *Figure 5-3.* Dissolved calcium decreases linearly with depth towards the SMTZ from the surface value of ~ 11 mM to a relatively constant value of ~ 3 mM below the SMTZ, reflecting precipitation of calcium carbonate due to conversion of methane to bicarbonate via AOM. Barium concentrations are < 1 μM above the SMTZ and increase linearly with depth below the SMTZ reaching a maximum of 56 μM at the base of L-GC03, ~ 50 cm below the SMTZ. High Ba concentrations reflect dissolution of barite in the absence of pore water sulphate.

5.4.3. Carbon and calcium content of sediments

The total organic and inorganic carbon content of the sediments is shown alongside the solid phase calcium concentration (normalized to titanium) data in *Figure 5-2*. The poor correlation between calcium and total inorganic carbon, both expected to predominantly reflect the carbonate concentration of the sediments, is attributed to the relatively low resolution of the TIC data. E-GC01, which has the highest resolution TIC record, shows the closest correlation between Ca/Ti and TIC. TOC and TIC values are in broad agreement with previously reported data from nearby sites (e.g. Elverhøi et al. [1995]; Winkelmann and Knies [2005]).

The inorganic carbon content of landward cores is relatively constant with depth at ~ 0.5 weight % (average 0.4 ± 0.2 %), with isolated (single data point) peaks reaching 1.1 % and dipping below 0.05 % in a few samples. Some peaks occur in sandy intervals. TIC is higher and more variable in GHSZ-limit cores with an average of 0.6 ± 0.3 %, and a maximum value of 1.65 %. This difference may reflect the addition of methane-derived carbonate, or a difference in the proportion of terrestrial material between water depths. The average TIC content corresponds to 4 ± 2 wt. % $CaCO_3$, if all inorganic carbon is present as calcium carbonate.

The near-continuous Ca/Ti records show significant variability which is not present in the lower resolution TIC data. Large broad peaks are typical of sandy intervals. In E-GC01 and L-GC03 these are superimposed on a relatively low stable background concentration which increases in steps with depth. L-GC03 contains a series of small Ca peaks with cannot be attributed to sand layers, and which do not correlate with depths from which small carbonate concretions were recovered. J-PC06 and K-PC07 both have slightly higher and much more variable calcium content, partially attributable to their larger proportion of discontinuous sand and silt layers. Accumulation of authigenic calcium carbonate at the present-day SMTZ depth in GHSZ-limit cores is not evident, but may be obscured by the presence of sandy layers.

The overall average sediment TOC content is 0.6 ± 0.3 wt. %. The highest resolution record (E-GC01) shows a decrease in TOC with depth in the uppermost sediments, and notably lower values in the lowermost sediments. K-PC07 has relatively low TOC throughout with little fluctuation. TOC in GHSZ-limit cores J-PC06 and L-GC03 is variable, with a decrease in the upper sediments similar to E-GC01.

5.4.4. Magnetic susceptibility and solid phase iron and sulphur

Magnetic susceptibility profiles are shown in *Figure 5-2*. Data discontinuities are indicated in the figure by gaps in the record, which occur at all of the section boundaries (every ~50 cm), and also where the scanner was disturbed by rough sandy layers or gaps and changes in surface height related to the presence of stones and carbonate nodules. The core scanner detector (1 cm diameter) needs to lie on a flat surface, which was often not possible due to the uneven nature of the sediments. Additionally, changes in sediment volume – or height of the split cores, affect the magnitude of the magnetic response. Evidence for covariance of magnetic susceptibility and core section surface height was observed in some intervals.

The magnetic susceptibility is very low overall (median: 13 x 10^{-5} SI). This reflects the generally low magnetic content of the sediments, which are predominantly composed of clay minerals except for quartz dominated silt and sand intervals, with ~10-20 % carbonates (terrestrial sourced dolomite and siderite in addition to foraminiferal calcite and limestones from Svalbard; Andersen et al. [1996]; Elverhøi et al. [1995]). All cores contain strong peaks in magnetic susceptibility corresponding to sandy layers, but not all sandy layers are characterized by high magnetic susceptibility. No correlation of magnetic susceptibility records between cores is evident, nor is there a clear difference between the GHSZ-limit cores where AOM currently releases sulphide within the recovered sediments, and the landward cores where the record is less likely to have been altered by methane seepage.

Solid phase iron (Fe) and sulphur (S) do not correlate with features in magnetic susceptibility profiles, indicating that the magnetic signal is not related to the bulk Fe and S phases present in the core. Fe/Ti is relatively constant between and within cores, indicating that Fe reflects the bulk terrigenous sediment input. Sulphur is typically below the limit of detection (< ~ 245 ppm [Croudace et al., 2006]) with the exception of a single broad interval in each of the GHSZ-limit cores: ~ 7 to 38 cm depth in J-PC06, and ~ 135 to 148 cm in L-GC03. The large S/Ti peak in L-GC03 correlates with a large Ca/Ti peak which extends into and also beyond a sandy interval, while the J-PC06 high sulphur section does not.

Reduced sulphur species and other reactive ferrimagnetic components may have been subject to oxidation and/or other chemical transformations between sampling and core-scanning measurements (~ 14 months storage of split cores at 4 °C). Reduction in magnetic susceptibility of a variety of soil types has been documented during sediment sample storage (average ~20 % reduction in magnetic susceptibility in 1 year; Oldfield et al. [1992]) and metastable greigite is expected to be particularly susceptible to loss during storage [Snowball and Thompson, 1988]. However, considering the expected instrument-specific differences in magnetic susceptibility, average values for these cores are in good agreement with available data for the West Spitsbergen margin (e.g. Jessen et al. [2010]).

5.4.5. Foraminiferal stable isotopes

Planktonic foraminiferal calcite stable isotope data are shown in *Figure 5-2*. Benthic $\delta^{13}C$ results are summarized in *Figure 5-4*, with complete $\delta^{13}C$ and $\delta^{18}O$ results given in *Supplementary Figures D-1* (depth profiles) and *D-2* (cross-plots).

Core E-GC01, the highest resolution record, shows low *N. Pachyderma s.* $\delta^{18}O$ values of ~2 ‰ in near-surface sediments, and relatively steady values of ~4 ‰ throughout most of the rest of the core with the exception of an ~ 30 cm interval with lower values close to those recorded near the core surface. Corresponding carbon isotope data vary within the narrow range of – 1 to 0.5 ‰, although one sample has lower $\delta^{13}C$ (-1.19 ‰), and a slightly higher $\delta^{18}O$ value of 2.39 ‰. *N. pachyderma s.* was not analysed in the other landward core (K-PC07). GHSZ-limit cores were sampled at lower depth resolution. Planktonic carbon isotopic data clearly indicate the incorporation of methane-derived carbon in the foraminiferal tests, with $\delta^{13}C$ values of as low as - 13.9 ‰. The extremely ^{13}C-depleted samples occur in intervals between samples with normal marine $\delta^{13}C$ values (> -1 ‰). While some intervals show sharp variation in both $\delta^{18}O$ and $\delta^{13}C$, this is not always the case. There is no overall relationship between *N. pachyderma s.* $\delta^{13}C$ and $\delta^{18}O$.

Benthic foraminiferal $\delta^{13}C$ values show a similar pattern. Landward cores exhibit a narrow range of values typical of the normal marine environment (- 1.9 to 0.3 ‰), while benthic foraminifera from GHSZ-limit cores are significantly more ^{13}C-depleted (-27.8 to -0.016 ‰). In both J-PC06 and L-GC03, the magnitude of negative isotopic excursions increases with depth, however, intervening intervals have higher to normal δ^{13}C. In many intervals, some species show normal isotopic signatures, while others are extremely ^{13}C-depeleted. Defining "normal" intervals as those in which no species have low δ^{13}C (< -2 ‰) yields: 0 – 22 cm, 83 - 94 cm and > 216 cm in J-PC06, and 27 - 38 cm and 135-136 cm in GC03. Given the large variability with depth and the relatively low depth resolution, the current data set is not expected to record all transitions between normal and ^{13}C-depleted conditions. Samples close to the depth of the present-day SMTZ have benthic foraminiferal δ^{13}C values ranging from normal (-1.45 ‰) to significantly ^{13}C-depeleted (-15 ‰).

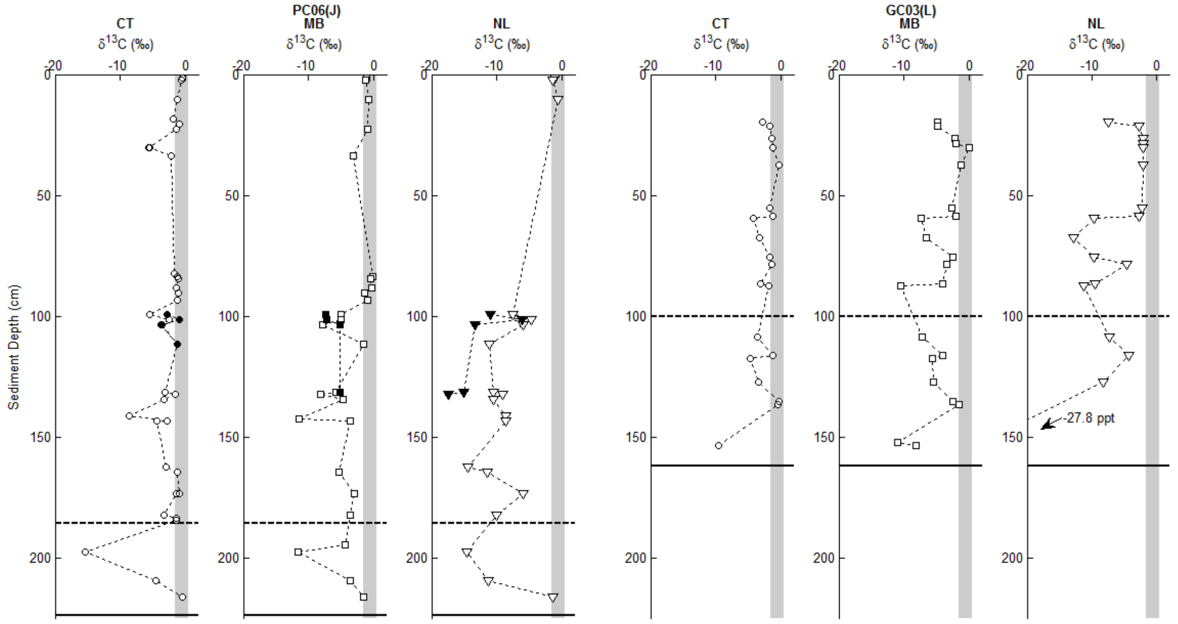

Figure 5-4 Benthic foraminiferal δ^{13}C of GHSZ-limit cores: J-PC06 (left) and L-GC03 (right). *C. neoteretis* (CT, circles), *M. barleanum* (MB, squares), and *N. labradorica* (NL, triangles). Filled symbols are samples which were subject to the more extensive oxidative cleaning procedure. Grey vertical bars indicate the range of values obtained in landward cores (E-GC01 and K-PC07). Dashed horizontal lines indicate the depth of the present-day SMTZ, solid horizontal lines indicate core length.

In the landward cores, there is a consistent pattern between the three species analysed: values for *C. neoteretis* are slightly heavier than for *N. labradorica* which is in turn consistently heavier than *M. barleanum*. The pattern of relative isotopic signatures between the three species observed in landward cores does not hold for GHSZ-limit cores. While *C. neoteretis* is generally heaviest, in some intervals it has the lightest carbon isotopic signature. *N. labradorica* is generally isotopically lightest with intermediate δ^{13}C observed for *M. barleanum*. In a core containing gas hydrates and evidence of seafloor methane seepage from nearby Vestnesa Ridge *C. neoteretis* was found to be isotopically lighter than *M. barleanum* [Panieri et al., 2014b].

The oxidatively cleaned benthic foraminifera samples from selected ^{13}C-depleted intervals in J-PC06 do not present a consistent δ^{13}C difference from bulk foraminiferal calcite (normally-prepared) results. All oxidatively cleaned *N. labradorica* samples were more ^{13}C-depleted than the normally-prepared samples from the same depth intervals, by 1.4 to 8.3 ‰. *C. neoteretis* samples show the opposite result, with oxidatively cleaned tests being closer to normal marine values than the normally-prepared samples from the same intervals by 0.1 to 2.6 ‰. Oxidative cleaning of *M. barleanum* produced both more ^{13}C-depleted results (by 2.4 and 2.2 ‰), and less ^{13}C-depleted results (by 2.6 and 0.7 ‰) compared to the normally prepared specimens.

We applied only the clay removal and oxidative steps of the cleaning procedure, omitting the reductive step reported elsewhere [Panieri et al., 2012; Panieri et al., 2014b; Pena et al., 2005], in an effort to reduce loss of primary calcite and retain enough mass for isotopic measurements despite the low availability of specimens. This may have prevented complete removal of an inner “kutnahorite-like” ($CaMn^{2+}(CO_3)_2$) authigenic mineral phase observed in foraminifera from the manganese-enriched Panama basin [Pena et al., 2005]. Application of both oxidative and reductive cleaning procedures to foraminifera from methane seepage environments, has previously yielded consistently higher δ^{13}C values (e.g. ~ 3.5 ‰ increase in δ^{13}C of oxidative and reductively cleaned *C. neoteretis* [Panieri et al., 2014b]), with the more intensively cleaned tests interpreted to represent the primary calcite signal.

Evaluation of the efficiency of cleaning remains difficult. While SEM imaging is often used to identify diagenetic overgrowths, it has been shown to be ineffective in some cases [Torres et al., 2010]. We were unable to image cleaned tests because the low foraminiferal abundance limited the available material. The presence of secondary overgrowths on un-cleaned individual foraminifera tests from both ‘normal’ and ^{13}C-depleted intervals in J-PC06 was investigated visually by SEM. *N. labradorica* specimens which appeared well-preserved under the light microscope show some evidence of possible corrosion of the outer test, while the inner test of some specimens reveal a thick and continuous crystalline overgrowth (*Figure 5-5*). This inner layer is consistent with the Mn-Mg rich carbonate layer described by Pena et al. [2008]. Planktonic *N. pachyderma s.* show evidence for crystalline overgrowths at all depths (*Figure 5-6*).

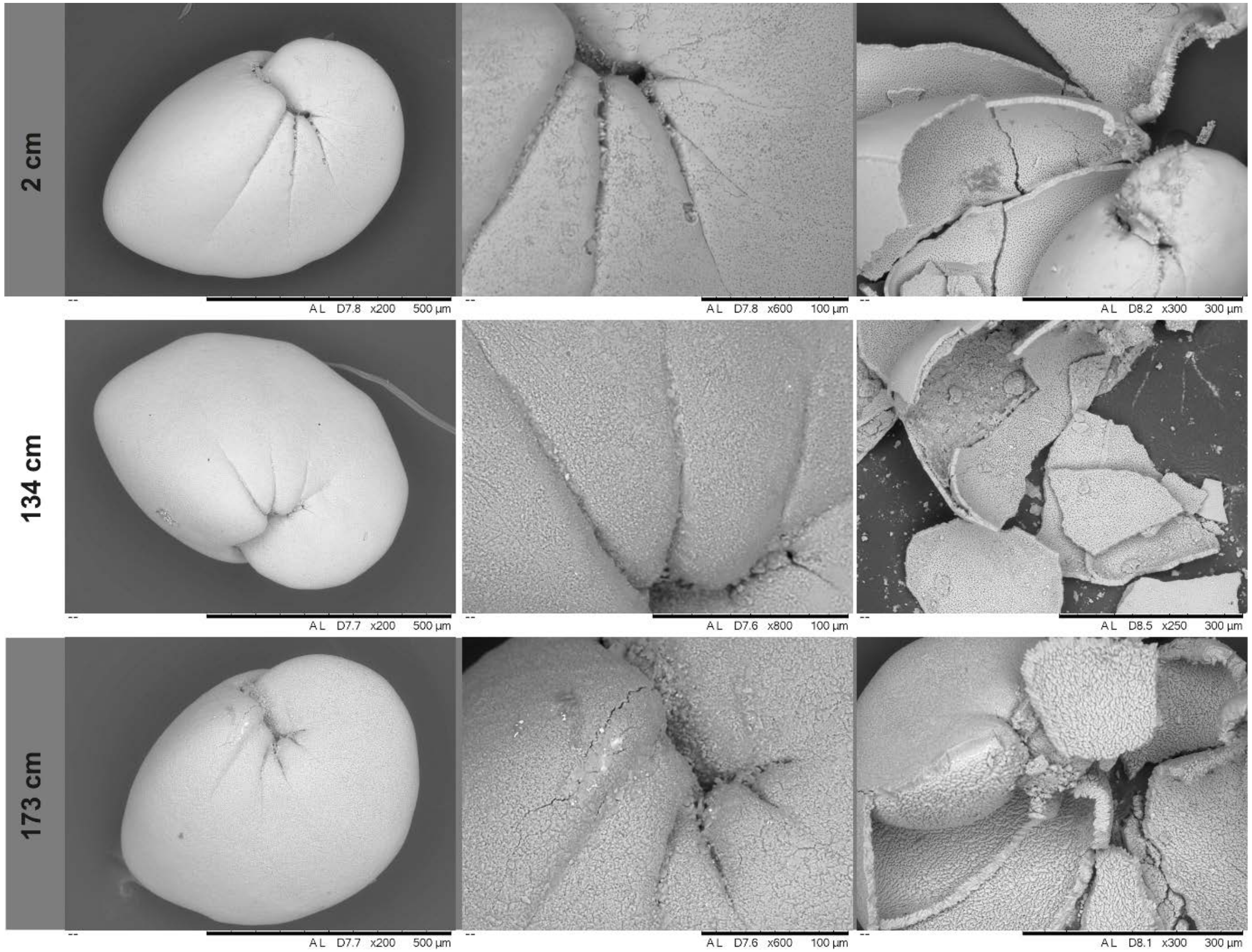

Figure 5-5 *N. labradorica* from J-PC06. Tests from shallow sediments (2 cm) have normal marine δ^{13}C values of > -2 ‰, while very light isotopic signatures (-3 to -10 ‰) were observed in tests from deeper sediments (134 and 173 cm sediment depth). Crystalline growths are observed on the inner test wall (right hand panel) of deeper specimens, in contrast to the well-preserved pore structure of the near-surface specimens.

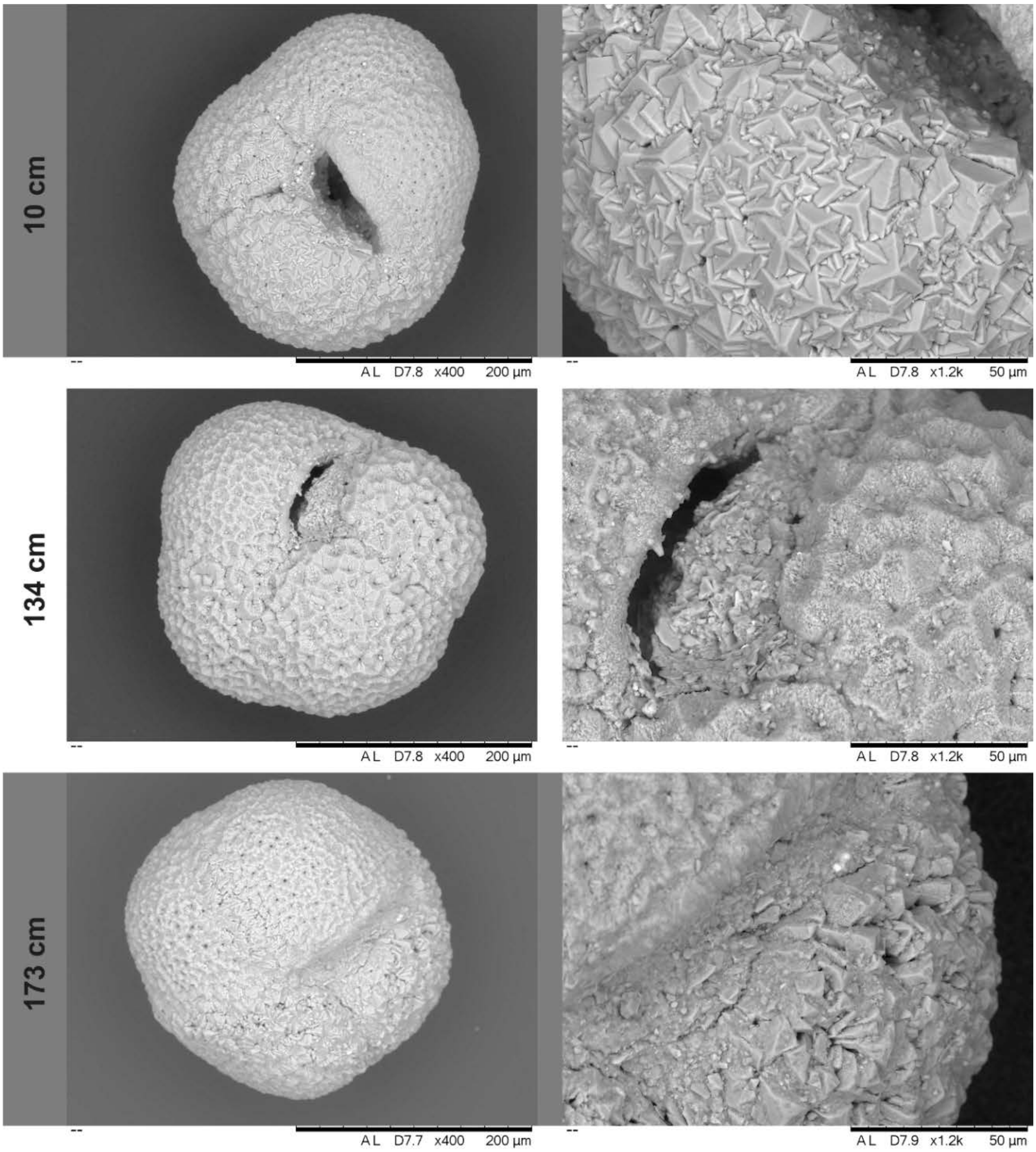

Figure 5-6 *N. pachyderma s.* from J-PC06. Tests from shallow sediments (10 cm) have normal marine $\delta^{13}C$ values of > -2 ‰, while very light isotopic signatures (-3 to -10 ‰) were observed in tests from deeper sediments (134 and 173 cm sediment depth).

5.4.6. Radiocarbon dating

Eleven radiocarbon dates were obtained for mixed planktonic foraminifera (predominantly *N. pachyderma s.*) for the four cores (*Table 5-2, Figure 5-2*). The low carbon isotopic signatures (-1.68 to -11.44 ‰) and very old radiocarbon dates (uncorrected AMS ^{14}C ages 40.3 to > 52 ka) in some samples imply a significant contribution from fossil methane-derived carbon. Since the landward cores show no evidence of primary or diagenetic influence of methane-derived carbon in down-core planktonic and benthic $\delta^{13}C$ profiles, the dates for J-PC06 and E-GC01 are assumed to reflect stratigraphic ages. In E-GC01, the younger of the two radiocarbon dates is from the deeper sample. Neither sediment interval shows evidence of non-sequential sediment deposition, and $\delta^{13}C$ values do not indicate the presence of methane-derived carbon. We reject the older date, and note that while the difference between the two dates is significant, in the context of the coarse age control of this study the choice is relatively inconsequential.

For GHSZ-limit cores, assuming that foraminiferal calcite carbon formed from a mixture of ‘normal’ surface ocean DIC and diagenetic overprinting with methane-derived carbon, the measured radiocarbon activity and $\delta^{13}C$ must reflect a mass balance between these two carbon sources. Present-day seep methane has a $\delta^{13}C$-CH_4 of -51 to -55 ‰ [*Chapter 3;* Sahling et al., 2014], with heavier gas seeping into shallower waters on the shelf (-45 ‰; *Chapter 3*; Sahling et al. [2014]) and found in shallow sediment gas hydrates further offshore (-45.6 ‰ at Vestnesa Ridge; Fisher et al. [2011]; Smith et al [2014]; -54.6 ‰ in a pockmark at ~900 m water depth; Fisher et al. [2011]). Geochemical and geophysical data point to a fossil thermogenic methane source [Thatcher et al., 2013; *Chapter 3*]. Mixing with small proportions of biogenic carbon produced in shallower sediments is likely to provide a small non-fossil contribution to seep carbon [Pohlman et al., 2009]. For a diagenetic carbonate end member, we use data from bulk sediments and carbonate concretions (including solid filling in a gastropod) from the seep region at the sediment surface and buried down to 240 cm depth with $\delta^{13}C$ values of -27 to -41 ‰ [Berndt et al., 2014]. The primary foraminiferal calcite end member is taken from the maximum and minimum $\delta^{13}C$ values for *N. pachyderma s.* in E-GC01: -1.2 and 0.5 ‰. The resulting minimum and maximum contributions of methane-derived carbonate diagenetic overprinting on the planktonic foraminiferal samples used for radiocarbon dating are given in *Table 5-2*.

The simple mass balance consideration of the radiocarbon dating data yields two interesting results. The first is that samples with the same $\delta^{13}C$, and therefore the same assumed

Table 5-2 Radiocarbon dates and $\delta^{13}C$ values for mixed planktonic foraminifera samples analysed at the National Ocean Sciences Accelerator Mass Spectrometry Facility (NOSAMS) radiocarbon laboratory at Woods Hole Oceanographic Institution (USA). Dates were determined using the Calib 7.0 software using the Marine13 calibration curve and reservoir correction of 7 ± 11 years. Minimum and maximum contributions of methane-derived carbon are calculated from mass balance, assuming with methane-derived carbonate has $\delta^{13}C$ values of between -41 and -27 ‰, and 'normal marine' planktonic foraminiferal carbonate has $\delta^{13}C$ values of between -1.2 and 0.5 ‰.

Core	Depth (cm)	NOSAMS Accession #	Uncorrected AMS ^{14}C age (kyr)	Corrected age (2σ, yr BP)	Mean corrected age (kyr BP)	$\delta^{13}C$ (‰ VPDB)	minimum % $C\text{-}CH_4$	maximum % $C\text{-}CH_4$
E-GC01	164	OS-114142	18.05	21000-21650	21.35 ± 0.09	-0.50	0	4
	213	OS-114143	16.60	19250-19800	19.55 ± 0.08	-0.34	0	3
K-PC07	132	OS-114152	30.80	33600-35300	34.40 ± 0.48	-0.60	0	4
L-GC03	26	OS-114144	40.3	41400-46200	43.7 ± 1.5	-1.68	1	8
	58	OS-114145	43.1	43000-49800	46.1 ± 2.1	-3.24	5	14
	116	OS-114146	44.3	43600-50000	47 ± 2.4	-4.92	9	20
	117	OS-114147	49.2 ± 4.4	-	-	-6.20	13	24
	153	OS-114148	>52 ± 7.4	-	-	-11.44	26	43
J-PC06	20	OS-114149	15.80	18500-18800	18.65 ± 0.07	-1.16	0	6
	81	OS-114150	18.55	21700-22300	22.0 ± 0.1	-1.69	1	8
	216	OS-114151	51.1 ± 5.6	-	-	-2.18	2	10

contribution from methane-derived carbon, have dramatically different ages: 46.1 ± 1.5 Cal ka BP at 58 cm depth in L-GC03, and 22.0 ± 0.1 Cal ka BP at 81 cm depth in J-PC06. The younger J-PC06 date shows the expected small methane-derived carbon effect from the δ^{13}C data. The very old L-GC03 date appears to suggest a significant contribution of methane derived carbon, which is not consistent with its δ^{13}C value. It seems unlikely that the sediments at this site reflect erosion or a depositional hiatus spanning the entire ages of the two landward cores recovered. The second interesting result of the mass balance is that despite the expected overprinting of methane-derived fossil ^{14}C signature on the stratigraphic record, both GHSZ cores show increasing age with depth. This is consistent with the accompanying decrease in δ^{13}C values, and may simply reflect that by chance, the eight samples selected for dating (5 in L-GC03 and 3 in J-PC06) were more affected by seepage at depth, which is not generally true in either core for the higher resolution *N. pachyderma s.* record. However, it allows the possibly of a stratigraphic component to the methane-derived carbon signal which warrants further investigation.

5.4.7. Stratigraphic controls

The obvious presence of ongoing and past methane seepage and shallow SMTZ in the study area essentially prohibits strict chronostratigraphic constraints from the available data. Radiocarbon dates reflect incorporation of fossil methane-derived carbon, magnetic susceptibility records are compromised by the irregular surface of split cores and may be altered by presence of sulphide, and the inorganic and calcium carbonate content of the sediments may reflect precipitation related to AOM rather than depositional variability. In addition, previous work on sediment cores in the area reveals highly variable sedimentation rates and broad hiatuses especially on the upper slope (e.g. Elverhøi et al. [1995]; Jessen et al. [2010]; Winkelmann and Knies [2005]; Zamelczyk et al. [2014]). Finally, the planktonic foraminiferal oxygen isotope curves in Nordic Seas are expected to reflect varying input from isotopically light melt water rather than the global average signal [Mangerud et al., 1998].

We adopt the following local stratigraphic constraints for the upper continental margin off Western Svalbard from the literature:

i. A decrease in planktonic δ^{18}O from ~ 4 ‰ to ~ 2 ‰ at the beginning of the Holocene, ~ 10 ka BP [Andersen et al., 1996; Elverhøi et al., 1995; Jessen et al., 2010; Mangerud et al., 1998],

ii. Spikes in δ^{18}O towards Holocene values at about 15 ka BP related to a local meltwater event, preceded by a decrease in TOC and simultaneous increase in $CaCO_3$ until about 20 ka BP [Andersen et al., 1996; Elverhøi et al., 1995; Lucchi et al., 2013],

iii. Mass transport deposits with low magnetic susceptibility at ~ 24-23.5 ka BP consisting of dark coarse, unsorted sediment with gravel sized clasts in a sticky, clayey, silty matrix [Jessen et al., 2010].

A basic stratigraphy based on these constrains and the radiocarbon dates is shown in *Figure 5-2*. The NGRIP ice core δ^{18}O record [Andersen et al., 2004] is shown alongside E-GC01, as well as a rough age model following Panieri et al. [2014b]. The NGRIP record is tied to the E-GC01 data by: (1) the shift in *N. pachyderma s.* δ^{18}O values in the uppermost part of the core which interpreted to represent the beginning of the Holocene, (2) the spikes in *N. pachyderma s.* δ^{18}O values which are interpreted to reflect meltwater-pulse-1A during the Bølling-Allerød interstadial, and (3) the core-base radiocarbon date of 19.55 ± 0.08 Cal ka BP, assuming a linear sedimentation rate and that the core top represents the present day. Resulting estimated sedimentation rates are 4 cm kyr^{-1} during the Holocene, and ~90 cm kyr^{-1} during the Younger Dryas stadial. The sedimentation rate for the Holocene is in good agreement with those previously reported on the upper Svalbard continental margin [Andersen et al., 1996; Elverhøi et al., 1995].

Age constraints for the other three cores are poor. In K-PC07, a thick sand and silt interval is interpreted to represent mass transport deposits from ~24 – 23.4 ka BP, in agreement with the core bottom radiocarbon date of 34 ± 0.48 Cal ka BP. This gives a low average sedimentation rate of 4 cm kyr^{-1}, which may imply that upper Holocene and Younger Dryas sediments are missing. This is consistent with the stratigraphy of nearby cores, which also show significant sediment hiatuses at the surface [Elverhøi et al., 1995; Jessen et al., 2010]. In J-PC06 we also infer that surface sediments have been lost either during sampling or due to winnowing by high bottom water currents as described by Winkelmann and Knies [2005]. Taking the upper sediment radiocarbon date (18.65 ± 0.07 Cal ka BP) with normal δ^{13}C (-1.16 ‰) to be unaffected by methane-derived carbon, we interpret the low δ^{18}O values of *N. pachyderma s.* in the upper part of the core to represent the end of meltwater pulse 1A during the Bølling-Allerød interstadial (~ 15 ka BP), and the underlying thick sediment interval of stiff mud containing numerous shells and isolated pebbles to represent the mass transport deposits of ~24 to 23.4 ka BP. There is no good age control for the base of this core. Finally, in L-GC03, all radiocarbon dates show a significant contribution from methane-derived carbon. The low resolution *N. pachyderma s.* δ^{18}O record appears to indicate that Holocene sediments are either absent or restricted to the upper ~ 20 cm. High calcium in the upper 20 cm is consistent with the Holocene and could indicate good recovery of surface sediments, but may also reflect seep-related authigenic carbonate formation. Conversely the very old radiocarbon age associated with near-normal δ^{13}C at 26 cm depth apparently indicates a significant loss of recent sediments; if the carbonate is only 1-8 % methane-derived carbon then the actual sediment date should be very close to the measured value (43.7 ± 1.5 Cal ka BP). This seems unlikely based on records from nearby cores. There is a drop in average TOC after ~ 60 cm depth which could be associated with the period from 15 – 20 ka BP. This would be consistent with uranium-thorium ages in carbonates from a core recovered less than 100 m away (13 – 11 ka at 60-120 cm depth [Berndt et al., 2014]), assuming the carbonates (which have δ^{13}C values of < - 35 ‰), reflect authigenic carbonate precipitation at the surface.

5.5. Discussion

5.5.1. Evidence for methane seepage from sediment-based proxies of AOM

None of the sediment-based proxies for methane seepage which have been described at other sites hosting methane hydrates and/or seafloor methane seeps record the presence of AOM in the sediments recovered offshore Western Svalbard either now, or in the past. This could indicate:

i. Lack of observation due to discontinuous measurements and/or sediment recovery,
ii. The sediments at this location are not suitable for recording the presence of AOM or for preserving an AOM signal,
iii. Methane fluxes are variable, such that the depth of the SMTZ is constantly shifting, and AOM signals have insufficient time to build up in the sediments.

We cannot exclude the first possibility: that we have failed to observe geochemical signals which are present due to gaps in core scanning records because of the uneven surface of the cores, or as a result of chemical alteration of the sediments during storage in an oxic environment. However, it seems unlikely that we failed to sample signals of AOM in all four cores for these reasons. Importantly, there is evidence of both ongoing AOM within the sediment recovered in the GHSZ limit cores, and a sediment record of past AOM in incorporation of isotopically light methane-derived carbon in foraminiferal calcite (see

Section 5.5.2). We therefore propose that our results support (ii) and (iii), and discuss the implications for each proxy.

5.5.1.1. Iron oxides

The observation of bulk sediment proxies of AOM requires not only active AOM, but also the availability of appropriate reactive solid phase species. The generally low and variable magnetic susceptibility reported in this and other studies for the Western Svalbard margin implies low concentrations of ferromagnetic iron oxides. It follows that despite high pore fluid sulphide concentrations, the lack of reactive iron phases indicates that iron remobilization at the SMTZ is limited. The variable (noisy) magnetic susceptibility records of all four cores also means that dissolution or precipitation of small quantities of iron oxide is impossible to distinguish from the background. High inputs of terrigenous material and the high ITRAX detection limit for sulphur also reduce the likelihood of observing minor dissolution and accumulation in the sediment records. The two intervals of high (detectable) solid phase sulphur in the GHSZ-limit cores could be related to the presence of iron sulphides, but are just as likely to be depositional features, particularly in L-GC03 where high solid phase sulphur occurs in a distinct sandy interval. We therefore conclude that magnetic susceptibility and iron (oxyhydr)oxide reductive dissolution is not an effective proxy for methane seepage offshore Western Svalbard.

5.5.1.2. Barite fronts

Accumulation of barite fronts requires the availability of a labile barite phase beneath the SMTZ. In the GHSZ-limit cores, increasing dissolved barium concentrations with depth beneath the STMZ provide evidence for active barite dissolution in the region of zero sulphate and re-precipitation above the SMTZ. However, there is no corresponding decrease in bulk sediment barium content below the STMZ due to dissolution, or significant Ba/Ti peaks at or above the SMTZ due to re-precipitation (*Figure 5-3*). This suggests that the labile barite proportion of the sediments is small, or that the depth of the STMZ has recently shifted. In the GHSZ-limit cores, old barite fronts within the sediments recovered but below the present-day SMTZ depth may have dissolved following upwards migration of the SMTZ due to increases in methane fluxes or by burial to below a stable STMZ depth. However, in the landward cores where the present-day SMTZ is below the depth of sediment recovered, dissolution of shallow barite fronts related to potential higher methane fluxes in the past is not expected.

Assuming that the linear dissolved barium profiles represent a diffusive flux (F_D) of barium to the SMTZ and applying Fick's first law of diffusion (*Equation 5-5*; Boudreau, [1997]), with a barium diffusion coefficient in free solution (D_0) of 144.7 cm^2 yr^{-1} (3 °C; Boudreau, [1997]), and the measured average porosity (φ) of 0.47, the supply of barium is 1.0×10^{-4} mol m^{-2} yr^{-1} in J-PC06 and 1.8×10^{-4} mol m^{-2} yr^{-1} in L-GC03. This is of similar magnitude to barite fluxes reported elsewhere (Congo Fan: $0.2 - 1 \times 10^{-3}$ mol m^{-2} yr^{-1}; Kasten et al. [2012], Blake Ridge: $0.6 - 4 \times 10^{-2}$; Snyder et al. [2007a], Japan Sea: $0.7 - 1 \times 10^{-4}$ mol m^{-2} yr^{-1} Snyder et al. [2007b]). Therefore, it seems unlikely that the absence of barite fronts can be attributed to unavailability of labile barite in the sediments offshore Svalbard.

$$F_D = D_0/(1-ln(\varphi^2)) \bullet \varphi \bullet \Delta C/\Delta z \qquad (5\text{-}5)$$

Re-precipitation of barium above the SMTZ would lead to accumulation of < 0.2 mg Ba kg^{-1} yr^{-1}, assuming a bulk sediment density of 2.65 g cm^{-3}. If the landward cores represent sediments unaffected by AOM, as suggested by their normal foraminiferal carbon isotopic records, then barite accumulation in excess of the variability observed in the landward cores, in which Ba/Ti can be up to six times the median value, is required to provide a proxy record of AOM. If background sediment barium concentrations are at the low end of those reported elsewhere where barium accumulation is observed (Congo Fan: ~ 0.2 g kg^{-1}; Kasten et al. [2012], Blake Ridge: ~0.4 g kg^{-1}; Dickens [2001], Japan Sea: 0.07 – 0.1 g kg^{-1}; Snyder et al. [2007b]), then the formation of a clear barite front in the sediment record offshore Svalbard would take ~ 5,000 years. We therefore infer that the depth of the SMTZ below the seafloor has not been fixed for this length of time.

The fixing of the SMTZ depth within a narrow sediment interval over thousand-year timescales requires both stable methane fluxes and a slow sedimentation rate. Offshore Namibia, accumulation of large barite fronts is attributed to fixing of the SMTZ in sediments following a dramatic decrease in sedimentation rates at the beginning of the Holocene [Riedinger et al., 2006], while the absence of a barite front despite pore fluid evidence for barite mobilization is attributed to high sedimentation rates on the flank of Blake Ridge [Snyder et al., 2007a]. Sedimentation rates on the upper continental shelf off Svalbard are low in the Holocene (~ 3 cm kyr^{-1}). High bottom water currents may also have prevented barium accumulation [Winkelmann and Knies, 2005], suggested by the absence of recent sediments in J-PC06. During colder periods where ice extended closer to the shelf edge, the sedimentation rate was much higher (~ 100 cm kyr^{-1}), during which time sediment burial would have moved sediments through the SMTZ too rapidly for barium to accumulate.

Sedimentation rates support the conclusion that methane fluxes have not remained stable for periods of longer than ~ 5,000 years during the Holocene.

5.5.1.3. Authigenic carbonate precipitation

The solid phase carbonate records (TIC, Ca) also have a high and variable background which implies that a large accumulation of authigenic carbonate related to AOM would be required to produce a record of AOM. This variable background is caused by changes in the provenance of sediments deposited during glacial advance and retreat in this area (e.g. Andersen et al. [1996]; Elverhøi et al. [1995]). While the bulk carbonate data do not show accumulation at the depth of the present-day STMZ, the slightly higher average carbonate content in the GHSZ-limit cores could reflect disseminated precipitation of authigenic carbonate. A relationship between the bulk calcium content and AOM is supported by the presence of carbonate nodules in the GHSZ-limit cores (*Figure 5-3*), but not in the landward cores. Further analysis of carbonates (elemental and isotopic composition), could confirm their association with methane-derived carbon, and indicate if they formed at the surface in times of high methane flux which favours aragonite precipitation, or at depth at the SMTZ, which favours high magnesium calcite precipitation [Bayon et al., 2007; Nöthen and Kasten, 2011; Ritger et al., 1987]. Their depth distribution is not closely tied to the present-day SMTZ depth, implying accumulation during periods of lower and higher methane fluxes, and possibly methane seepage at the surface. Carbon isotope analyses of carbonates in a sediment core taken within 100 m of L-GC03 confirm that the carbonates are related to methane seepage, and increasing age with depth (from 3 ka BP at the surface to 23 ka BP at 120-240 cm below the seafloor) suggests that these carbonates formed at the seafloor [Berndt et al., 2014].

5.5.2. δ^{13}C of foraminiferal calcite

5.5.2.1. Absence of ^{13}C-depleted foraminiferal calcite in landward cores

The primary result of the foraminiferal isotope data is that the landward cores contain no evidence for input of methane-derived carbon. It is possible that this is due to inadequate sampling resolution, low deposition and erosion, or discontinuous core recovery, but given that the GHSZ-limit cores, in which significant ^{13}C-depletion was observed, had similar sediment recovery and lower sampling resolution, this is unlikely. The implications of this result are two-fold. First, low δ^{13}C-DIC bottom and surface waters were not present in the vicinity of the landward cores during the past ~ 20,000 to 35,000 years. The 1 km distance between the landward sampling sites offshore Svalbard and the GHSZ-limit sites where there is clear evidence of methane-derived carbon incorporation into foraminiferal calcite places an upper limit on the spatial range of the proxy in this setting. The second implication is that the SMTZ has never been located within the sediments recovered at these water depths (320 – 340 m), preventing methane seepage in the immediate vicinity of the core sites during the last ~ 20,000 to 35,000 years. Foraminiferal calcite provides an excellent nucleation site for carbonate precipitation, so is expected to be quite sensitive to carbonate precipitation where active AOM provides calcium carbonate supersaturation [Pena et al., 2008; Torres et al., 2010].

5.5.2.2. ^{13}C- and ^{14}C -depleted planktonic foraminiferal calcite

Planktonic foraminifera calcify in surface waters, and therefore cannot record the carbon isotopic composition of methane released at the seafloor in the absence of a strong (regional) ^{12}C-enriched DIC signal. Because there is no evidence for low δ^{13}C-DIC waters in the landward cores ~ 1 km away, the incorporation of ^{13}C and ^{14}C-depleted carbon in *N pachyderma s.* tests must be due to diagenetic overprinting. Secondary calcite precipitation may occur immediately after the planktonic foraminiferal tests were deposited in near-surface sediments during intervals of seafloor methane seepage, or after significant burial when sediments pass through carbonate saturated pore waters resulting from AOM at the SMTZ. Mass balance calculations indicate that up to 55 % of carbonate in *N pachyderma s.* with δ^{13}C = -14.6 ‰ is authigenic. However, SEM images of the outside part of *N pachyderma s.* tests do not show obvious evidence for diagenetic overprinting.

Post-depositional diagenetic overprinting will also affect the benthic foraminiferal δ^{13}C record. In benthic foraminifera, primary calcite may additionally incorporate methane-derived carbon during periods of active seepage, as demonstrated by low δ^{13}C values measured in living *C. neoteretis* tests from the Håkon Mosby Mud Volcano in the Barents Sea [Mackensen et al., 2006]. Intervals with low benthic foraminiferal δ^{13}C values also have low planktonic foraminiferal δ^{13}C in the GHSZ-limit cores. Thus planktonic foraminifera may provide a proxy for methane seepage even in the absence of low shelf-wide δ^{13}C-DIC values.

Low foraminiferal δ^{13}C values cannot be attributed to authigenic carbonate precipitation due to AOM at the depth of the present-day SMTZ because there is no relationship between δ^{13}C and proximity to the depth of sulphate depletion. Crucially, intervals with lowest δ^{13}C values are separated by intervals with normal marine δ^{13}C values. While ^{13}C-depletion below the present STMZ could indicate sediment burial following authigenic carbonate precipitation, intervals with low $\delta^{13}C$ above the present-day STMZ require that higher methane fluxes in the past pushed the SMTZ closer to the seafloor, potentially allowing methane seepage at the surface. Subsequent retreat of the STMZ to its present-day depth would have caused the reaction zone to pass through the intervening sediments. As low $\delta^{13}C$ values are not continuous, $\delta^{13}C$ must be a proxy for methane seepage rather than SMTZ retreat [Panieri et al., 2014b]. However, if there are rapid changes in sedimentation rate, or the depth of the SMTZ (e.g. due to a change in methane flux), then there may be insufficient time for accumulation of ^{13}C-depleted calcite overgrowths. The presence of a foraminiferal-$\delta^{13}C$ record of methane-derived carbon in the absence of other geochemical STMZ proxies (barite fronts and magnetic susceptibility drawdown) suggests that the time required for measureable carbonate precipitation on foraminiferal tests is relatively short.

5.5.2.3. Benthic foraminiferal $\delta^{13}C$

^{13}C-depletion of planktonic foraminifera confirms the occurrence of diagenetic overprinting with ^{13}C-depleted carbonate. The more extensive cleaning procedure was expected to remove this secondary calcite to leave behind the carbon isotopic signature of the primary calcite. However, even oxidatively-cleaned foraminifera have $\delta^{13}C$ values ~30 – 50% lower than the normal marine value in the majority of samples across all three species. This means either that the oxidative cleaning was not 100% effective, or that the primary calcite also incorporated ^{13}C-depleted carbon. As the degree of diagenetic overprinting in similar environments is ~10-20 % (e.g. Martin et al. [2007] Millo et al. [2005b]), our data strongly suggest that both primary and secondary calcite incorporate methane-derived carbon signatures offshore Western Svalbard. The primary calcite $\delta^{13}C$ therefore records a stratigraphic record of methane seepage over the past ~ 30,000 years.

If the oxidatively cleaned foraminiferal results represent the pure primary signal, the foraminifera tests are more ^{13}C-depleted (- 6 to - 17 ‰ for *N. labradorica*, and -5 to - 7 ‰ for *M. barleanum*) than minimum values reported for living foraminifera in modern seep environments (-4.2 ‰; Panieri et al. [2014a], -7.5 ‰; Mackensen et al. [2006], -15.3 ‰; Martin et al. [2010], and -21.2 ‰; Hill et al. [2004]). The variable differences between oxidatively cleaned and normally-prepared samples from the same depth intervals could result from the averaging of several individuals (4 – 15 specimens) recording calcification over a broad time interval with variable methane fluxes and variable overgrowth precipitation. Within-species differences between single specimen $\delta^{13}C$ in living foraminifera from active seep sites are high (up to 12 ‰; Hill et al. [2004]).

The apparently species-specific effects of the cleaning procedure on $\delta^{13}C$ indicates that both primary and secondary foraminiferal calcite methane-derived carbon records may be species-specific. Pena et al. [2008] show that the more porous *Globigerinoides ruber* accumulates more secondary calcite than *Neogloboquadrina dutertrei* because their shell architecture provides better nucleation sites for authigenic carbonate precipitation. The larger difference between oxidatively cleaned and normally-prepared $\delta^{13}C$ in *N. labradorica* could indicate that these larger tests (compared to *C. neoteretis* and *M. barleanum*) allow more secondary overgrowth. Studies of living foraminifera at active seep sites show that incorporation of ^{13}C-depleted carbon in the test due to methane seepage is also species-dependent (e.g. Mackensen et al. [2006]). This is attributed to differences in the ability to calcify in an active seep environment, different vital effects leading to species-specific disequilibrium with pore fluid DIC, and/or different microhabitats with different $\delta^{13}C$-DIC. A detailed study on shallow sediment cores from 50 sites on the continental margin off Northern Svalbard and from the Arctic Ocean found similar depth habitats for *N. labridorica* and *C. neoteresis* [Wollenburg and Mackensen, 1998], and *M. barleanum* is also an infaunal species [Wollenburg and Kuhnt, 2000], so all three are expected to calcify in a similar pore fluid environment. This is consistent with results for the landward cores, which have similar $\delta^{13}C$ for all three species. Differences in the pattern of $\delta^{13}C$ between these three species in the ^{13}C-depleted intervals compared to the normal marine environment (landward cores), suggests that species-specific effects related to methane seepage are being record.

The most ^{13}C-depleted *N. labradorica samples* have consistently lower $\delta^{13}C$ in oxidatively cleaned samples, the generally least ^{13}C-depleted *C. neoteretis* have consistently higher $\delta^{13}C$ in oxidatively cleaned samples relative to normally-prepared tests, whereas *M. barleanum* display mixed results. The relationship between the amount of ^{13}C-depletion in normally-prepared samples and the magnitude and direction of change due to oxidative cleaning suggests that the material removed during cleaning has an intermediate $\delta^{13}C$: more ^{13}C-depleted than normally-prepared *C. neoteretis* $\delta^{13}C$ and less ^{13}C-depleted than normally-prepared *N. labradorica*. This implies that *N. labradorica* record a strong primary methane-derived carbon signal, while *C. neoteretis* are in disequilibrium with the low $\delta^{13}C$-DIC seep environment. More research is required to better understand the types of secondary calcite overprinting in methane seep environments and the efficiency of different cleaning procedures in order to fully interpret species-specific variability.

5.5.3. Relationship between methane seepage and hydrate stability offshore Western Svalbard over the last ~ 30,000 years

5.5.3.1. Absence of methane seepage in landward cores

Hydrate accumulation in sediments at 340 m water depth is expected to have occurred as recently as 1970, with the hydrate stability zone predicted to have extended up to ~ 300 m water depth during the last glacial period [Ferré et al., 2012; Thatcher et al., 2013]. The absence of a sedimentary record of past methane seepage at 340 m (E-GC01) or 323 m (K-PC07) water depth therefore implies that any upslope advance of the GHSZ was not accompanied by methane seepage through the sediments towards the seafloor. This could indicate that periods of colder conditions were too short to allow accumulation of enough hydrate to release sufficient methane for it to reach the seafloor. While heterogeneity in sediment permeability has been shown to play a role in controlling the position of methane seeps in this area, there is no indication of a change in the lithology (and therefore permeability) of sediments between the GHSZ-limit and the landward sites (< 1 km upslope) [Sarkar et al., 2012].

Given that the present-day seafloor seeps at the GHSZ-limit are separated by an average of 100-150 m [Thatcher et al., 2013], it is possible that seepage occurred landward of the current GHSZ limit but is not sampled in our cores. For example, Panieri et al. [2014a] observed that benthic foraminifera at ~ 240 m distance from active seeps do not record low $\delta^{13}C$ values. Furthermore, near-surface sediments in J-PC06 appear unaffected by methane seepage that occurs ~ 200 m away. This is likely a reflection of poor recovery of the near-surface sediments. However, the clear record of methane seepage in both GHSZ-limit cores over thousand year timescales means that small-scale spatial variability is likely to be captured if the seep density at the landward site was similar to that at the GHSZ limit today.

5.5.3.2. Sediment record of methane seepage at the GHSZ limit

As temperature and sea level changes in the past shifted the landward limit of the GHSZ, the region where seafloor seepage is presently observed would have moved in and out of the hydrate stability field (e.g. Ferré et al. [2012]; Marín-Moreno et al. [2013]). While methane seepage within the GHSZ is observed (e.g. Vestnesa Ridge; Panieri et al. [2014b], Blake Ridge offshore Souteastern North America; Panieri et al. [2014a], Hydrate Ridge offshore Northwestern United States; Torres [2003]), the formation of solid hydrate is expected to partly (if not completely) prevent seepage of methane at the seafloor. The episodic nature of the methane seepage record, if not indicative of small-scale variability in seep locations, supports intermittent seepage potentially related to temperature-driven hydrate dynamics. Differences in the magnitude of ^{13}C-depletion between intervals of seepage may be related to venting characteristics (e.g. methane flux and duration; Panieri et al. [2014b]).

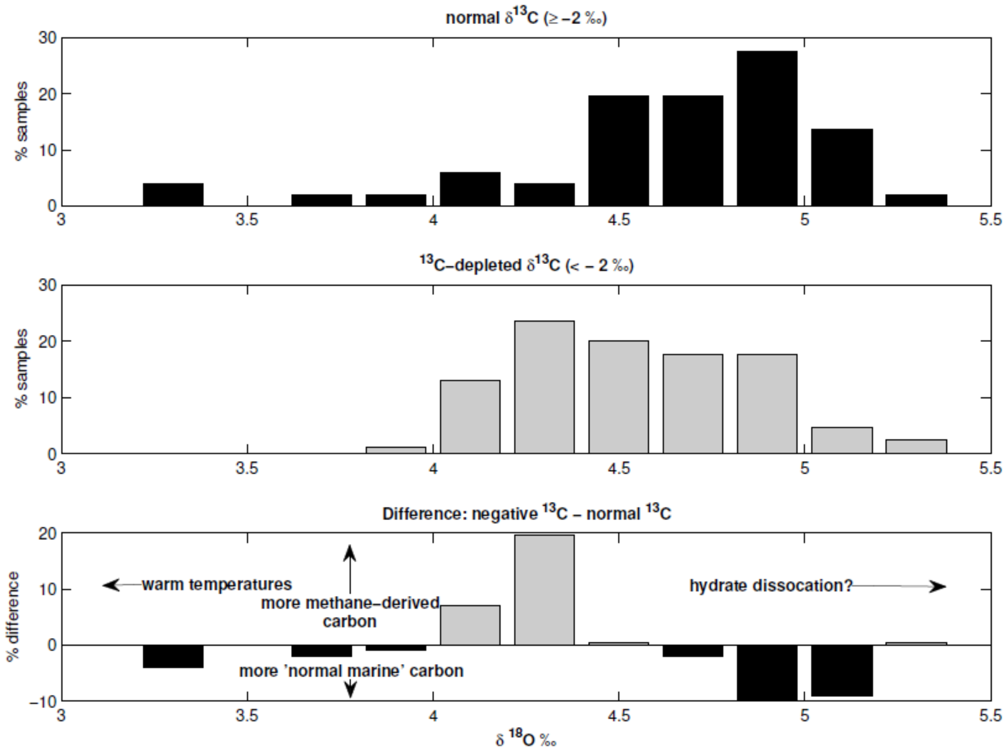

Figure 5-7 Histograms of the percentage of δ^{18}O values associated with normal marine δ^{13}C values (> -2 ‰ upper panel), ^{13}C-depleted δ^{13}C values (central panel), and the difference between the two (lower panel) in benthic foraminiferal calcite (*N. labradorica*, *C. neoteretis,* and *M. barleanum*) in GHSZ-limit cores (L-GC03 and J-PC06). Bin size is 0.2 ‰. There is no correlation between the δ^{18}O and δ^{13}C of individual samples ($R^2 <$ 0.1 for all species).

Crucially, if bottom water temperature is the dominant control on methane seepage, we would expect to see a correlation between foraminiferal δ^{18}O and foraminiferal δ^{13}C (e.g. Cook et al. [2011]), with lower δ^{18}O (higher temperature) accompanied by lower δ^{13}C (methane release). However, Mackensen et al. [2006] note that ^{18}O-enrichment of pore fluids can result from release of water from hydrate dissociation, which could potentially mask any shift in δ^{18}O related to warming of bottom waters. Since shifts in hydrate stability are expected to influence the occurrence, but not necessarily the magnitude, of δ^{13}C excursions, we also checked for differences between δ^{18}O of ^{13}C-depeleted (δ^{13}C < -2 ‰) samples and those with normal marine δ^{13}C values (*Figure 5-6*). Methane-related carbon isotopic signatures are more commonly observed at slightly lower δ^{18}O than normal marine δ^{13}C, but are not observed at the lowest δ^{18}O values. This could indicate that because seepage is related to hydrate dynamics, it reflects a transitional temperature regime: when temperatures warm after cold periods have allowed the accumulation of hydrate on the upper slope. Therefore, when bottom waters are warmest, methane seepage may have shifted further downslope, or stopped because all of the accumulated methane had already been released.

The low sampling resolution and poor age control on the GHSZ-limit cores, due to alteration of the stratigraphic record by the high methane flux environment, prohibits linking $\delta^{13}C$ events to specific climate intervals.

5.6. Conclusions

The sedimentary record in the vicinity of the GHSZ limit of the Western Svalbard upper continental margin provides new insight into the history of seafloor methane seepage in this climate-sensitive environment, as well as the applicability of different proxies of AOM in this setting.

- Magnetic susceptibility, i.e. the alteration of primary iron oxides following the release of sulphide by AOM at the SMTZ, does not record the depth of the SMTZ in this setting.
- The absence of barite fronts associated with the depth of the SMTZ indicates that the depth of the SMTZ has not been maintained for periods of longer than ~ 5,000 years.
- Despite the presence of authigenic carbonate nodules and methane-derived (^{13}C-depleted and fossil) authigenic carbonate overgrowths on foraminiferal calcite, there is no evidence in the bulk sediment inorganic carbon record or sedimentary calcium record for accumulation of carbonate due to AOM at the depth of the SMTZ.
- Neither planktonic nor benthic foraminifera in sediments at 340 and 320 m water depth, ~ 1 km upslope of the present day seafloor methane seeps near the GHSZ limit, record a methane-derived carbon isotopic signature. Therefore, upslope migration of the GHSZ during times of colder ocean bottom water temperatures has not been accompanied by methane seepage at the seafloor. Furthermore, a regional depletion in bottom or surface seawater $\delta^{13}C$-DIC related to the release of methane from hydrate dissociation is not recorded in the sedimentary record for the last ~ 20,000 to 30,000 years.
- Immediately upslope of the present-day GHSZ limit, where present-day active seafloor methane seepage occurs, both planktonic and benthic foraminiferal $\delta^{13}C$

> record episodic seafloor methane seepage in the past. The foraminiferal oxygen isotope record indicates that the relationship between episodes of seafloor methane seepage, bottom water temperature, and hydrate dissociation, is complex.

Our study highlights that the effects of methane seepage on foraminiferal $\delta^{13}C$ records are variable. For example, we report the presence of a methane-derived carbon record from planktonic foraminifera, as did Millo et al. [2005a]; [2005b] offshore Greenland, but this was not observed at Blake Ridge [Panieri et al., 2014a]. We also observe that *M. barleanum* is consistently more ^{13}C-depleted than *C. neoteretis* in seep environments, while Panieri et al. [2014b] observed the opposite trend at Vestnesa Ridge. Furthermore, applying an extensive oxidative cleaning protocol to ^{13}C-depleted benthic foraminifera was found to yield species-specific results, while similar cleaning has previously been reported to consistently remove the more ^{13}C-depleted authigenic carbonate overgrowth and produce $\delta^{13}C$ closer to normal marine values (e.g. Panieri et al. [2012]; [2014b]). Further work is required to continue to improve our understanding of the ability of foraminifera to record primary and secondary $\delta^{13}C$ signals related to methane-derived carbon and methods for differentiating, and towards deconvoluting these signals.

Several important questions are also raised pertaining to the relationship between seafloor seepage aligned immediately upslope of the present-day GHSZ limit offshore Western Svalbard, and temperature driven hydrate destabilization. Migration of the GHSZ limit does not appear to have caused focused seafloor seepage further upslope of the current seepage area in past periods of colder bottom water temperatures during the last ~ 30 thousand years, implying that as yet unidentified lithological controls may distinguish the present-day seepage region from subsurface gas flow regimes immediately upslope. Within the area of present-day seafloor seepage, temperature-driven GHSZ limit migration may have led to episodic seafloor seepage. When the GHSZ limit was further upslope, methane hydrate would have accumulated, blocking gas escape from the seabed. Increased temperatures and downslope GHSZ limit retreat would have released gas and led to seafloor seepage, but only if sufficient methane had accumulated during the preceding cold interval. After the accumulated methane was released, upward methane fluxes may have decreased enough to allow AOM to consume all methane beneath the seafloor so that no seepage occurred, despite the downslope position of the GHSZ limit. Therefore, the absence of a simple relationship between foraminiferal ^{13}C-depletion and bottom water temperature does not preclude a link between seafloor seepage and methane release from gas hydrate.

Unfortunately, the dynamic and locally variable depositional environment of the sediments offshore Svalbard provides a challenging setting for the application of sedimentary proxies, which is compounded by the effects of high methane fluxes in shallow sediments on the stratigraphic record. We are therefore unable to correlate episodes of seafloor methane seepage with local or global climate events. Furthermore, the evolution of the methane-hydrate stability zone offshore Western Svalbard at > 2,000 years is unknown, but will reflect a complex relationship between water temperature and sea level due to ice formation and ice loading.s

CHAPTER 6

Concluding remarks

Contents

6.1. Summary

This thesis presents a comprehensive geochemical characterization of the sediments and water column in the vicinity of seafloor methane seepage at the landward limit of the gas hydrate stability zone on the upper continental margin offshore Western Svalbard. This site has been the focus of a number of ongoing multidisciplinary studies since the seafloor seeps were discovered in 2008. The results of this dissertation represent a significant contribution to understanding this methane seepage system both now and in the past.

The isotopic and molecular composition of the gas indicates subsurface gases and seafloor bubble plumes, are made up of thermogenic methane which has migrated laterally from offshore. This same gas forms hydrate in shallow sediments further down the continental slope.

Sediment pore water chemistry profiles on the upper slope reveal active anaerobic methane oxidation which efficiently consumes methane before it reaches the seafloor, except near seeps where highly focused subsurface methane flow allows bubbles to escape into the water column. Modelling of pore water chemistry profiles shows that diffusive methane fluxes are significantly lower than fluxes of methane escaping the seafloor in the gas phase at bubble plume sites. This demonstrates that focusing of gas flow in small cracks and fractures in the low-permeability glaciogenic surface sediments provides a mechanism for gas to escape anaerobic oxidation. Shallow subsurface methane fluxes are largely at a steady sate outside the hydrate stability zone, while in sediments where hydrate may be present subsurface diffusive methane fluxes appear to be more dynamic. Hydrate destabilization at the base of the stability zone due to warming ocean bottom waters is likely responsible for the observed increased methane fluxes.

The distribution of methane in the water column is characterised by elevated concentrations in the bottom waters above seafloor seeps. This is due to dissolution of gas bubbles; no methane remains in the gas phase more than 200 m above the seafloor, and highest dissolved concentrations are restricted to the bottom 75 m. Methane concentrations in intermediate and surface waters are much lower, but are also supersaturated with respect to the atmosphere. Northward-flowing bottom water currents carry the methane-saturated bottom waters away from the seafloor seeps before it has a chance to mix vertically upwards into surface waters. In order for methane from seafloor seeps to reach the atmosphere, enhanced vertical mixing in the water column is therefore required. In the absence of such mixing, methane will eventually be aerobically oxidized at depth – making a minor contribution to the dissolved carbon dioxide inventory. Supersaturation of surface waters is attributed to intense seafloor seepage at < 100 m water depths on the continental shelf, where gas bubbles inject methane directly into the surface mixed layer and the overlying atmosphere. This marine methane source is not large enough to increase atmospheric methane concentrations nor to affect the carbon isotopic signature of methane in the immediate vicinity of the study site.

The sedimentary record shows that high methane fluxes have been a feature of sediments at ~400 m water depth in this area for more than 20,000 years. However, sedimentary proxies of methane seepage do not record present or past sediment depths of anaerobic oxidation of methane, suggesting that the input of methane has not been stable on timescales of longer than a few thousand years. This is supported by the foraminiferal calcite δ^{13}C record which indicates that methane seepage is episodic. The absence of a correlation between foraminiferal calcite δ^{13}C and δ^{18}O, in addition to the absence of evidence for past seepage upslope of the current seepage area, indicates that the relationship between seafloor seepage and temperature-driven migration of the hydrate stability zone is complex.

6.2. Conclusions

The specific objectives explored in this thesis, the outcomes of which are summarized in the preceding section, contribute to answering the following overarching questions:

1) Is temperature-driven methane hydrate destabilization a driver for seafloor methane seepage offshore Western Svalbard?
2) Does methane in shallow sediments reach the overlying atmosphere?
3) How is methane seepage likely to evolve in the future in the context of continued warming ocean bottom waters?

Geophysical evidence (e.g. Sarkar et al. [2012]), temperature studies (e.g. Berndt et al. [2014]; Ferré et al. [2012]; Thatcher et al. [2013]; Westbrook et al. [2009]), acoustic bubble plume mapping [Sahling et al., 2014], and hydrate stability modelling (e.g. Marín-Moreno et al. [2013]; Reagan and Moridis [2009]) all support the hypothesis that temperature-driven methane hydrate destabilization contributes to methane seepage at the present day landward limit of hydrate stability offshore Svalbard. Analyses of the chemical and isotopic composition of the seep gases cannot unequivocally distinguish between gas which has recently been released by dissociating shallow hydrate and that which has migrated through sediments without ever being in the hydrate phase. Nevertheless, geochemical data are consistent with descriptions of gas migration in the shallow subsurface based on seismic data (Rajan et al. [2012]; Sarkar et al. [2012], summarized and reviewed in Thatcher et al. [2013]). Specifically, the geochemical data:

- confirm that hydrate-bound and seep gas have the same source,
- provide evidence for significant lateral migration of thermogenic gas from offshore into shallow upper slope sediments,
- support ongoing redistribution of hydrate saturation closer to the seabed in sediments where temperature fluctuations are reducing the extent of, but not eliminating, hydrate stability.

Constraints on the spatial and temporal stability of seafloor seepage further test the hydrate destabilization hypothesis. Apparent steady-state diffusive pore fluid depth profiles of species involved in anaerobic oxidation of methane indicate that throughout most of the seepage area, shallow subsurface methane fluxes do not respond to seasonal or decadal fluctuations in temperature, which can affect the position of the gas hydrate stability zone. Thus, it seems likely that hydrate is unaffected by transient temperature fluctuations, unless it occurs only in very localized pockets of sediment not sampled in this study. Such a heterogeneous distribution of hydrate is suggested by the heterogeneous distribution of the seafloor methane seeps. Analysis of bulk sediments indicates that on timescales of >1000 years, methane fluxes in shallow sediments have not been stable enough to allow accumulation of sedimentary proxies of anaerobic oxidation of methane in distinct intervals. Temporally variable methane fluxes within the current seepage area are further demonstrated by evidence for intermittent seepage in the foraminiferal calcite $\delta^{13}C$ record. However, the foraminiferal $\delta^{13}C$ record provides no evidence for methane seepage from sediments immediately upslope at any time over the past ~ 30,000 years. Thus, a picture emerges of a complex relationship between ocean bottom water temperature, hydrate stability, and seafloor methane seepage. While the data do not support a straightforward migration of seafloor seepage with the temperature-driven hydrate stability zone limit water depth, they also do not indicate continuous, hydrate stability independent, seafloor seepage.

There is no direct methane transport from seafloor seeps near the hydrate stability zone limit into the overlying atmosphere. While focused high fluxes and gas-phase transport allow ~ 90 % of the gas flux into shallow sediments to enter ocean bottom waters, gas bubbles dissolve near the seafloor. The bottom waters of the West Spitsbergen Current then rapidly sweep water containing high methane concentrations northwards while the methane is slowly oxidized and diluted by mixing horizontally and vertically. In the absence of a mechanism for enhanced vertical mixing, methane is effectively trapped at depth. Concentrations and rates of bubble influx are not high enough relative to background dissolved oxygen and dissolved inorganic carbon for methane oxidation to affect inventories of these species. In the current oceanographic setting, hydrate destabilization offshore Svalbard is not likely to be a significant source of methane to the atmosphere.

Extending the implications of this study on the West Spitsbergen upper continental margin to the broader global and future implications of temperature-driven hydrate destabilization: the magnitude and timescale of current warming are unlikely to produce a hydrate-destabilization atmospheric methane feedback. In other words, the interval of time over which global, and particularly Arctic, temperatures have been rising is not sufficient for the destabilization and release of enough methane from the continental margin hydrate reservoir to significantly perturb the local or global carbon and climate cycles. There is potential for significant methane release in the future, but the available evidence does not support a catastrophic short-term release mechanism.

6.3. Future work

When marine methane hydrate climate feedback was proposed, its proponents (e.g. Dickens [2011]; Kennett et al. [2003]) called for more research to test their hypotheses. The response to this call is evidenced by the growing body of literature on the subject (e.g. *Figure 1-9*; Milkov [2004]). The emerging consensus does not support catastrophic gas escape. While adding to evidence refuting the basic clathrate-gun-type hypothesis of methane hydrate climate feedback, the results of this work point to a number of specific and more general areas for future study:

- Thus far, studies of the methane seepage site offshore Western Svalbard have neglected the physical oceanographic controls, which have emerged as a key factor determining the eventual fate of methane released into the water column from hydrate destabilization in the sediments. Future studies need to better characterize the oceanographic controls on the fate of methane, and focus sampling downstream to further constrain the atmospheric methane flux.
- Sediment pore water chemistry profiles reveal the critical role of small cracks and faults in allowing methane to escape oxidation beneath the seafloor. While the rocky sediment surface of the upper margin off Svalbard makes core recovery extremely challenging, better spatial coverage – in the seepage region, within the hydrate

stability zone, and in shallower water – is required to further constrain flux heterogeneity.

- Better understanding of the temporal variability must follow from the initial work at the GHSZ limit seepage site west of Svalbard. The water column dissolved methane concentration distribution demonstrates small-scale temporal variability of gas phase methane fluxes into the water column, and of oceanographic controls. Conversely, the climatic implications are on very long temporal scales, which cannot be understood without long-term monitoring. For example, continued multi-year seafloor observatory deployment. The lack of evidence for a catastrophic warming result should not reduce the focus on multi-decadal study of this important environment.
- On the global scale, more sites need to be studied with the same multidisciplinary, multi-year interest which the West Svalbard margin has attracted. Echosounder and seismic surveys are likely to continue to identify sites of interest (e.g. the Antarctic; Römer et al. [2014], eastern North America; Skarke et al. [2014], and western North America; Hautala et al. [2014]). Is the Svalbard margin typical of shallow gas systems in the context of downslope methane hydrate stability zone retreat? The conclusions must be tested on a more globally representative scale.

APPENDIX A

Water column methanotrophy controlled by a rapid oceanographic switch

Manuscript in Review with *Nature Geoscience*

Supplementary Material is provided in **Appendix B**

Lea Steinle[1,2,*], Carolyn A. Graves[3], Tina Treude[2,4], Bénédicte Ferré[5], Arne Biastoch[2], Ingeborg Bussmann[6], Christian Berndt[2], Sebastian Krastel[7], Rachael H. James[3], Erik Behrens[2,8], Claus W. Böning[2], Jens Greinert[2,4,9], Célia-Julia Sapart[10,11], Markus Scheinert[2], Stefan Sommer[2], Moritz F. Lehmann[1] and Helge Niemann[1,*]

*Correspondence to: lea.steinle@unibas.ch, helge.niemann@unibas.ch

[1] Department of Environmental Sciences, University of Basel, 4056 Basel, Switzerland
[2] GEOMAR, Helmholtz Centre for Ocean Research Kiel, 24148 Kiel, Germany
[3] Ocean and Earth Science, National Oceanography Centre Southampton, Southampton SO14 3ZH, U.K.
[4] Present address: University of California, Los Angeles, Department of Earth, Planetary & Space Sciences and Atmospheric & Oceanic Sciences, Los Angeles CA 90095, USA
[5] CAGE-Centre for Arctic Gas Hydrate, Environment and Climate, Department of Geology, University of Tromsø, 9037 Tromsø, Norway
[6] Alfred Wegener Institute, Marine Station Helgoland, 27498 Helgoland, Germany
[7] Institute of Geosciences, University of Kiel, 24118 Kiel, Germany
[8] National Institute of Water and Atmospheric Research, Wellington 6021, New Zealand
[9] Royal Netherlands Institute for Sea Research NIOZ, Texel, The Netherlands
[10] Laboratoire de Glaciologie, Université Libre de Bruxelles, 1050 Brussels, Belgium
[11] Institute for Marine and Atmospheric Research, Utrecht University, 3584CC Utrecht, The Netherlands

Large amounts of the greenhouse gas methane are released from the seabed to the water column[1] where it may be consumed by aerobic methanotrophic bacteria[2]. This microbial filter is consequently the last marine sink for methane before its liberation to the atmosphere. The size and activity of methanotrophic communities, which determine the capacity of the water column methane filter, are thought to be mainly controlled by nutrient and redox dynamics[3-7], but little is known about the effects of ocean currents. Here we show that cold bottom water at methane seeps west off Svalbard, containing a large number of aerobic methanotrophs, was rapidly displaced by warmer water with a considerably smaller methanotrophic community. This water mass exchange, caused by short-term variations of the West Spitsbergen Current, constitutes an oceanographic switch severely reducing methanotrophic activity in the water column. Strong and fluctuating currents are widespread oceanographic features common at many methane seep systems and are thus likely to globally affect methane oxidation in the ocean water column.

Large amounts of methane are stored in the subsurface of continental margins as solid gas hydrates, gaseous reservoirs or dissolved in pore water[8]. At cold seeps, various physical, chemical, and geological processes force subsurface methane to ascend along pathways of structural weakness to the sea floor where a portion of this methane is utilised by anaerobic and aerobic methanotrophic microbes[1,9]. On a global scale, about 0.02 Gt yr^{-1} (3-3.5% of the atmospheric budget[10]) of methane bypasses the benthic filter system and is liberated to the ocean water column[1] where some of it is oxidised aerobically (aerobic oxidation of methane - MOx) (ref 2), or less commonly where the water column is anoxic, anaerobically (anaerobic oxidation of methane – AOM) (refs 2, 11). MOx is performed by methanotrophic bacteria (MOB) typically belonging to the Gamma- (type I) or Alphaproteobacteria (type II) (refs 12, 13):

$CH_4 + 2\,O_2 \rightarrow CO_2 + 2\,H_2O$

Water column MOx is consequently the final sink for methane before its release to the atmosphere, where it acts as a potent greenhouse gas. The water column MOx filter could become more important in the future because environmental change may induce bottom water warming, which in turn may accelerate release of methane from the seafloor[14], in particular along the Arctic continental margins[15]. Despite the paramount importance of MOx for mitigating the release of methane to the atmosphere, little is known about environmental controls on the efficiency of the water column filter system. Known important factors determining the structure, activity and size of MOx communities are the availability of methane[5-7] and oxygen[3], or the abundance of trace metals (e.g. iron and copper) (refs 4, 7). Moreover, evolutionary adaptations to specific environmental conditions select for certain types of methanotrophs[13]. In addition to environmental selection, the physical transport of water masses harbouring distinct microbial communities has been identified as an important factor in shaping the biogeography of prokaryotic communities[16]. However, the potential effects of advective processes on the distribution of methanotrophs and the efficiency of the water column MOx filter system remain unconstrained[11,17,18].

During two research cruises to the Svalbard continental margin with R/V Poseidon (cruise POS419) and R/V Maria S. Merian (cruise MSM21/4) in August 2011 and 2012, respectively, we investigated methane dynamics and the activity levels and size of the water column MOx community in relation to water mass properties (*Figure A-1*). The Svalbard margin hosts an extensive, elongated (~22 km) cold seep system that is influenced by gas hydrates (*Figure A-1a*) (ref 19). Numerous gas flares emanate from the sea floor between the 350 and 400 m isobath[19,20], which corresponds to the landward termination of the gas hydrate stability zone. Seep sites have also been mapped on the shelf[19-21], and elevated methane levels have been observed in several of the fjords in the Svalbard archipelago[6,22,23]. The hydrodynamics west of Svalbard are governed by the West Spitsbergen Current (WSC), a 100 km-wide branch of the Norwegian Atlantic Current, which transports large amounts (up to 10 Sv) of warm and salty Atlantic Water (AW; >1°C, >35 psu) northward into the Fram Strait[24]. The WSC flows above cold Arctic Intermediate Water (AIW; <1°C, ~34.9 psu) (ref 25). It is steered topographically, and its eastern extension is constrained by the shelf break[26]. East of the WSC on the shelf, the comparably slow East Spitsbergen Current transports cold and relatively fresh Arctic Water (ArW; <3°C, <34.8 psu) to the north[27].

During two sampling surveys in late August 2012, we measured methane concentrations, MOx activity and MOx biomass, as well as temperature, salinity and oxygen along a transect perpendicular to the line of the methane flares. The two mid-transect stations were at the MASOX site (named after the MASOX observatory[19]), which is located at 380 m water depth in the centre of the gas flare area both along slope and down slope. During both surveys, methane concentrations were highest in bottom waters, frequently exceeding 100 nmol L^{-1} (*Figure A-1b*). Surface water methane concentrations (9 nmol CH_4 L^{-1} on average) were ~3-fold supersaturated with respect to the local atmospheric equilibrium, indicating methane efflux to the atmosphere from this seep system[19]. Methane dissolved in the water column apparently originates from gas bubbles, which we observed visually during dives with the submersible *Jago*, and which were detected as flares in the middle of the transect with hydroacoustic single-beam systems[19]. Despite the constant supply of methane from the sea floor, we found considerable spatial and temporal variability in MOx activity (*Figure A-1c, Supplementary Figure B-1*). MOx was highest in bottom waters (>300 m water depth) during the first survey (Aug. 18/19) with methane turnover rates of up to 3.2 nmol L^{-1} d^{-1} (*Figure A-1c, Table A-1*). These rates were similar to maximum rates detected at seeps on the Svalbard shelf[21] and in a nearby fjord[6]. In contrast, overall MOx activity was strongly reduced during the second survey (Aug. 30/31, *Figure A-1c, Table A-1*). Consistent with the MOx activity measurements, cell enumeration conducted in the mid-transect region revealed a maximum in type I MOB cells on August 18/19 (up to 3.0×10^4 cells mL^{-1}; *Table A-1*, Supplementary *Figure B-1*), but ~75% lower cell numbers during the second survey (up to 7.6×10^3 type I MOx cells mL^{-1}). The distributions of MOx activity and cell numbers translate to relatively constant, although low[12,28], cell-specific MOx rates of 1.54 to 1.66×10^{-2} fmol h^{-1} during the two sampling campaigns (*Table A-1*). This constancy suggests that the efficiency of the methanotrophic filter system in the water column was controlled by the size of the MOx community rather than by an environmental stimulus or suppression mechanism of MOx activity at the organismic level (*Supplementary Figure B-2a, b*).

Together with the reduction in MOx activity and community size, we observed a strong spatiotemporal change in the distribution of water mass properties. During the August 18/19 survey, bottom waters consisted of cold AW with admixture of AIW and ArW (*Figure A-1d, e*), which we subsequently refer to as cold AW (cAW). The cAW has water mass properties (temperature and salinity) akin to those of bottom waters found on the shelf[21]. By August 30/31, the cAW at the bottom was replaced by warmer Atlantic water (wAW, *Figure A-1d, e*). As the standing stock of methanotrophs in wAW was much lower compared to the cAW, rapid water mass exchange constitutes an oceanographic switch, causing a system-wide reduction of the efficiency of water column MOx. This apparent mechanistic link between MOx activity and the presence of either cAW or wAW is reflected in all water column profiles measured in 2012, as well as 2011 (*Supplementary Figure B-1n, 2c*).

We simulated the observed hydrodynamics using the high-resolution (1/20°, ~2.5 km grid space) VIKING20 model, which is nested in the global ocean/sea-ice model ORCA025 and represents ocean circulation variability in the northern North Atlantic at great verisimilitude[29] (*Supplementary Figure B-3*). For the WSC, the model yields two modes (offshore and nearshore) with respect to the meandering of the main, warm core of the WSC (*Figure A-2, Supplementary Figure B-3d, e*). During the offshore mode, the WSC separates into a warm offshore component and a cold undercurrent, which flows closely along the shelf break. The increase of the undercurrent causes stronger tilts of the isotherms and results in comparably cold bottom water temperatures. As a consequence, bottom waters at the shelf break and on the shelf are of similar density. The ArW on the shelf and fjord waters, both of which are characterised by a high MOx capacity[6,21], can thus be entrained downslope and contribute to the cAW, a situation that we observed during the August 18/19 survey. As a result, it is plausible that the high standing stock of methanotrophs in cAW partly originates from the shelf. The slow-flowing East Spitsbergen Current and the sheltered fjords lead to comparably long water mass residence times, ensuring continuity of methane supply and supporting MOx community development in the shelf waters. During the nearshore mode, which is representative of the situation that we encountered during the August 30/31 survey, the warm core of the WSC flows closely along the shelf break, replacing the cAW with wAW and separating shelf and deeper AIW. The open-ocean origin of the WSC[24] makes an exposure to elevated methane concentrations in the history of the wAW unlikely, and could therefore explain the low standing stock of methanotrophs in this water mass.

The dynamics and magnitudes of bottom water temperatures and current velocities simulated by our model correspond well to recorded long-term measurements at the shelf break of the Svalbard margin[19,24]. Modelled and observational data indicate a transition time of 5-10 days between the two described modes. The meandering of the WSC appears to be associated with far-field variations and internal variability of the WSC, but this causality is non-linear so that the exact timing of the observed switch between the off- and nearshore mode cannot be predicted. Yet, both our model results as well as measured data from previous work[19,24] indicate that the WSC predominantly flows along the shelf break, whereas the offshore mode, with cAW at the bottom and a high MOx capacity in the water column, occurs only 15 % of the time.

At the Svalbard margin, methane flares were observed along a 22 km-long stretch of the upper slope at around 390 m water depth[19,20]. Our model results, together with the measurements of MOx activity and water mass properties, indicate that the entire area is similarly affected by water mass exchange. When spatially extrapolating MOx rate measurements from the transect samplings to the whole seep area (66 km^2), total MOx amounted to 0.28 t CH_4 d^{-1} on August 18/19, and was reduced by 66 % on August 30/31 (*Table A-1*). Based on the maximum measurements, the capacity of the MOx filter in the studied seep area could well exceed 100 t CH_4 yr^{-1}, but this potential remains largely unexploited because the predominant nearshore mode of the WSC reduces MOx capacity to 45 t CH_4 yr^{-1}.

Similar to our measurements, varying MOx activities were detected in systems affected by differential circulation patterns and water mass mixing (Black Sea[11]; Santa Monica Basin[18]), and only low water column MOx activities were found at highly active methane seeps influenced by strong bottom currents (Hydrate Ridge[17]; Haakon Mosby Mud Volcano[30]). Currents result in relatively short water mass residence times above methane point sources, so that not enough time and continuity is provided for the development of large methanotrophic communities. Similarly, a well-established MOx community will be swept away from the methane source with the onset of water mass exchange. Dissolved methane, together with the methanotrophic community, will be dispersed leeward where ongoing MOx activity reduces methane concentrations further[7], most probably at rates controlled by the size of the MOx community. With respect to methane emission to the atmosphere, the impact of currents on water column MOx thus seems strongest in shallow-water cold seep environments, where the spatiotemporal distance between seafloor methane venting, water column methane consumption and methane evasion to the atmosphere is short. Most methane seeps are located along continental margins, where bottom water currents are commonly strong and fluctuating, as shown by our results from a global, high-resolution circulation model (ORCA12; *Figure A-, Supplementary Figure B-4*). We thus argue that the variability of physical water mass transport is a globally important control on the distribution and abundance of methanotrophs and, as a consequence, on the efficiency of methane oxidation above point sources.

Data Availability

All data presented in this paper are available in the PANGAEA data library (www.pangaea.de). In-depth information on the ORCA12 and VIKING20 models (data and code) will be provided on request.

Acknowledgements

We thank the Captains, crews and shipboard scientific parties of R/V Poseidon and R/V Maria S. Merian for their help at sea. This work received financial support through a D-A-CH project funded by the Swiss National Science Foundation and German Research foundation (grant no. 200021L_138057). Further support was provided through the EU COST Action PERGAMON (ESSEM 0902), a Postgraduate Scholarship of the National Research Council of Canada, the Centre of Excellence “CAGE” funded by the Norwegian Research Council (grant no. 223259) and the Cluster of Excellence “The Future Ocean” funded by the German Research Foundation.

Figures

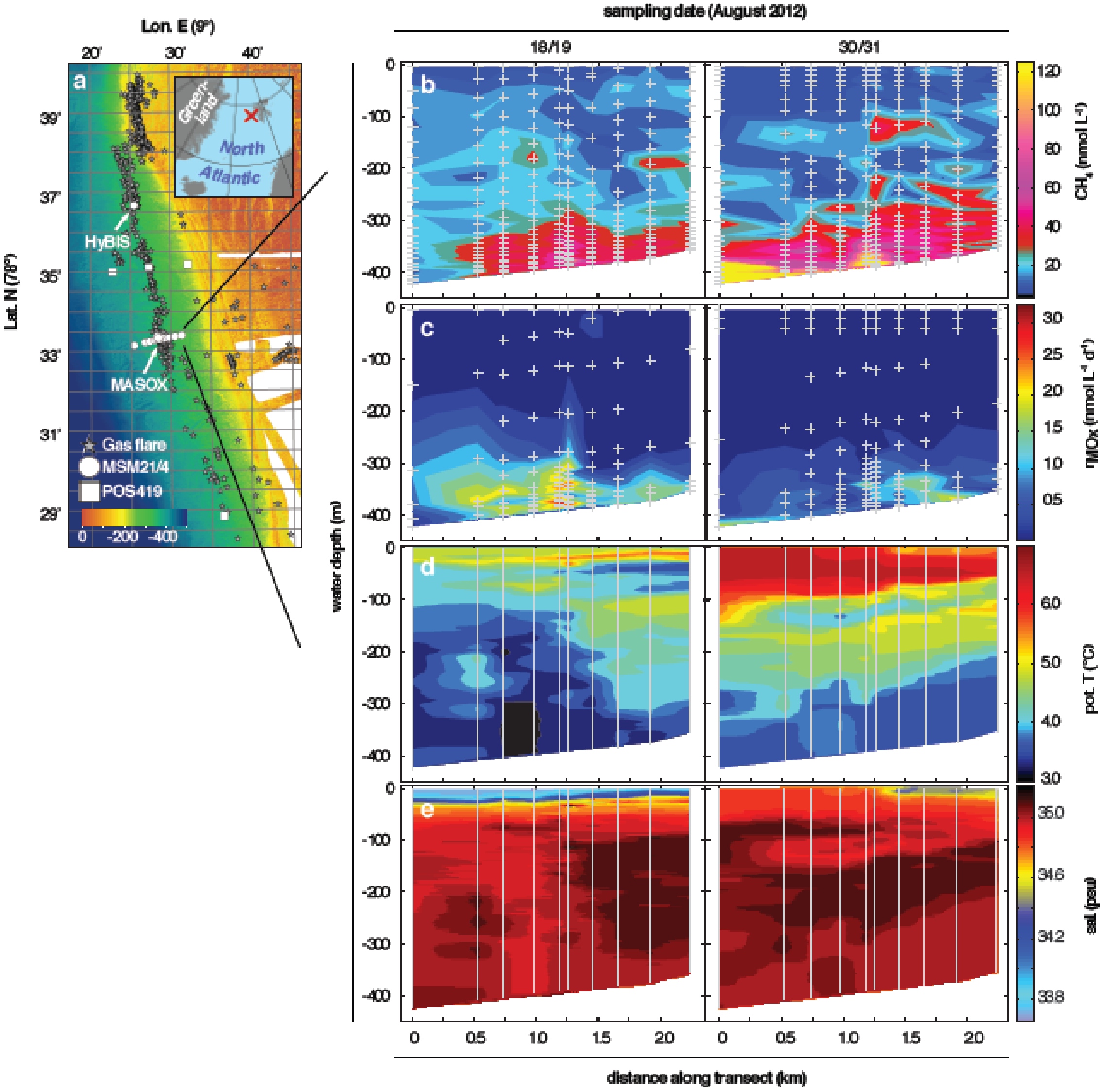

Figure A-1: Study area and distribution of aerobic methanotrophy and physicochemical parameters above methane seeps at the Svalbard continental margin. **a,** Map of the seep system with numerous methane flares (grey stars) emanating from the sea floor around the depth of the landward termination of the gas hydrate stability zone. Sampling locations are indicated (squares: POS419, 2011; circles: MSM21/4, 2012). Distribution of **b,** methane, **c,** aerobic methane oxidation rates (r_{MOx}), **d,** temperature and **e,** salinity measured during two sampling surveys along the same transect crossing the MASOX site[19]. **b-e**, Positions of discrete samples (crosses) and continuous measurements (lines) are indicated.

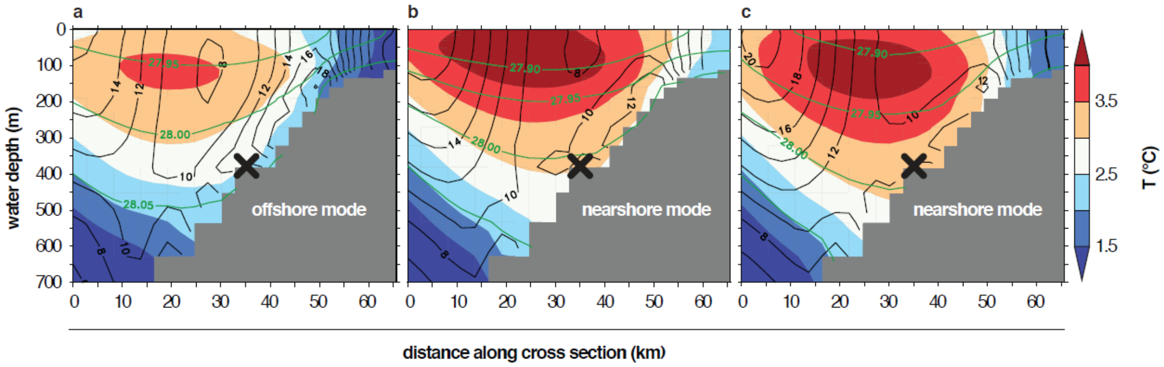

Figure A-2: Modelled cross-slope distribution of water column temperature and current velocity in the West Spitsbergen Current. Modelled time-averaged water column temperature (°C), sigma-t (green contours, kg m^{-3}-1000) and current velocity (black contours, cm s^{-1}) for **a,** cold temperature anomalies, **b,** mean temperature and **c,** warm temperature anomalies. Anomalies were defined as one standard deviation below or above the seasonally and interannually varying temperature mean in bottom waters at the MASOX site (cross mark; cf. *Supplementary Figure B-3c*). During times of cold temperature anomalies, the WSC is in its offshore mode, with a cold undercurrent along the slope.

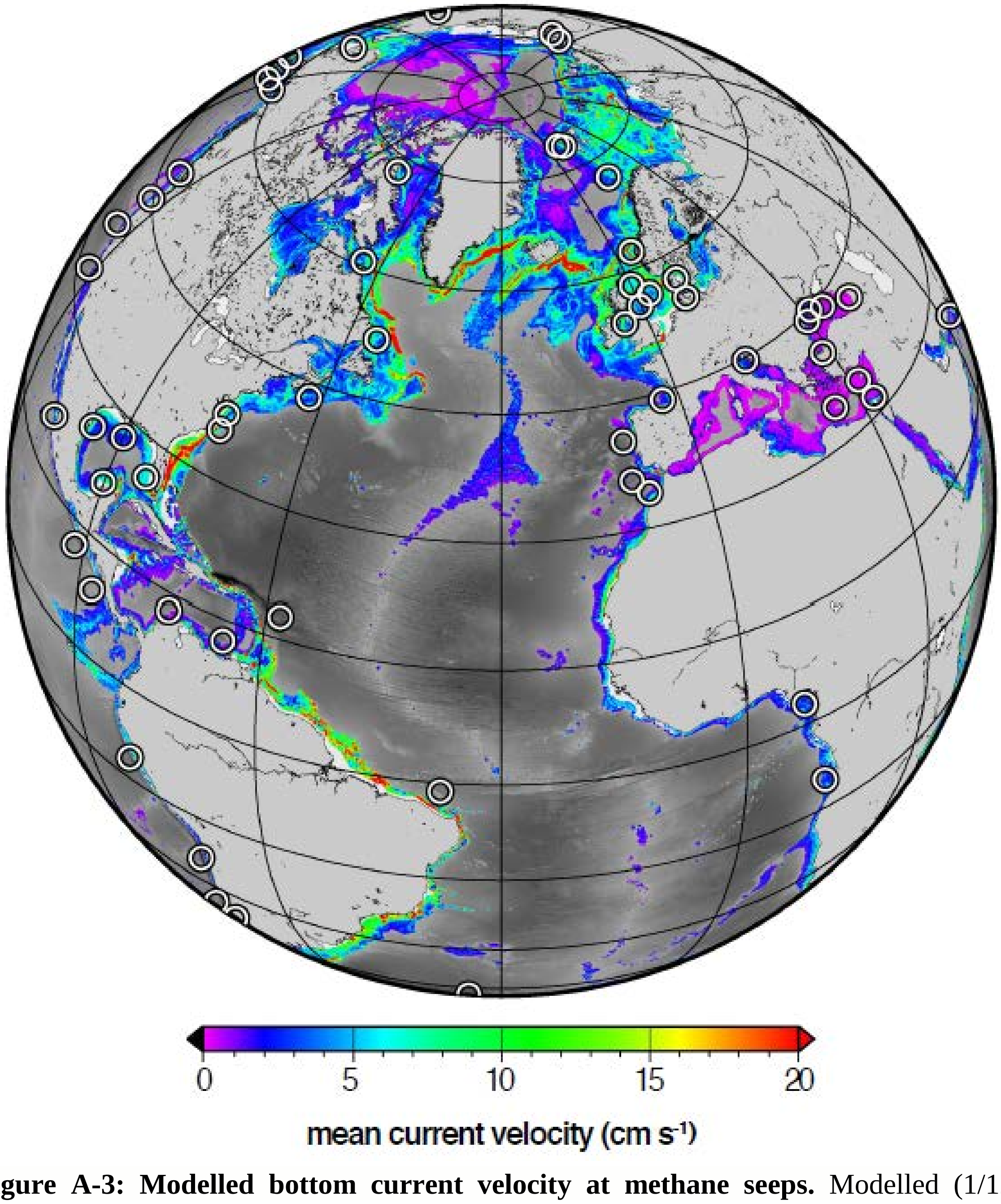

Figure A-3: Modelled bottom current velocity at methane seeps. Modelled (1/12° resolution) mean annual (year 2000) bottom water current velocities for bottom depths between 100 and 2500 m. Current velocities at continental margins, where most methane seeps are located, frequently exceed 10 cm s^{-1} and can be highly variable (cf. *Supplementary Figure B-4*). Locations of selected methane seeps are indicated by white circles.

Tables

Table A-1: Comparison of methane consumption and methanotrophic cell numbers between the two transect sampling campaigns in 2012. Total CH_4 oxidised in the seep area was calculated by extrapolation of average MOx rates calculated for each sampling date to the total seep-affected water mass volume (3 km width × 22 km length × 0.388 km average water depth). Highest MOB cell numbers and fraction (in %) of total cell numbers are indicated. Cell-specific MOx rates represent the average of all samples counted on the respective transects (±standard error. n=12, Aug. 18/19; n=15, Aug. 30/31).

	sampling date (August 2012)	
	18/19	**30/31**
bottom water type	cAW	wAW
WSC mode	offshore	nearshore
max. MOx activity	3.2 nmol L^{-1} d^{-1}	2.1 nmol L^{-1} d^{-1}
CH_4 oxidized in seep area	17.82 kmol d^{-1} (0.28 t d^{-1})	5.57 kmol d^{-1} (0.09 t d^{-1})
max. MOB cells	29.7×10^3 mL^{-1}	3.65×10^3 mL^{-1}
max. MOB cells (% of tot. cells)	8.3	2.5
cell specific MOx activity	$1.54 \pm 0.34 \times 10^{-2}$ fmol h^{-1} ($0.22 – 5.74 \times 10^{-2}$ fmol h^{-1})	$1.66 \pm 0.37 \times 10^{-2}$ fmol h^{-1} ($0.06 – 5.66 \times 10^{-2}$ fmol h^{-1})

References

1. Boetius, A. & Wenzhofer, F. Seafloor oxygen consumption fuelled by methane from cold seeps. *Nat. Geosci.* **6,** 725-734 (2013).
2. Reeburgh, W. S. Oceanic methane biogeochemistry. *Chem. Rev.* **107,** 486-513 (2007).
3. Sansone, F. J. & Martens, C. S. Methane oxidation in Cape Lookout Bight, North Carolin. *Limnol. and Oceanogr.* **23,** 349-355 (1978).
4. Semrau, J. D., DiSpirito, A. A. & Yoon, S. Methanotrophs and copper. *FEMS Microbiol. Rev.* **34,** 496-531 (2010).
5. Kessler, J. D., Valentine, D. L., Redmond, M. C., Du, M. R., *et al.* A Persistent Oxygen Anomaly Reveals the Fate of Spilled Methane in the Deep Gulf of Mexico. *Science* **331,** 312-315 (2011).
6. Mau, S., Blees, J., Helmke, E., Niemann, H. & Damm, E. Vertical distribution of methane oxidation and methanotrophic response to elevated methane concentrations in stratified waters of the Arctic fjord Storfjorden (Svalbard, Norway). *Biogeosciences* **10,** 6267-6278 (2013).
7. Crespo-Medina, M., Meile, C. D., Hunter, K. S., Diercks, A. -R., *et al.* The rise and fall of methanotrophy following a deepwater oil-well blowout. *Nat. Geosci.* **7,** 423-427 (2014).
8. Wallmann, K., Pinero, E., Burwicz, E., Haeckel, M., *et al.* The Global Inventory of Methane Hydrate in Marine Sediments: A Theoretical Approach. *Energies* **5,** 2449-2498 (2012).
9. Knittel, K. & Boetius, A. Anaerobic Oxidation of Methane: Progress with an Unknown Process. *Annu. Rev. of Microbiol.* **63,** 311-334 (2009).
10. Kirschke, S., Bousquet, P., Ciais, P., Saunois, M., *et al.* Three decades of global methane sources and sinks. *Nat. Geosci.* **6,** 813-823 (2013).
11. Reeburgh, W. S., Ward, B. B., Whalen, S. C., Sandbeck, K. A., *et al.* Black-Sea Methane Geochemistry. *Deep-Sea Res. Pt. I* **38,** 1189-1210 (1991).
12. Hanson, R. S. & Hanson, T. E. Methanotrophic bacteria. *Microbiol. Rev.* **60,** 439-471 (1996).
13. Murrell, J. C. in *Handbook of Hydrocarbon and Lipid Microbiology* (eds Timmis, K. N.) 1953-1966 (Springer, Berlin, 2010).
14. Ferré, B., Mienert, J. & Feseker, T. Ocean temperature variability for the past 60 years on the Norwegian-Svalbard margin influences gas hydrate stability on human time scales. *J. Geophy. Res.-Oceans* **117,** 10.1029/2012JC008300 (2012).

15. Biastoch, A., Treude, T., Rüpke, L. H., Riebesell, U., *et al.* Rising Arctic Ocean temperatures cause gas hydrate destabilization and ocean acidification. *Geophys. Res. Lett.* **38,** DOI: 10.1029/2011GL047222 (2011).
16. Wilkins, D., van Sebille, E., Rintoul, S. R., Lauro, F. M. & Cavicchioli, R. Advection shapes Southern Ocean microbial assemblages independent of distance and environment effects. *Nat. Commun.* **4,** (2013).
17. Heeschen, K. U., Collier, R. W., de Angelis, M. A., Suess, E., *et al.* Methane sources, distributions, and fluxes from cold vent sites at Hydrate Ridge, Cascadia Margin. *Glob. Biogeochem. Cy.* **19,** (2005).
18. Heintz, M. B., Mau, S. & Valentine, D. L. Physical control on methanotrophic potential in waters of the Santa Monica Basin, Southern California. *Limnol. Oceanogr.* **57,** 420-432 (2012).
19. Berndt, C., Feseker, T., Treude, T., Krastel, S., *et al.* Temporal Constraints on Hydrate-Controlled Methane Seepage off Svalbard. *Science* **343,** 284-287 (2014).
20. Westbrook, G. K., Thatcher, K. E., Rohling, E. J., Piotrowski, A. M., *et al.* Escape of methane gas from the seabed along the West Spitsbergen continental margin. *Geophys. Res. Lett.* **36,** (2009).
21. Gentz, T., Damm, E., Schneider von Deimling, J., Mau, S., *et al.* A water column study of methane around gas flares located at the West Spitsbergen continental margin. *Cont. Shelf Res.* **72,** 107-118 (2014).
22. Damm, E., Mackensen, A., Budéus, G., Faber, E. & Hanfland, C. Pathways of methane in seawater: Plume spreading in an Arctic shelf environment (SW-Spitsbergen). *Cont. Shelf Res.* **25,** 1453-1472 (2005).
23. Damm, E., Kiene, R. P., Schwarz, J., Falck, E. & Dieckmann, G. Methane cycling in Arctic shelf water and its relationship with phytoplankton biomass and DMSP. *Mar. Chem.* **109,** 45-59 (2008).
24. Schauer, U., Fahrbach, E., Osterhus, S. & Rohardt, G. Arctic warming through the Fram Strait: Oceanic heat transport from 3 years of measurements. *J. Geophy. Res.-Oceans* **109,** 14 (2004).
25. Blindheim, J. Arctic intermediate water in the Norwegian sea. *Deep-Sea Res. Pt. I* **37,** 1475-1489 (1990).
26. Bourke, R. H., Weigel, A. M. & Paquette, R. G. The westward turning branch of the West Spitsbergen Current. *J. Geophy. Res.-Oceans* **93,** 14065-14077 (1988).
27. Loeng, H. Features of the physical oceanographic conditions of the Barents Sea. *Polar Res.* **10,** 5-18 (1991).

28. Carini, S., Bano, N., LeCleir, G. & Joye, S. B. Aerobic methane oxidation and methanotroph community composition during seasonal stratification in Mono Lake, California (USA). *Environ. Microbiol.* **7,** 1127-1138 (2005).
29. Fischer, J., Karstensen, J., Zantopp, R., Visbeck, M., *et al.* Intra-seasonal variability of the DWBC in the western subpolar North Atlantic. *Prog. Oceanogr.* 10.1016/j.pocean.2014.04.002 (2014).
30. Sauter, E. J., Muyakshin, S. I., Charlou, J. L., Schluter, M., *et al.* Methane discharge from a deep-sea submarine mud volcano into the upper water column by gas hydrate-coated methane bubbles. *Earth Planet. Sc. Lett.* **243,** 354-365 (2006).

Author Contributions

L.S., C.G., T.T., I.B., J.G., C.J.S. S.S. and H.N. collected the samples and performed measurements of biogeochemical rates and/or physicochemical parameters. L.S. carried out enumeration of microbial cells. A.B., B.F., J.G., E.B., C.W.B. and M.S. conducted oceanographic modelling, interpretation and/or graphical representation. C.B. and S.K. were responsible for acoustic measurements. H.N., T.T., R.H.J. and M.F.L supervised research. L.S. and H.N led the development of the manuscript and all co-authors contributed to data interpretation and writing of manuscript.

The authors declare no competing financial interests.

APPENDIX B

Supplemental Material for Appendix A: Water column methanotrophy controlled by a rapid oceanographic switch

---

Manuscript in Review with *Nature Geoscience*

Lea Steinle[1,2,*], Carolyn A. Graves[3], Tina Treude[2,4], Bénédicte Ferré[5], Arne Biastoch[2], Ingeborg Bussmann[6], Christian Berndt[2], Sebastian Krastel[7], Rachael H. James[3], Erik Behrens[2,8], Claus W. Böning[2], Jens Greinert[2,4,9], Célia-Julia Sapart[10,11], Markus Scheinert[2], Stefan Sommer[2], Moritz F. Lehmann[1] and Helge Niemann[1,*]

*Correspondence to: lea.steinle@unibas.ch, helge.niemann@unibas.ch

[1] Department of Environmental Sciences, University of Basel, 4056 Basel, Switzerland
[2] GEOMAR, Helmholtz Centre for Ocean Research Kiel, 24148 Kiel, Germany
[3] Ocean and Earth Science, National Oceanography Centre Southampton, Southampton SO14 3ZH, U.K.
[4] Present address: University of California, Los Angeles, Department of Earth, Planetary & Space Sciences and Atmospheric & Oceanic Sciences, Los Angeles CA 90095, USA
[5] CAGE-Centre for Arctic Gas Hydrate, Environment and Climate, Department of Geology, University of Tromsø, 9037 Tromsø, Norway
[6] Alfred Wegener Institute, Marine Station Helgoland, 27498 Helgoland, Germany
[7] Institute of Geosciences, University of Kiel, 24118 Kiel, Germany
[8] National Institute of Water and Atmospheric Research, Wellington 6021, New Zealand
[9] Royal Netherlands Institute for Sea Research NIOZ, Texel, The Netherlands
[10] Laboratoire de Glaciologie, Université Libre de Bruxelles, 1050 Brussels, Belgium
[11] Institute for Marine and Atmospheric Research, Utrecht University, 3584CC Utrecht, The Netherlands

B.1. Physiochemical and biogeochemical water column parameters

B.1.1 Temperature and salinity

Temperature and salinity were measured with a Seabird SBE911 CTD (CTD: conductivity/temperature/density probe; Seabird-Electronics, USA) equipped with dual temperature and conductivity sensors. For monitoring sensor performance, we conducted several CTD casts with a third set of temperature and conductivity sensors (SAIV A/S SN363, Norway, calibrated by SAIV A/S directly before the cruise). The offsets between the Seabird and SAIV were ≤0.01°C and ≤0.04 psu. During the MSM21/4 cruise, most CTD casts were taken at the MASOX site (78°33.3'N, 9°28.6'E; ~380 m water depth; ref 1) and/or along a transect crossing this site. One additional CTD cast was performed ~6.4 km further north at the HyBIS site (78°36.68'N, 009°25.50'E; cf. *Figure A-1a*; ref 1). During the POS419 cruise, CTD casts were also performed using a Seabird SBE911 device at three stations between the MASOX and HyBIS site and at one station ~8.8 km south of the MASOX site (*Figure A-1a*). For a complete station list see *Supplementary Table B-1*.

B.1.2. Methane concentrations

For analysis of methane concentrations and MOx rates at discrete water depths, we sampled the water column with 24 × 10 L PTFE-lined Niskin bottles mounted on a CTD/Rosette sampler and sub-samples were taken immediately upon recovery of the sampler[1]. During the MSM21/4 cruise, methane was analysed with a headspace technique and gas chromatography with flame ionisation detection[1]. Briefly, ~ 600 mL seawater was subsampled bubble-free into triple-layer Evarex Barrier Bags (Oxford Nutrition, U.K.) followed by the addition of a headspace (20 mL N_2) and equilibration for several hours. Methane concentrations were determined by gas chromatography (Agilent 7890A GC; 80/100 mesh HayeSep Q packed stainless steel column, 1.83 m length, 2 mm i.d.; flame ionization detector set at 250 °C; oven operated isocratically at 60 °C; N_2 carrier gas at 33 mL min^{-1}) from a 2 mL aliquot of the headspace. The GC system was calibrated with external standards (20 ppm methane standard, Air Liquide, Germany), and reproducibility (determined by 3 replicate analyses of an individual sample) was < ± 5 %. During the POS419 cruise, methane concentrations were analysed with a slightly modified headspace method with respect to sampling vials (120 mL glass vials, 5 mL N_2 headspace, fixed with 0.5 mL saturated aqueous $HgCl_2$ solution) and manufacturers of analytical instruments (Thermo Scientific FOCUS GC, direct injection; Resteck packed column HayeSep Q

80/100, 2 m length, 2 mm i.d.; flame ionization detector set at 170 °C; oven temperature was ramped from 40 to 120 °C in steps, H_2 carrier gas at 33 mL min^{-1}). Seawater methane concentrations and the degree of saturation with respect to the atmospheric equilibrium were calculated with consideration of sample and headspace volume, temperature, salinity, atmospheric pressure and atmospheric CH_4 mixing ratio[2,3].

B.1.3. Methane oxidation rates

MOx rates were determined at sea from *ex situ* incubations with trace amounts of tritium-labelled methane (^3H-CH_4) similarly to published methods[4,5] with some modifications[6]. For each depth, four crimp-top vials (20 mL) were filled bubble-free and closed with bromobutyl stoppers (Helvoet Pharme, Belgium), amended with 10 µl gaseous ^3H-CH_4/N_2 mixture (~25 kBq, <50 pmol CH_4, American Radiolabeled Chemicals, USA) and incubated for 72 h at *in situ* temperature in the dark. Linearity of MOx during the incubation time period (~72 h) was confirmed by replicate incubations at 24, 48 and 72 h. MOx rates were corrected for (insubstantial) tracer turnover in killed controls (addition of 100 µl, saturated aqueous $HgCl_2$ solution). Rates on the POS419 cruise were measured analogously, but instead of 20 ml we incubated in 120 ml bromobutyl-sealed (Ochs, Germany) crimp top vials with an amendment of 100 µl tracer gas. Single or triplicate incubations were conducted for each depth. MOx rates were calculated from the fractional turnover of labelled CH_4 and water column CH_4 concentration assuming first order kinetics[5]. Average standard deviation between replicates was ±20.4 % for MSM21/4 incubations and ±38 % for POS419 incubations.

B.1.4. Biomass estimation of methanotrophs

The identity and abundance of aerobic methanotrophic bacteria (MOB) was investigated by catalysed reporter deposition fluorescence *in situ* hybridisation (CARD-FISH; refs 7,8) from samples collected during the MSM 21/4 cruise. A 100 ml seawater aliquot was fixed for ~4 h with formaldehyde (1.5 % final concentration) at 4 °C. The fixed sample was filtered through a polycarbonate filter (Whatman Nuclepore black track-etched polycarbonate membrane filter, 25 mm diameter, 0.2 µm pore size) with a gentle vacuum-pressure of 0.5 bar. Filters were air-dried and stored at -20 °C until further analyses. Cells embedded on the filter were permeabilised with lysozyme[7], followed by inactivation of endogenous peroxidases in a 0.15 % H_2O_2/methanol solution for 30 min at room temperature. Filters were then washed successively in sterile MilliQ (1 min) and aqueous ethanol solution (96 %, v/v; 2 min) and finally air-dried. Filters were hybridised with ~300 µl hybridisation buffer for 3 h at 46 °C. The buffer contained either a mix of probes Mγ705-HRP and Mγ84-HRP (0.3 ng µL^{-1} each), or probe Mα450-HRP (0.6 ng µL^{-1}) for the detection of Type I and Type II MOx communities, respectively[9]. Negative controls (sulphide-oxidizing mixed culture, enriched from a freshwater lake) were used to ensure specificity of probe binding with our hybridisation conditions. Catalysed reporter deposition and DAPI staining was carried out according to published recommendations[8] with an amplification time of 20 min at 37 °C in a buffer containing 1 µL of the labelled tyramide (Alexa488: Invitrogen A20000, lot 1252193; USA). Filters were finally washed for 10 min in PBS. We used Citifluor AF1 (Citifluor Ltd., U.K.) as mountant for fluorescence microscopy. CARD-FISH- and DAPI-stained samples were examined with an epifluorescence microscope (Leica DM2500 equipped with the external ultraviolet light source, EL6000) at a 1000-fold magnification. For each sample, ~1000 DAPI-stained cells in ≥ 10 microscopic fields were counted. Total cell numbers in the lowest 200 m of the water column were similar between sampling dates ($2.09 \pm 0.14 \times 10^5$ cells mL^{-1}), while surface water generally contained higher cell numbers (up to 10.8×10^5 cells mL^{-1}) with higher variations between sampling dates (data not shown).

Type I MOB cells occurred as single/double cells (*Supplementary Figure B-1m*) or as loose 'aggregates' (*Supplementary Figure B-1j*). To account for the heterogeneous distribution of the aggregates, we counted 70 microscopic fields for each sample (average StDev. of MOB cell numbers between grids for one sample: ± 37%). Type II MOB cells accounted for less than 1 % of all MOB cells (data not shown), and were thus of minor importance for the water column MOx filter capacity.

Water samples collected at the MASOX site during the MSM21/4 cruise concomitantly showed elevated type I MOB cell numbers and MOx rates (*Supplementary Figure B-1*). Vice versa, water samples characterised by low MOx rates generally contained low numbers of MOB cells. Although MOx was maximal in bottom waters with elevated methane concentrations (*Figure A-1c*, *Supplementary Figure B-1*), we frequently encountered low levels of MOx activity (and methanotrophic biomass) in bottom water samples with high methane concentrations. MOx activity was thus determined by MOx biomass rather than methane substrate availability (*Supplementary Figure B-2a*, *b*). Furthermore, together with the MOx community size, the MOx filter capacity (see MOx rates in *Supplementary Figure B-1*) was only elevated in relatively cold and saline bottom waters (<4 °C, >34.9 psu, *Supplementary Figure B-2c*), which were only present during the offshore mode of the West Spitsbergen Current (WSC).

B.1.5. Interpolation and extrapolation of physiochemical and biogeochemical water column parameters.

Values of physiochemical and biogeochemical water column parameters were measured at discrete stations, and, in case of methane concentration and MOx activity, in discrete water depths, during the transect sampling campaigns (Aug. 18/19 and 30/31). Depth-integrated areal MOx rates were determined by linear interpolation between measured rates and extrapolation to a water column of 1 m^2. For representation as contour plots (Fig 1b-e), discrete values were linearly interpolated by using the Matlab software package. For extrapolating MOx rates to the known seep area, we first calculated weighted averages from the interpolated MOx rates (*Figure A-1c*) for the two sampling campaigns. These averages (0.7 and 0.2 nmol L^{-1} d^{-1} for Aug. 18/19 and 30/31, respectively) were then extrapolated to the whole water volume in the seep area (3 km width × 22 km length × 0.388 km average water depth).

B.2. Regional hydrographic changes in a wider oceanographic context

For a deeper understanding of the hydrographic changes west off the Svalbard shelf and the interplay with the large-scale circulation, we utilised 5-daily output from the VIKING20 model, a high-resolution ocean/sea-ice simulation[10,11]. Based on the NEMO code[12], VIKING20 has a 1/20° grid cell size of the subpolar/subarctic North Atlantic (32°N - 85°N) (ref 10) and is two-way nested[13] in a global 1/4° configuration (ORCA025 grid; ref 11). It is forced by atmospheric data covering synoptic (6-hourly to daily), seasonal, interannual to decadal timescales of the years 1948-2007 (ref 11). With a ~2.5 km grid space off West-Spitsbergen and 46 vertical levels (20 in the upper 500 m), VIKING20 realistically captures both the large-scale circulation and the mesoscale variability in the subpolar/subarctic North Atlantic by great verisimilitude[14], both with detailed mean flow characteristics[15] and temporal variability on short-term to decadal time scales[16]. The circulation in the Fram Strait, for instance, shows the same variability along the eastern boundary, with northward velocities up to 40 cm s^{-1} and beyond, as observed by Schauer et al., 2004 (ref 17). Modelled bottom current velocity (*Figure A-2*) agrees well with measurement data from the MASOX observatory (10 cm s^{-1} on average; ref 1).

Water column temperatures at the MASOX site (*Supplementary Figure B-3a, b*) greatly vary on seasonal and interannual timescales, but also show distinct minima and maxima (*Supplementary Figure B-3c*) strongly deviating from the (seasonally and interannually varying) temperature mean. These minima and maxima are caused by the variable position of the main, warm core of the WSC. *Supplementary Figure B-3d* shows time-averaged circulation patterns of the WSC along the offshore flank of the study area at 300 m water depth (the MASOX position is indicated with a cross mark). During time periods of cold bottom water temperature anomalies (i.e., greater than one standard deviation below the seasonally and interannually varying temperature mean; blue line in *Supplementary Figure B-3c*), the main core of the WSC is located offshore, giving rise to a cold undercurrent at the shelf break (*Supplementary Figure B-3d*), and thus to the observed and modelled cold bottom water temperatures at the shelf break. The comparably strong northward tilting of the flares that we observed during hydroacoustic surveys just before our samplings on August 17 and 18/19 (data not shown) indicates the presence of this fast undercurrent. In contrast, when the main core is meandering to the shore, the warm water of the WSC replaces the cold bottom water, resulting in the rise of bottom water temperatures. This nearshore mode corresponds to observed and modelled average and anomalously warm bottom water temperatures (i.e., values above one standard deviation above the seasonally and interannually varying temperature mean; red line in *Supplementary Figure B-3c*). The time-averaged circulation pattern of the nearshore mode is shown in *Supplementary Figure B-3e*. The meandering of the main core is caused by far-field and internal variations of the WSC, leading to a nonlinear behavior of the current with transition times between offshore- and nearshore mode of 5-10 days.

Global bottom water velocities at continental margins were analyzed using a global variant of the ocean/sea-ice model at 1/12° resolution (ORCA12). Similar to VIKING20, this model has been forced by atmospheric data[14], but over a shorter timeframe (1978-2003). Highly variable near-bottom currents are common along continental slopes and below regions of strong surface currents[18].

Figures

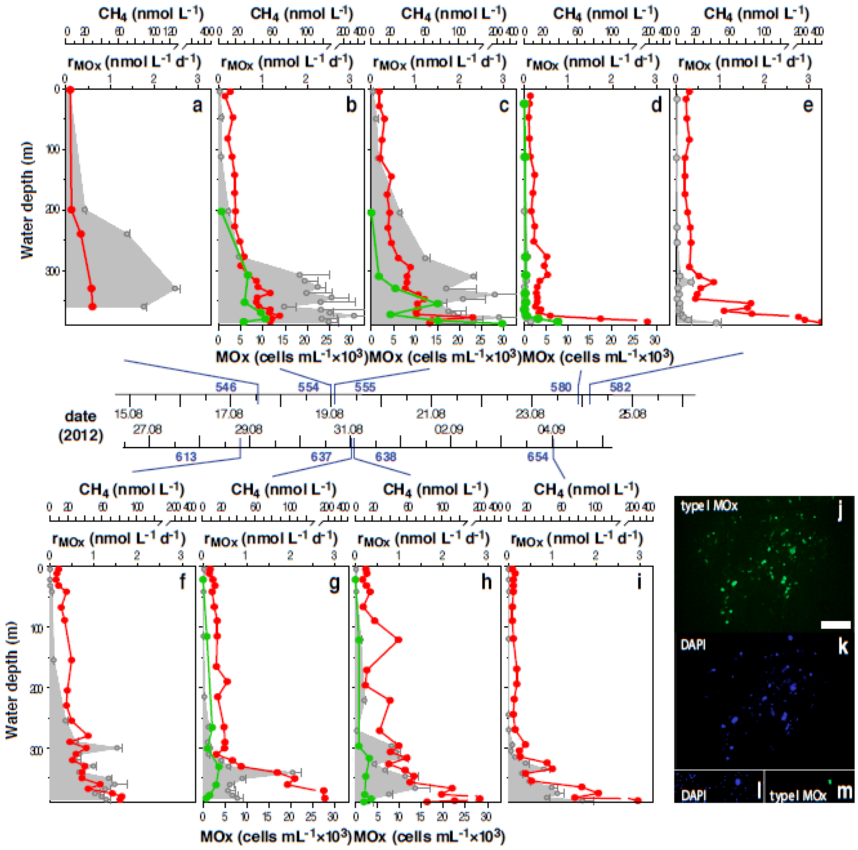

n

Date (2012)	Stat. no.	Site	BW conditions	WSC mode	MOx max (nmol L^{-1} d^{-1})	MOx depth integr. (µmol m^{-2} d^{-1})
17 Aug.	546	MASOX	cAW	offshore	2.5	349
19 Aug.	554	MASOX	cAW	offshore	3.1	251
19 Aug.	555	MASOX	cAW	offshore	2.9	314
23 Aug.	580	MASOX	wAW	onshore	0.2	7
24 Aug.	582	MASOX	wAW	onshore	0.9	16
28 Aug.	613	MASOX	wAW/cAW	on-/offshore	1.5	147
31 Aug.	637	MASOX	wAW	onshore	2.0	72
31 Aug.	638	MASOX	wAW	onshore	1.4	121
04 Sep.	654	MASOX	wAW	onshore	1.7	61

Supplementary Figure B-1 Methane concentrations, methane oxidation rates and methanotrophic cell numbers from repeated sampling campaigns at the MASOX station. **a-i**, Methane concentration (red), methane oxidation rates (grey), and **b**, **c**, **d**, **g**, **h**, cell numbers of type I aerobic methanotrophic bacteria (MOB; green), at the MASOX site measured during the MSM21/4 cruise at different dates (chronological station numbers are indicated in blue). Error bars of MOx represent standard deviation (n=4). **j-m**, Micrographs of water column microbes from samples collected at 380 m water depth at the MASOX site (station 554). Type I MOB cells were quantified by CARD-FISH (**j**, **m**; in green; mixture of probes Mγ705-HRP and Mγ84-HRP) and DAPI (=total cells; **k**, **l**, in blue) staining, followed by epifluorescence microscopy. The scale bar represents 10 µm. Type I MOB cells occurred as **m**, single/double cells, or **j**, as loose 'aggregates'. Stations 554/555 and 637/638 were sampled during transect samplings on Aug. 18/19 and Aug. 30/31, respectively. **n**, Maximum and depth integrated MOx rates at the MASOX site (cf. **a-g**) in relation to the presence of cAW or wAW at the sea floor. Together with the MOx community size, the MOx filter capacity was only elevated in relatively cold and saline bottom waters (<4 °C, >34.9 psu; cf. *Supplementary Figure B-2a*), which were solely present during the offshore mode of the WSC.

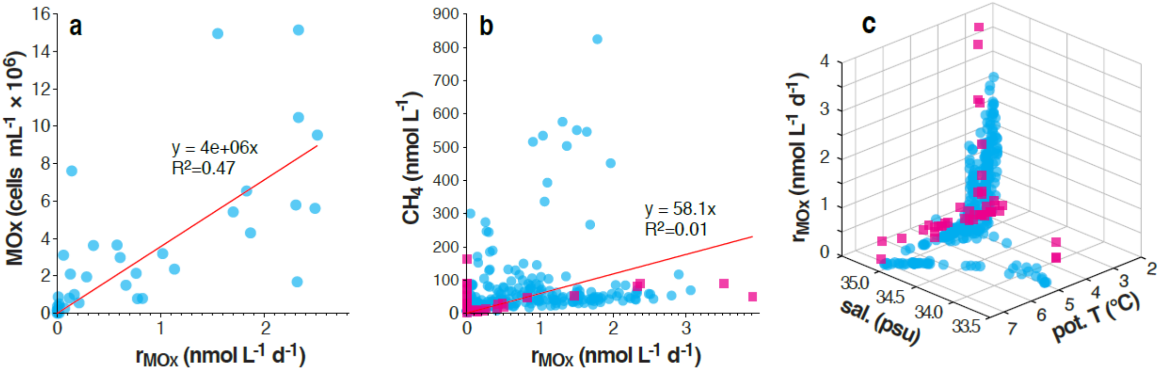

Supplementary Figure B-2 Aerobic methane oxidation in relation to bottom water properties. a, Methane oxidation rates (rMOX) in relation to **a**, cell numbers of type I aerobic methane oxidising bacteria, **b** methane concentration and, **c** salinity and temperature, measured during the MSM21/4 (cyan dots) and POS419 (pink squares) cruise. Note that MOB cell numbers were only determined from selected samples from the MASOX site collected during the MSM21/4 cruise, while methane concentration, salinity and temperature were determined for all samples designated for MOx rate measurements. Linear correlation for **b**, includes all samples from MSM21/4 and POS419**.**

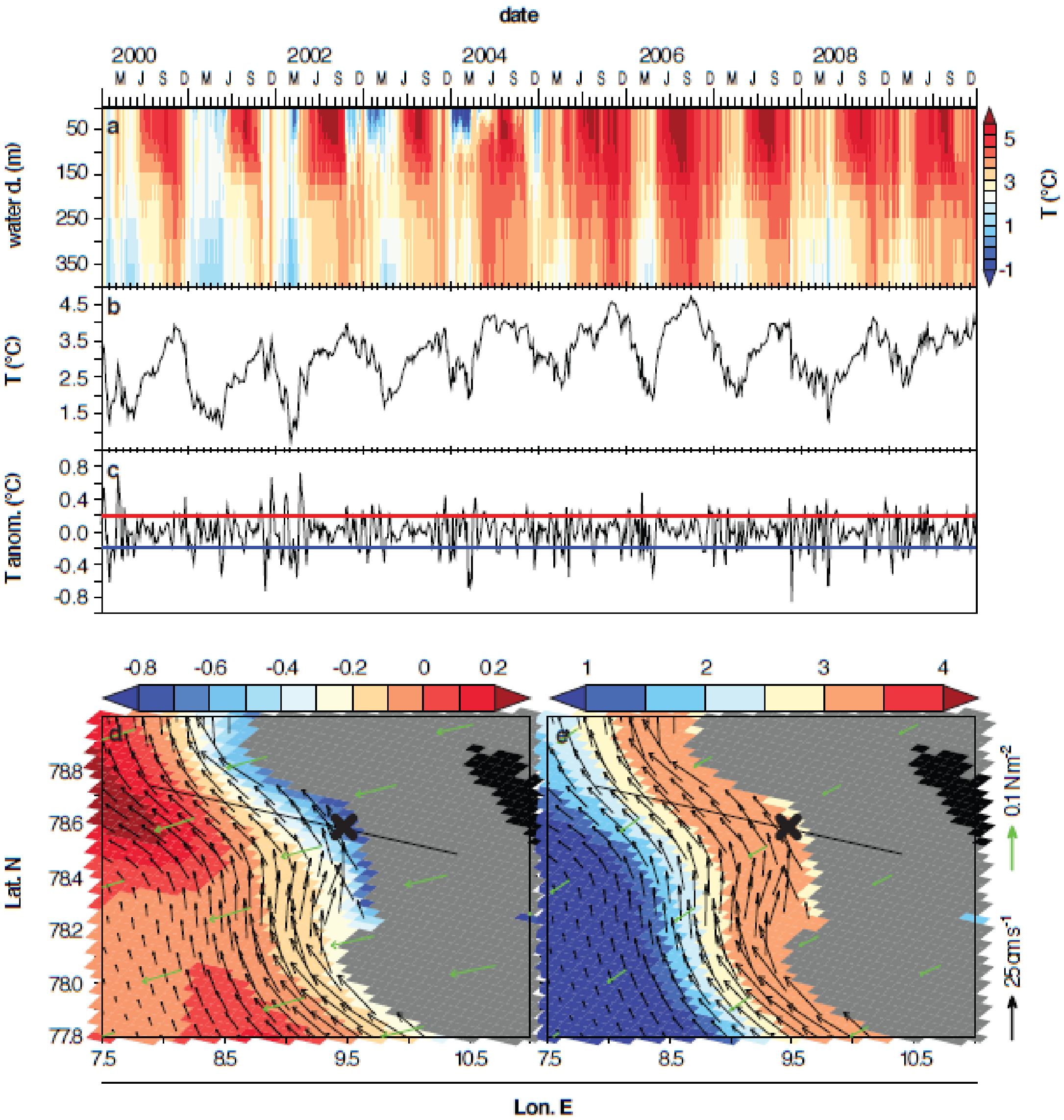

Supplementary Figure B-3: Modelled temporal progression of water temperature and circulation patterns of the WSC. Temperature distribution in **a**, the entire water column (surface to bottom), and **b**, bottom waters (300 m water depth), as well as **c**, bottom water temperature corrected for seasonal and interannual temperature variations at the MASOX site. **d**, Time-averaged circulation patterns of the WSC at 300 m water depth during the offshore mode (temperature anomaly against long-term average, colour-coded, °C), and **e**, the nearshore mode (long-term averaged temperature, colour-coded, °C). The MASOX position is indicated with a cross mark. Current velocities are indicated as black arrows and wind forcing as green arrows. The vertical distribution of time-averaged temperature, density and current velocity, respectively, along a cross-section over the MASOX site (black line) is shown in *Supplementary Figure B-2*.

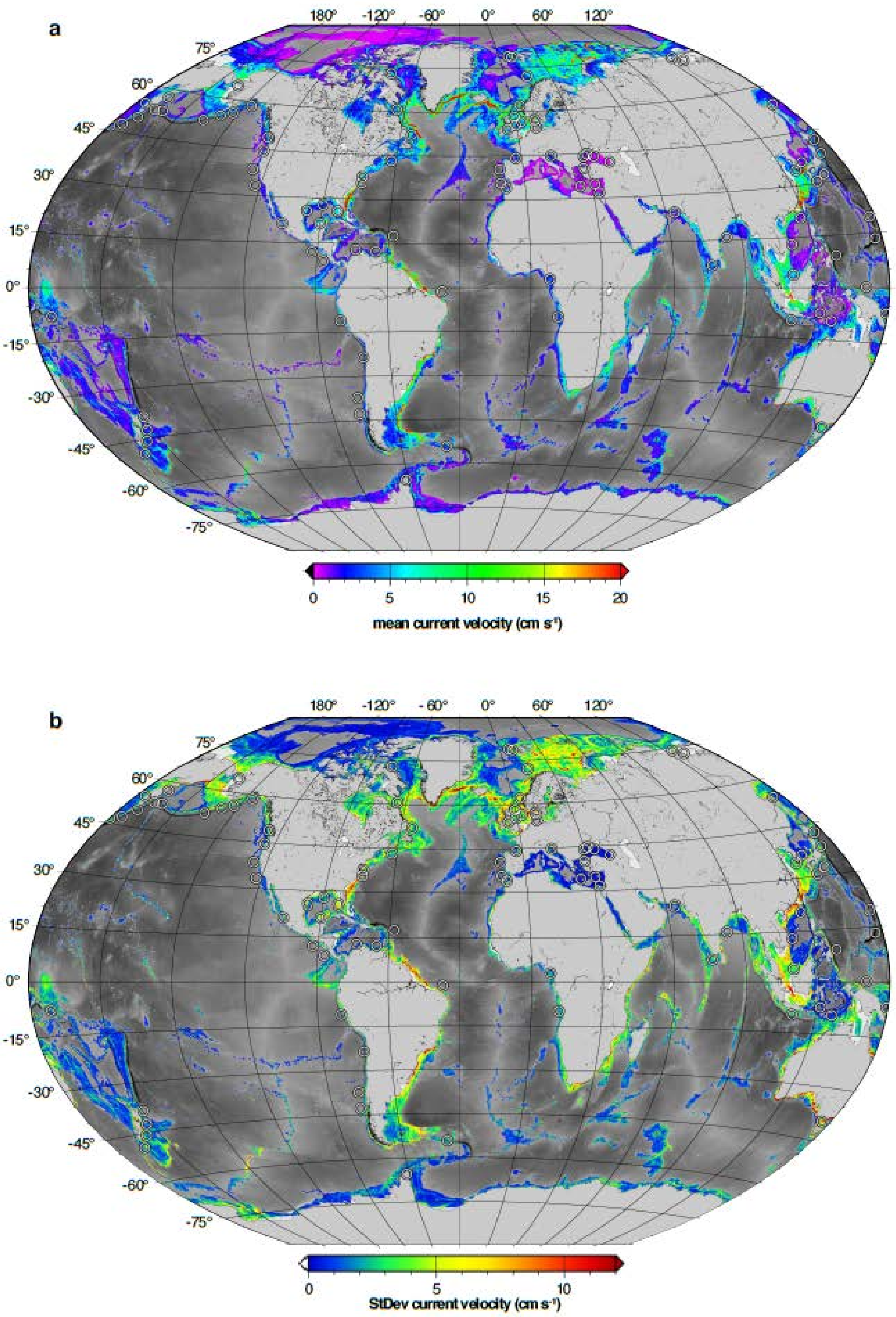

Supplementary Figure B-4 Modelled bottom current velocity and standard deviation of current velocities at methane seeps. a, Modelled (1/12° resolution) mean annual (year 2000) bottom water current velocities and, **b**, standard deviation of bottom current velocities (based on 5-day averages) for bottom depths between 100 and 2500 m. Bottom current velocities at continental margins, where most methane seeps are located, frequently exceed 10 cm s^{-1} and are highly variable. Standard deviations typically exceed 50% of the mean flow. Locations of selected methane seeps are indicated by white circles.

Supplementary Table 1: List of Stations sampled during the POS419 and MSM21/4 cruises. The numbers of bottles sampled per CTD cast are indicated.

									# niskin bottles sampled		
Cruise	**Station**	**Transect**	**Site**	**Date**	**Lat. (N)**	**Lon. (E)**	**Salinity**	**Temperature**	**CH4**	**MOx**	**CARD-FISH**
POS419	599	-	CTD-2	13.08.11	78.585	9.458	x	x	12	12	-
POS419	615	-	CTD-9	17.08.11	78.585	9.456	x	x	12	12	-
POS419	654	-	CTD-33	23.08.11	78.585	9.455	x	x	12	12	-
POS419	671	-	CTD-36	27.08.11	78.585	9.456	x	x	12	12	-
MSM21/4	546	-	MASOX	17.08.12	78.555	9.477	x	x	5	5	-
MSM21/4	550	1st	-	18.08.12	78.553	9.423	x	x	24	6	-
MSM21/4	551	1st	-	18.08.12	78.554	9.446	x	x	24	6	-
MSM21/4	552	1st	-	18.08.12	78.554	9.455	x	x	24	10	-
MSM21/4	553	1st	-	19.08.12	78.555	9.466	x	x	24	14	-
MSM21/4	554	1st	MASOX	19.08.12	78.555	9.475	x	x	24	17	6
MSM21/4	555	1st	MASOX	19.08.12	78.555	9.479	x	x	24	17	7
MSM21/4	556	1st	-	19.08.12	78.555	9.487	x	x	24	14	-
MSM21/4	557	1st	-	19.08.12	78.556	9.496	x	x	23	10	-
MSM21/4	558	1st	-	19.08.12	78.556	9.508	x	x	23	6	-
MSM21/4	558	1st	-	19.08.12	78.557	9.522	x	x	23	6	-
MSM21/4	580	-	MASOX	23.08.12	78.556	9.474	x	x	24	16	10
MSM21/4	581	-	-	24.08.12	78.556	9.472	x	x	23	16	-
MSM21/4	582	-	MASOX	24.08.12	78.556	9.476	x	x	23	16	-
MSM21/4	583	-	-	24.08.12	78.555	9.476	x	x	23	16	-
MSM21/4	584	-	-	24.08.12	78.555	9.472	x	x	23	16	-
MSM21/4	613	-	MASOX	28.08.12	78.555	9.476	x	x	24	18	-
MSM21/4	633	2nd	-	30.08.12	78.553	9.423	x	x	24	7	-
MSM21/4	634	2nd	-	30.08.12	78.554	9.446	x	x	24	7	-
MSM21/4	635	2nd	-	30.08.12	78.554	9.456	x	x	23	10	-
MSM21/4	636	2nd	-	31.08.12	78.555	9.466	x	x	24	14	-
MSM21/4	637	2nd	MASOX	31.08.12	78.555	9.476	x	x	24	17	8
MSM21/4	638	2nd	MASOX	31.08.12	78.555	9.479	x	x	24	17	8
MSM21/4	639	2nd	-	31.08.12	78.556	9.487	x	x	24	14	-
MSM21/4	640	2nd	-	31.08.12	78.556	9.497	x	x	24	10	-
MSM21/4	641	2nd	-	31.08.12	78.556	9.508	x	x	24	7	-
MSM21/4	642	2nd	-	31.08.12	78.557	9.523	x	x	23	7	-
MSM21/4	654	-	MASOX	04.09.12	78.556	9.473	x	x	24	17	-
MSM21/4	655	-	HyBIS	04.09.12	78.611	9.425	x	x	24	17	-

References

1. Berndt, C., Feseker, T., Treude, T., Krastel, S., *et al.* Temporal Constraints on Hydrate-Controlled Methane Seepage off Svalbard. *Science* **343,** 284-287 (2014).
2. Wiesenburg, D. A. & Guinasso, N. L. Equilibrium solubilities of methane, carbon monoxide, and hydrogen in water and sea water. *J. Chem. Eng. Data* **24,** 356-360 (1979).
3. Fisher, R. E., Sriskantharajah, S., Lowry, D., Lanoisellé, M., *et al.* Arctic methane sources: Isotopic evidence for atmospheric inputs. *Geophys. Res. Lett.* **38,** DOI: 10.1029/2011GL049319 (2011).
4. Valentine, D. L., Blanton, D. C., Reeburgh, W. S. & Kastner, M. Water column methane oxidation adjacent to an area of active hydrate dissociation, Eel River Basin. *Geochim. Cosmochim. Ac.* **65,** 2633-2640 (2001).
5. Reeburgh, W. S. Oceanic methane biogeochemistry. *Chem. Rev.* **107,** 486-513 (2007).
6. Niemann, H., Steinle, L., Blees, J. H., Krause, S., *et al.* Toxic effects of butyl elastomers on aerobic methane oxidation. *Limnolog and Oceanography: Methods.* **in press** (2015).
7. Pernthaler, A., Pernthaler, J. & Amann, R. Fluorescence In Situ Hybridization and Catalyzed Reporter Deposition for the Identification of Marine Bacteria. *Appl. Env. Microb.* **68,** 3094-3101 (2002).
8. Pernthaler, A. & Pernthaler, J. Fluorescence in situ hybridization for the identification of environmental microbes. *Methods Mol. Biol.* **353,** 153-164 (2007).
9. Eller, G., Stubner, S. & Frenzel, P. Group-specific 16S rRNA targeted probes for the detection of type I and type II methanotrophs by fluorescence in situ hybridisation. *FEMS Microbiol. Lett.* **198,** 91-97 (2001).
10. Behrens, E. *The oceanic response to Greenland melting: the effect of increasing model resolution* (Christian Albrechts University, Kiel , Germany, 2013).
11. Behrens, E., Biastoch, A. & Böning, C. W. Spurious AMOC trends in global ocean sea-ice models related to subarctic freshwater forcing. *Ocean Model.* **69,** 39-49 (2013).
12. Madec, G. *Nemo ocean engine, Note du Pole de modélisation, Institut Pierre-Simon Laplace (IPSL) No 27, France* 2008).
13. Debreu, L., Vouland, C. & Blayo AGRIF: Adaptive Grid Refinement in Fortran. *Comput. Geosci.* **34,** 8-13 (2008).
14. Large, W. G. & Yeager, S. G. The global climatology of an interannually varying air–sea flux data set. *Clim. Dynam.* **33,** 341-364 (2009).

15. Mertens, C., Rhein, M., Walter, M., Böning, C. W., *et al.* Circulation and transports in the Newfoundland Basin, western subpolar North Atlantic. *J. Geophys. Res.-Oceans* **119,** 7772-7793 (2014).

16. Fischer, J., Karstensen, J., Zantopp, R., Visbeck, M., *et al.* Intra-seasonal variability of the DWBC in the western subpolar North Atlantic. *Prog. Oceanogr.* 10.1016/j.pocean.2014.04.002 (2014).

17. Schauer, U., Fahrbach, E., Osterhus, S. & Rohardt, G. Arctic warming through the Fram Strait: Oceanic heat transport from 3 years of measurements. *J. Geophys. Res.-Oceans* **109,** 14 (2004).

18. Cronin, M. F., Tozuka, T., Biastoch, A., Durgadoo, J. V. & Beal, L. M. Prevalence of strong bottom currents in the greater Agulhas system. *Geophys. Res. Lett.* **40,** 1772-1776 (2013).

APPENDIX C

Supplemental Material for Chapter 4: Fluxes and fate of dissolved methane released at the seafloor at the landward limit of the gas hydrate stability zone offshore Western Svalbard

Contents

Supplemental Figure C-1

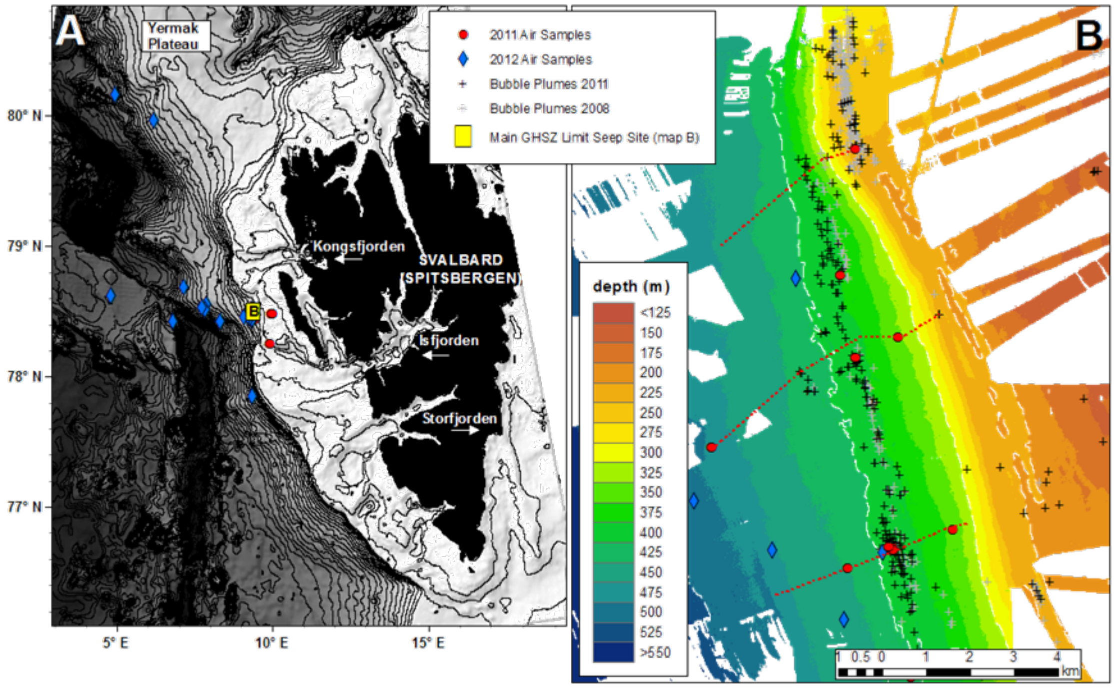

Map of study area and atmospheric sampling sites. Bathymetry in **A** is from The GEBCO_08 Grid version 20100927, http://gebco.net, **B** shows shipboard bathymetry from cruise JR253. Red lines indicate water column sampling transects shown in *Figure 4-2*.

Supplemental Figure C-2

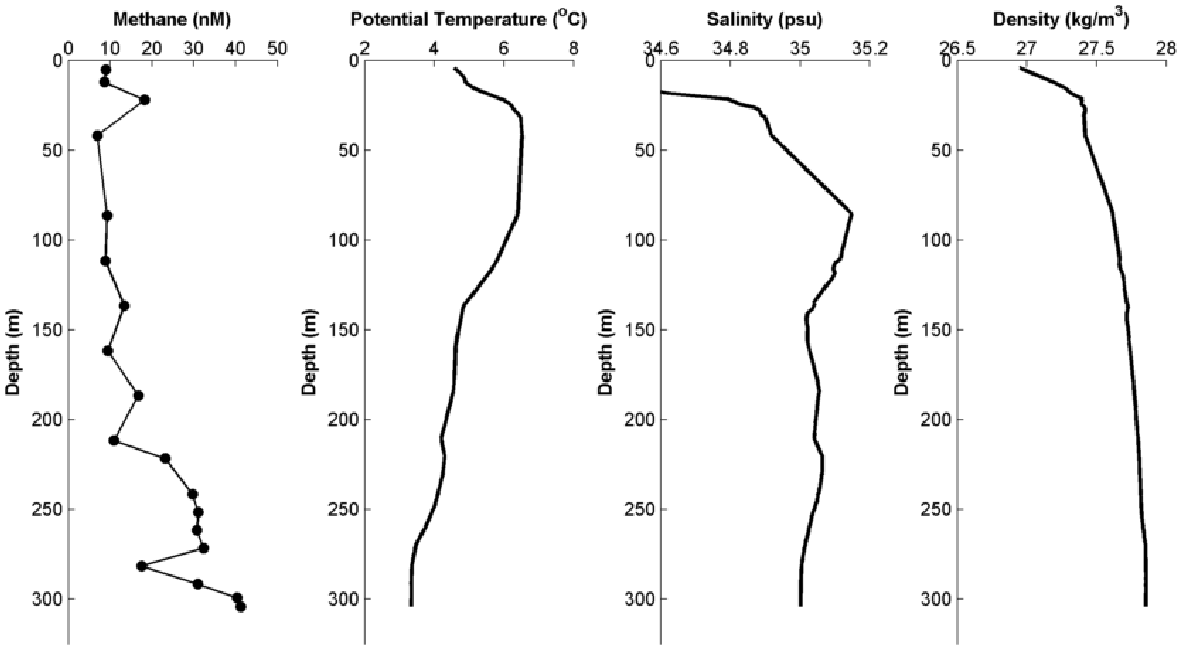

Southern station (MSM 658), ~ 30 km south of main seepage site – providing evidence for undiscovered methane seepage in this area.

Supplemental Table C-1

Water column sampling stations for depth profiles at the main gas hydrate stability zone limit seafloor seep site (left), and on the shelf (right).

CTD-ID	Date	Latitude (N)	Longitude (E)	Water Depth (m)
Cruise JR253				
3	07/08/2011	78 ° 33.296 '	9 ° 28.58 '	384
4	08/08/2011	78 ° 32.772 '	9 ° 21.35 '	458
5	08/08/2011	78 ° 33.538 '	9 ° 32.05 '	343
6	08/08/2011	78 ° 33.611 '	9 ° 33.10 '	313
7	09/08/2011	78 ° 36.187 '	9 ° 31.62 '	217
8	09/08/2011	78 ° 35.903 '	9 ° 29.11 '	323
9	09/08/2011	78 ° 35.500 '	9 ° 22.98 '	407
12	12/08/2011	78 ° 34.576 '	9 ° 17.44 '	463
13	12/08/2011	78 ° 35.915 '	9 ° 26.65 '	375
14	13/08/2011	78 ° 37.064 '	9 ° 25.36 '	371
15	14/08/2011	78 ° 37.062 '	9 ° 18.15 '	440
16	14/08/2011	78 ° 38.114 '	9 ° 24.35 '	315
17	14/08/2011	78 ° 38.241 '	9 ° 26.48 '	218
18	15/08/2011	78 ° 33.295 '	9 ° 28.66 '	385
Cruise MSM21/4				
550	18/08/2012	78 ° 33.152 '	9 ° 25.38 '	424
551	18/08/2012	78 ° 33.227 '	9 ° 26.76 '	402
552	18/08/2012	78 ° 33.249 '	9 ° 27.33 '	403
553	19/08/2012	78 ° 33.280 '	9 ° 27.96 '	396
554	19/08/2012	78 ° 33.300 '	9 ° 28.52 '	387
555	19/08/2012	78 ° 33.308 '	9 ° 28.72 '	390
556	19/08/2012	78 ° 33.330 '	9 ° 29.22 '	387
557	19/08/2012	78 ° 33.348 '	9 ° 29.79 '	381
558	19/08/2012	78 ° 33.374 '	9 ° 30.49 '	376
559	19/08/2012	78 ° 33.402 '	9 ° 31.35 '	354
580	23/08/2012	78 ° 33.332 '	9 ° 28.43 '	387
581	24/08/2012	78 ° 33.354 '	9 ° 28.30 '	387
582	24/08/2012	78 ° 33.355 '	9 ° 28.54 '	389
583	24/08/2012	78 ° 33.316 '	9 ° 28.56 '	391
584	24/08/2012	78 ° 33.313 '	9 ° 28.30 '	388
613	28/08/2012	78 ° 33.310 '	9 ° 28.56 '	391
633	30/08/2012	78 ° 33.160 '	9 ° 25.39 '	424
634	30/08/2012	78 ° 33.240 '	9 ° 26.78 '	403
635	30/08/2012	78 ° 33.260 '	9 ° 27.34 '	404
636	31/08/2012	78 ° 33.290 '	9 ° 27.97 '	395
637	31/08/2012	78 ° 33.310 '	9 ° 28.53 '	385
638	31/08/2012	78 ° 33.320 '	9 ° 28.73 '	391
639	31/08/2012	78 ° 33.340 '	9 ° 29.22 '	387
640	31/08/2012	78 ° 33.360 '	9 ° 29.80 '	380
641	31/08/2012	78 ° 33.380 '	9 ° 30.50 '	376
642	31/08/2012	78 ° 33.410 '	9 ° 31.36 '	354
654	04/09/2012	78 ° 33.340 '	9 ° 28.39 '	391
655	04/09/2012	78 ° 36.670 '	9 ° 25.48 '	380
656	04/09/2012	78 ° 39.300 '	9 ° 26.01 '	244
658	04/09/2012	78 ° 18.840 '	9 ° 41.64 '	244

Latitude (N)	Longitude (E)	Water Depth (m)
On shelf Stations		
16/08 to 23/08, 2011		
78 ° 35.05 '	10 ° 7.72 '	77
78 ° 34.504 '	10 ° 7.72 '	80
78 ° 33.977 '	10 ° 7.72 '	89
78 ° 33.976 '	10 ° 10.40 '	77
78 ° 33.959 '	10 ° 13.15 '	110
78 ° 34.506 '	10 ° 13.11 '	138
78 ° 35.041 '	10 ° 13.18 '	136
78 ° 35.036 '	10 ° 10.40 '	106
78 ° 34.722 '	10 ° 9.32 '	90
78 ° 34.510 '	10 ° 9.30 '	86
78 ° 34.288 '	10 ° 9.36 '	76
78 ° 34.289 '	10 ° 10.40 '	83
78 ° 34.288 '	10 ° 11.49 '	104
78 ° 34.506 '	10 ° 11.49 '	102
78 ° 34.721 '	10 ° 11.49 '	104
78 ° 34.720 '	10 ° 10.39 '	91
78 ° 34.614 '	10 ° 9.87 '	91
78 ° 34.516 '	10 ° 9.83 '	88
78 ° 34.403 '	10 ° 9.84 '	85
78 ° 34.399 '	10 ° 10.38 '	88
78 ° 34.400 '	10 ° 10.92 '	95
78 ° 34.509 '	10 ° 10.86 '	95
78 ° 34.612 '	10 ° 10.88 '	99
78 ° 34.612 '	10 ° 10.42 '	88
78 ° 34.513 '	10 ° 10.10 '	89
78 ° 34.456 '	10 ° 10.12 '	89
78 ° 34.450 '	10 ° 10.42 '	88
78 ° 34.451 '	10 ° 10.69 '	90
78 ° 34.507 '	10 ° 10.68 '	90
78 ° 34.568 '	10 ° 10.67 '	91
78 ° 34.568 '	10 ° 10.38 '	87
78 ° 34.569 '	10 ° 10.10 '	87
78 ° 34.501 '	10 ° 10.44 '	87

Supplemental Table C-2

Depth averaged methane concentrations and oxidation rate constants for on-seep and off-seep stations (page 1 of 2).

cruise	CTD-ID	sampling date	sampling time (UTC)	latitude minutes (78°N)	longitude minutes (9° E)	water depth (m)	$[CH_4]$ in methane input volume (nM)	$[CH_4]$ in upper water column (nM)	k_{MOX} in methane input volume (day^{-1})	k_{MOX} in upper water column (day^{-1})	distance from seepage region (m)	$\delta C/\delta x$ ($nM\ m^{-1}$)
on seep stations												
JR253	3	07/08/2011	23:12	33.296	28.579	371	60	5.7	-	-	-	-
JR253	8	09/08/2011	5:27	35.903	29.111	375	91	6.8	-	-	-	-
JR253	13	12/08/2011	13:39	35.915	26.652	384	372	19	-	-	-	-
JR253	14	13/08/2011	18:42	37.064	25.360	385	69	27	-	-	-	-
MSM21-4	552-557						44	18	3.5E-2	1.2E-2		
MSM21-4	*552*	*18/08/2012*	*22:53*	*33.249*	*27.33*	*403*	*44*	*20*	*3.9E-2*	*1.5E-3*	-	-
MSM21-4	*553*	*19/08/2012*	*0:05*	*33.280*	*27.96*	*396*	*37*	*21*	*4.5E-2*	*2.6E-3*	-	-
MSM21-4	*554*	*19/08/2012*	*1:25*	*33.300*	*28.52*	*387*	*51*	*18*	*4.4E-2*	*3.1E-3*	-	-
MSM21-4	*555*	*19/08/2012*	*2:36*	*33.308*	*28.72*	*390*	*56*	*19*	*3.2E-2*	*6.8E-3*	-	-
MSM21-4	*556*	*19/08/2012*	*3:52*	*33.330*	*29.22*	*387*	*44*	*15*	*2.7E-2*	*4.8E-2*	-	-
MSM21-4	*557*	*19/08/2012*	*5:09*	*33.348*	*29.79*	*381*	*34*	*14*	*2.5E-2*	-	-	-
MSM21-4	580-584						88	16	4.2E-3	-		
MSM21-4	*580*	*23/08/2012*	*22:47*	*33.332*	*28.43*	*387*	*31*	*11*	*9.0E-4*	-	-	-
MSM21-4	*581*	*24/08/2012*	*1:00*	*33.354*	*28.30*	*387*	*62*	*16*	*2.3E-3*	-	-	-
MSM21-4	*582*	*24/08/2012*	*2:35*	*33.355*	*28.54*	*389*	*97*	*14*	*2.3E-3*	-	-	-
MSM21-4	*583*	*24/08/2012*	*4:00*	*33.316*	*28.56*	*391*	*100*	*18*	*5.6E-3*	-	-	-
MSM21-4	*584*	*24/08/2012*	*5:23*	*33.313*	*28.30*	*388*	*149*	*20*	*9.7E-3*	-	-	-
MSM21-4	613	28/08/2012	19:23	33.310	28.56	391	50	21	6.1E-3	-	-	-
MSM21-4	635-640						64	19	1.5E-2	1.7E-3		
MSM21-4	*635*	*30/08/2012*	*22:48*	*33.260*	*27.34*	*404*	*69*	*15*	*9.7E-3*	*1.4E-3*	-	-
MSM21-4	*636*	*31/08/2012*	*0:02*	*33.290*	*27.97*	*395*	*40*	*15*	*1.2E-2*	*2.9E-3*	-	-
MSM21-4	*637*	*31/08/2012*	*1:15*	*33.310*	*28.53*	*385*	*85*	*18*	*1.0E-2*	*1.4E-3*	-	-
MSM21-4	*638*	*31/08/2012*	*2:45*	*33.320*	*28.73*	*391*	*81*	*26*	*1.2E-2*	*1.4E-3*	-	-
MSM21-4	*639*	*31/08/2012*	*4:02*	*33.340*	*29.22*	*387*	*55*	*18*	*2.0E-2*	*1.7E-3*	-	-
MSM21-4	*640*	*31/08/2012*	*5:10*	*33.360*	*29.80*	*380*	*54*	*21*	*2.5E-2*	*1.4E-3*	-	-
MSM21-4	655	04/09/2012	2:09	36.670	25.48	380	239	11	1.3E-2	3.4E-3	-	-
MSM21-4	654	04/09/2012	0:55	33.340	28.39	391	74	8.1	2.3E-2	3.2E-3	-	-
on seep averages……………………………………………………………….…						**388**	**93**	**15**	**1.6E-2**	**5.2E-3**		

Supplemental Table C-2

Depth averaged methane concentrations and oxidation rate constants for on-seep and off-seep stations (page 2 of 2).

cruise	CTD-ID	sampling date	sampling time (UTC)	latitude minutes (78°N)	longitude minutes (9° E)	water depth (m)	$[CH_4]$ in methane input volume (nM)	$[CH_4]$ in upper water column (nM)	k_{MOX} in methane input volume (day^{-1})	k_{MOX} in upper water column (day^{-1})	distance from seepage region (m)	$\delta C/\delta x$ (nM m^{-1})
deeper stations												
JR253	4	08/08/2011	2:00	32.772	21.35	458	5.8	6.9	-	-	2700	0.03
JR253	9	09/08/2011	9:31	35.500	22.98	407	4.6	4.5	-	-	1000	0.09
JR253	12	12/08/2011	9:05	34.576	17.44	463	3.3	3.2	-	-	3500	0.03
MSM21-4	550	18/08/2012	19:02	33.152	25.38	424	45	20	-	-	1000	0.05
MSM21-4	633	30/08/2012	19:41	33.160	25.39	424	83	15	-	-	1000	0.01
MSM21-4	551	18/08/2012	21:14	33.227	26.76	402	35	21	-	-	570	0.10
MSM21-4	634	30/08/2012	21:27	33.240	26.78	403	55	14	-	-	570	0.07
shallower stations												
JR253	5	08/08/2011	17:49	33.538	32.05	343	30	9	-	-	1000	0.06
JR253	8	09/08/2011	5:27	35.903	29.11	323	17	10	-	-	1000	0.08
JR253	7	09/08/2011	2:00	36.187	31.62	217	-	9	-	-	1959	-
JR253	6	08/08/2011	22:02	33.611	33.10	313	-	10	-	-	1770	-
MSM21-4	558	19/08/2012	6:22	33.374	30.49	376	33	20	-	-	400	0.15
MSM21-4	641	31/08/2012	6:26	33.380	30.50	376	50	21	-	-	400	0.11
MSM21-4	559	19/08/2012	7:32	33.402	31.35	354	38	19	-	-	700	0.08
MSM21-4	642	31/08/2012	8:02	33.410	31.36	354	41	15	-	-	700	0.07

Supplemental material for air-sea flux calculations

Parameterizations of gas transfer velocity

A number of different parameterizations for the gas transfer velocity (k) in terms of wind-speed are shown in *Supplemental Table C-3*. This list includes parameterizations used in similar studies of sea-air methane flux, and is demonstrative rather than exhaustive. While the choice of k parameterisation can significantly impact estimations of sea-air flux, a range of equations are used in recent literature concerning marine methane air-sea exchange. The functional forms of the equations are based on theoretical understanding of air-sea gas exchange [Wanninkhof et al., 2009], and fit to experimental and observational data including the global natural and bomb-^{14}C-CO_2 constraints, wind tunnel experiments, and shipboard deliberate tracer studies. The range of wind speeds and time intervals of wind-speed averaging are important considerations in the choice of parameterization as the functionality of the dependence of k on u_{10} likely differs between low, average, and high wind speeds (e.g. Liss and Merlivat [1986]; Wanninkhof et al. [2009]) and fit constants depend on the averaging interval of wind speed data (e.g. [Wannikhof and McGillis, 1999; Wanninkhof, 1992]).

To demonstrate the effect different of k parameterization choices, we use those of Liss and Merlivat [1986] (LM86), Wanninkhof [1992] (W92), Nightengale et al. [2000] (N00), McGillis et al. [2001] (M01) and Wanninkhof et al. [2009] (W09). These parameterisations allow comparison to earlier works (LM86 and W92 are widely cited), and also include the revised quadratic form of W09. N00 and M01 are included to test the effects of the different functional forms (linear term in N00, and cubic in M01). The limited fetch conditions in the N00 data are appropriate for the relatively near-shore Svalbard seepage site [Saloranta and Svendsen, 2001], and the high wind conditions incorporated in both N00 and M01 reflect the high winds observed during 2012 (above prevailing global average wind speeds of 6-10 m s^{-1} [Wanninkhof et al., 2009]).

The resulting sea-air fluxes calculated with the five chosen gas transfer velocity parameterizations are given in *Supplemental Table C-4*. The difference between flux results due to choice of k parameterization is relatively small compared to the uncertainty contribution from the observed variability of the measured parameters incorporated in the calculation (on the order of ± 50 %, see *Section 4.3.2*). This dominant source of uncertainty

Supplemental Table C-3 Gas transfer velocity wind speed parameterizations**.** k_{660} is the gas transfer velocity for a gas with a Schmidt number (Sc) of 660 (ie: CO_2 at T=20 °C).. Equations in bold have been applied in this study. Applications in literature are examples of use for sea to air methaen fluxes.

Parameterization (k_{660} [cm hr^{-1}])	**Source**	**Method**	**Wind-Averaging**	**Applications in Literature**
0.1595 u_{10} for $u_{10} \le 3.6$ **2.717 u_{10} -9.201 for $3.6 < u_{10} \le 13$** **5.625 u_{10} - 47.006 for $u_{10} > 13$ ***	**Liss and Merlivat, [1986]**	extrapolation of SF_6 tracer experiment over a lake to all wind speeds using composite of available wind tunnel experiment data	short term	Kourtidis et al. [2006]; Rehder and Suess [2001]
0.39 u_{10}^2	Wanninkhof [1992]	quadratic relationship assumed, global ocean bomb and natural ^{14}C-CO_2 and Red Sea bomb ^{14}C-CO_2 gas exchange data, with long term average u_{10}	long term	Schmale et al. [2001]
0.31 u_{10}^2	**Wanninkhof et al. [2009]**	as above, but assuming a Weibull distribution about the u_{10}	short term	Bussmann [2013]; Florez-Leiva et al. 2013; Kourtidis et al. [2006]; Mau et al. [2007]; [2012]; Shakhova et al. [2010]; Solomon et al. [2009]
0.0283 u_{10}^3	Wannikhof and McGillis [1999]	fit to shipboard CO_2 covariance data from GasEx-98 experiment and global bomb ^{14}C-CO_2 data with global u_{10} distribution; explicitly limit to CO_2 only due to gas solubility effects on bubble-mediated transfer which justifies the cubic wind-speed relationship**	short term	-
0.3175 u_{10} + 0.2117 u_{10}^2 *	**Nightingale et al. [2000]**	release of SF_6 and ^3He tracers at ~25 m water depth, 35 km from coast (fetch limited, North Sea)	short term	Daniel et al. [2013]; Mau et al. [2007]; [2012]
3.3 + 0.026 u_{10}^3	**McGillis et al. [2001]**	fit to GasEx-98 data: simultaneous application of multiple shipboard methods, North Atlantic, observed u_{10} 1-16 m s^{-1}	short term	Kourtidis et al [2006]; Mau et al [2007];[2012]
0.257 u_{10}^2 *	Ho et al. [2006]	deliberate tracer study with SF_6 and ^3He, including u_{10} up to 16 cm s^{-1}	short term	Mau et al. [2007]; [2012]
0.27 u_{10}^2	Sweeney et al. [2007]	update of Wanninkhof [1992], scaled to a revised global ^{14}C-CO_2 bomb constraint and applying more representative globally varied CO_2 solubility parameters, and global u_{10} distribution	short term	Hu et al. [2012]; Yoshida et al. [2011]; Zhang et al [2014]
3 + 0.1 u_{10} + 0.064u_{10}^2 + 0.011 u_{10}^3	Wanninkhof et al. [2009]	semi-empirical hybrid model using global bomb ^{14}C-CO_2 constraint and global u_{10} distribution; chemical enhancement for CO_2 accounts for 2.3 cm hr^{-1} of the constant term	short term	-
0.24 u_{10}^2	**Wanninkhof et al. [2009]**	quadratic fit to semi-empirical hybrid model using global bomb ^{14}C-CO_2 constraint and global u_{10} distribution; agrees with hybrid model for u_{10} < 15 m s^{-1}	short term	Gülzow et al. [2013]

* parameterizations published in terms of k_{600}, converted to k_{660} for comparison

** the solubility of CO_2 is ~20 times that of CH_4 at average observed study conditions of T=6° C and S=34 (Bunsen solubilities calculated following Weiss [1974] and [Wisenburg and Guinasso [1979] in sea-air methane flux reflects the unavoidable uncertainty related to extrapolating spatially and temporally limited observations over a heterogeneous study area and to seasonal to annual time scales.

Supplemental Table C-4 Gas transfer velocities and methane sea-air fluxes calculated by different wind-speed parameterizations.

	gas transfer velocity (*k*) (m day^{-1})					**sea-air flux (mmol m^{-2} day^{-1})**				
	LM86	**W92**	**N00**	**M01**	**W09**	**LM86**	**W92**	**N00**	**M01**	**W09**
Depth Profiles										
2011										
average u_{10}	**2.0**	**3.2**	**2.6**	**2.6**	**2.4**					
u_{10} distribution	**2.1**	**3.7**	**2.9**	**3.6**	**2.8**	**12**	**21**	**16**	**20**	**16**
minimum (u_{10}, *Sc*)	0.00	0.00	0.01	0.50	0.00					
maximum (u_{10}, *Sc*)	9	16	12	25	13					
2012										
average u_{10}	**2.4**	**3.9**	**3.1**	**3.5**	**3.0**					
u_{10} distribution	**2.9**	**5.2**	**4.0**	**5.9**	**4.0**	**22**	**40**	**31**	**45**	**31**
minimum (u_{10}, *Sc*)	0.06	0.35	0.37	0.60	0.27					
maximum (u_{10}, *Sc*)	8.1	15	11	22	12					
Equilibrator										
GHSZ limit seeps	*average*					**3**	**5**	**4**	**5**	**4**
	maximim					*12*	*23*	*17*	*31*	*17*
deep	*average*					**1**	**1**	**1**	**1**	**1**
	maximim					*7*	*13*	*10*	*14*	*10*
north	*average*					**1**	**1**	**1**	**1**	**1**
	maximim					*4*	*6*	*5*	*5*	*4*
south	*average*					**2**	**4**	**3**	**4**	**3**
	maximim					*12*	*23*	*17*	*30*	*18*
outer Shelf	*average*					**5**	**8**	**7**	**9**	**6**
	maximim					*16*	*32*	*24*	*38*	*25*
inner Shelf	*average*					**6**	**11**	**9**	**10**	**8**
	maximim					*26*	*47*	*42*	*40*	*36*

Uncertainties related to averaging of observed parameters for depth profile data

The uncertainty contribution due to variability in atmospheric parameters and surface seawater temperature and salinity is relatively small (< 10 %). The temporal variability in wind speed is accounted for by calculating the sea-air flux for the distribution of observations and averaging the result. Shipboard wind speed measurements may be subject to airflow distortions and can overestimate wind speeds by 5-10 % [Ho et al., 2006; Popinet et al., 2004]. The magnitude of such effects on our data are unquantified and therefore no correction has been made. The most significant contribution to the overall uncertainty in the sea-air methane flux is the surface seawater methane concentration. While concentrations are generally higher than atmospheric equilibrium, the degree of supersaturation varies significantly: from -20 to 200 % in 2011 and 35 to 470 % in 2012 (*Supplemental Table C-5*). A best representative estimate of the surface seawater supersaturation is calculated from the midpoint of concentration data for each year, in order to avoid the sampling bias effect of averaging limited observations. Uncertainty is estimated as the average deviation of measurements from the midpoint: ~ ± 40 % for the 2011 data and 30 % for 2012. Combined with the uncertainty estimates for the other parameters, the total uncertainty in the sea-air flux is expected to be ~ ± 50 %.

Supplemental Table C-5 Observed and calculated parameters involved in the calculation of sea-air methane flux for depth profile data, and their contribution to the overall uncertainty due to variability during sampling.

	total atmospheric pressure	atmospheric methane	methane partial pressure	surface seawater temperature	surface seawater temperature	surface seawater salinity	Bunsen solubility coefficient	equilibrium surface seawater methane	observed surface seawater methane	% super-saturation	Schmidt number (*Sc*)	wind speed (u_{10})
	(mbar)	(ppb)	(mbar x 10^3)	C	K	psu	-	nM	nM	%	-	m s^{-1}
2011												
average	**1014**	**1866**	**1.89**	**5.0**	**278**	**33.0**	**0.039**	**3.3**	**8.9**	**271**	**1518**	**8**
minimum	989	1852	1.83	3.4	277	29.1	0.038	3.0	2.9	298	1391	0
maximum	1023	1890	1.93	6.5	280	34.6	0.042	3.6	9.0	81	1668	18
2012												
average	**999**	**1891**	**1.89**	**5.0**	**278**	**34.3**	**0.039**	**3.3**	**11**	**336**	**1518**	**9**
minimum	989	1883	1.86	4.8	278	33.7	0.037	3.0	4.5	572	1351	3
maximum	1005	1899	1.91	7.0	280	35.1	0.039	3.3	17	136	1536	17
overall average	**1007**	**1879**	**1.89**	**5.0**	**278**	**33.65**	**0.039**	**3.3**	**9.9**	**303**	**1518**	**8**
minimum	989	1852	1.83	3.4	277	29.10	0.037	3.0	2.9	81	1351	0
maximum	1023	1899	1.94	7.0	280	35.10	0.042	3.6	17	573	1668	18
- % uncertainty	*-2*	*-1*	*-3*	*-32*	*-0.6*	*-14*	*-5.9*	*-8.8*	*-70*	*-73*	*-11*	*-97*
+ % uncertainty	*2*	*1*	*3*	*40*	*0.7*	*4*	*7.7*	*9.8*	*75*	*89*	*10*	*110*

APPENDIX D

Supplemental Material for Chapter 5: History of methane seepage on the upper continental margin offshore Western Svalbard

Contents

Supplemental Figure D-1a

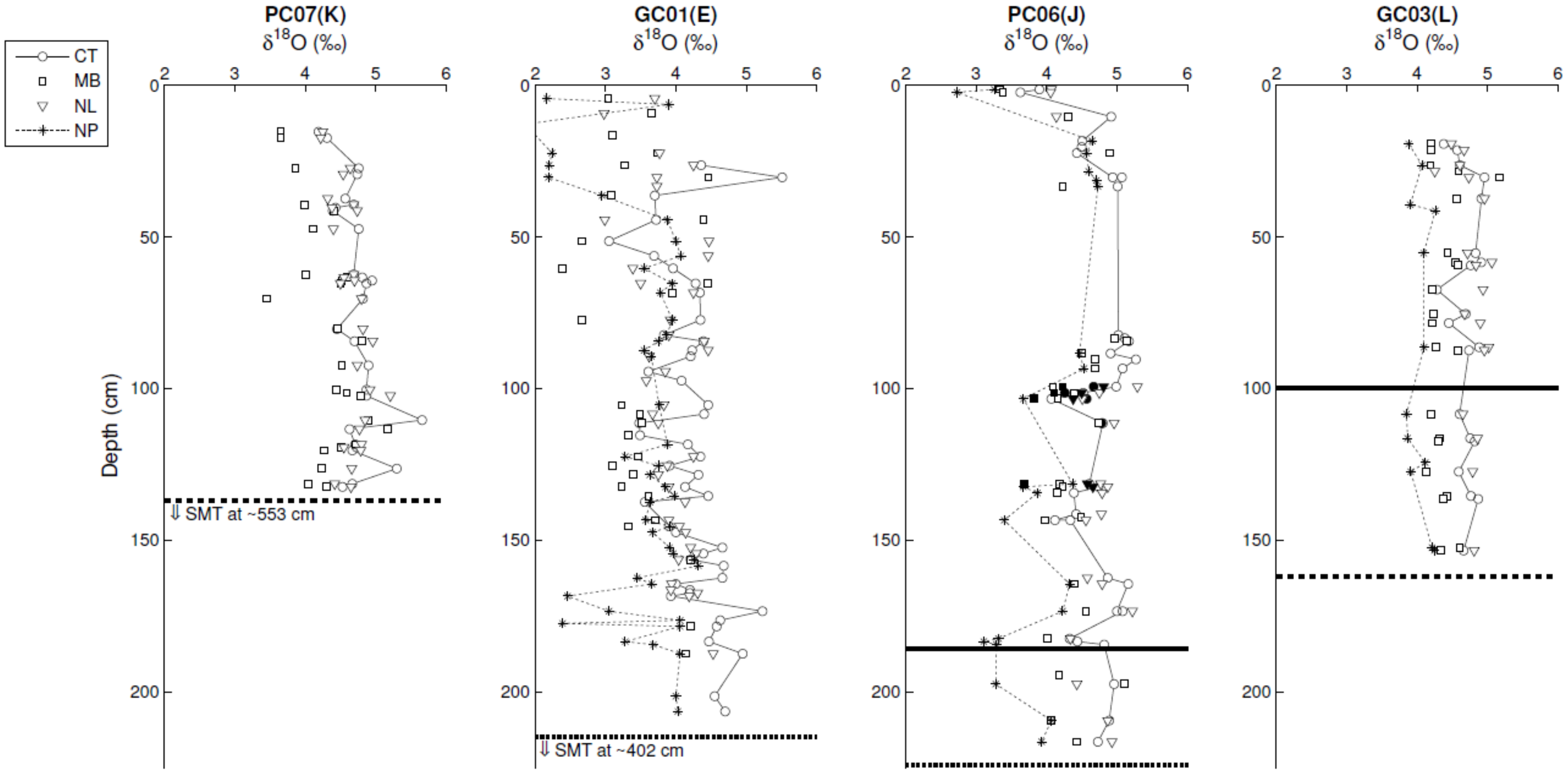

Depth profiles of δ^{13}C for planktonic (NP: *N. pachyderma s.*, stars), and benthic (CT: *C. neoteretis*, MB: *M. barleanum*, and NL: *N labradorica*) foraminifera Solid horizontal lines show the depth of the present-day sulphate-methane transition zone, and dashed horizontal line indicate the depth of sediment recovered in the cores.

Supplemental Figure D-1b

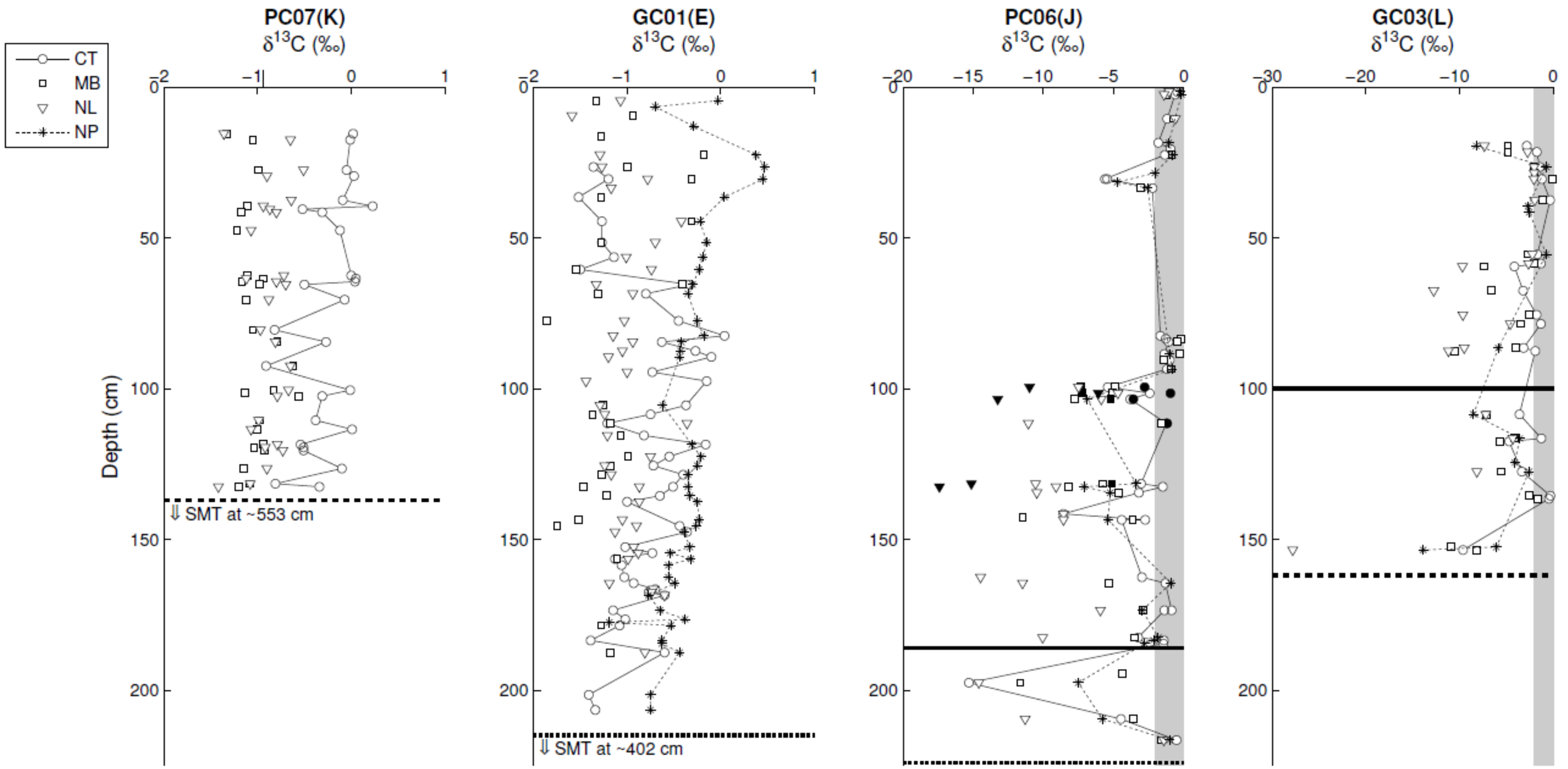

Depth profiles of δ^{13}C for planktonic (NP: *N. pachyderma s.*, stars), and benthic (CT: *C. neoteretis*, MB: *M. barleanum*, and NL: *N labradorica*) foraminifera Filled symbols are samples which have been subject to more extensive oxidative cleaning process. Shaded regions of GHSZ-limit cores (PC06 and GC03) indicate the x-axis range shown for landward cores. Solid horizontal lines show the depth of the present-day sulphate-methane transition zone, and dashed horizontal line indicate the depth of sediment recovered in the cores.

Supplemental Figure D-2

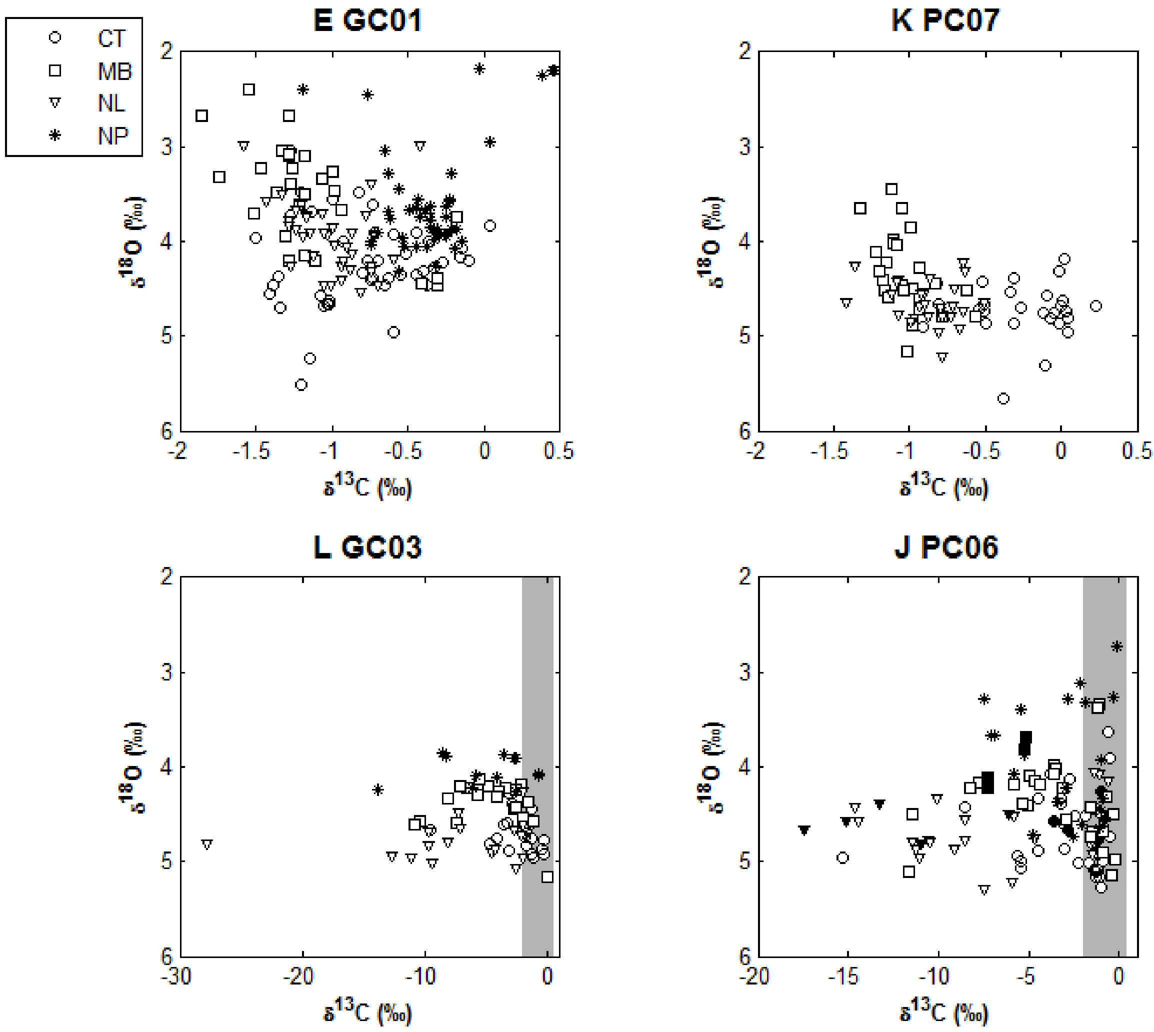

Cross plots of δ^{18}O and δ^{13}C for planktonic (NP: *N. pachyderma s.*, stars), and benthic (CT: *C. neoteretis*, MB: *M. barleanum*, and NL: *N labradorica*) foraminifera. Grey bars indicate the range of δ13C plotted for off-seep cores. There is no correlation between δ^{18}O and δ^{13}C values.

References

Aagaard, K., Foldvik, A. and Hillman, S.R. (1987) The West Spitsbergen Current: Disposition and water mass transformation. *Journal of Geophysical Research* **92**, 3778-3784.

Andersen, E.S., Dokken, T.M., Elverhøi, A., Solheim, A. and Fossen, I. (1996) Late Quaternary sedimentation and glacial history of the western Svalbard continental margin. *Marine Geology* **133**, 123-156.

Andersen, K.K., Azuma, N., Barnola, J.M., Bigler, M., Biscaye, P., Caillon, N., Chappellaz, J., Clausen, H.B., Dahl-Jensen, D., Fischer, H., Fluckiger, J., Fritzsche, D., Fujii, Y., Goto-Azuma, K., Grønvold, K., Gundestrup, N.S., Hansson, M., Huber, C., Hvidberg, C.S., Johnsen, S.J., Jonsell, U., Jouzel, J., Kipfstuhl, S., Landais, A., Leuenberger, M., Lorrain, R., Masson-Delmotte, V., Miller, H., Motoyama, H., Narita, H., Popp, T., Rasmussen, S.O., Raynaud, D., Rothlisberger, R., Ruth, U., Samyn, D., Schwander, J., Shoji, H., Siggard-Andersen, M.-L., Steffensen, J.P., Stocker, T., Sveinbjornsdottir, A.E., Svensson, A., Takata, M., Tison, J.-L., Thorsteinsson, T., Watanabe, O., Wilhelms, F. and White, J.W.C. (2004) High-resolution record of Northern-Hemisphere climate extending into the last interglacial period. *Nature* **431**, 147-151.

Archer, D. (2007) Methane hydrate stability and anthropogenic climate change. *Biogeosciences* **4**, 521-544.

Archer, D., Buffett, B. and Brovkin, V. (2009a) Ocean methane hydrates as a slow tipping point in the global carbon cycle. *Proceedings of the National Academy of Sciences* **106**, 20596-20601.

Archer, D., Eby, M., Brovkin, V., Ridgwell, A., Cao, L., Mikolajewicz, U., Caldeira, K., Matsumoto, K., Munhoven, G., Montenegro, A. and Tokos, K. (2009b) Atmospheric lifetime of fossil fuel carbon dioxide. *Annual Review of Earth and Planetary Sciences* **37**, 117-134.

Arndt, S., Jørgensen, B.B., LaRowe, D.E., Middelburg, J.J., Pancost, R.D. and Regnier, P. (2013) Quantifying the degradation of organic matter in marine sediments: A review and synthesis. *Earth-Science Reviews* **123**, 53-86.

Baumgartner, M., Schilt, A., Eicher, O., Schmitt, J., Schwander, J., Spahni, R., Fischer, H. and Stocker, T.F. (2012) High-resolution interpolar difference of atmospheric methane around the Last Glacial Maximum. *Biogeosciences* **9**, 3961-3977.

Bayon, G., Pierre, C., Etoubleau, J., Voisset, M., Cauquil, E., Marsset, T., Sultan, N., Le Drezen, E. and Fouquet, Y. (2007) Sr/Ca and Mg/Ca ratios in Niger Delta sediments: Implications for authigenic carbonate genesis in cold seep environments. *Marine Geology* **241**, 93-109.

Beal, E.J., House, C.H. and Orphan, V.J. (2009) Manganese- and iron-dependent marine methane oxidation. *Science* **325**, 184-187.

Bernard, B.B., Brooks, J.M. and Sackett, W.M. (1976) Natural gas seepage in the Gulf of Mexico. *Earth and Planetary Science Letters* **31**, 48-54.

Berndt, C., Feseker, T., Treude, T., Krastel, S., Liebetrau, V., Niemann, H., Bertics, V.J., Dumke, I., Dunnbier, K., Ferre, B., Graves, C., Gross, F., Hissmann, K., Huhnerbach, V., Krause, S., Lieser, K., Schauer, J. and Steinle, L. (2014) Temporal constraints on hydrate-controlled methane seepage off Svalbard. *Science* **343**, 284-287.

Bhatnagar, G., Chatterjee, S., Chapman, W.G., Dugan, B., Dickens, G.R. and Hirasaki, G.J. (2011) Analytical theory relating the depth of the sulfate-methane transition to gas hydrate distribution and saturation. *Geochemistry Geophysics Geosystems* **12**, Q03003.

Biastoch, A., Treude, T., Rupke, L.H., Riebesell, U., Roth, C., Burwicz, E.B., Park, W., Latif, M., Boning, C.W., Madec, G. and Wallmann, K. (2011) Rising Arctic Ocean temperatures cause gas hydrate destabilization and ocean acidification. *Geophysical Research Letters* **38**, L08602.

Bock, M., Schmitt, J., Möller, L., Spahni, R., Blunier, T. and Fischer, H. (2010) Hydrogen isotopes preclude marine hydrate CH_4 emissions at the onset of Dansgaard-Oeschger events. *Science* **328**, 1686-1689.

Boetius, A. and Wenzhofer, F. (2013) Seafloor oxygen consumption fuelled by methane from cold seeps. *Nature Geoscience* **6**, 725-734.

Boetius, A., Ravenschlag, K., Schubert, C.J., Rickert, D., Friedrich, W., Gieseke, A., Amann, R., Jørgensen, B.B., Witte, U. and Pfannkuche, O. (2000) A marine microbial consortium apparently mediating anaerobic oxidation of methane. *Nature* **407**, 623-626.

Borowski, W.S., Paull, C.K. and Ussler, W. (1996) Marine pore-water sulfate profiles indicate in situ methane flux from underlying gas hydrate. *Geology* **24**, 655.

Borowski, W.S., Paull, C.K. and Ussler, W.I. (1997) Carbon cycling within the upper methanogenic zone of continental rise sediments: An example from the methane-rich sediments overlying the Blake Ridge gas hydrate deposits. *Marine Chemistry* **57**, 229-311.

Boudreau, B.P. (1997) Diagenetic Models and their Implementation: Modelling Transport and Reactions in Aquatic Sediments. Springer, London, 414 pp.

Boudreau, B.P. (2012) The physics of bubbles in surficial, soft, cohesive sediments. *Marine and Petroleum Geology* **38**, 1-18.

Bowen, G.J., Maibauer, B.J., Kraus, M.J., Röhl, U., Westerhold, T., Steimke, A., Gingerich, P.D., Wing, S.L. and Clyde, W.C. (2014) Two massive, rapid releases of carbon during the onset of the Palaeocene–Eocene thermal maximum. *Nature Geoscience* **8**, 44-47.

Boyd, T.J. and D'Asaro, E.A. (1994) Cooling of the West Spitsbergen Current: Wintertime observations west of Svalbard. *Journal of Geophysical Research* **99**, 22597-22618.

Brass, M. and Röckmann, T. (2010) Continuous-flow isotope ratio mass spectrometry method for carbon and hydrogen isotope measurements on atmospheric methane. *Atmospheric Measurement Techniques* **3**, 1707-1721.

Brook, E.J., Harder, S., Severinghaus, J., Steig, E.J. and Sucher, C.M. (2000) On the origin and timing of rapid changes in atmospheric methane during the Last Glacial Period. *Global Biogeochemical Cycles* **14**, 559-572.

Buffett, B. and Archer, D. (2004) Global inventory of methane clathrate: sensitivity to changes in the deep ocean. *Earth and Planetary Science Letters* **227**, 185-199.

Bünz, S., Polyanov, S., Vadakkepuliyambatta, S., Consolaro, C. and Mienert, J. (2012) Active gas venting through hydrate-bearing sediments on the Vestnesa Ridge, offshore W-Svalbard. *Marine Geology* **332-334**, 189-197.

Burwicz, E.B., Rüpke, L.H. and Wallmann, K. (2011) Estimation of the global amount of submarine gas hydrates formed via microbial methane formation based on numerical reaction-transport modeling and a novel parameterization of Holocene sedimentation. *Geochimica et Cosmochimica Acta* **75**, 4562-4576.

Bussmann, I. (2013) Distribution of methane in the Lena Delta and Buor-Khaya Bay, Russia. *Biogeosciences* **10**, 4641-4652.

Calvert, S. and Pedersen, T. (2007) Elemental proxies for palaeoclimatic and palaeoceanographic variability in marine sediments: Interpretation and applications, in: Hillaire-Marcel, C., Anne, d.V. (Eds.), Proxies in Late Cenozoic Paleoceanography. Elsevier Science & Technology, Amsterdam, NLD.

Carcione, J.M., Gei, D., Rossi, G. and Madrussani, G. (2005) Estimation of gas-hydrate concentration and free-gas saturation at the Norwegian-Svalbard continental margin. *Geophysical Prospecting* **53**, 803-810.

Chabert, A., Minshull, T.A., Westbrook, G.K., Berndt, C., Thatcher, K.E. and Sarkar, S. (2011) Characterization of a stratigraphically constrained gas hydrate system along the western continental margin of Svalbard from ocean bottom seismometer data. *Journal of Geophysical Research* **116**, B12102.

Chappellaz, J., Blunier, T., Kints, S., Dällenbach, A., Barnola, J.-M., Schwander, J., Raynaud, D. and Stauffer, B. (1997) Changes in the atmospheric CH_4 gradient between Greenland and Antarctica during the Holocene. *Journal of Geophysical Research* **102**, 15987-15997.

Chappellaz, J., Blunier, T., Raynaud, D., Barnola, J.M., Schwander, J. and Stauffer, B. (1993) Synchornous changes in atmospheric CH_4 and Greenland climate between 40 and 8 kyr BP. *Nature* **366**, 443-445.

Ciais, P., Sabine, C., Bala, G., Bopp, L., Brovkin, V., Canadell, J., Chhabra, A., DeFries, R., Galloway, J., Heimann, M., Jones, C., Le Quéré, C., Myneni, R.B., Piao, S. and Thornton, P. (2013) Carbon and other biogeochemical cycles, in: Stocker, T.F., Qin, D., Plattner, G.-K., Tignor, M., Allen, S.K., Boschung, J., Nauels, A., Xia, Y., Bex, V., Midgley, P.M. (Eds.), Climate Change 2013: The Physical Science Basis. Contribution of Working Group I to the Fifth Assessment Report of the Intergovernmental Panel on Climate Change. Cambridge University Press, Cambridge, United Kingdom.

Claypool, G.E., Milkov, A.V., Lee, Y.J., Torres, M.E., Borowski, W.S. and Tomaru, H. (2006) Microbial methane generation and gas trasport in shallow sediments of an accretionary complex, southren Hydrate Ridge (ODP Leg 204), offshore Oregon, USA, in: Trehu, A.M., Bohrmann, G., Torres, M.E., Colwell, F.S. (Eds.), Proceedings of the Ocean Drilling Program, Scientific Results.

Clennell, M.B., Hovland, M., Booth, J.S., Henry, P. and Winters, W.J. (1999) Formation of natural gas hydrates in marine sediments 1. Conceptual model of gas hydrate growth conditioned by host sediment properties. *Journal of Geophysical Research* **104**, 22985-23003.

Cook, M.S., Keigwin, L.D., Birgel, D. and Hinrichs, K.-U. (2011) Repeated pulses of vertical methane flux recorded in glacial sediments from the southeast Bering Sea. *Paleoceanography* **26**, PA2210.

Cottier, F.R. and Venables, E.J. (2007) On the double-diffusive and cabbeling environment of the Arctic Front, West Spitsbergen. *Polar Research* **26**, 152-159.

Croudace, I.W., Rindby, A. and Rothwell, R.G. (2006) ITRAX: description and evaluation of a new multi-function X-ray core scanner, in, Rothwell, R.G. (Ed.), New Techniques in Sediment Core Analysis. Geological Society of London, London, UK, pp. 51-63.

Cubasch, U., D. Wuebbles, D. Chen, M.C. Facchini, D. Frame, N. Mahowald and Winther, J.-G. (2013) Introduction, in: Stocker, T.F., Qin, D., Plattner, G.-K., Tignor, M., Allen, S.K., Boschung, J., Nauels, A., Xia, Y., Bex, V., Midgley, P.M. (Eds.), Climate Change 2013: The Physical Science Basis. Contribution of Working Group I to the Fifth Assessment Report of the Intergovernmental Panel on Climate Change. Cambridge University Press, Cambridge, United Kingdom.

Dale, A.W., Aguilera, D.R., Regnier, P., Fossing, H., Knab, N.J. and Jorgensen, B.B. (2008a) Seasonal dynamics of the depth and rate of anaerobic oxidation of methane in Aarhus Bay (Denmark) sediments. *Journal of Marine Research* **66**, 127-155.

Dale, A.W., Van Cappellen, P., Aguilera, D.R. and Regnier, P. (2008b) Methane efflux from marine sediments in passive and active margins: Estimations from bioenergetic reaction–transport simulations. *Earth and Planetary Science Letters* **265**, 329-344.

Damm, E., Helmke, E., Thoms, S., Schauer, U., Nothig, E., Bakker, K. and Kiene, R.P. (2010) Methane production in aerobic oligotrophic surface water in the central Arctic Ocea. *Biogeosciences* **7**, 1099-1108.

Damm, E., Kiene, R.P., Schwarz, J., Falck, E. and Dieckmann, G. (2008) Methane cycling in Arctic shelf water and its relationship with phytoplankton biomass and DMSP. *Marine Chemistry* **109**, 45-59.

Damm, E., Mackensen, A., Budeus, G., Faber, E. and Hanfland, C. (2005) Pathways of methane in seawater: Plume spreading in an Arctic shelf environment (SW-Spitsbergen). *Continental Shelf Research* **25**, 1453-1472.

Daniel, I., DeGrandpre, M. and Farías, L. (2013) Greenhouse gas emissions from the Tubul-Raqui estuary (central Chile 36°S). *Estuarine, Coastal and Shelf Science* **134**, 31-44.

Deng, Z., Yu, T., Shi, S., Jin, J. and Wu, K. (2014) The global distribution of diapycnal mixing and mixing coefficient tensor in the upper 2000 m ocean from argo observations. *Marine Geodesy* **37**, 337-353.

Dewangan, P., Basavaiah, N., Badesab, F.K., Usapkar, A., Mazumdar, A., Joshi, R. and Ramprasad, T. (2013) Diagenesis of magnetic minerals in a gas hydrate/cold seep environment off the Krishna–Godavari basin, Bay of Bengal. *Marine Geology* **340**, 57-70.

Dickens, G.R. (2001) Sulfate profiles and barium fronts in sediment on the Blake Ridge: Present and past methane fluxes through a large gas hydrate reservoir. *Geochimica et Cosmochimica Acta* **65**, 529-543.

Dickens, G.R. (2003) Rethinking the global carbon cycle with a large, dynamic and microbially mediated gas hydrate capacitor. *Earth and Planetary Science Letters* **213**, 169-183.

Dickens, G.R. (2011) Down the rabbit hole: Toward appropriate discussion of methane release from gas hydrate systems during the Paleocene-Eocene thermal maximum and other past hyperthermal events. *Climate of the Past* **7**, 831-846.

Dlugokencky, E.J., Nisbet, E.G., Fisher, R. and Lowry, D. (2011) Global atmospheric methane: budget, changes and dangers. *Philosophical Transactions Series A, Mathematical, Physical, and Engineering Sciences* **369**, 2058-2072.

Ebbesen, H., Hald, M. and Eplet, T.H. (2007) Lateglacial and early Holocene climatic oscillations on the western Svalbard margin, European Arctic. *Quaternary Science Reviews* **26**, 1999-2011.

Egeberg, P.K. and Dickens, G.R. (1999) Thermodynamic and pore water halogen constraints on gas hydrate distribution at ODP Site 997 (Blake Ridge). *Chemical Geology* **153**, 43-79.

Egger, M., Rasigraf, O., Sapart, C.J., Jilbert, T., Jetten, M.S., Rockmann, T., van der Veen, C., Banda, N., Kartal, B., Ettwig, K.F. and Slomp, C.P. (2015) Iron-mediated anaerobic oxidation of methane in brackish coastal sediments. *Environmental Science and Technology* **49**, 277-283.

Eiken, O. and Hinz, K. (1993) Contourites in the Fram Strait. *Sedimentary Geology* **82**, 15-32.

Elliott, S., Maltrud, M., Reagan, M., Moridis, G. and Cameron-Smith, P. (2011) Marine methane cycle simulations for the period of early global warming. *Journal of Geophysical Research* **116**, G01010.

Elverhøi, A., Andersen, E.S., Dokken, T., Hebbeln, D., Spielhagen, R., Svendsen, J.I., Sorflaten, M., Rornes, A., Hald, M. and Forsberg, C.F. (1995) The growth and decay of the Late Weichselian ice sheet in western Svalbard and adjacent areas based on provenance studies of marine sediments. *Quaternary Research* **44**, 303-316.

Emerson, S. and Hedges, J. (2003) Sediment diagenesis and benthic flux, in: Turekian, H.D.H.K. (Ed.), Treatise on Geochemistry. Pergamon, Oxford, pp. 293-319.

Ettwig, K.F., Butler, M.K., Le Paslier, D., Pelletier, E., Mangenot, S., Kuypers, M.M.M., Schreiber, F., Dutilh, B.E., Zedelius, J., de Beer, D., Gloerich, J., Wessels, H.J.C.T., van Alen, T., Luesken, F., Wu, M.L., van de Pas-Schoonen, K.T., Op den Camp, H.J.M., Janssen-Megens, E.M., Francoijs, K.-J., Stunnenberg, H., Weissenbach, J., Jetten, M.S.M. and Strous, M. (2010) Nitrite-driven anaerobic methane oxidation by oxygenic bacteria. *Nature* **464**, 543-548.

Fahrbach, E., Meincke, J., Osterhus, S., Rohardt, G. and Schauer, J. (2001) Direct measurements of volume transports through Fram Strait. *Polar Research* **20**, 217-224.

Fehn, U., Lu, Z. and Tomaru, H. (2006) Data report: ^{129}I/I ratios and halogen concentrations in pore water of Hydrate Ridge and their relevance for the origin of gas hydrates: a progress report, in: Trehu, A.M., Bohrmann, G., Torres, M.E., Colwell, F.S. (Eds.), Proceedings of the Ocean Drilling Program Scientific Results 204, College Station, TX.

Felden, J., Lichtschlag, A., Wenzhofer, F., de Beer, D., Feseker, T., Pop Ristova, P., de Lange, G. and Boetius, A. (2013) Limitations of microbial hydrocarbon degradation at the Amon mud volcano (Nile deep-sea fan). *Biogeosciences* **10**, 3269-3283.

Ferré, B., Mienert, J. and Feseker, T. (2012) Ocean temperature variability for the past 60 years on the Norwegian-Svalbard margin influences gas hydrate stability on human time scales. *Journal of Geophysical Research* **117**, C10017.

Fisher, R., Lowry, D., Wilkin, O., Sriskantharajah, S. and Nisbet, E.G. (2006) High-precision, automated stable isotope analysis of atmospheric methane and carbon dioxide using continuous-flow isotope-ratio mass spectrometry. *Rapid Communications in Mass Spectrometry* **20**, 200-208.

Fisher, R.E., Sriskantharajah, S., Lowry, D., Lanoisellé, M., Fowler, C.M.R., James, R.H., Hermansen, O., Lund Myhre, C., Stohl, A., Greinert, J., Nisbet-Jones, P.B.R., Mienert, J. and Nisbet, E.G. (2011) Arctic methane sources: Isotopic evidence for atmospheric inputs. *Geophysical Research Letters* **38**, L21803.

Florez-Leiva, L., Damm, E. and Farías, L. (2013) Methane production induced by dimethylsulfide in surface water of an upwelling ecosystem. *Progress in Oceanography* **112-113**, 38-48.

Forman, S.L., Lubinski, D.J., Ingolfsson, O., Zeeberg, J.J., Snyder, J.A., Siegert, M.J. and Matishov, G.G. (2004) A review of postglacial emergence on Svalbard, Franz Josef Land and Novaya Zemlya, northern Eurasia. *Quaternary Science Reviews* **23**, 1391-1434.

Forwick, M., Baeten, N.J. and Vorren, T.O. (2009) Pockmarks in Spitsbergen fjords. *Norwegian Journal of Geology* **89**, 65-77.

Frederick, J.M. and Buffett, B.A. (2014) Taliks in relict submarine permafrost and methane hydrate deposits: Pathways for gas escape under present and future conditions. *Journal of Geophysical Research: Earth Surface* **119**, 106-122.

Froelich, P.N., Klinkhammer, G., Bender, M.L., Luedtke, N.A., Heath, G.R., Cullen, D., Dauphin, P., Hammond, D., Hartman, B. and Maynard, V. (1979) Early oxidation of organic matter in pelagic sediments of the eastern equatorial Atlantic: suboxic diagenesis. *Geochimica et Cosmochimica Acta* **43**, 1075-1090.

Garming, J.F.L., Bleil, U. and Riedinger, N. (2005) Alteration of magnetic mineralogy at the sulfate–methane transition: Analysis of sediments from the Argentine continental slope. *Physics of the Earth and Planetary Interiors* **151**, 290-308.

Gascard, J.-C., Richez, C. and Rouault, C. (1995) New insights on large-scale oceanography in Fram Strait: The West Spitsbergen Current. **49**, 131-182.

Gentz, T., Damm, E., Schneider von Deimling, J., Mau, S., McGinnis, D.F. and Schlüter, M. (2014) A water column study of methane around gas flares located at the West Spitsbergen continental margin. *Continental Shelf Research* **72**, 107-118.

Gingele, F.X., Zabel, M., Kasten, S., Bonn, W.J. and Numberg, C.C. (1999) Biogenic barium as a proxy for paleoproductivity: Methods and limitations of application, in: Fischer, G., Wefer, G. (Eds.), Use of Proxies in Paleoceanography: Examples from the South Atlantic. Springer-Verlag, Berlin, pp. 345-364.

Greinert, J., Hobrmann, G. and Seuess, E. (2001) Gas hydrate associated carbonates and methane-venting at Hydrate Ridge: Classification, distribution, and origin of authigenic lithologies, in: Paull, C.K., Dillon, W.P. (Eds.), Natural Gas Hydrates: Occurrence, Distribution, and Detection. AGU, Washington, D. C., pp. 99-113.

Gülzow, W., Rehder, G., Schneider v. Deimling, J., Seifert, T. and Tóth, Z. (2013) One year of continuous measurements constraining methane emissions from the Baltic Sea to the atmosphere using a ship of opportunity. *Biogeosciences* **10**, 81-99.

Gülzow, W., Rehder, G., Schneider, B., Deimling, J.S.v. and Sadkowiak, B. (2011) A new method for continuous measurement of methane and carbon dioxide in surface waters using off-axis integrated cavity output spectroscopy (ICOS): An example from the Baltic Sea. *Limnol. Oceanogr. Methods* **9**, 176-184.

Haacke, R.R., Westbrook, G.K. and Hyndman, R.D. (2007) Gas hydrate, fluid flow and free gas: Formation of the bottom-simulating reflector. *Earth and Planetary Science Letters* **261**, 407-420.

Haacke, R.R., Westbrook, G.K. and Riley, M.S. (2008) Controls on the formation and stability of gas hydrate-related bottom-simulating reflectors (BSRs): A case study from the west Svalbard continental slope. *Journal of Geophysical Research* **113**, B05104.

Haeckel, M., Boudreau, B.P. and Wallmann, K. (2007) Bubble-induced porewater mixing: A 3-D model for deep porewater irrigation. *Geochimica et Cosmochimica Acta* **71**, 5135-5154.

Haese, R.R., Meile, C., Van Cappellen, P. and De Lange, G.J. (2003) Carbon geochemistry of cold seeps: Methane fluxes and transformation in sediments from Kazan mud volcano, eastern Mediterranean Sea. *Earth and Planetary Science Letters* **212**, 361-375.

Hanson, R.S. and Hanson, T.E. (1996) Methanotrophic bacteria. *Microbiological reviews* **60**, 439-471.

Hartmann, D.L., Tank, A.M.G.K., Rusticucci, M., Alexander, L.V., Brönnimann, S., Charabi, Y., Dentener, F.J., Dlugokencky, E.J., Easterling, D.R., Kaplan, A., Soden, B.J., Thorne, P.W., Wild, M. and Zhai, P.M. (2013) Observations: Atmosphere and surface, in: Stocker, T.F., Qin, D., Plattner, G.-K., Tignor, M., Allen, S.K., Boschung, J., Nauels, A., Xia, Y., Bex, V., Midgley, P.M. (Eds.), Climate Change 2013: The Physical Science Basis. Contribution of Working Group I to the Fifth Assessment Report of the Intergovernmental Panel on Climate Change. Cambridge University Press, Cambridge, United Kingdom.

Hautala, S.L., Solomon, E.A., Johnson, H.P., Harris, R.N. and Miller, U.K. (2014) Dissociation of Cascadia margin gas hydrates in response to contemporary ocean warming. *Geophysical Research Letters* **41**, 8486–8494.

Hayduk, W. and Laudie, H. (1974) Prediction of diffusion coefficients for nonelectrolytes in dilute aqueous solutions. *AlChE Journal* **20**, 611-615.

He, X., Sun, L., Xie, Z., Huang, W., Long, N., Li, Z. and Xing, G. (2013) Sea ice in the Arctic Ocean: Role of shielding and consumption of methane. *Atmospheric Environment* **67**, 8-13.

Heeschen, K.U., Collier, R.W., de Angelis, M.A., Suess, E., Rehder, G., Linke, P. and Klinkhammer, G.P. (2005) Methane sources, distributions, and fluxes from cold vent sites at Hydrate Ridge, Cascadia Margin. *Global Biogeochemical Cycles* **19**, GB2016.

Henkel, S., Strasser, M., Schwenk, T., Hanebuth, T.J.J., Hüsener, J., Arnold, G.L., Winkelmann, D., Formolo, M., Tomasini, J., Krastel, S. and Kasten, S. (2011) An interdisciplinary investigation of a recent submarine mass transport deposit at the continental margin off Uruguay. *Geochemistry, Geophysics, Geosystems* **12**, Q08009.

Henry, P., Thomas, M. and Clennell, M.B. (1999) Formation of natural gas hydrates in marine sediments 2. Thermodynamic calculations of stability conditions in porous sediments. *Journal of Geophysical Research* **104**, 23005-23002.

Hensen, C., Zabel, M., Pfeifer, K., Schwenk, T., Kasten, S., Riedinger, N., Schulz, H.D. and Boetius, A. (2003) Control of sulfate pore-water profiles by sedimentary events and the significance of anaerobic oxidation of methane for the burial of sulfur in marine sediments. *Geochimica et Cosmochimica Acta* **67**, 2631-2647.

Herguera, J.C., Paull, C.K., Perez, E., Ussler, W. and Peltzer, E. (2014) Limits to the sensitivity of living benthic foraminifera to pore water carbon isotope anomalies in methane vent environments. *Palaeogeography* **29**, 273–289.

Hesse, R. (2003) Pore water anomalies of submarine gas-hydrate zones as tool to assess hydrate abundance and distribution in the subsurface What have we learned in the past decade? *Earth-Science Reviews* **61**, 149-179.

Hesse, R. and Harrison, W.E. (1981) Gas hydrates (clathrates) causing pore-water freshening and oxygen isotope fractionation in deep-water sedimentary sections of terrigenous continental margins *Earth and Planetary Science Letters* **55**, 453-462.

Hester, K.C. and Brewer, P.G. (2009) Clathrate hydrates in nature. *Annual Review of Marine Science* **1**, 303-327.

Hill, T.M., Kennett, J.P. and Valentine, D.L. (2004) Isotopic evidence for the incorporation of methane-derived carbon into foraminifera from modern methane seeps, Hydrate Ridge, Northeast Pacific. *Geochimica et Cosmochimica Acta* **68**, 4619-4627.

Ho, D.T., Law, C.S., Smith, M.J., Schlosser, P., Harvey, M. and Hill, P. (2006) Measurements of air-sea gas exchange at high wind speeds in the Southern Ocean: Implications for global parameterizations. *Geophysical Research Letters* **33**, L16611.

Hoehler, T.M., Alperin, M.J., Albert, D.B. and Martens, C.S. (1994) Field and laboratory studies of methane oxidation in an anoxic marine sediment: Evidence for a methanogen-sulfate reducer consortium. *Global Biogeochemical Cycles* **8**, 451-464.

Hoehler, T.M., Borowski, W.S., Alperin, M.J., Rodriguez, N.M. and Paull, C.K. (2000) Model, stable isotope, and radiotracer characterization of anaerobic methane oxidation in gas hydrate-bearing sediments of the Blake Ridge, in: Paull, C.K., Matsumoto, R., Wallace, P.J., Dillon, W.P. (Eds.), Proceedings of the Ocean Drilling Program, Scientific Results. Ocean Drilling Program, College Station, TX, pp. 113-126.

Holmes, C.D., Prather, M.J., Søvde, O.A. and Myhre, G. (2013) Future methane, hydroxyl, and their uncertainties: key climate and emission parameters for future predictions. *Atmospheric Chemistry and Physics* **13**, 285-302.

Hong, W.-L., Torres, M.E., Kim, J.-H., Choi, J. and Bahk, J.-J. (2014) Towards quantifying the reaction network around the sulfate–methane-transition-zone in the Ulleung Basin, East Sea, with a kinetic modeling approach. *Geochimica et Cosmochimica Acta* **140**, 127-141.

Hsu, S.A., Meindl, E.A. and Gilhousen, D.B. (1994) Determining the power-law wind-profile exponent under near-neutral stability conditions at Sea. *Journal of Applied Meteorology* **33**, 757-765.

Hu, L., Yvon-Lewis, S.A., Kessler, J.D. and MacDonald, I.R. (2012) Methane fluxes to the atmosphere from deepwater hydrocarbon seeps in the northern Gulf of Mexico. *Journal of Geophysical Research* **117**, C01009.

Hunter, S.J., Goldobin, D.S., Haywood, A.M., Ridgwell, A. and Rees, J.G. (2013) Sensitivity of the global submarine hydrate inventory to scenarios of future climate change. *Earth and Planetary Science Letters* **367**, 105-115.

IPCC. (1990) Climate Change: The IPCC Scientific Assessment. Cambridge University Press, Cambridge, United Kingdom.

Jessen, S.P., Rasmussen, T.L., Nielsen, T. and Solheim, A. (2010) A new Late Weichselian and Holocene marine chronology for the western Svalbard slope 30,000–0 cal years BP. *Quaternary Science Reviews* **29**, 1301-1312.

Joseph, C., Campbell, K.A., Torres, M.E., Martin, R.A., Pohlman, J.W., Riedel, M. and Rose, K. (2013) Methane-derived authigenic carbonates from modern and paleoseeps on the Cascadia margin: Mechanisms of formation and diagenetic signals. *Palaeogeography, Palaeoclimatology, Palaeoecology* **390**, 52-67.

Judd, A. and Hovland, M. (2007) Seabed Fluid Flow: The Impact on Geology, Biology and the Marine Environment. Cambridge University Press, Cambridge, 492 pp.

Judd, A.G. (2003) The global importance and context of methane escape from the seabed. *Geo-Marine Letters* **23**, 147-154.

Judd, A.G. (2004) Natural seabed gas seeps as sources of atmospheric methane. *Environmental Geology* **46**, 988-996.

Kannberg, P.K., Tréhu, A.M., Pierce, S.D., Paull, C.K. and Caress, D.W. (2013) Temporal variation of methane flares in the ocean above Hydrate Ridge, Oregon. *Earth and Planetary Science Letters* **368**, 33-42.

Karl, D.M., Beversdorf, L., Björkman, K.M., Church, M.J., Martinez, A. and Delong, E.F. (2008) Aerobic production of methane in the sea. *Nature Geoscience* **1**, 473-478.

Karlin, R. and Levi, S. (1983) Diagenesis of magnetic minerals in Recent haemipelagic sediments. *Nature* **303**, 327-330.

Kasten, S., Nöthen, K., Hensen, C., Spieß, V., Blumenberg, M. and Schneider, R.R. (2012) Gas hydrate decomposition recorded by authigenic barite at pockmark sites of the northern Congo Fan. *Geo-Marine Letters* **32**, 515-524.

Kennett, J.P. (2000) Carbon Isotopic evidence for methane hydrate instability during Quaternary interstadials. *Science* **288**, 128-133.

Kennett, P.P., Cannariato, K.G., Hendy, I.L. and Behl, R.J. (2003) Methane Hydrates in Quaternary Climate Change: The Clathrate Gun Hypothesis. American Geophysical Union, Washington, D.C., 216 pp.

Ker, S., Le Gonidec, Y., Marsset, B., Westbrook, G.K., Gibert, D. and Minshull, T.A. (2014) Fine-scale gas distribution in marine sediments assessed from deep-towed seismic data. *Geophysical Journal International* **196**, 1466-1470.

Kessler, J.D., Valentine, D.L., Redmond, M.C., Du, M., Chan, E.W., Mendes, S.D., Quiroz, E.W., Villanueva, C.J., Shusta, S.S., Werra, L.M., Yvon-Lewis, S.A. and Weber, T.C. (2011) A persistent oxygen anomaly reveals the fate of spilled methane in the deep Gulf of Mexico. *Science* **331**, 312-315.

Kirschke, S., Bousquet, P., Ciais, P., Saunois, M., Canadell, J.G., Dlugokencky, E.J., Bergamaschi, P., Bergmann, D., Blake, D.R., Bruhwiler, L., Cameron-Smith, P., Castaldi, S., Chevallier, F., Feng, L., Fraser, A., Heimann, M., Hodson, E.L., Houweling, S., Josse, B., Fraser, P.J., Krummel, P.B., Lamarque, J.-F., Langenfelds, R.L., Le Quéré, C., Naik, V., O’Doherty, S., Palmer, P.I., Pison, I., Plummer, D., Poulter, B., Prinn, R.G., Rigby, M., Ringeval, B., Santini, M., Schmidt, M., Shindell, D.T., Simpson, I.J., Spahni, R., O'Doherty, S., Palmer, P.I., Pison, I., Plummer, D., Poulter, B., Prinn, R.G., Rigby, M., Ringeval, B., Santini, M., Schmidt, M., Shindell, D.T., Simpson, I.J., Spahni, R., Steele, L.P., Strode, S.A., Sudo, K., Szopa, S., van der Werf, G.R., Voulgarakis, A., van Weele, M., Weiss, R.F., Williams, J.E. and Zeng, G. (2013) Three decades of global methane sources and sinks. *Nature Geoscience* **6**, 813-823.

Klauda, J.B. and Sandler, S.I. (2005) Global distribution of methane hydrate in ocean sediments. *Energy and Fuels* **19**, 459-470.

Knies, J., Damm, E., Gutt, J., Mann, U. and Pinturier, L. (2004) Near-surface hydrocarbon anomalies in shelf sediments off Spitsbergen: Evidences for past seepages. *Geochemistry Geophysics Geosystems* **5**, Q06003.

Knittel, K. and Boetius, A. (2009) Anaerobic oxidation of methane: Progress with an unknown process. *Annual review of microbiology* **63**, 311-334.

Kopf, A.J. (2003) Global methane emission through mud volcanoes and its past and present impact on the Earth's climate. *International Journal of Earth Sciences* **92**, 806-816.

Kort, E.A., Wofsy, S.C., Daube, B.C., Diao, M., Elkins, J.W., Gao, R.S., Hintsa, E.J., Hurst, D.F., Jimenez, R., Moore, F.L., Spackman, J.R. and Zondlo, M.A. (2012) Atmospheric observations of Arctic Ocean methane emissions up to 82° north. *Nature Geoscience* **5**, 318-321.

Kourtidis, K., Kioutsioukis, I., McGinnis, D.F. and Rapsomanikis, S. (2006) Effects of methane outgassing on the Black Sea atmosphere. *Atmospheric Chemistry and Physics* **6**, 5173-5182.

Krey, V., Canadell, J.G., Nakicenovic, N., Abe, Y., Andruleit, H., Archer, D., Grubler, A., Hamilton, N.T.M., Johnson, A., Kostov, V., Lamarque, J.-F., Langhorne, N., Nisbet, E.G., O'Neill, B., Riahi, K., Riedel, M., Wang, W. and Yakushev, V. (2009) Gas hydrates: Entrance to a methane age or climate threat? *Environmental Research Letters* **4**, 034007.

Kvenvolden, K.A. (1993) Gas hydrates: Geological perspective and global change. *Reviews of Geophysics* **31**, 173-187.

Kvenvolden, K.A. (1995) A review of the geochemistry of methane in natural gas hydrate. *Organic Geochemistry* **23**, 997-1008.

Kvenvolden, K.A. (1999) Potential effects of gas hydrate on human welfare. *Proceedings of the National Academy of Sciences of the United States of America* **96**, 3429-3426.

Kvenvolden, K.A. and Rogers, B.W. (2005) Gaia's breath—global methane exhalations. *Marine and Petroleum Geology* **22**, 579-590.

Lamarque, J.-F. (2008) Estimating the potential for methane clathrate instability in the 1%-CO2IPCC AR-4 simulations. *Geophysical Research Letters* **35**, L19806.

Lapham, L.L., Wilson, R.M. and Chanton, J.P. (2012) Pressurized laboratory experiments show no stable carbon isotope fractionation of methane during gas hydrate dissolution and dissociation. *Rapid Communications in Mass Spectrometry* **26**, 32-36.

Largier, J.L. (2003) Considerations in estimating larval dispersal distances from oceanographic data. *Ecological Applications* **13**, S71-S89.

Larrasoaña, J.C., Roberts, A.P., Musgrave, R.J., Gràcia, E., Piñero, E., Vega, M. and Martínez-Ruiz, F. (2007) Diagenetic formation of greigite and pyrrhotite in gas hydrate marine sedimentary systems. *Earth and Planetary Science Letters* **261**, 350-366.

Ledwell, J.R., Montgomery, E.T., Polzin, K.L., St. Laurent, L.C., Schmitt, R.W. and Toole, J.M. (2000) Evidence for enhanced mixing over rough topography in the abyssal ocean. *Nature* **403**, 179-182.

Ledwell, J.R., Watson, A.J. and Law, C.S. (1993) Evidence for slow mixing accross the pycnocline from and open-ocean tracer-release experiment. *Nature* **364**, 701-703.

Ledwell, J.R., Watson, A.J. and Law, C.S. (1998) Mixing of a tracer in the pycnocline. *Journal of Geophysical Research* **103**, 21499-21539.

Leifer, I. and Patro, R.K. (2002) The bubble mechanism for methane transport from the shallow sea bed to the surface: A review and sensitivity study. *Continental Shelf Research* **22**, 2409-2428.

Leifer, I., Luyendyk, B.P., Boles, J. and Clark, J.F. (2006) Natural marine seepage blowout: Contribution to atmospheric methane. *Global Biogeochemical Cycles* **20**, GB3003.

Liss, P.S. and Merlivat, L. (1986) Air-sea gas exchange rates: Introduction and synthesis, in: Buat-Menard, P. (Ed.), The role of Air-Sea Exchange in Geochemical Cycling. Reidel, Boston, MA, pp. 113-129.

Liss, P.S. and Slater, P.G. (1974) Flux of gases across the air-sea interface. *Nature* **247**, 181-184.

Liu, Q., Roberts, A.P., Larrasoaña, J.C., Banerjee, S.K., Guyodo, Y., Tauxe, L. and Oldfield, F. (2012) Environmental magnetism: Principles and applications. *Reviews of Geophysics* **50**, 2012RG000393.

Liu, X. and Flemings, P.B. (2006) Passing gas through the hydrate stability zone at southern Hydrate Ridge, offshore Oregon. *Earth and Planetary Science Letters* **241**, 211-226.

Lucchi, R.G., Camerlenghi, A., Rebesco, M., Colmenero-Hidalgo, E., Sierro, F.J., Sagnotti, L., Urgeles, R., Melis, R., Morigi, C., Bárcena, M.A., Giorgetti, G., Villa, G., Persico, D., Flores, J.A., Rigual-Hernández, A.S., Pedrosa, M.T., Macri, P. and Caburlotto, A. (2013) Postglacial sedimentary processes on the Storfjorden and

Kveithola trough mouth fans: Significance of extreme glacimarine sedimentation. *Global and Planetary Change* **111**, 309-326.

Luff, R., Wallmann, K. and Aloisi, G. (2004) Numerical modeling of carbonate crust formation at cold vent sites: significance for fluid and methane budgets and chemosynthetic biological communities. *Earth and Planetary Science Letters* **221**, 337-353.

Mackensen, A., Wollenburg, J. and Licari, L. (2006) Low $\delta^{13}C$ in tests of live epibenthic and endobenthic foraminifera at a site of active methane seepage. *Paleoceanography* **21**, PA2022.

Malinverno, A. and Pohlman, J.W. (2011) Modeling sulfate reduction in methane hydrate-bearing continental margin sediments: Does a sulfate-methane transition require anaerobic oxidation of methane? *Geochemistry Geophysics Geosystems* **12**, Q7006.

Mangerud, J., Bondevik, S., Gulliksen, S., Karin Hufthammer, A. and Høisæter, T. (2006) Marine 14C reservoir ages for 19th century whales and molluscs from the North Atlantic. *Quaternary Science Reviews* **25**, 3228-3245.

Mangerud, J., Dokken, T., Hebbeln, D., Heggen, B., Ingolfsson, O., Landvik, J.Y., Mejdahl, V., Svendsen, J.I. and Vorren, T.O. (1998) Fluctuations of the Svalbard-Barents Sea ice sheet during the last 150 000 years. *Quaternary Science Reviews* **17**, 11-42.

Marín-Moreno, H., Minshull, T.A., Westbrook, G.K., Sinha, B. and Sarkar, S. (2013) The response of methane hydrate beneath the seabed offshore Svalbard to ocean warming during the next three centuries. *Geophysical Research Letters* **40**, 5159–5163.

Martin, R.A., Nesbitt, E.A. and Campbell, K.A. (2007) Carbon stable isotopic composition of benthic foraminifera from Pliocene cold methane seeps, Cascadia accretionary margin. *Palaeogeography, Palaeoclimatology, Palaeoecology* **246**, 260-277.

Martin, R.A., Nesbitt, E.A. and Campbell, K.A. (2010) The effects of anaerobic methane oxidation on benthic foraminiferal assemblages and stable isotopes on the Hikurangi Margin of eastern New Zealand. *Marine Geology* **272**, 270-284.

März, C., Hoffmann, J., Bleil, U., de Lange, G.J. and Kasten, S. (2008) Diagenetic changes of magnetic and geochemical signals by anaerobic methane oxidation in sediments of the Zambezi deep-sea fan (SW Indian Ocean). *Marine Geology* **255**, 118-130.

Mau, S., Heintz, M.B. and Valentine, D.L. (2012) Quantification of CH_4 loss and transport in dissolved plumes of the Santa Barbara Channel, California. *Continental Shelf Research* **32**, 110-120.

Mau, S., Valentine, D.L., Clark, J.F., Reed, J., Camilli, R. and Washburn, L. (2007) Dissolved methane distributions and air-sea flux in the plume of a massive seep field, Coal Oil Point, California. *Geophysical Research Letters* **34**, L22603.

Mazumdar, A., João, H.M., Peketi, A., Dewangan, P., Kocherla, M., Joshi, R.K. and Ramprasad, T. (2012) Geochemical and geological constraints on the composition of marine sediment pore fluid: Possible link to gas hydrate deposits. *Marine and Petroleum Geology* **38**, 35-52.

McGillis, W.R., Edson, J.B., Ware, J.D., Dacey, J.W.H., Hare, J.E., Fairall, C.W. and Wannikhof, R. (2001) Carbon dioxide flux techniques performed during GasEx-98. *Marine Chemistry* **75**, 267–280.

McGinnis, D.F., Greinert, J., Artemov, Y., Beaubien, S.E. and Wüest, A. (2006) Fate of rising methane bubbles in stratified waters: How much methane reaches the atmosphere? *Journal of Geophysical Research* **111**, C09007.

McInerney, F.A. and Wing, S.L. (2011) The Paleocene-Eocene thermal maximum: A perturbation of carbon cycle, climate, and biosphere with implications for the future. *Annual Review of Earth and Planetary Sciences* **39**, 489-516.

Meister, P., Liu, B., Ferdelman, T.G., Jørgensen, B.B. and Khalili, A. (2013) Control of sulphate and methane distributions in marine sediments by organic matter reactivity. *Geochimica et Cosmochimica Acta* **104**, 183-193.

Milkov, A.V. (2004) Global estimates of hydrate-bound gas in marine sediments: How much is really out there? *Earth-Science Reviews* **66**, 183-197.

Milkov, A.V. (2005) Molecular and stable isotope compositions of natural gas hydrates: A revised global dataset and basic interpretations in the context of geological settings. *Organic Geochemistry* **36**, 681-702.

Milkov, A.V. and Sassen, R. (2002) Economic geology of offshore gas hydrate accumulations and provinces. *Marine and Petroleum Geology* **19**, 1-11.

Milkov, A.V., Claypool, G.E., Lee, Y.-J. and Sassen, R. (2005) Gas hydrate systems at Hydrate Ridge offshore Oregon inferred from molecular and isotopic properties of hydrate-bound and void gases. *Geochimica et Cosmochimica Acta* **69**, 1007-1026.

Milkov, A.V., Claypool, G.E., Lee, Y.-J., Torres, M.E., Borowski, W.S., Tomaru, H., Sassen, R. and Long, P.E. (2004a) Ethane enrichment and propane depletion in subsurface gases indicate gas hydrate occurrence in marine sediments at southern Hydrate Ridge offshore Oregon. *Organic Geochemistry* **35**, 1067-1080.

Milkov, A.V., Vogt, P.R., Crane, K., Lein, A.Y., Sassen, R. and Cherkashev, G.A. (2004b) Geological geochemical and microbial processes at the hydrate-bearing Håkon Mosby mud volcano: A review. *Chemical Geology* **205**, 347-366.

Millo, C., Sarnthein, M., Erlenkeuser, H. and Frederichs, T. (2005a) Methane-driven late Pleistocene δ^{13}C minima and overflow reversals in the southwestern Greenland Sea. *Geology* **33**, 873-876.

Millo, C., Sarnthein, M., Erlenkeuser, H., Grootes, P.M. and Andersen, N. (2005b) Methane-induced early diagenesis of foraminiferal tests in the southwestern Greenland Sea. *Marine Micropaleontology* **58**, 1-12.

Milucka, J., Ferdelman, T.G., Polerecky, L., Franzke, D., Wegener, G., Schmid, M., Lieberwirth, I., Wagner, M., Widdel, F. and Kuypers, M.M. (2012) Zero-valent sulphur is a key intermediate in marine methane oxidation. *Nature* **491**, 541-546.

Moller, L., Sowers, T., Bock, M., Spahni, R., Behrens, M., Schmidtt, J., Miller, H. and Fisher, H. (2013) Independent variations of CH_4 emissions and isotopic composition over the past 160,000 years. *Nature Geoscience* **6**, 885-890.

Myhre, G., Shindell, D., Bréon, F.-M., Collins, W., Fuglestvedt, J., Huang, J., Koch, D., Lamarque, J.-F., D. Lee, B.M., Nakajima, T., Robock, A., Stephens, G., Takemura, T. and Zhang, H. (2013) Anthropogenic and natural radiative forcing, in: Stocker, T.F., Qin, D., Plattner, G.-K., Tignor, M., Allen, S.K., Boschung, J., Nauels, A., Xia, Y., Bex, V., Midgley, P.M. (Eds.), Climate Change 2013: The Physical Science Basis. Contribution of Working Group I to the Fifth Assessment Report of the Intergovernmental Panel on Climate Change. Cambridge University Press, Cambridge, United Kingdom.

Nauhaus, K., Boetius, A., Krüger, M. and Widdel, F. (2002) *In vitro* demonstration of anaerobic oxidation of methane coupled to sulphate reduction in sediment from a marine gas hydrate area. *Environmental Microbiology* **4**, 296-305.

Naudts, L., Greinert, J., Artemov, Y., Staelens, P., Poort, J., Van Rensbergen, P. and De Batist, M. (2006) Geological and morphological setting of 2778 methane seeps in the Dnepr paleo-delta, northwestern Black Sea. *Marine Geology* **227**, 177-199.

Neef, L., van Weele, M. and van Velthoven, P. (2010) Optimal estimation of the present-day global methane budget. *Global Biogeochemical Cycles* **24**,GB4024.

Neretin, L., Böttcher, M., Jørgensen, B.B., Volkov, I.I., Lüschen, H. and Hilgenfeldt, K. (2004) Pyritization processes and greigite formation in the advancing sulfidization front in the Upper Pleistocene sediments of the Black Sea. *Geochimica et Cosmochimica Acta* **68**, 2081-2093.

Niemann, H., Losekann, T., de Beer, D., Elvert, M., Nadalig, T., Knittel, K., Amann, R., Sauter, E.J., Schluter, M., Klages, M., Foucher, J.P. and Boetius, A. (2006) Novel microbial communities of the Haakon Mosby mud volcano and their role as a methane sink. *Nature* **443**, 854-858.

Nightingale, P.D., Malin, G., Law, C.S., Watson, A.J., Liss, P.S., Liddicoat, M.I., Boutin, J. and Upstill-Goddard, R.C. (2000) In situ evaluation of air-sea gas exchange parameterizations using novel conservative and volatile tracers. *Global Biogeochemical Cycles* **14**, 373-387.

Nisbet, E.G. (2002) Have sudden large releases of methane from geological reservoirs occurred since the Last Glacial Maximum, and could such releases occur again? *Philosophical Transactions. Series A, Mathematical, Physical, and Engineering sciences* **360**, 581-607.

Nisbet, E.G., Allen, G., Cain, M., Dlugokencky, E.J., Fisher, R.E., France, J.L., Gallagher, M.W., Lowry, D., Myhre, C.L., Minshull, T.A., Pyle, J.A., C.D. Ruppel, Warwick, N.J., Westbrook, G.K. and Worthy, D.E.J. (2013) Response of methane sources to rapid Arctic warming. Nature.com Nature Publishing Group: <http://www.nature.com/nature/report/index.html?comment=59763&doi=10.1038/499401a>

Nisbet, E.G., Dlugokencky, E.J. and Bousquet, P. (2014) Methane on the rise—again. *Science* **343**, 493-495.

Nöthen, K. and Kasten, S. (2011) Reconstructing changes in seep activity by means of pore water and solid phase Sr/Ca and Mg/Ca ratios in pockmark sediments of the Northern Congo Fan. *Marine Geology* **287**, 1-13.

Notz, D., Brovkin, V. and Heimann, M. (2013) Arctic: Uncertainties in methane link. *Nature* **500**, 529.

Nuzzo, M., Hornibrook, E.R.C., Gill, F., Hensen, C., Pancost, R.D., Haeckel, M., Reitz, A., Scholz, F., Magalhães, V.H., Brückmann, W. and Pinheiro, L.M. (2009) Origin of light volatile hydrocarbon gases in mud volcano fluids, Gulf of Cadiz — Evidence for multiple sources and transport mechanisms in active sedimentary wedges. *Chemical Geology* **266**, 350-363.

O'Hara, K.D. (2008) A model for late Quaternary methane ice core signals: Wetlands versus a shallow marine source. *Geophysical Research Letters* **35**, L02712.

Oldfield, F., Darnley, I., Yates, G., France, D.E. and Hilton, J. (1992) Storage diagenesis versus sulphide authigenesis: possible implications in environmental magnetism. *Journal of Paleolimnology* **7**, 179-189.

Orcutt, B.N., Boetius, A., Lugo, S.K., MacDonald, I.R., Samarkin, V.A. and Joye, S.B. (2004) Life at the edge of methane ice: microbial cycling of carbon and sulfur in Gulf of Mexico gas hydrates. *Chemical Geology* **205**, 239-251.

Panieri, G. (2006) Foraminiferal response to an active methane seep environment: A case study from the Adriatic Sea. *Marine Micropaleontology* **61**, 116-130.

Panieri, G., Aharon, P., Sen Gupta, B.K., Camerlenghi, A., Ferrer, F.P. and Cacho, I. (2014a) Late Holocene foraminifera of Blake Ridge diapir: Assemblage variation and stable-isotope record in gas-hydrate bearing sediments. *Marine Geology* **353**, 99-107.

Panieri, G., Camerlenghi, A., Cacho, I., Cervera, C.S., Canals, M., Lafuerza, S. and Herrera, G. (2012) Tracing seafloor methane emissions with benthic foraminifera: Results from the Ana submarine landslide (Eivissa Channel, Western Mediterranean Sea). *Marine Geology* **291-294**, 97-112.

Panieri, G., James, R.H., Camerlenghi, A., Westbrook, G.K., Consolaro, C., Cacho, I., Cesari, V. and Sanchez Cervera, C. (2014b) Record of methane emissions from the West Svalbard continental margin during the last 23,500 years revealed by $\delta^{13}C$ of benthic foraminifera. *Global and Planetary Change* **122**, 151-160.

Pape, T., Bahr, A., Rethemeyer, J., Kessler, J.D., Sahling, H., Hinrichs, K.-U., Klapp, S.A., Reeburgh, W.S. and Bohrmann, G. (2010) Molecular and isotopic partitioning of low-molecular-weight hydrocarbons during migration and gas hydrate precipitation in deposits of a high-flux seepage site. *Chemical Geology* **269**, 350-363.

Parmentier, F.-J. W., Christensen, T.R., Sørensen, L.L., Rysgaard, S., McGuire, A.D., Miller, P.A. and Walker, D.A. (2013) The impact of lower sea-ice extent on Arctic greenhouse-gas exchange. *Nature Climate Change* **3**, 195-202.

Parmentier, F.-J.W. and Christensen, T.R. (2013) Arctic: Speed of methane release. *Nature* **500**, 529.

Peltier, W. R., and R. G. Fairbanks (2006), Global glacial ice volume and Last Glacial Maximum duration from an extended Barbados sea level record, *Quaternary Science Reviews*, **25**, 3322-3337.

Pena, L.D., Cacho, I., Calvo, E., Pelejero, C., Eggins, S. and Sadekov, A. (2008) Characterization of contaminant phases in foraminifera carbonates by electron microprobe mapping. *Geochemistry, Geophysics, Geosystems* **9**, Q07012.

Pena, L.D., Calvo, E., Cacho, I., Eggins, S. and Pelejero, C. (2005) Identification and removal of Mn-Mg-rich contaminant phases on foraminiferal tests: Implications for Mg/Ca past temperature reconstructions. *Geochemistry, Geophysics, Geosystems* **6**. Q09P02

Petrenko, V.V., Smith, A.M., Brook, E.J., Lowe, D., Riedel, K., Brailsford, G., Hua, Q., Schaefer, H., Reeh, N., Weiss, R.F., Etheridge, D. and Severinghaus, J.P. (2009) $^{14}CH_4$ Measurements in Greenland Ice: Investigating Last Glacial Termination CH_4 Sources. *Science* **324**, 506-508.

Phrampus, B.J. and Hornbach, M.J. (2012) Recent changes to the Gulf Stream causing widespread gas hydrate destabilization. *Nature* **490**, 527-530.

Piñero, E., Marquardt, M., Hensen, C., Haeckel, M. and Wallmann, K. (2013) Estimation of the global inventory of methane hydrates in marine sediments using transfer functions. *Biogeosciences* **10**, 959-975.

Pohlman, J.W., Bauer, J.E., Canuel, E.A., Grabowski, K.S., Knies, D.L., Mitchell, C.S., Whiticar, M.J. and Coffin, R.B. (2009) Methane sources in gas hydrate-bearing cold seeps: Evidence from radiocarbon and stable isotopes. *Marine Chemistry* **115**, 102-109.

Popinet, S., Smith, M. and Stevens, C. (2004) Experimental and numerical study of the turbulence characteristics of airflow around a research vessel. *Journal of Atmospheric and Oceanic Technology* **21**, 1575-1589.

Prinzhofer, A. and Pernaton, E. (1997) Isotopically light methane in natural gas: Bacterial imprint or diffusive fractionation? *Chemical Geology* **142**, 193-200.

Rajan, A., Mienert, J. and Bunz, S. (2012) Acoustic evidence for a gas migration and release system in Arctic glaciated continental margins offshore NW-Svalbard. *Marine and Petroleum Geology* **21**, 36-49.

Rasmussen, S.O., Andersen, K.K., Svensson, A.M., Steffensen, J.P., Vinther, B.M., Clausen, H.B., Siggaard-Andersen, M.L., Johnsen, S.J., Larsen, L.B., Dahl-Jensen, D., Bigler, M., Röthlisberger, R., Fischer, H., Goto-Azuma, K., Hansson, M.E. and Ruth, U. (2006) A new Greenland ice core chronology for the last glacial termination. *Journal of Geophysical Research* **111**, D06102.

Ravelo, A.C. and Hillaire-Marcel, C. (2007) The use of oxygen and carbon isotopes of foraminifera in paleoceanography, in: Hillaire-Marcel, C., de Vernal, A. (Eds.), Proxies in Late Cenozoic Paleoceanography. Elsevier Science & Technology, Amsterdam, NLD.

Reagan, M.T. and Moridis, G.J. (2007) Oceanic gas hydrate instability and dissociation under climate change scenarios. *Geophysical Research Letters* **34**, L22709.

Reagan, M.T. and Moridis, G.J. (2008) Dynamic response of oceanic hydrate deposits to ocean temperature change. *Journal of Geophysical Research* **113**, C12023.

Reagan, M.T. and Moridis, G.J. (2009) Large-scale simulation of methane hydrate dissociation along the West Spitsbergen Margin. *Geophysical Research Letters* **36**, L23612.

Reeburgh, W.S. (2007) Oceanic methane biogeochemistry. *Chemical Reviews* **107**, 486-513.

Regnier, P., Dale, A.W., Arndt, S., LaRowe, D.E., Mogollón, J. and Van Cappellen, P. (2011) Quantitative analysis of anaerobic oxidation of methane (AOM) in marine sediments: A modeling perspective. *Earth-Science Reviews* **106**, 105-130.

Rehder, G. and Suess, E. (2001) Methane and pCO_2 in the Kuroshio and the South China Sea during maximum summer surface temperatures. *Marine Chemistry* **75**, 89-108.

Rehder, G., Brewer, P., Peltzer, E. and Friederich, G. (2002) Enhanced lifetime of methane bubble streams within the deep ocean. *Geophysical Research Letters* **29**, 21-1 - 21-4.

Rehder, G., Keir, R.S., Suess, E. and Rhein, M. (1999) Methane in the northern Atlantic controlled by microbial oxidation and atmospheric history. *Geophysical Research Letters* **26**, 587-590.

Rehder, G., Leifer, I., Brewer, P.G., Friederich, G. and Peltzer, E.T. (2009) Controls on methane bubble dissolution inside and outside the hydrate stability field from open ocean field experiments and numerical modeling. *Marine Chemistry* **114**, 19-30.

Reimer, P.J., Bard, E., Bayliss, A., Beck, J.W., Blackwell, P.G., Ramsey, C.B., Buck, C.E., Cheng, H., Edwards, R.L., Friedrich, M., Grootes, P.M., Guilderson, T.P., Haflidason, H., Hajdas, I., Hatté, C., Heaton, T.J., Hoffmann, D.L., Hogg, A.G., Hughen, K.A., Kaiser, K.F., Kromer, B., Manning, S.W., Niu, M., Reimer, R.W., Richards, D.A., Scott, E.M., Southon, J.R., Staff, R.A., Turney, C.S.M. and Pli, J.v.d. (2013) INTCAL13 and MARINE13 radiocarbon age calibration curves 0-50,000 year Cal BP. *Radiocarbon* **55**, 1869-1887.

Rhee, T.S., Kettle, A.J. and Andreae, M.O. (2009) Methane and nitrous oxide emissions from the ocean: A reassessment using basin-wide observations in the Atlantic. *Journal of Geophysical Research* **114**, D12304.

Richards, K.J. (1990) Processes in the benthic boundary layer. *Philosophical Transactions of the Royal Society of London. Series A, Mathematical and Physical Sciences* **331**, 3-13.

Riedinger, N., Kasten, S., Gröger, J., Franke, C. and Pfeifer, K. (2006) Active and buried authigenic barite fronts in sediments from the Eastern Cape Basin. *Earth and Planetary Science Letters* **241**, 876-887.

Riedinger, N., Pfeifer, K., Kasten, S., Garming, J.F.L., Vogt, C. and Hensen, C. (2005) Diagenetic alteration of magnetic signals by anaerobic oxidation of methane related to a change in sedimentation rate. *Geochimica et Cosmochimica Acta* **69**, 4117-4126.

Ritger, S., Carson, B. and Suess, E. (1987) Methane-derived authigenic carbonates formed by subduction-induced pore-water expulsion along the Oregon/Washington margin. *Geological Society of America Bulletin* **98**, 147-156.

Römer, M., Torres, M., Kasten, S., Kuhn, G., Graham, A.G.C., Mau, S., Little, C.T.S., Linse, K., Pape, T., Geprägs, P., Fischer, D., Wintersteller, P., Marcon, Y., Rethemeyer, J. and Bohrmann, G. (2014) First evidence of widespread active methane seepage in the Southern Ocean, off the sub-Antarctic island of South Georgia. *Earth and Planetary Science Letters* **403**, 166-177.

Rosen, J.L., Brook, E.J., Severinghaus, J.P., Blunier, T., Mitchell, L.E., Lee, J.E., Edwards, J.S. and Gkinis, V. (2014) An ice core record of near-synchronous global climate changes at the Bølling transition. *Nature Geoscience* **7**, 459-463.

Rowan, C.J., Roberts, A.P. and Broadbent, T. (2009) Reductive diagenesis, magnetite dissolution, greigite growth and paleomagnetic smoothing in marine sediments: A new view. *Earth and Planetary Science Letters* **277**, 223-235.

Sahling, H., Romer, M., Pape, T., Berges, B., dos Santos Fereirra, C., Boelmann, J., Geprags, P., Tomczyk, M., Nowald, N., Dimmler, W., Schroedter, L., Glockzin, M. and Bohrmann, G. (2014) Gas emissions at the continental margin west of Svalbard: Mapping, sampling, and quantification. *Biogeosciences* **11**, 6029-6046.

Saloranta, T.M. and Haugan, P.M. (2004) Northward cooling and freshening of the warm core of the West Spitsbergen Current. *Polar Research* **23**, 79-88.

Saloranta, T.M. and Svendsen, H. (2001) Across the Arctic front west of Spitsbergen: High-resolution CTD sections from 1998-2000. *Polar Research* **20**, 177-184.

Sapart, C.J., van der Veen, C., Vigano, I., Brass, M., van de Wal, R.S.W., Bock, M., Fischer, H., Sowers, T., Buizert, C., Sperlich, P., Blunier, T., Behrens, M., Schmitt, J., Seth, B. and Röckmann, T. (2011) Simultaneous stable isotope analysis of methane and nitrous oxide on ice core samples. *Atmospheric Measurement Techniques* **4**, 2607-2618.

Sarkar, S., Berndt, C., Chabert, A., Masson, D.G., Minshull, T.A. and Westbrook, G.K. (2011) Switching of a paleo-ice stream in northwest Svalbard. *Quaternary Science Reviews* **30**, 1710-1725

Sarkar, S., Berndt, C., Minshull, T.A., Westbrook, G.K., Klaeschen, D., Masson, D.G., Chabert, A. and Thatcher, K.E. (2012) Seismic evidence for shallow gas-escape features associated with a retreating gas hydrate zone offshore west Svalbard. *Journal of Geophysical Research* **117**, B09102.

Sasakawa, M., Tsunogai, U., Kameyama, S., Nakagawa, F., Nojiri, Y. and Tsuda, A. (2008) Carbon isotopic characterization for the origin of excess methane in subsurface seawater. *Journal of Geophysical Research* **113**, C03012.

Sassen, R., Roberts, H.H., Carney, R., Milkov, A.V., DeFreitas, D.A., Lanoil, B. and Zhang, C. (2004) Free hydrocarbon gas, gas hydrate, and authigenic minerals in chemosynthetic communities of the northern Gulf of Mexico continental slope: relation to microbial processes. *Chemical Geology* **205**, 195-217.

Schaefer, H., Whiticar, M.J., Brook, E.J., Petrenko, V.V., Ferretti, D.F. and Severinghaus, J.P. (2006) Ice record of $\delta^{13}C$ for atmospheric CH_4 across the Younger Dryas-Preboreal transition. *Science* **313**, 1109-1112.

Schauer, U. (2004) Arctic warming through the Fram Strait: Oceanic heat transport from 3 years of measurements. *Journal of Geophysical Research* **109**, C06026.

Schmale, O., Greinert, J. and Rehder, G. (2005) Methane emission from high-intensity marine gas seeps in the Black Sea into the atmosphere. *Geophysical Research Letters* **32**, L07609.

Schmale, O., Haeckel, M. and McGinnis, D.F. (2011) Response of the Black Sea methane budget to massive short-term submarine inputs of methane. *Biogeosciences* **8**, 911-918.

Schneider von Deimling, J., Rehder, G., Greinert, J., McGinnnis, D.F., Boetius, A. and Linke, P. (2011) Quantification of seep-related methane gas emissions at Tommeliten, North Sea. *Continental Shelf Research* **31**, 867-878.

Schoell, M. (1983) Genetic characterization of natural gases. *American Association of Petroleum Geologists Bulletin* **67**, 2225-2238.

Shakhova, N., Semiletov, I., Leifer, I., Salyuk, A., Rekant, P. and Kosmach, D. (2010a) Geochemical and geophysical evidence of methane release over the East Siberian Arctic Shelf. *Journal of Geophysical Research* **115**, C08007.

Shakhova, N., Semiletov, I., Leifer, I., Sergienko, V., Salyuk, A., Kosmach, D., Chernykh, D., Stubbs, C., Nicolsky, D., Tumskoy, V. and Gustafsson, Ö. (2014) Ebullition and storm-induced methane release from the East Siberian Arctic Shelf. *Nature Geoscience* **7**, 64-70.

Shakhova, N., Semiletov, I., Salyuk, A., Yusupov, V., Kosmach, D. and Gustafsson, O. (2010b) Extensive methane venting to the atmosphere from sediments of the East Siberian Arctic Shelf. *Science* **327**, 1246-1250.

Sivan, O., Schrag, D.P. and Murray, R.W. (2007) Rates of methanogenesis and methanotrophy in deep-sea sediments. *Geobiology* **5**, 141-151.

Skarke, A., Ruppel, C., Kodis, M., Brothers, D. and Lobecker, E. (2014) Widespread methane leakage from the sea floor on the northern US Atlantic margin. *Nature Geoscience* **7**, 657-661.

Sloan, E.D. and Koh, C.A. (2008) Clathrate Hydrates of Natural Gases, 3rd ed. CRC Press, Taylor and Francis Group, Boca Raton, FL.

Sloan, E.D.J. (2003) Fundamental principles and applications of natural gas hydrates. *Nature* **426**, 353-359.

Smith, A.J., Mienert, J., Bunz, S. and Greinert, J. (2014) Thermogenic methane injection via bubble transport into the upper Arctic Ocean from the hydrate-charged Vestnesa Ridge, Svalbard. *Geochemistry Geophysics Geosystems* **15**, 1945-1959.

Snowball, I. and Thompson, R. (1988) The occurrence of Greigite in sediments from Loch Lomond. *Journal of Quaternary Science* **3**, 121-125.

Snyder, G.T., Dickens, G.R. and Castellini, D.G. (2007a) Labile barite contents and dissolved barium concentrations on Blake Ridge: New perspectives on barium cycling above gas hydrate systems. *Journal of Geochemical Exploration* **95**, 48-65.

Snyder, G.T., Hiruta, A., Matsumoto, R., Dickens, G.R., Tomaru, H., Takeuchi, R., Komatsubara, J., Ishida, Y. and Yu, H. (2007b) Pore water profiles and authigenic mineralization in shallow marine sediments above the methane-charged system on Umitaka Spur, Japan Sea. *Deep Sea Research Part II: Topical Studies in Oceanography* **54**, 1216-1239.

Solomon, E.A., Kastner, M., MacDonald, I.R. and Leifer, I. (2009) Considerable methane fluxes to the atmosphere from hydrocarbon seeps in the Gulf of Mexico. *Nature Geoscience* **2**, 561-565.

Spielhagen, R.F., Werner, K., Sorensen, S.A., Zamelczk, K., Kandiano, E., Budeus, G., Husum, K., Marchitto, T.M. and Hald, M. (2011) Enhanced modern heat transfer to the Arctic by warm Atlantic Water. *Science* **331**, 450-453.

Stanford, J. D., R. Hemingway, E. J. Rohling, P. G. Challenor, M. Medina-Elizalde, and A. J. Lester (2011), Sea-level probability for the last deglaciation: A statistical analysis of far-field records, *Global and Planetary Change*, **79**, 193-203.

Stein, R., Brass, G., Graham, D., Pimmel, A. and The Shipboard Scientific Party. (1995) Hydrocarbon measurements at Artic gateway sites, in: Myhre, A.M., Thiede, J., Firth, J.V. (Eds.), Proceedings of the Ocean Drilling Program, Initial Reports. Ocean Drilling Program, College Station, Texas.

Steinle, L., Graves, C.A., Treude, T., Ferre, B., Biastoch, A., Bussmann, I., Berndt, C., Krastel, S., James, R.H., Behrens, E., Böning, C.W., Greinert, J., Sommer, S., Sapart, C.-J., Lehmann, M.F. and Niemann, H. (In Review) Water column methanotrophy controlled by a rapid oceanographic switch. *Nature Geoscience*.

Stocker, T.F., Qin, D., Plattner, G.-K., Tignor, M., Allen, S.K., Boschung, J., Nauels, A., Xia, Y., Bex, V. and Midgley, P.M. (2013) Climate Change 2013: The Physical Science Basis. Contribution of Working Group I to the Fifth Assessment Report of the Intergovernmental Panel on Climate Change. Cambridge University Press, Cambridge, United Kingdom, p. 1535.

Stoner, J.S. and St-Onge, G. (2007) Magnetic stratigraphy in paleocraonography: reversals, excursions, paleointensity, and secular variation, in: Hillaire-Marcel, C., de Vernal, A. (Eds.), Proxies in Late Cenozoic Paleoceanography. Elsevier Science & Technology, Amsterdam, NLD.

Stott, L.D., Bunn, T., Prokopenko, M., Mahn, C., Gieskes, J. and Bernhard, J.M. (2002) Does the oxidation of methane leave an isotopic fingerprint in the geologic record? *Geochemistry Geophysics Geosystems* **3**, 2001GC000196.

Stuvier, M. and Reimer, P.J. (2014) CALIB Radiocarbon Calibration Program, 7.0.2 ed.

Suess, E. (2010) Marine cold seeps, in: Timmis, K.N. (Ed.), Handbook of Hydrocarbon and Lipid Microbiology. Spreinger-Verlang, Berlin, pp. 187-203.

Sun, X. and Turchyn, A.V. (2014) Significant contribution of authigenic carbonate to marine carbon burial. *Nature Geoscience* **7**, 201-204.

Sundermeyer, M.A. and Price, J.F. (1998) Lateral mixing and the North Atlantic Tracer Release Experiment: Observations and numerical simulations of Lagrangian particles and a passive tracer. *Journal of Geophysical Research* **103**, 481-497.

Sweeney, C., Gloor, E., Jacobson, A.R., Key, R.M., McKinley, G., Sarmiento, J.L. and Wanninkhof, R. (2007) Constraining global air-sea gas exchange for CO_2 with recent bomb ^{14}C measurements. *Global Biogeochemical Cycles* **21**, GB2015.

Teigen, S.H., Nilsen, F. and Gjevik, B. (2010) Barotropic instability in the West Spitsbergen Current. *Journal of Geophysical Research* **115**, C07016.

Thatcher, K.E., Westbrook, G.K., Sarkar, S. and Minshull, T.A. (2013) Methane release from warming-induced hydrate dissociation in the West Svalbard continental margin:

Timing, rates, and geological controls. *Journal of Geophysical Research: Solid Earth* **118**, 22-38.

Torres, M.E. (2003) Is methane venting at the seafloor recorded by $\delta^{13}C$ of benthic foraminifera shells? *Paleoceanography* **18**, 1062.

Torres, M.E., Borhrmann, G. and Suess, E. (1996a) Authigenic barites and fluxes of barium associated with fluid seeps in the Peru subduction zone. *Earth and Planetary Science Letters* **144**, 469-481.

Torres, M.E., Brumsack, H.J., Bohrmann, G. and Emeis, K.C. (1996b) Barite fronts in continental margin sediments: A new look at barium remobilization in the zone of sulfate reduction and formation of heavy barites in diagenetic fronts. *Chemical Geology* **127**, 125-139.

Torres, M.E., Martin, R.A., Klinkhammer, G.P. and Nesbitt, E.A. (2010) Post depositional alteration of foraminiferal shells in cold seep settings: New insights from flow-through time-resolved analyses of biogenic and inorganic seep carbonates. *Earth and Planetary Science Letters* **299**, 10-22.

Torres, M.E., Wallmann, K., Tréhu, A.M., Bohrmann, G., Borowski, W.S. and Tomaru, H. (2004) Gas hydrate growth, methane transport, and chloride enrichment at the southern summit of Hydrate Ridge, Cascadia margin off Oregon. *Earth and Planetary Science Letters* **226**, 225-241.

Treude, T., Boetius, A., Knittel, K., Wallmann, K. and Jorgensen, B.B. (2003) Anaerobic oxidation of methane above gas hydrates at Hydrate Ridge, NE Pacific Ocean. *Marine Ecology Progress Series* **264**, 1-14.

Treude, T., Krause, S., Maltby, J., Dale, A.W., Coffin, R. and Hamdan, L.J. (2014) Sulfate reduction and methane oxidation activity below the sulfate-methane transition zone in Alaskan Beaufort Sea continental margin sediments: Implications for deep sulfur cycling. *Geochimica et Cosmochimica Acta* **144**, 217-237.

Valentine, D.L. (2011) Emerging Topics in Marine Methane Biogeochemistry. *Annual Review of Marine Science* **3**, 147-171.

Valentine, D.L. and Reeburgh, W.S. (2000) New perspectives on anaerobic methane oxidation. *Environmental Microbiology* **2**, 477-484.

Vanneste, H., Kelly-Gerreyn, B.A., Connelly, D.P., James, R.H., Haeckel, M., Fisher, R.E., Heeschen, K. and Mills, R.A. (2011) Spatial variation in fluid flow and geochemical fluxes across the sediment–seawater interface at the Carlos Ribeiro mud volcano (Gulf of Cadiz). *Geochimica et Cosmochimica Acta* **75**, 1124-1144.

Vanneste, H.L.A.E. (2010) Seepage of Hydrocarbon Bearing Fluids at the Carlos Riberiro and Darwin Mud Volcanoes (Gulf of Cardiz), Faculty of Natural and Environmental Sciences, School of Ocean and Earth Science. University of Southampton, Southampton, p. 204.

Vanneste, M., Guidard, S. and Mienert, J. (2005) Bottom-simulating reflections and geothermal gradients across the western Svalbard margin. *Terra Nova* **00**, 1-7.

Vogt, P.R., Crane, K., Sundvor, E., Max, M.D. and Pfirman, S.L. (1994) Methane-generated(?) pockmarks on young, thickly sedimented oceanic crust in the Arctic: Vestnesa ridge, Fram strait. *Geology* **22**, 255-258.

Vogt, P.R., Gardner, J. and Crane, K. (1999) The Norwegian-Barents-Svalbard (NBS) continental margin: Introducing a natural laboratory of mass wasting, hydrates, and ascent of sediment, pore water, and methane. *Geo-Marine Letters* **19**, 2-21.

Wallmann, K., Pinero, E., Burwicz, E., Haeckel, M., Hensen, C., Dale, A. and Ruepke, L. (2012) The global inventory of methane hydrate in marine sediments: A theoretical approach. *Energies* **5**, 2449-2498.

Wanninkhof, R. (1992) Relationship between wind speed and gas exchange over the ocean. *Journal of Geophysical Research* **97**, 7373-7382.

Wanninkhof, R. and McGillis, W.R. (1999) A cubic relationship between air-sea CO_2 exchange and wind speed. *Geophysical Research Letters* **26**, 1889-1892.

Wanninkhof, R., Asher, W.E., Ho, D.T., Sweeney, C. and McGillis, W.R. (2009) Advances in quantifying air-sea gas exchange and environmental forcing. *Annual Review of Marine Science* **1**, 213-244.

Warzinski, R.P., Lynn, R., Haljasmaa, I., Leifer, I., Shaffer, F., Anderson, B.J. and Levine, J.S. (2014) Dynamic morphology of gas hydrate on a methane bubble in water: Observations and new insights for hydrate film models. *Geophysical Research Letters* **41**, 6841-6847.

Weber, T.C., Mayer, L., Jerram, K., Beaudoin, J., Rzhanov, Y. and Lovalvo, D. (2014) Acoustic estimates of methane gas flux from the seabed in a 6000 km^2 region in the Northern Gulf of Mexico. *Geochemistry, Geophysics, Geosystems* **15**, 1911-1925.

Weiss, R.F. (1974) Carbon dioxide in water and seawater: the solubility of a non-ideal gas. *Marine Chemistry* **2**, 203-215.

Werner, K., Spielhagen, R.F., Bauch, D., Hass, H.C. and Kandiano, E. (2013) Atlantic Water advection versus sea-ice advances in the eastern Fram Strait during the last 9 ka: Multiproxy evidence for a two-phase Holocene. *Paleoceanography* **28**, 1-13.

Westbrook, G.K., Thatcher, K.E., Rohling, E.J., Piotrowski, A.M., Pälike, H., Osborne, A.H., Nisbet, E.G., Minshull, T.A., Lanoisellé, M., James, R.H., Hühnerbach, V., Green, D., Fisher, R.E., Crocker, A.J., Chabert, A., Bolton, C., Beszczynska-Möller, A., Berndt, C. and Aquilina, A. (2009) Escape of methane gas from the seabed along the West Spitsbergen continental margin. *Geophysical Research Letters* **36**, L15608.

Whiteman, G., Hope, C. and Wadhams, P. (2013) Vast costs of Arctic change. *Nature* **299**, 401-403.

Whiticar, M.J. (1999) Carbon and hydrogen isotope systematics of bacterial formation and oxidation of methane. *Chemical Geology* **161**, 291-314.

Wiesenburg, D.A. and Guinasso, N.L.J. (1979) Equilibrium solubilities of methane, carbon monoxide, and hydrogen in water and sea water. *Journal of Chemical and Engineering Data* **24**, 356-360.

Winkelmann, D. and Knies, J. (2005) Recent distribution and accumulation of organic carbon on the continental margin west off Spitsbergen. *Geochemistry Geophysics Geosystems* **6**, Q09012.

Wollenburg, J.E. and Kuhnt, W. (2000) The response of benthic foraminifers to carbon flux and primary productive in the Arctic Ocean. *Marine Micropaleontology* **40**, 189-231.

Wollenburg, J.E. and Mackensen, A. (1998) On the vertical distribution of living (Rose Bengal stained) benthic foraminifers in the Arctic Ocean. *Journal of Foraminiferal Research* **28**, 268-285.

Wuebbles, D.J. and Hayhoe, K. (2002) Atmospheric methane and global change. *Earth-Science Reviews* **57**, 177-210.

Xu, W. and Ruppel, C. (1999) Predicting the occurrence, distribution, and evolution of methane gas hydrate in porous marine sediments. *Journal of Geophysical Research* **104**, 5081-5095.

Yoshida, O., Inoue, H.Y., Watanabe, S., Suzuki, K. and Noriki, S. (2011) Dissolved methane distribution in the South Pacific and the Southern Ocean in austral summer. *Journal of Geophysical Research* **116**, C07008.

Yoshikawa, C., Hayashi, E., Yamada, K., Yoshida, O., Toyoda, S. and Yoshida, N. (2014) Methane sources and sinks in the subtropical South Pacific along 17°S as traced by stable isotope ratios. *Chemical Geology* **382**, 24-31.

Yoshinaga, M.Y., Holler, T., Goldhammer, T., Wegener, G., Pohlman, J.W., Brunner, B., Kuypers, M.M.M., Hinrichs, K.-U. and Elvert, M. (2014) Carbon isotope equilibration during sulfate-limited anaerobic oxidation of methane. *Nature Geoscience* **7**, 190-194.

Zabel, M. and Schulz, H.D. (2001) Importance of submarine landslides for non-steady state conditions in pore water systems - lower Zaire (Congo) deep-sea fan. *Marine Geology* **176**, 87-99.

Zachos, J.C., Bohaty, S.M., John, C.M., McCarren, H., Kelly, D.C. and Nielsen, T. (2007) The Palaeocene-Eocene carbon isotope excursion: Constraints from individual shell planktonic foraminifer records. *Philosophical Transactions. Series A, Mathematical, Physical, and Engineering Sciences* **365**, 1829-1842.

Zamelczyk, K., Rasmussen, T.L., Husum, K., Godtliebsen, F. and Hald, M. (2014) Surface water conditions and calcium carbonate preservation in the Fram Strait during marine isotope stage 2, 28.8-15.4 kyr. *Paleoceanography* **29**, 1-12.

Zhang, T. and Krooss, B.M. (2001) Experimental investigation on the carbon isotope fractionation of methane during gas migration by diffusion through sedimentary rocks at elevated temperature and pressure. *Geochimica et Cosmochimica Acta* **65**, 2723-2742.

Zhang, Y., Zhao, H.D., Zhai, W.D., Zang, K.P. and Wang, J.Y. (2014) Enhanced methane emissions from oil and gas exploration areas to the atmospherethe central Bohai Sea. *Marine Pollution Bulletin* **81**, 157-165.